



Université du Québec à Chicoutimi

**Improvement of Mechanical Strength and Electrical
Conductivity in 6xxx Series Aluminum Conductor Alloys**

By

Siamak Nikzad Khangholi

Under supervision of Prof. X.-Grant Chen and co-supervision of Prof. Mousa Javidani

**Manuscript-Based Thesis Presented to Université du Québec à Chicoutimi in Partial
Fulfillment of the Requirements for the Degree of Doctor of Philosophy Ph.D.**

Defended on 08 December 2021

BOARD OF EXAMINERS:

Professor Dilip Sarkar, department of Applied Sciences at UQAC, President of the board of examiners

Dr. Paul Rometsch, Rio Tinto Aluminum, Saguenay, Quebec, External Member of examiners

Professor Emad Elgallad, department of Applied Sciences at UQAC, Internal Member of examiners

Professor X.-Grant Chen, department of Applied Sciences at UQAC, Internal Member of examiners

Professor Mousa Javidani, department of Applied Sciences at UQAC, Internal Member of examiners

Québec, Canada

© Siamak Nikzad Khangholi, 2021

Amélioration de la résistance mécanique et de la conductivité électrique dans les alliages conducteurs d'aluminium de la série 6xxx

Résumé

L'exigence industrielle de faible densité, de haute résistance mécanique et de conductivité électrique (CE) a mené au développement d'alliages conducteurs Al-Mg-Si pour la ligne de transport d'énergie. Les précipités, les dislocations, les atomes de soluté et les joints de grains augmentent les résistances mécaniques des alliages conducteurs Al-Mg-Si. Cependant, ceux-ci augmentent la résistivité électrique à cause des perturbations de la périodicité atomique dans une structure cristalline. En conséquence, les paramètres améliorant la résistance mécanique engendrent la résistivité électrique dans les alliages conducteurs Al-Mg-Si, montrant que la résistance mécanique et la conductivité électrique sont de comportement contradictoire. Par conséquent, l'amélioration simultanée de la résistance mécanique et la conductivité électrique représente un défi à relever. Dans cette étude, de meilleures combinaisons de résistances mécaniques et de CE dans les alliages conducteurs Al-Mg-Si ont été obtenues grâce à (a) des éléments d'alliage principaux optimaux (Mg et Si); b) le vieillissement naturel et la modification du traitement thermomécanique; c) des éléments d'alliage supplémentaires (Ag et Cu).

Dans la première partie de cette étude, l'effet des différents rapports Mg/Si (2, 1.5, 1, 0.86) sur la résistance mécanique et la CE des alliages conducteurs Al-Mg-Si a été étudié. La valeur du Mg a été maintenue constante (0,65 % en masse) et les quantités de Si ont été modifiées. Il est constaté que la résistance mécanique maximale augmentait avec la diminution du rapport Mg/Si tandis que la CE correspondante diminuait. Par conséquent, un temps de vieillissement plus long a été nécessaire pour que les alliages ayant un rapport Mg/Si inférieur répondent au minimum requis en CE (52,5 % IACS). L'alliage avec un rapport Mg/Si de 0,86 a montré la résistance mécanique maximale la plus élevée parmi tous les alliages. Cependant, il était essentiel de prolonger le temps de vieillissement (>34 h) pour dépasser la CE (52,5 % IACS), ce qui entraînait une baisse significative de la résistance mécanique avec une marge étroite de résistances mécaniques et d'CE. L'alliage avec un rapport Mg/Si de ~ un a montré la résistance mécanique la plus élevée dans la gamme CE (52,5-54 % IACS). Le modèle de résistances mécaniques développé a montré qu'une résistance mécanique plus élevée de cet alliage pouvait

correspondre aux contributions plus élevées du durcissement par précipité, du durcissement par l'écrouissage et du durcissement par solutés. Cependant, si la CE est la priorité, l'alliage avec un rapport Mg/Si de $\sim 1,5$ a montré un meilleur compromis entre la résistance mécanique et la CE à une CE élevée de (54-56 % IACS).

Dans la deuxième partie, les impacts du vieillissement naturel et du traitement thermomécanique modifié sur la résistance mécanique et la CE des alliages conducteurs Al-Mg-Si étirés ont été étudiés. Les échantillons vieillis naturellement sont ceux exposés à 70 °C pendant 10 h ou 20 h suivis de deux semaines à température ambiante. Le traitement thermomécanique modifié est appelé pré-vieillissement pendant 5 h à 180 °C avant tréfilage. Les résultats du DSC ont montré que le vieillissement naturel avait une influence négative sur les précipitations avant le processus de tréfilage. Cependant, le tréfilage a pu neutraliser l'effet néfaste du vieillissement naturel sur le durcissement par précipitation après le tréfilage et le post-vieillissement. En d'autres mots, les échantillons naturellement vieillis présentaient une résistance mécanique plus élevée à une CE au dessus de (52.5 % IACS) par rapport à ceux des échantillons sans vieillissement naturel. L'analyse de la microscopie électronique en transmission (MET) a révélé que les échantillons naturellement vieillis avaient des densités numériques de précipités plus élevées par rapport à celles des échantillons qui n'étaient pas exposés au vieillissement naturel. Le modèle de résistances mécaniques a également montré un durcissement par précipité plus élevé dans les échantillons naturellement vieillis par rapport aux échantillons sans vieillissement naturel. Le traitement thermomécanique a été modifié par le pré-vieillissement (5h à 180 °C) avant le tréfilage. En conséquence, le traitement thermomécanique modifié a mené à la résistance mécanique la plus élevée (369 MPa) avec une CE acceptable (53% IACS) parmi toutes les conditions. Les modèles de résistances mécaniques et de résistivité électrique ont montré que le traitement thermomécanique modifié a mené à un durcissement par précipité remarquablement et plus élevé avec une résistivité électrique moyenne. Il a également été constaté que la contribution au durcissement par écrouissage diminuait avec le traitement thermomécanique modifié. Cependant, il s'est révélé que le durcissement par précipité était plus élevé et a surmonté le durcissement par écrouissage qui était moins élevé dans le traitement thermomécanique modifié.

Dans la troisième partie, les effets des additions d'Ag et de Cu sur la résistance mécanique et la CE des alliages conducteurs Al-Mg-Si ont été étudiés par le traitement thermomécanique

conventionnel et modifié. Semblable à la deuxième partie, le traitement thermomécanique modifié est référé à un traitement dans lequel le pré-vieillessement a été appliqué sur les échantillons avant le tréfilage. Les alliages avec Ag-/Cu ajoutés ont montré une résistance mécanique légèrement supérieure par rapport à l'alliage de base à une CE au dessus de (52,5 % IACS) sous le traitement thermomécanique conventionnel. Cependant, la modification du traitement thermomécanique a remarquablement amélioré l'effet de durcissement par ajout d'Ag et de Cu à une CE au-dessus de (52,5 % IACS). De plus, le traitement thermomécanique modifié a réduit le temps du vieillissement pour atteindre la CE minimale requise (52,5 % IACS) par rapport au traitement thermomécanique conventionnel (en particulier pour les alliages à Cu ajouté). Le modèle de résistance mécanique a montré que la modification du traitement thermomécanique augmentait le durcissement par précipité de l'alliage de base de 60%, bien qu'il ait détérioré le durcissement par écrouissage. Les ajouts d'Ag et de Cu ont encore amélioré le durcissement par précipité sous le traitement thermomécanique modifié. Malgré le durcissement par écrouissage réduit, les précipités sont les facteurs prometteurs pour faire durcir les matériaux sous le traitement thermomécanique modifié. Le modèle de résistivité électrique a montré que les précipités ont causé la résistivité électrique moyenne.

Pour toutes les parties du projet, les caractéristiques microstructurelles ont été quantitativement adaptées à la résistance mécanique et à l'CE à l'aide des modèles de résistance mécanique et de résistivité électrique.

Improvement of Mechanical Strength and Electrical Conductivity in 6xxx Series

Aluminum Conductor Alloys

Abstract

The industrial requirement for low density, high strength, and desirable electrical conductivity (EC) have led to the development of Al-Mg-Si conductor alloys for the power transmission line. The precipitates, dislocations, solute atoms, and grain boundaries result in strengthening the Al-Mg-Si conductor alloys. However, these give rise to electrical resistivity due to disruptions in atomic periodicity in a crystal structure. Accordingly, the parameters improving the strength cause the electrical resistivity in Al-Mg-Si conductor alloys, showing conflicting behaviors of strength and EC. Therefore, the concurrent improvement in strength and EC turns out as a challenging issue. In this study, better combinations of strength and EC in Al-Mg-Si conductor alloys were obtained through (a) optimum principal alloying elements (Mg and Si); (b) natural aging and the modification of the thermo-mechanical treatment; (c) additional alloying elements (Ag and Cu).

In the first part of this study, the effect of the various Mg/Si ratios (2, 1.5, 1, 0.86) on the strength and EC of Al-Mg-Si conductor alloys was investigated. The Mg content was kept constant (0.65 wt.%) while the Si amounts were changed. It was found that the peak strength increased with decreasing the Mg/Si ratio while the corresponding EC reduced. Therefore, a longer aging time was required for the alloys with a lower Mg/Si ratio to fulfill the minimum required EC (52.5 %IACS). The alloy with an Mg/Si ratio of 0.86 showed the highest peak strength among all alloys. However, prolonging the aging time (>34 h) was essential to exceed EC (52.5 %IACS), causing a significant drop in the strength with a narrow window of strength and EC. The alloy with Mg/Si ratio of ~ one showed the highest strength in the range of EC (52.5-54 %IACS). The developed strength model exhibited that the higher strength of this alloy could correspond to the higher contributions of the precipitate strengthening, strain hardening, and solute hardening. However, if EC is the main concern, the alloy with Mg/Si ratio of ~ 1.5 showed a better trade-off between strength and EC at high end EC (54-56 %IACS).

In the second part, the impacts of natural aging and the modified thermomechanical treatment on the strength and EC of the drawn Al-Mg-Si conductor alloys were studied. The natural aged

samples is referred to those exposed to 70 °C for 10 h or 20 h followed by two weeks at room temperature. The modified thermomechanical treatment is referred to the pre-aging for 5 h at 180 °C before wire drawing. DSC results showed that natural aging had a negative influence on precipitation before the drawing process. However, wire drawing could neutralize the detrimental effect of natural aging on precipitation hardening. In other word, the naturally aged samples exhibited a higher strength above EC (52.5 %IACS) relative to those of the samples without natural aging. The TEM analysis revealed that the naturally aged samples had the higher precipitate number densities relative to those of the samples that were not exposed to natural aging. The strength model also showed the higher precipitate strengthening in the naturally aged samples relative to the samples without natural aging. The thermomechanical treatment was modified with applying the pre-aging (5h at 180 °C) before the wire drawing. Accordingly, the modified thermomechanical treatment led to the highest ultimate tensile strength (369 MPa) with a desirable EC (53% IACS) among all conditions. The strength and electrical resistivity models showed that the modified thermomechanical treatment resulted in a remarkably higher precipitate strengthening with a medium electrical resistivity. It was also found that strain hardening contribution reduced with the modified thermomechanical treatment. However, it revealed that the superior precipitate strengthening overcame the inferior strain hardening in the modified thermomechanical treatment.

In the third part, the effects of Ag and Cu additions on strength and EC of Al-Mg-Si conductor alloys were studied under the conventional and modified thermomechanical treatment. Similar to the second part, the modified thermomechanical treatment is referred to a treatment in which pre-aging was applied to the samples before wire drawing. The Ag-/Cu-added alloys showed a slightly higher strength relative to the base alloy above EC (52.5 %IACS) under the conventional thermomechanical treatment. However, the modification of the thermomechanical treatment remarkably improved the strengthening effect of Ag and Cu additions above 52.5 %IACS. In addition, the modified thermomechanical treatment shortened the post-aging time to reach the minimum required EC (52.5 %IACS) compared to the conventional thermomechanical treatment (especially for Cu-added alloys). The strength model showed that modifying the thermomechanical treatment increased the precipitate hardening for the base alloy by 60%, although it deteriorated the strain hardening. The Ag and Cu additions further improved the precipitate hardening under the modified thermomechanical treatment. In spite of the reduced

strain hardening, the precipitates are the promising factors to strengthen the materials under the modified thermomechanical treatment. The electrical resistivity model exhibited that precipitates gave rise to the medium electrical resistivity.

For all parts of the project, the microstructural features were quantitatively tailored to the mechanical strength and EC using the strengthening and electrical resistivity models.

Table of Contents

Résumé	III
Abstract	VI
Table of Contents	IX
List of Tables	XII
List of Figures.....	XIII
List of Abbreviations.....	XVIII
List of Symbols.....	XX
DEDICATION.....	XXIV
ACKNOWLEDGMENT	XXV
Chapter 1 : Introduction	1
1.1. Problem statement.....	3
1.2. Objectives.....	5
1.3. Originality statement.....	7
1.4. Thesis outline.....	9
1.5. References	10
Chapter 2 : Critical review on recent progress in Al-Mg-Si 6xxx conductor alloys (Article1) ...	13
2.1. Introduction	14
2.2. Fabrication processes of 6xxx electrical conductors	18
2.3. Effects of chemical composition on strength and EC	20
2.3.1. Principal alloying elements (Mg and Si).....	20
2.3.2. Additional alloying elements.....	26
2.3.3. Grain refiners and modifiers.....	32
2.4. Effects of thermal and thermomechanical treatments on strength and EC	34
2.4.1. Thermomechanical treatments.....	34
2.4.2. Severe plastic deformation	46
2.5. Recent development in modeling Al-Mg-Si conductor properties.....	53
2.5.1. Strength model in Al-Mg-Si alloys.....	53
2.5.2. Electrical resistivity model.....	56
2.5.3. Case study of strength and electrical resistivity models	57
2.6. Summary	60

2.7. References	62
Chapter 3 : Optimization of mechanical properties and electrical conductivity in Al-Mg-Si 6201 alloys with different Mg/Si ratios (Article2)	70
3.1. Introduction	71
3.2. Experimental procedure	73
3.3. Results	75
3.3.1. Mechanical properties and EC.....	75
3.3.2. DSC analysis	78
3.3.3. Strain hardening of cold wire drawing.....	80
3.3.4. Microstructures	80
3.4. Discussion	83
3.4.1. Correlation between strength and EC	83
3.4.2. Strengthening mechanisms.....	85
3.4.3. Comparison of achievable strength and EC in Al-Mg-Si conductor alloys.....	91
3.5. Conclusions	92
Acknowledgment.....	93
3.6. References	94
Chapter 4 : Effects of natural aging and pre-aging on the strength and electrical conductivity in Al-Mg-Si AA6201 conductor alloys (Article3).....	97
4.1. Introduction	98
4.2. Experimental procedure	101
4.3. Results	104
4.3.1. Strength and EC.....	104
4.3.2. DSC analysis	108
4.3.3. TEM microstructural analysis	110
4.3.4. Strain hardening contribution.....	114
4.4. Discussion	116
4.4.1. Constitutive modeling for strength and EC.....	116
4.4.2. Microstructural evolution.....	124
4.5. Conclusions	128
Acknowledgements	130
Credit authorship contribution statement.....	130
4.6. References	131
Chapter 5 : Effect of Ag and Cu additions on the strength and electrical conductivity in Al-Mg-Si alloys using conventional and modified thermomechanical treatment (Article4).....	134

5.1. Introduction	135
5.2. Experimental procedure	138
5.3. Results	140
5.3.1. Mechanical and electrical properties	140
5.3.2. DCS results.....	145
5.3.3. Precipitate observation by TEM.....	149
5.3.4. Effect of wire drawing on strength and EC.....	156
5.4. Discussion	158
5.4.1. Strength and EC model	158
5.4.2. Correlation between strength and electrical conductivity	167
5.5. Conclusions	169
5.6. References	171
Chapter 6 Conclusions	175
General conclusions.....	175
Recommendations	179
Appendix I: Supporting information for article 2.....	180
Appendix II: The general description of procedure.....	182
List of the publications	185
Journal papers:.....	185
Posters	185
Presentation	186

List of Tables

Table 2.1: Mechanical and electrical properties of the heat-treated wires defined in EN-50183, ASTM B398 and ASTM B317 for Al–Mg–Si alloys	18
Table 2.2: Chemical composition (wt.%) of the studied alloys [24].	23
Table 2.3: Effect of Zr content of Al–Mg–Si alloys on mechanical and electrical properties [62].	28
Table 2.4: Mechanical properties and EC in AA6201 with La addition [64].	29
Table 2.5: Microstructure, mechanical properties and EC of AA6201 alloy at the different conditions (d, grain size; dp, precipitate size; a, lattice parameter; CG, coarse grain; UFG, ultrafine grain) [16].	48
Table 3.1: The chemical composition of experimental alloys with various Mg/Si ratios.....	74
Table 5.1: Chemical compositions of all studied alloys (wt.%)	139
Table(AII) 1: General description of the hot rolling process	184

List of Figures

Figure 2.1: Scheme of AAAC and ACSR conductors with their cross section [8].	15
Figure 2.2: Plot of strength versus EC for several commercial aluminum alloys [12].	16
Figure 2.3: Production chain of Properzi process followed by wire drawing and aging treatment for aluminum conductive cables	20
Figure 2.4: (a) Strength and (b) EC as a function of aging time at 180°C. (c) strength versus EC for all aging times for 6101 alloy samples [24].	23
Figure 2.5: Hardness as a function of EC for Al-Mg-Si-Sc alloys with different grain size and Mg/Si ratio, of which the best hardness/EC combination are selected for all sets of samples. The line is a guide for the eyes [25].	25
Figure 2.6: The relation between electrical resistivity and (a) yield strength (b) tensile strength for Al-0.72Mg-0.71Si and Al-0.56Mg-0.56Si alloys at different aging temperatures (100-240 °C) and various aging times(0-24 h) [61].	26
Figure 2.7: Effect of solutes on the electrical conductivity of 99.99% Aluminum [6].	27
Figure 2.8: (a) EC (b) UTS in Al-0.5Mg-0.35Si alloys with/without Fe over ageing times [14].	30
Figure 2.9: (a) A plot of strength and EC for AA6201 alloy with element additions for wires with 2.65 mm (width) square (b) enlarged view of (a) [12].	32
Figure 2.10: (a) % improvement in EC versus time after AlB ₂ addition (b) % improvement in EC versus boron excess [5]	33
Figure 2.11: The plot of the strength and EC for samples with NA (10NA and 20NA), NA followed by preaging (20NA-PA), and without NA; all samples followed by cold wire drawing and aging at 180 °C. Reprinted with permission from [37].	38
Figure 2.12: TEM images of (a) No-NA sample aged for 5 h (b) 20NA sample aged for 5 h (c) 20NA-PA sample aged for 5 h, (d) the precipitate number densities and (e) the average length and the cross section of precipitates. A and B correspond to the cross-sectional projections of lath-like and needle-shaped precipitates in <002> direction; C and D correspond to the longitudinal projections lath-like and needle-shaped precipitates, respectively. Reprinted with permission from [37]	39
Figure 2.13: (a) hardness vs. electrical conductivity in Al–Mg–Si–Cu alloys treated by C-TMP and M-TMP; (b) mechanical properties of the C-TMP and M-TMP samples re-aged at 180 °C [19].	43
Figure 2.14: (a) Microhardness (b) EC for AA6101 processed by HPT at room temperature followed by artificial aging at various temperatures. Microhardness of the sample for T4 and T6 tempers are brought for comparison purpose [18].	49
Figure 2.15: A comparison of strength and EC for (AL2–AL7) in EN 50183 standard (green box) with those obtained by severe plastic deformation (red box) for AA6201 alloy [16].	50
Figure 2.16: (a) Hardness (b) EC for AA6101 exposed to different hydrostatic extrusion (HE) reductions and aged at 180 °C up to 24 h [33].	52

Figure 2.17: EBSD microstructure images of AA6101 Alloy after 2, 4, and 8 passes of ECAP-BP (a–c) without aging, (d–f) BP after aging at 130 °C for 72 h, in the sample cross section [98].	53
Figure 2.18: The contribution to the strength and electrical resistivity from precipitates (mean precipitate spacing = 50 nm), dislocations (density = 10^{15} m^{-2}), grain boundaries (grain size = 400 nm) and solutes (Mg = 0.3 wt.% and Si = 0.3 wt.%)	60
Figure. 3.1: Scheme of the wire fabrication process	75
Figure. 3.2: Evolution of (a) microhardness (b) UTS (c) elongation to failure (d) EC as a function of aging time	77
Figure. 3.3: (a) UTS versus EC of four alloys and (b) the enlarged view of the right corner of Figure. 3.3a above the minimum UTS and EC requirements (305 MPa and 52.5% IACS)	78
Figure. 3.4: (a) DSC curves of the different alloys in the as-drawn condition (b) the enlarged view of the precipitation peak I	79
Figure. 3.5: Grain structures of (a) Si4-3h, (b) Si6-5h, and (c) Si9-34h alloys parallel in the drawing direction; (d) the average grain sizes of three alloys	81
Figure. 3.6: Bright field TEM micrographs for (a) Si4-3h, (b) Si6-5h, and (c) Si9-34h alloys (d) the mean precipitate length and (e) the average number density of precipitates	83
Figure. 3.7: (a) UTS as a function of Mg/Si ratio and (b) Hardness as a function of EC above the minimum required EC (52.5% IACS) for four alloys	85
Figure. 3.8: Comparison between calculated and experimentally measured hardness for the Si4-3h, Si6-5h and Si9-34h alloys	89
Figure. 3.9: Comparison of hardness and EC of various Al-Mg-Si conductor alloys	92
Figure. 4.1: Schematic Properzi process for aluminum conductive wires	99
Figure. 4.2: A scheme of the experimental procedures (a) without natural aging (b) with natural aging (c) natural aging combined with pre-aging. Arrows show where wire drawing was applied	104
Figure. 4.3: Evolution of (a) HV hardness and (b) EC as a function of the aging time, (c) HV hardness as a function of EC for all aging times and (d) enlarged HV hardness as a function of EC above 52 % IACS. Error bars are omitted for the clarity in Figure. 4.3d.	107
Figure. 4.4: (a) the ultimate tensile strengths above 52.5 %IACS along with their EC values and (b) comparison of the ultimate tensile strengths of the present work with the materials referred in EN 50183 standard [24] for the $\phi 4.7$ mm wires.	108
Figure. 4.5: DSC curves of the samples under different natural aging conditions, (a) before wire drawing, (b) a close view of peaks I in Figure. 4.5a, (c) after wire drawing and (d) an enlarged view of peaks I _d in Figure. 4.5c.	110
Figure. 4.6: Bright-field TEM micrographs of (a) No-NA sample after 5 h aging (b) 20NA sample after 5 h aging (c) 20NA-PA sample after 5 h aging, (d) the number density of precipitates and (e) the average length and the cross section of precipitates.	113
Figure. 4.7: (a) precipitates formed along the dislocations in No-NA sample at peak aging condition, (b) No-NA sample aged for 5 h, and (c) 20NA sample aged for 5 h. A and B	

correspond to the cross-sectional projections of lath-like and needle-shaped precipitates in $\langle 002 \rangle$ direction; C and D correspond to the longitudinal projections lath-like and needle-shaped precipitates, respectively.....	113
Figure. 4.8: Bright-field TEM micrographs of 20NA-PA samples (a) before wire drawing, (b) after wire drawing, (c) after wire drawing and 5 h aging, (d) the precipitate number density and (e) the average precipitate length and their cross section.	114
Figure. 4.9: The hardness increments via strain hardening from wire drawing in three samples.	115
Figure. 4.10: The dislocation cell substructures for (a) No-NA ; (b) 20NA ; (c) 20NA-PA samples after 5 h aging taken from $\langle 011 \rangle$ zone axis close to (111) planes.....	116
Figure. 4.11: The comparison between predicted and experimentally measured hardness for the No-NA, 20NA, and 20NA-PA samples aged at 180 °C for 5 h.	121
Figure. 4.12: Plot of the hardness vs the electrical conductivity (% IACS) for estimated and measured values for all drawn samples.....	124
Figure 4.13: Sketches to illustrate the microstructural evolution in the samples with NA and PA compared to the conventional sample (No-NA) before and after aging treatment: (a) as-drawn No-NA sample, (b) drawn No-NA sample after 5 h aging, (c) GP zones in 20NA sample prior to wire drawing, (d) as-drawn 20NA sample, (e) drawn 20NA sample aged for 5 h, (f) 20NA-PA before wire drawing, (g) as-drawn 20NA-PA sample, and (f) drawn 20NA-PA aged for 5 h.	129
Figure 5.1: Schematic sketch of the time/temperature curves for (a) conventional thermomechanical treatment (CTMT) (b) modified thermomechanical treatment (MTMT)- Arrows show where wire drawing was carried out. The curves are just for a schematic purpose, and it does not show the time frame.	140
Figure 5.2: Evolution of (a) HV hardness and (b) electrical conductivity (EC) as a function of the aging time using conventional thermomechanical treatment (CTMT); (c) HV hardness and (d) electrical conductivity (EC) as a function of the aging time using modified thermomechanical treatment (MTMT)	143
Figure 5.3: HV hardness as a function of EC above 52 %IACS for all alloys using conventional and modified thermomechanical treatment	144
Figure 5.4: (a) the ultimate tensile strengths above 52.5 %IACS for Base-2h, Ag5-4h, Cu3-24h, and Ag3Cu1-24h alloys treated by conventional thermomechanical treatment; and for Base-0.5h, Ag5-2h, Cu3-5h, and Ag3Cu1-7h alloys treated by modified thermomechanical treatment; (b) a comparison between the strengths of the studied alloys and the values defined in EN50183 standard for the wire with a diameter of ~ 4.37mm.....	145
Figure 5.5: DSC curves of the base, Ag5, Cu3, and Ag3Cu1 alloys in (a) as-quenched condition and in (b) as-drawn condition; (c) an enlarged view of peaks I and II for the as-quenched base and Ag5 alloys; and a close view of peak I _d for the as-drawn base alloy; AQ stands for “as-quenched”, and AD stands for “as-drawn”.	147

Figure 5.6: Bright-field TEM micrographs of (a) base alloy after 2h aging (b) Ag5 alloy after 4h aging (c) Cu3 alloy after 24h aging (d) Ag3Cu1 alloy after 24h aging using the conventional thermomechanical treatment; (e) the number density of precipitates (f) the average length and the cross section of precipitates. C stands for conventional thermomechanical treatment.....	150
Figure 5.7: Bright-field TEM micrographs of (a) base alloy after 6h aging (b) Ag5 alloy after 6h aging (c) Cu3 alloy after 6h aging (d) Ag3Cu1 alloy after 6h aging without wire drawing (after pre-aging) (e) the number density of precipitates (d) the average length and the cross section of precipitates. BD stands for before drawing.	153
Figure 5.8: Bright-field TEM micrographs of (a) base alloy after 0.5h aging (b) Ag5 alloy after 2h aging (c) Cu3 alloy after 5h aging (d) Ag3Cu1 alloy after 7h aging using the modified thermomechanical treatment; (e) the number density of precipitates (f) the average length and the cross section of precipitates. M stands for modified thermomechanical treatment.	154
Figure 5.9: TEM micrographs to show the partially deviated precipitates in <001> zone axis in (a) MTMT Ag3Cu1-7h; (b) MTMT Cu3-5h alloys.....	155
Figure 5.10: The increased hardness and decreased electrical conductivity with wire drawing in the base alloy processed by conventional thermomechanical treatment; and base, Cu3, Ag5, and Ag3Cu1 alloys processed by modified thermomechanical treatment	157
Figure 5.11: The dislocation cell substructures for (a) CTMT base after 2 h; (b) MTMT Cu3 after 5 h aging; (c) MTMT Ag5 after 2 h aging; (d) MTMT Ag3Cu1 after 7 h aging. All were taken from <011> zone axis close to (111) planes.	158
Figure 5.12: The comparison between predicted and experimentally measured hardness for C.Base-2h; M.Base-0.5h; M.Ag5-2h; M.Cu3-5h; and M.Ag3Cu1-7h alloys. C and M stand for the CTMT and MTMT, respectively.	162
Figure 5.13: Electrical resistivity contributions of the different strengthening factors for all alloys. The resistivities of grain boundaries and dislocations to are not obvious here due to their small resistivity portions.	166
Figure 5.14: The comparison of the hardness/EC values between the estimated and experimental method.....	166
Figure(AI) 1: Distribution of Fe-rich intermetallics after homogenization in (a) Si4 (b) Si6 (c) Si9 alloys; (d) the area percentage of Fe-rich intermetallics in three alloys	180
Figure(AI) 2: Precipitate distribution at peak aging state for (a) Si4 alloy after 2h (b) Si6 alloy after 1h (c) Si9 alloy after 1h (aging at 180 °C); (d) the average number density of precipitates for three alloys; (e) the mean precipitate length and inter-precipitate spacing for three alloys	181
Figure(AII) 3: (a) Casting the alloys in the shape of Y-block; (b) Cutting the as-cast samples in rectangular block (30mm*40mm*55 mm); (c) Scalping (1.75mm from each side)	183
Figure(AII) 4: (a) Performing the hot rolling process on the plate with the thickness of 26.5mm into 7.6mm at 380-480°C; (b) Cutting and machining the hot-rolled samples into the square	

rods with the cross section of (6.5...7mm)*(6.5...7mm); wire drawing down to the diameter of 4.3...4.7mm184

List of Abbreviations

EC	Electrical Conductivity
IACS	International annealed copper standard
UTS	Ultimate tensile strength
Wt	Weight
TEM	Transmission electron microscope
MPa	Megapascal
ACSR	Aluminum conductor steel reinforced
AAAC	All-aluminum alloy conductor
AA	Aluminum Association
ASTM	American Society for Testing and Materials
CTMT	Conventional thermomechanical treatment
MTMT	Modified thermomechanical treatment
DC	Direct Chill
GP	Guinier–Preston
DSC	Differential scanning calorimetry
OM	Optical microscope
TM	Transition metals
NA	Natural aging
PA	Pre-aging
K/s	Kelvin per second
TRC	Twin-roll casting

SPD	Severe plastic deformation
HPT	High-pressure torsion
ECAP	Equal-channel angular pressing
ARB	Accumulative roll bonding
HE	Hydrostatic extrusion
CG	Coarse grain
UFG	Ultrafine grain
HE	Hydrostatic extrusion
DRX	Dynamic recrystallization
Eq	Equation
FCC	Faced centered cubic
CCR	Continuous casting–rolling
CBED	Convergent beam electron diffraction
No-NA	No Natural aging
AD	As-drawn
AQ	As-quenched
BD	Before drawing

List of Symbols

Al	Aluminium
Mg	Magnesium
Si	Silicon
Ag	Silver
Cu	Copper
β	Beta precipitate
β'	Beta prime precipitate
β''	Beta double prime precipitate
HV	Hardness (Vickers)
mm	Millimeter
$^{\circ}\text{C}$	Centigrade degree
h	Hour
B	Boron
Ti	Titanium
\emptyset	Diameter
Sc	Scandium
nm Ω	Nanometer Ohm
Zr	Zirconium
V	Vanadium
Mn	Manganese
Cr	Chromium

La	Lanthanum
Sr	Strontium
Fe	Iron
Ce	Cerium
α -Al ₈ Fe ₂ Si	Alpha intermetallics
β -Al ₅ FeSi	Beta intermetallics
In	Indium
Sn	Tin
Bi	Bismuth
Pb	Lead
T8	Solution heat treated, cold worked, then artificially aged
T6	Solution heat treated, then artificially aged
d	Grain size
d _p	Precipitate size
a	Lattice parameter
σ_{total}	Total strength
σ^{Al}	Strength of the aluminum matrix
σ^{PREC}	Precipitate hardening
σ^{DISLO}	Strain hardening via dislocation forest
σ^{GB}	Grain boundary strengthening
σ_i^{SOL}	Solute strengthening
M	Taylor factor
G	Shear modulus

b	Burger vector of the dislocations
N_v	Volume density of precipitates
r_p	Mean size of precipitates
r_c	Transition radius from precipitate shearing to bypassing
F	The mean obstacle strength of precipitate
L^{PREC}	The mean particle spacing
L^{dislo}	Density number of dislocations
k_i	Scaling factor
ρ_{total}	Total resistivity
ρ^{Al}	Resistivity of aluminum matrix
ρ^{PREC}	Resistivity of precipitates
ρ^{DISLO}	Resistivity of dislocation
ρ^{GB}	Resistivity of grain boundaries
ρ^{SOL}	Resistivity of solutes
μm	Micrometre
HV_{total}	Total hardness
HV^{Al}	Hardness of the aluminum matrix
HV^{dislo}	Contribution of strain hardening
HV^{prec}	Precipitation hardening
HV^{gb}	Contribution of grain boundary strengthening
HV_i^{sol}	Hardness contribution via solute strengthening
C_i	Concentration of the solute i
kHz	kilohertz

kV	Kilovolt
N	The number of precipitates
A	Area of the matrix containing the precipitates
t	TEM foil thickness
λ	Corrected average precipitate length
ρ	Dislocation number density

DEDICATION

This thesis is dedicated to my respectful parents, Hourieh Ahmadi and Nobakht Nikzad Khangholi, and beloved wife, Armita Rastegari, without whose constant support this work would not have been possible.

At the same time, my thanks also go to my caring brothers, Hassan and Hossein, who always inspire me.

Finally, my special dedication is toward my lovely and blessed twins, Aveen and Arteen, which enlighten our life path.

ACKNOWLEDGEMENT

Foremost, I would like to express my sincere gratitude to my supervisor, Prof. X Grant Chen, for his continuous guidance, support, and trust during my PhD. He provided great opportunities for me to become a better researcher and to learn many invaluable skills.

I would like to express my special thanks to my academic co-supervisor, Prof. Mousa Javidani, for his technical and scientific discussions, comments, and support at each step of this long journey, ended up with the improvements in my research quality.

I would like to thank my industrial co-supervisor, Dr. Alexandre Maltais, whose technical and industrial comments help me to consider the industrial needs in this project.

I am deeply grateful to the members of my committee, Prof. Dilip Sarkar, Prof. Emad Elgallad, and Dr. Paul Rometsch, for their worthwhile comments, guidance, and support.

I would like to thank Prof. Duygu Kocaeefe and Prof. Yasar Kocaeefe for their help while we lived in Chocoutimi.

I am grateful to Rio Tinto company to for their help and providing the equipment.

I would like to thank Mr. Dany Racine, Mr. Samuel Dessureault and Mr. Felix Tremblay for their countless technical helps at every moment of my PhD life.

Then, I would like to express my gratitude to Prof. Zhan Zhang and Mr. zhixing chen for their help in characterization analysis in SEM, TEM, and DSC.

My appreciation goes toward Prof. Kun Liu for their valuable help in the experimental and technical discussion during my PhD.

I also thank Dr. Khaled Ragab, who once offered me valuable courses and advice during my study.

Meanwhile, I am also deeply indebted to my colleagues for their fruit collaboration, scientific discussions and sharing their research experiences with me: Ali Elashery, Ahmed Algendy, Chaima Hajji, Esmail Pourkhorshid, Mohammadreza Mofarreh, Mohamed Ahmed, Mohamed Qassem, Peng Hu, Liying Cui, Shuai Wang, Cong Li, Zimeng Wang, Jovid Rakhmonov, Dong Li, Redouane Farid, Henry Agbe, Karthikeyan Rajan, and Lanfeng Jin.

Finally, I would like to thank my beloved wife, Armita Rastegari, and my family for their love and support throughout this project.

Chapter 1 : Introduction

The industrial sector is in continuously growing demand for Al conductor alloys owing to their high strength, high electrical conductivity, and low weight [1-3]. Aluminum is less conductive than copper (~ 60%), but it has lower density than copper (one third). It means that a wire of aluminum weighs half as much as that of copper with the same electrical resistance [2].

Aluminum Conductors are of different types such as (i) aluminum conductor steel reinforced (ACSR); (ii) all-aluminum alloy conductor (AAAC). ACSR involves the aluminum conductor (such as AA1350) reinforced with steel core. The central steel core is surrounded by a number of aluminum strands. On the other hand, AAAC is made of Al-Mg-Si alloys (such as AA6101 and AA6201 cables). AAAC provides excellent resistance against corrosion. They are becoming more popular than ACSR for the last two decades in high voltage transmission lines because they could be strengthened via the precipitation hardening with a desirable electrical conductivity [4-7].

The principal strengthening mechanisms of aluminum alloy conductors are the main sources of electrical resistivity. Accordingly, the factors enhancing the strength cause electrical resistivity, meaning that strength and electrical conductivity are mutually exclusive. Therefore, the simultaneous improvement in EC and strength turns out as a complicated subject [8-11]. The minimum required EC and strength for Al-Mg-Si conductor alloys are provided in EN 50183 and ASTM B398 standards [12, 13], which will be discussed in the first chapter. Overall, a better optimization of strength and EC in Al-Mg-Si conductor alloys can be acquired via:

- i. Chemical compositions
 - a. Optimizing the content of the main alloying elements [9, 14-17].
 - b. Adding the optimum level of other alloying elements [18, 19].
 - c. Adding the grain refiners and modifiers [4, 20].
- ii. Thermo-mechanical processes
 - a. Conventional/Modified thermo-mechanical treatment [11, 18, 21-23].
 - b. Severe plastic deformation [10, 24-27].

The main scope of this project is to address the strength and EC development in Al-Mg-Si conductor alloys via (1) optimal amounts of the major alloying elements (Mg and Si); (2) pre-natural aging combined with pre-aging (modified thermo-mechanical treatment) (3) the additional alloying elements (such as Ag and Cu) using the conventional and modified thermo-mechanical treatment.

1.1. Problem statement

To optimize the electrical conductivity and strength in Al-Mg-Si conductor alloys, it is required to find out the role of the alloying elements and thermo-mechanical treatments on precipitation. The effects of excessive Si and Mg (relative to the Mg/Si ratio of β'' (~1)) on strength and EC of age-hardenable Al-Mg-Si conductor alloys have been barely addressed, and the contribution of each strengthening mechanism has not been investigated in alloy with various Mg/Si ratios.

Besides, the effect of natural aging on the strength and electrical conductivity in Al-Mg-Si conductor alloys is less reported. Furthermore, the microstructure investigation is still lacking in the conductor alloys exposing to the natural aging. Therefore, it would be worth investigating the effect of the natural aging on the evolution of strength and EC in these alloys.

The conventional thermomechanical treatment in the fabrication of the Al-Mg-Si conductors is comprised of solution treatment, wire drawing, and post-aging. However, several studies have been devoted to the modified thermomechanical treatment (MTMT) with artificial pre-aging (before the drawing process and post-aging) to achieve a better trade-off between strength and EC compared to those achieved by the conventional thermomechanical treatment (CTMT) [11, 21, 22]. It should be noted that pre-aging prior to wire drawing was applied to samples in the modified thermomechanical treatment. However, there are conflicting discussions elaborating the efficiency of modified thermomechanical treatment [21, 22, 28]. Therefore, the exact strengthening mechanisms in the MTMT samples remain controversial.

Furthermore, no investigations have been found studying the effect of minor amounts of Ag and Cu on strength and EC in Al-Mg-Si conductor alloys while these elements promote precipitation in Al-Mg-Si alloys. It should be noted that the maximum allowable copper content

is only 0.1 wt.% for AA6201 and AA6101 based on ASTM B398 and B317 standards [29, 30]. Adding the copper beyond 0.1 wt.% to promote the precipitates could be challenging in terms of electrical conductivity requirement.

1.2. Objectives

The general objective of this project is to study and improve the strength and EC evolution of Al-Mg-Si alloys under various parameters. To achieve the objective, the research plan is listed as below:

1. Optimization of mechanical properties and electrical conductivity in Al-Mg-Si 6201 alloys with different Mg/Si ratios

- a. Study the evolution of strength and EC for the samples with various Mg/Si ratios over the aging time
- b. Investigate the microstructure of the samples of which strength and EC are above the minimum required values
- c. Establish the strength model
- d. Compare the strength and EC in this study with the literature

2. Effects of natural aging and combined pre-aging on the strength and electrical conductivity in Al-Mg-Si AA6201 conductor alloys

- a. Study the evolution of strength and EC for the naturally-aged and pre-aged samples over the aging time
- b. Investigate the microstructure of the samples of which strength and EC are above the minimum required values
- c. Develop the strength and EC model
- d. Compare the strength and EC in this study with EN50183 standard
- e. Microstructural evolution

3. Effect of Ag and Cu additions on the strength and electrical conductivity in Al-Mg-Si conductor alloys using conventional and modified thermo-mechanical treatment

- a. Study the evolution of strength and EC for Ag-added and Cu-added samples over the aging time using the conventional and modified thermo-mechanical treatment
- b. Investigate the microstructure of the samples of which strength and EC are above the minimum required values
- c. Develop the strength and EC model
- d. Compare the strength and EC in this study with EN50183 standard

1.3. Originality statement

In this project, we focused on three different strategies to enhance the strength and electrical conductivity in Al-Mg-Si conductor alloys: optimizing the Mg/Si ratio, modifying the thermomechanical treatment, and adding the additional alloying elements (Cu and Ag). As the first approach, the effects of various Mg/Si ratios on the strength and electrical conductivity were evaluated using the conventional thermomechanical treatment. This study suggested the various Mg/Si ratios for the high end of strength (Mg/Si \approx 1) and high end of electrical conductivity (Mg/Si \approx 1.5). We also used the strength modeling to reveal the most effective strengthening mechanism on the final strength.

In the second part, we modified the thermomechanical treatment by applying the pre-aging (5 h at 180 °C) before wire drawing for the alloy with Mg/Si ratio of \sim 1. The results showed the highly enhancement in the strength (369 MPa) with an acceptable electrical conductivity (53% IACS). The strength and electrical resistivity were modeled using the constitutive equations to reveal the promising strengthening factors. To the best of our knowledge, the effect of the various strengthening factors on the strength and electrical conductivity using the modified thermomechanical treatment for the Al-Mg-Si conductor alloys has been less reported. The strength and electrical resistivity models exhibited that the precipitate hardening is strongly improved by the modified thermomechanical treatment with a medium electrical resistivity contribution. Besides for the first time, we revealed the effect of the industrial natural aging on the strength and electrical conductivity with the comprehensive microstructural study in the Al-Mg-Si conductor alloys.

In the third part, we added the copper and silver additions to Al-Mg-Si conductor alloys under conventional and modified thermomechanical treatment. Based on ASTM B398 and B317

standards, the maximum required copper must be 0.1 wt.% for AA6201 and AA6101 [29, 30]. To the best of our knowledge, the Ag and Cu additions to the Al-Mg-Si conductor alloys were not studied in terms of strength and electrical conductivity in the literature. This study showed that the Ag and Cu additions had a negligible effect on the strength using the conventional thermomechanical treatment. On the other hand, the Cu additions strongly limited the electrical conductivity under the conventional thermomechanical treatment. However, the modified thermomechanical treatment boosted the effect of the Ag and Cu additions on the strengthening. In addition to the increased strength, the modified thermomechanical treatment could enhance the electrical conductivity of the alloys compared to the counterparts under conventional thermomechanical treatment.

1.4. Thesis outline

The present Ph.D. thesis contains six chapters. Following the introduction, a comprehensive literature review regarding “review on recent progress in Al-Mg-Si 6xxx conductor alloys” is presented in chapter 2. In the literature review chapter, the improvement of strength and EC was discussed by means of different methods such as chemical composition and thermal/thermomechanical treatments. Besides, the methods to model strength and electrical resistivity is presented based on the microstructural features. To prepare this chapter, a review paper entitled “critical review on recent progress in Al-Mg-Si 6xxx conductor alloys” submitted to *Journal of Materials Research*, and it is under review currently.

In chapter 3, the published paper “Optimization of mechanical properties and electrical conductivity in Al-Mg-Si 6201 alloys with different Mg/Si ratios” in *Journal of materials research* is presented. This paper is drawn from the results of the first part of this project, showing the optimum Mg/Si ratio in terms of priority in strength or EC. It also addresses the strengthening model based on the microstructure analysis, showing the promising strengthening mechanisms.

In chapter 4, the paper “Effects of natural aging and pre-aging on the strength and electrical conductivity in Al-Mg-Si AA6201 conductor alloys” published in the journal of *Materials Science and Engineering: A* is presented. In this article, first the effect of the natural aging on the evolution of strength and EC is revealed and discussed in Al-Mg-Si conductor alloys. Then, the impact of pre-aging prior to wire drawing on the strength and EC is addressed. Then, it will show the reliability of modeling in the strength and electrical resistivity, compared to the experimental values. For better understanding, the schematic of the microstructural evolution in the samples with natural aging and pre-aging is presented in this paper.

In chapter 5, the manuscript entitled “Effect of Ag and Cu additions on the strength and electrical conductivity in Al-Mg-Si conductor alloys using conventional and modified thermomechanical treatment” is presented, which is submitted to “*Journal of alloys and compounds*”. In this work, the impact of Cu and Ag additions on the strength and EC were assessed in 6xxx series aluminum conductor alloys through the conventional and modified thermomechanical treatment. This work aims at providing the maximized efficiency of Ag and Cu additions in terms of the strengthening above the minimum required electrical conductivity. The precipitation was studied via the DSC and TEM analysis, and dislocations were analyzed using TEM. The microstructural features were correlated to the strength and electrical conductivity using the quantitative equations.

Finally in chapter 6, conclusions and recommendations for future work are presented. In addition to these main body chapters, appendix I is also included at the end of this thesis providing supplementary information for articles 2. Appendix II explains the description of the fabrication process of the wires in this project.

1.5. References

- [1] L. Pan, K. Liu, F. Breton, X. Grant Chen, Effect of Fe on Microstructure and Properties of 8xxx Aluminum Conductor Alloys, *J. Mater. Eng. Perform.* 25(12) (2016) 5201-5208.
- [2] L. Pan, F.A. Mirza, K. Liu, X.G. Chen, Effect of Fe-rich particles and solutes on the creep behaviour of 8xxx alloys, *Mater. Sci. Technol.* 33(9) (2016) 1130-1137.
- [3] L. Pan, K. Liu, F. Breton, X.G. Chen, Effects of minor Cu and Mg additions on microstructure and material properties of 8xxx aluminum conductor alloys, *J. Mater. Res.* 32(06) (2017) 1094-1104.
- [4] S. Karabay, Influence of AlB_2 compound on elimination of incoherent precipitation in artificial aging of wires drawn from redraw rod extruded from billets cast of alloy AA-6101 by vertical direct chill casting, *Materials & Design* 29(7) (2008) 1364-1375.

- [5] S. Karabay, Modification of AA-6201 alloy for manufacturing of high conductivity and extra high conductivity wires with property of high tensile stress after artificial aging heat treatment for all-aluminium alloy conductors, *Materials & Design* 27(10) (2006) 821-832.
- [6] E. Cervantes, M. Guerrero, J. A. Ramos, S.A. Montes, Influence of Natural Aging and Cold Deformation on the Mechanical and Electrical Properties of 6201-T81 Aluminum Alloy Wires, *Mater. Res. Soc. Symp. Proc* (2010) 03-09.
- [7] M. Iraizoz, N. Rossello, M. Amado, Influence of Solution Heat Treatment Temperature in the Final Properties of AA6201 Drawn Wire, in: M. Hyland (Ed.), *Light Metals 2015*, Springer International Publishing (2016) 183-187.
- [8] Q. Zhao, Z. Qian, X. Cui, Y. Wu, X. Liu, Influences of Fe, Si and homogenization on electrical conductivity and mechanical properties of dilute Al–Mg–Si alloy, *J. Alloys Compd.* 666 (2016) 50-57.
- [9] Y. Han, D. Shao, B.A. Chen, Z. Peng, Z.X. Zhu, Q. Zhang, X. Chen, G. Liu, X.M. Li, Effect of Mg/Si ratio on the microstructure and hardness–conductivity relationship of ultrafine-grained Al–Mg–Si alloys, *Journal of Materials Science* 52(8) (2016) 4445-4459.
- [10] R.Z. Valiev, M.Y. Murashkin, I. Sabirov, A nanostructural design to produce high-strength Al alloys with enhanced electrical conductivity, *Scripta Mater.* 76 (2014) 13-16.
- [11] C.H. Liu, J. Chen, Y.X. Lai, D.H. Zhu, Y. Gu, J.H. Chen, Enhancing electrical conductivity and strength in Al alloys by modification of conventional thermo-mechanical process, *Materials & Design* 87 (2015) 1-5.
- [12] E. Standard, EN 50183. Conductors for overhead lines, aluminium magnesium silicon alloy wires (2000) 1-7.
- [13] ASTM, Annual Book of ASTM Standards, Electrical Conductors (2002).
- [14] X. Xu, Z. Yang, Y. Ye, G. Wang, X. He, Effects of various Mg/Si ratios on microstructure and performance property of Al-Mg-Si alloy cables, *Mater. Charact.* 119 (2016) 114-119.
- [15] S. Jiang, R. Wang, Grain size-dependent Mg/Si ratio effect on the microstructure and mechanical/electrical properties of Al-Mg-Si-Sc alloys, *Journal of Materials Science & Technology* 35(7) (2019) 1354-1363.
- [16] S. Nikzad Khangholi, M. Javidani, A. Maltais, X.G. Chen, Optimization of mechanical properties and electrical conductivity in Al–Mg–Si 6201 alloys with different Mg/Si ratios, *J. Mater. Res.* 35(20) (2020) 2765-2776.
- [17] S. Nikzad Khangholi, M. Javidani, A. Maltais, X.G. Chen, Investigation on electrical conductivity and hardness of 6xxx aluminum conductor alloys with different Si levels, *MATEC Web of Conferences* 326 (2020) 1-7.
- [18] F.U. Flores, D.N. Seidman, D.C. Dunand, N.Q. Vo, Development of High-Strength and High-Electrical-Conductivity Aluminum Alloys for Power Transmission Conductors, *Light Metals* (2018) 247-251.
- [19] M.H. Mulazimoglu, A. Zaluska, F. Paray, J.E. Gruzleski, The effect of strontium on the Mg₂Si precipitation process in 6201 aluminum alloy, *Metallurgical and Materials Transactions A* 28(6) (1997) 1289-1295.

- [20] X. Cui, Y. Wu, G. Zhang, Y. Liu, X. Liu, Study on the improvement of electrical conductivity and mechanical properties of low alloying electrical aluminum alloys, *Composites Part B: Engineering* 110 (2017) 381-387.
- [21] G. Lin, Z. Zhang, H. Wang, K. Zhou, Y. Wei, Enhanced strength and electrical conductivity of Al–Mg–Si alloy by thermo-mechanical treatment, *Materials Science and Engineering: A* 650 (2016) 210-217.
- [22] C. Bunte, M. Glassel, C. Medina, D. Zalcmán, Proposed Solution for Random Characteristics of Aluminium Alloy Wire Rods Due to the Natural Aging, *Procedia Materials Science* 9 (2015) 97-104.
- [23] J.P. Hou, Q. Wang, Z.J. Zhang, Y.Z. Tian, X.M. Wu, H.J. Yang, X.W. Li, Z.F. Zhang, Nano-scale precipitates: The key to high strength and high conductivity in Al alloy wire, *Materials & Design* 132 (2017) 148-157.
- [24] X. Sauvage, E.V. Bobruk, M.Y. Murashkin, Y. Nasedkina, N.A. Enikeev, R.Z. Valiev, Optimization of electrical conductivity and strength combination by structure design at the nanoscale in Al–Mg–Si alloys, *Acta Mater.* 98 (2015) 355-366.
- [25] K. Majchrowicz, Z. Pakieła, W. Chrominski, M. Kulczyk, Enhanced strength and electrical conductivity of ultrafine-grained Al-Mg-Si alloy processed by hydrostatic extrusion, *Mater. Charact.* 135 (2018) 104-114.
- [26] M.Y. Murashkin, I. Sabirov, V.U. Kazykhanov, E.V. Bobruk, A.A. Dubravina, R.Z. Valiev, Enhanced mechanical properties and electrical conductivity in ultrafine-grained Al alloy processed via ECAP-PC, *Journal of Materials Science* 48(13) (2013) 4501-4509.
- [27] M. Murashkin, A. Medvedev, V. Kazykhanov, A. Krokhnin, G. Raab, N. Enikeev, R. Valiev, Enhanced Mechanical Properties and Electrical Conductivity in Ultrafine-Grained Al 6101 Alloy Processed via ECAP-Conform, *Metals* 5(4) (2015) 2148-2164.
- [28] L.M. Cheng, W.J. Poole, J.D. Embury, D.J. Lloyd, The influence of precipitation on the work-hardening behavior of the aluminum alloys AA6111 and AA7030, *Metallurgical and Materials Transactions A* 34(11) (2003) 2473-2481.
- [29] ASTM, Annual Book of ASTM Standards: Electrical Conductors. Section 2. Volume 02.03, (2002).
- [30] ASTM, Annual Book of ASTM Standards: Nonferrous metal products. Aluminum and magnesium alloys. Section 2. Volume 02.02 (2003).

Chapter 2 : Critical review on recent progress in Al-Mg-Si 6xxx conductor alloys (Article1)

Siamak Nikzad Khangholi ¹, Mousa Javidani ¹, Alexandre Maltais ², X.-Grant Chen ¹

¹ Department of Applied Science, University of Québec at Chicoutimi, Saguenay,
Québec, G7H 2B1, Canada

² Arvida Research and Development Center, Rio Tinto Aluminum, Saguenay, Quebec,
G7S 4K8, Canada

This article is under review at:

Journal of Materials Research

Abstract

The mechanical strength and electrical conductivity (EC) in Al-Mg-Si 6xxx conductor alloys are key characteristics but mutually exclusive properties. This review paper critically elucidates the correlation between the mechanical properties and electrical conductivity in Al-Mg-Si conductor alloys with respect to various conditions. Primarily, the significance of Al-Mg-Si conductor alloys is discussed in terms of mechanical and electrical properties. Subsequently, various strategies to obtain a better trade-off between these two competing characteristics, including alloying engineering, modified thermomechanical treatments and severe plastic deformation, are elaborated. Finally, the impact of the various microstructural features on the mechanical and electrical properties is addressed in detail using strength and electrical resistivity models. A principal conclusion drawn in this review is that the strength ought to be enhanced by creating barriers (such as sessile dislocations and precipitates) for dislocation movement while

having a less detrimental effect on the electrical conductivity. Considering the potential of Al-Mg-Si conductor alloys, future directions are outlined.

Keywords: Al-Mg-Si conductor alloys, mechanical properties, electrical conductivity, alloying elements, thermomechanical treatment, strength model, electrical resistivity model.

2.1. Introduction

Owing to the ever-increasing demands, developing high-strength and highly conductive cables has received great attention in research in recent decades. Aluminum alloys have been considered an appropriate substitution for copper conductors owing to their distinctive properties, such as lower cost and higher strength/weight ratio, relative to Cu conductors [1-3]. Conductors made of aluminum alloys present inferior electrical conductivity (EC), but their density is one-third that of Cu conductors. The mass resistivity is defined by the combination of the electrical resistivity and density. Therefore, the high mass resistivity of Cu conductors, which is approximately twice as high as that of aluminum conductors, implies a relatively higher conduction capacity in Al conductors than in Cu conductors with the same weight [2].

Aluminum conductors are categorized into two groups: aluminum conductor steel reinforced (ACSR) and all-aluminum alloy conductor (AAAC) (Fig. 2.1). ACSR is composed of steel in the core surrounded by high conductivity pure aluminum (such as AA1350) [4-8]. Due to the low strength of pure Al alloys, ACSR is reinforced by the steel core to sustain a large stress [4]. To respect the high corrosion resistance and mechanical property requirements in high voltage transmission lines, AAAC has been introduced as an alternative for ACSR in recent years, which are self-supporting overhead power lines. Among aluminum alloys, 6xxx series (Al-Mg-Si) conductor alloys are known as materials used in AAAC owing to their high strength via the aging

process with a desirable EC [5-7, 9]. Despite the relatively high corrosion resistance of 6xxx series alloys, their corrosion resistance has also been taken into account for further improvement in some research works [10, 11].

In general, there is a compromise between strength and EC in aluminum alloys, as shown in Fig. 2.2 [12]. However, two well-known AA6101 and AA6201 alloys that serve as conductors in AAAC show a better trade-off between strength and EC among 6xxx series conductor alloys [5, 6, 12, 13]. Overall, the AA6201 alloy possesses higher Mg and Si than the AA6101 alloy, yielding a higher strength and lower EC than the AA6101 alloy [5, 6]. Based on Fig. 2.2, the dotted line shows the upper limit for commercial aluminum alloys in terms of the combination between strength and EC. Therefore, the achievement of strength and EC above the dotted line is technically a challenging issue [12].

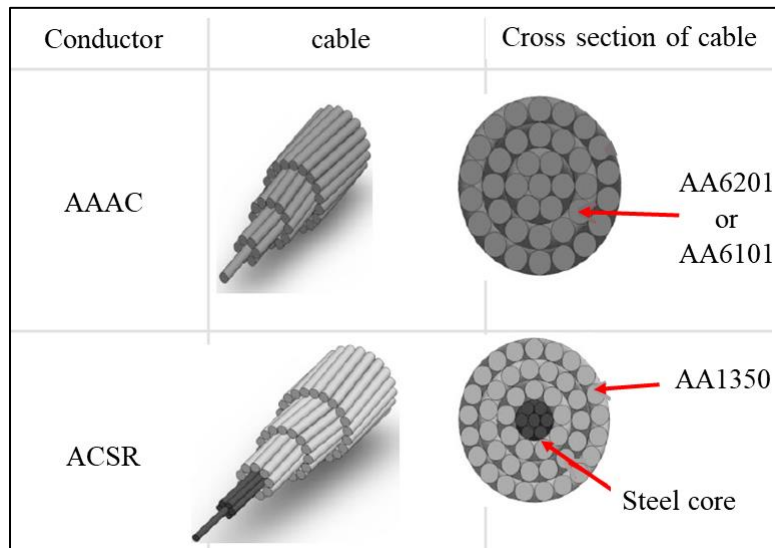


Figure 2.1 Scheme of AAAC and ACSR conductors with their cross section [8].

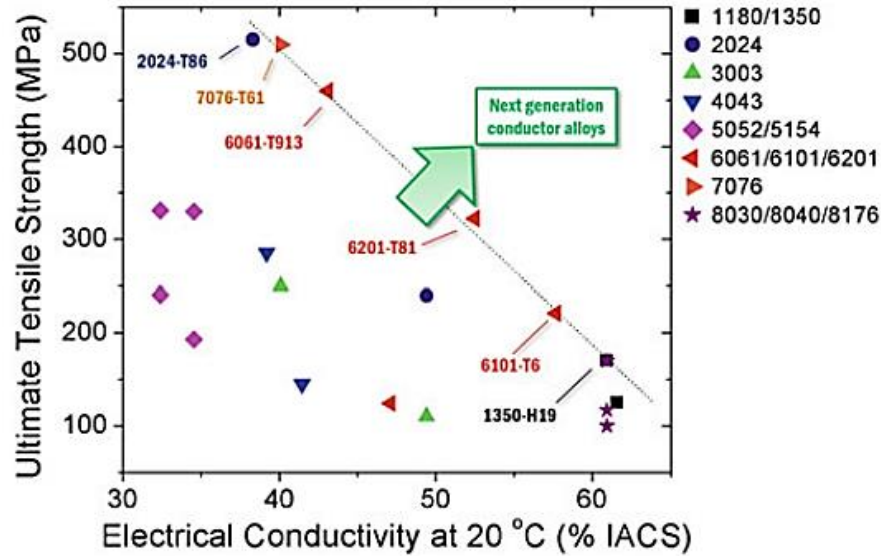


Figure 2.2 Plot of strength versus EC for several commercial aluminum alloys [12].

The principal strengthening mechanisms of aluminum alloys are precipitation hardening, work hardening, solute strengthening, and grain boundary strengthening. On the other hand, the EC of metals is correlated with the behavior of valence electrons. Similarly, the cause of electrical resistivity is the disruption of the atomic periodicity in a crystal structure, resulting from crystal defects (e.g., vacancies, dislocations, and grain boundaries), precipitates, and impurity atoms in a pure metal lattice [14-17]. Among these parameters, impurity atoms in the matrix along with Guinier–Preston (GP) zones possess the most detrimental effects on EC [15, 16, 18]. Consequently, it could be inferred that the parameters resulting in an improvement in strength give rise to higher electrical resistivity, meaning that EC and strength are mutually exclusive [14-16, 19]. The minimum required EC and strength for Al-Mg-Si conductor alloys are provided in the EN 50183, ASTM B398 and ASTM B317 standards (Table 2.1) [20-22].

Aside from the EC and mechanical properties of all aluminum alloy conductors, their fatigue life and failure analysis have been investigated recently [4, 23]. It is well understood that the

wind along with the dead load of the conductors is among the main forces, ending up to conductor damage. The applied forces could cause the bending of cable strands, subsequently leading to friction between the conductor and the suspension clamp known as fretting fatigue/wear phenomena [4, 23]. The service life of the conductors is planned to be ~30 years.

The main scope of this paper is to address the strength and EC improvement in Al-Mg-Si conductor alloys. Although significant efforts have been directed toward a simultaneous enhancement of electrical and mechanical properties in Al-Mg-Si conductor alloys, the correlation between strength/EC and microstructure is still debatable in terms of the different variables influencing chemical composition and thermomechanical treatment. The present study aims to discuss and critically review the effects of various parameters on the improvement of electrical and mechanical properties of 6xxx series conductor alloys.

In general, a better combination of strength and EC in 6xxx series conductor cables could be obtained through:

2. Chemical compositions
 - a. Optimal levels of the principal alloying elements [15, 24-27].
 - b. Desirable amounts of additional alloying elements [12, 28].
 - c. Grain refiners and modifiers [5, 29].
3. Thermomechanical processes
 - a. Conventional/modified thermomechanical treatment [12, 19, 30-32].
 - b. Severe plastic deformation [16, 18, 33-35].

Table 2.1 Mechanical and electrical properties of the heat-treated wires defined in EN-50183, ASTM B398 and ASTM B317 for Al–Mg–Si alloys

Type	Nominal EC (%IACS)	Nominal Diameter (mm)		Minimum tensile strength (MPa)	Minimum elongation after fracture on 250mm (%)	Standard
		Min	Max			
AL2	52.5	1.5	3.5	325	3.0	EN 50183 [20]
		3.5	5.0	315	3.0	
AL3	53	1.5	5.0	295	3.5	
AL4	52.9	1.5	3.5	325	3.0	
		3.5	5.0	315	3.0	
AL5	55.25	1.5	5.0	295	3.5	
AL6	55.6	1.5	3.5	314	3.5	
		3.5	5.0	304	3.5	
AL7	57.5	1.5	2.5	300	3.0	
		2.5	3.0	290	3.0	
		3.0	3.5	275	3.0	
		3.5	4.0	265	3.0	
		4.0	5.0	255	3.0	
AA6201-T81	52.5	1.5	3.25	315	3	
		3.25	4.75	305	3	
AA6101	55-59.5	Refer to [22]		83-221	Refer to [22]	ASTM B317 [22]

2.2. Fabrication processes of 6xxx electrical conductors

In the upcoming sections, the effect of the various parameters during the fabrication process on the strength and EC will be discussed. Thus, it is worthwhile to identify the stages of different fabrication processes.

Over the last decades, two distinct fabrication processes have been developed to produce redraw rods: a) direct chill (DC) casting followed by an extrusion process and b) continuous casting followed by a hot rolling process [6, 36]. In the former case, the prepared molten metal in the furnace is inoculated (e.g., by Al-B master alloy) while being transferred to the cast mold through a tundish. The DC-cast billets are subsequently hot-extruded into 9.5 mm rods after being homogenized (such as at 560 °C for 6 h) [6].

The predominant fabrication process of the redraw rods is by means of Properzi continuous casting followed by a hot rolling process (Fig. 2.3) [37]. In the process, once the target chemical composition is achieved, the molten metal is further treated inside the furnace by adding an appropriate grain refiner and modifier (such as Al-Ti-B and Al-B master alloys). Subsequently, the molten metal is transferred via a tundish and poured into a grooved wheel mold made of copper (Fig. 2.3a). The mold, which is partially surrounded by a steel belt, is exposed to water spray cooling to ensure desirable solidification conditions [6, 38-40]. This casting technique, which is called Properzi caster, produces cast bars with a trapezoidal cross section. The cast bar is subsequently directed to an in-line multiple hot rolling process unit, through which the trapezoidal cross section of the bar is transformed into a circular rod with a diameter of 9.5 mm (Fig. 2.3b) [6, 39]. The temperature of the cast bar before hot rolling is carefully controlled to keep the alloys above the solvus temperature to ensure the supersaturated solid solution. The rolled aluminum rod is finally packaged as a coil of several tons [38]. Afterwards, the coils are transported to a downstream fabricator of wire drawing (Fig. 2.3c), through which the rods are drawn to wires with desired diameters ($\phi = 1.5\text{-}5.0$ mm). The drawn wires are subsequently subjected to artificial aging treatment to improve the strength and EC (Fig. 2.3d) [6, 39]. Other manufacturing techniques, such as horizontal continuous casting and semisolid continuous

casting followed by an extrusion process, can also be employed to produce aluminum wire rods [36, 41]; however, these techniques may not be as commercially viable as the first two aforementioned techniques.

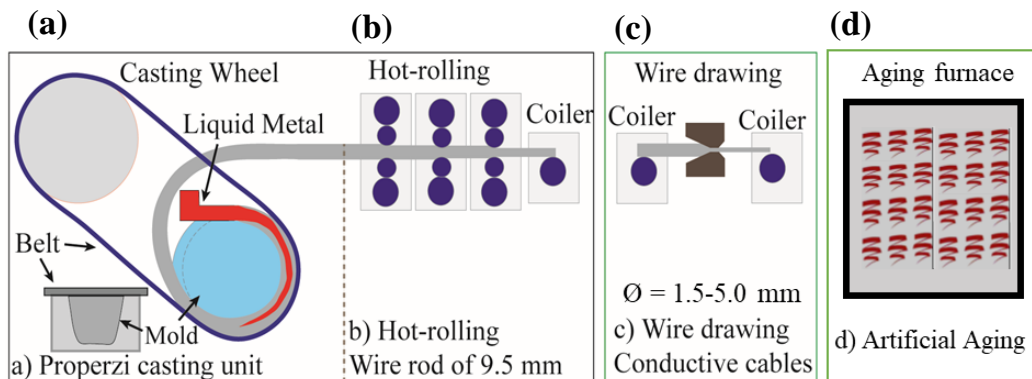


Figure 2.3 Production chain of Properzi process followed by wire drawing and aging treatment for aluminum conductive cables

2.3. Effects of chemical composition on strength and EC

2.3.1. Principal alloying elements (Mg and Si)

Magnesium and silicon are known as the major alloying elements in 6xxx series alloys, leading to the precipitation of strengthening β''/β' phases during aging treatment. Therefore, it is initially valuable to address the effect of magnesium and silicon (or various Mg/Si ratios) on the strength and EC in these conductor alloys [24]. The precipitation sequence of the as-quenched 6xxx aluminum alloys is as follows: independent clusters of Mg and Si atoms; coclusters of Mg and Si atoms; GP zones; β'' needle-like precipitates; β' rod-shaped precipitates (and B' lath-shaped precipitates); and equilibrium β - Mg_2Si [42, 43]. The β'' precipitates are known as the main hardening phases in the peak-aged condition (T6). The MgSi phases are different with respect to

their crystal structures and Mg/Si ratios. The Mg/Si ratios of these phases (in at.%) are as follows: β'' (Mg/Si~1), β' (Mg/Si~1.7) and β (Mg/Si=2) [44]. As mentioned above, the as-quenched materials are commonly drawn prior to aging treatment. Accordingly, the cold drawing after solution treatment could disturb the precipitation sequence due to the introduction of a large number of dislocations. Therefore, β'' formation could be suppressed, and the β' phase was heterogeneously promoted along the dislocations [45-47]. Lath-like precipitates were also observed as the predominant microstructure feature, of which the crystal structure was similar to that of the β' phase [45]. The precipitation sequences in the as-deformed condition became clusters/GP zones; β' ; and equilibrium β -Mg₂Si [46, 47].

Xu et al. [24] reported the effect of different Mg/Si ratios on the strength and EC in as-drawn AA6101 conductor alloys, and the results are shown in Fig. 2.4. The chemical compositions along with the Mg/Si ratio in the experimental alloys studied are listed in Table 2.2. According to Xu et al. [24], an alloy with a Mg/Si ratio of 1.73 wt.% (2 in at.%) was considered a balanced alloy, although the Mg/Si ratio of the strengthening precipitates (β'') was approximately one (in at.%) [42, 44, 48-51]. It is worth pointing out that the maximum solubilities of Mg and Si are 14.9 wt.% at 449 °C and 1.65 wt.% at 577 °C, respectively, and they are 1.7 wt.% for Mg and trivial for Si at room temperature [52].

Based on the results in Fig. 2.4, the higher the excessive Si level is, the higher the precipitation kinetics. Moreover, the peak strength was improved in Si excessive alloys by 25%, which mainly resulted from a large number of strengthening precipitates, confirmed using DSC results and TEM analysis. However, excessive Mg exhibited no strengthening effect on the Al-Mg-Si conductor alloys [24, 25]. Moreover, Gupta et al. [53] also reported that the yield strength increased with increasing Si content. During the aging treatment, it was reported that the

quenched vacancies were primarily trapped by Si atoms due to the higher diffusion rate, through which Si-rich clusters are formed. Subsequently, by slow diffusion of Mg atoms toward Si-rich clusters, Mg-Si clusters are formed [44, 54, 55]. This implies the key role of Si in the early stage of aging. Furthermore, Si₂ columns or Si grids as a skeleton of precipitates were observed in the core of precipitates from GP zones to β'' precipitates [49, 56, 57]. Moreover, it was detected that the Mg/Si ratio of strengthening phases decreased with increasing Si, indicating that the precipitation was closely connected with Si atoms rather than Mg atoms. As a consequence, precipitate strengthening was strongly governed by Si solutes in Al-Mg-Si conductors [58]. Although cold drawing might disrupt the precipitation sequence [45-47], excessive Si still exhibited a higher strength in as-drawn Al-Mg-Si conductor alloys [24, 26].

However, the Si excessive alloy showed a relatively lower EC (Fig. 2.4b), which stems from Si solutes due to the larger difference in atomic radius of Al and Si [14, 24]. Although silicon has limited solubility in Al-Mg-Si alloys, DSC analysis confirmed that excessive Si remained in the aluminum matrix until the fully overaged state [59]. Therefore, optimized strength and EC were attained in the overaged condition after 8 h (Fig. 2.4c) in Si excessive samples (alloy #1). Despite the longer time required for overaging, the Si excessive sample presented a superior strength compared to the peak-aged strength of other samples (Fig. 2.4c). Excessive Mg alloys showed negligible superiority in strength. Alloy #5 (highly excessive Mg) exhibited the lowest EC due to the scattering electrons and had an insignificant impact on the strength [24]. Based on Fig. 2.4b, as the aging time increased, EC initially showed rapid growth and then moderately increased for all samples. An increase in EC could be attributed to the fact that the detrimental impact of precipitates on EC is inferior to that of solutes [24, 60].

Table 2.2 Chemical composition (wt.%) of the studied alloys [24].

Alloys	Si	Mg	Fe	Mg/Si	Types
1	0.49	0.58	0.18	1.18	Si excessive
2	0.39	0.59	0.19	1.51	Si excessive
Balanced	0.35	0.60	0.17	1.73	----
3	0.35	0.76	0.18	2.17	Mg excessive
4	0.35	0.86	0.18	2.46	Mg excessive
5	0.35	0.96	0.17	2.74	Mg excessive

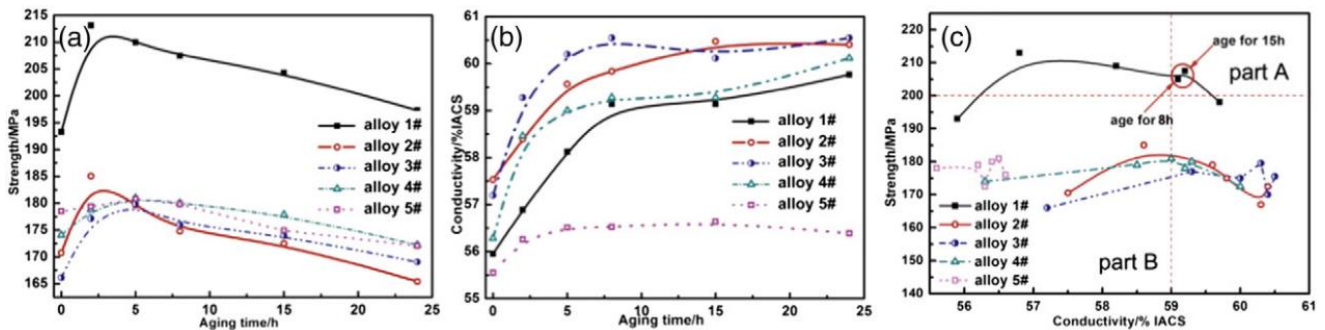


Figure 2.4 (a) Strength and (b) EC as a function of aging time at 180°C. (c) strength versus EC for all aging times for 6101 alloy samples [24].

In our recent work [26], the optimization of strength and EC was studied at different Mg/Si ratios for drawn wire samples (50% reduction). The sample with Mg/Si~1 exhibited the highest strength among all samples with the minimum required EC (52.5 %IACS). However, the sample with Mg/Si~1.5 showed a better trade-off between strength and EC, provided EC is the main concern. The sample with Mg/Si~0.86 (excessive Si) showed the highest peak strength. However, longer aging times were required to fulfill the minimum EC, giving rise to

deterioration of precipitation strengthening and lower strength. Accordingly, the sample with Mg/Si~0.86 showed a limited window of hardness and EC [26, 27].

Jiang et al. [25] investigated the effect of the Mg/Si ratio on hardness and EC for ultrafine and coarse grain structures in Al-Mg-Si-Sc alloys aged at 200 °C. Fig. 2.5 shows EC versus hardness for these conductors in terms of their best trade-off between hardness and EC. As observed in Fig. 2.5 for the coarse-grained structure, excess Si led to a higher hardness compared to excess Mg with a slight reduction in EC, which resulted from the promoted precipitation hardening. A high number density of precipitates with a spacing of several tens of nanometers might impair EC insignificantly. It is worthwhile to point out that the grain boundary precipitates barely formed in the coarse-grained Al-Mg-Si alloys. However, in the alloys with ultrafine grains, EC was more connected with the Mg/Si ratio, suggesting that excess Si led to a higher EC relative to excess Mg. Silicon promoted grain boundary precipitation, causing the depletion of dissolved Si and precipitates inside grains [25]. Silicon atoms diffuse toward grain boundaries to segregate, resulting in a depletion of Si within grains [15]. This is because the Si diffusion coefficient is larger than that of Mg, and the energy of the grain boundaries is high. Therefore, age softening took place in Si-excessive alloys with fine grains. In general, in ultrafine-grained structures, Si-excessive alloys displayed a lower hardness than Mg-excessive alloys, resulting from the deterioration in age hardening due to grain boundary precipitates. [25]. Although the ultra-fine grains enhanced the hardness, the age softening deteriorated the final hardness of these alloys. Similar results were also seen for ultrafine-grained samples by Han et al. [15]. It was reported that the optimization of hardness and EC was achieved when the Mg/Si ratio of the alloy was 1.48. From Fig. 2.5, it is apparent that a competing approach is still attained between hardness and EC even with the different Mg/Si ratios in the coarse/fine-grained structures.

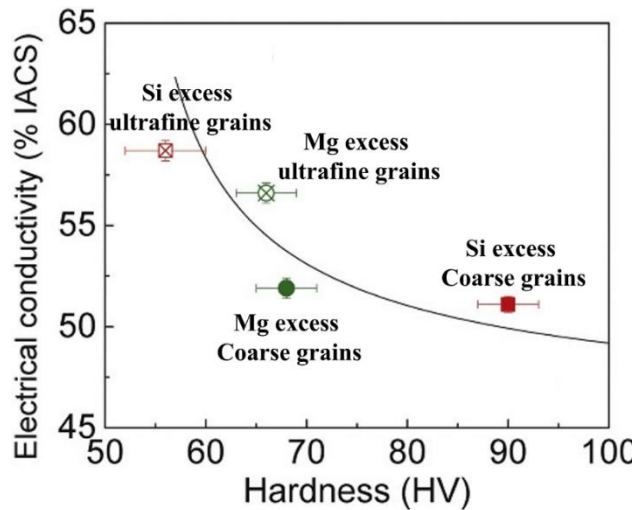


Figure 2.5 Hardness as a function of EC for Al-Mg-Si-Sc alloys with different grain size and Mg/Si ratio, of which the best hardness/EC combination are selected for all sets of samples. The line is a guide for the eyes [25].

Smyrak et al. [61] also studied two alloys with different levels of Mg and Si while having the same Mg/Si ratio (~1): Al-0.72Mg-0.71Si (HA) and Al-0.56Mg-0.56Si (LA). The alloys were subjected to a solution treatment for 12 h at 550 °C, followed by natural aging for 24 h and then artificial aging at different temperatures (from 100 to 240 °C) and various time intervals (0-24 h); the associated results are displayed in Fig. 2.6. The data at high resistivity levels are attributed to aging temperatures less than 150 °C, and the data at low resistivity are ascribed to aging temperatures above 150 °C in both alloys. As shown in Fig. 2.6, an increase in Mg and Si elements (0.15 wt.%) led to an increase in the strength by 25 MPa at the expense of EC (1 nmΩ). However, the HA alloy exhibited a higher strength at the high resistivity end relative to the LA alloy, presumably owing to a larger density number of precipitates in the HA alloy. It was reported that the optimal strength and EC (200 MPa – 57.5% IACS) were acquired at 150 °C

within 4 -10 h for both alloys, which are favorable for the subsequent wire drawing to produce wires with high strength and high EC [61].

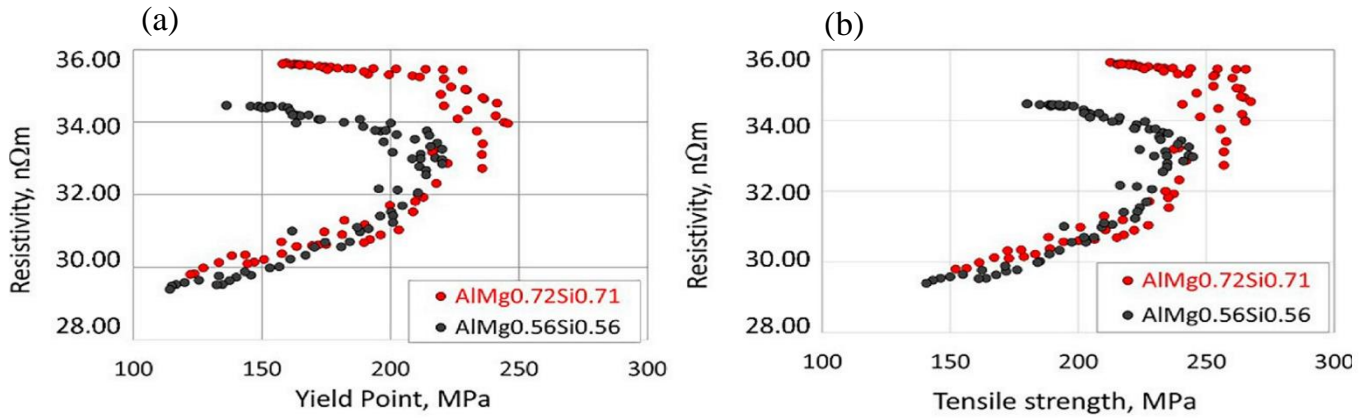


Figure 2.6 The relation between electrical resistivity and (a) yield strength (b) tensile strength for Al-0.72Mg-0.71Si and Al-0.56Mg-0.56Si alloys at different aging temperatures (100-240 °C) and various aging times(0-24 h) [61].

2.3.2. Additional alloying elements

Alloying elements and impurities that dissolve into the matrix as solute atoms have the strongest effects on electrical resistivity [14]. In addition, several alloying elements promote precipitation hardening [12, 28] in Al-Mg-Si alloys. Therefore, it is worth considering the effect of other alloying elements (aside from Mg and Si) on the strength and EC in Al-Mg-Si conductors. Among all alloying elements, transition elements exhibited the most detrimental impact on the EC (for example, Ti, Zr, V, Mn, Cr, etc.), as shown in Fig. 2.7 [5, 6].

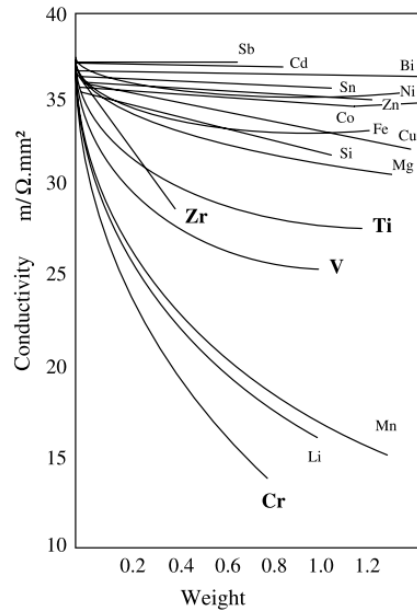


Figure 2.7 Effect of solutes on the electrical conductivity of 99.99% Aluminum [6].

Zirconium is one of the most commonly used transient elements in aluminum alloys, affecting the mechanical and electrical properties. The mechanical properties and EC in AA6101 alloy with Zr and without Zr are shown in Table 2.3 [62]. The results indicated that the mechanical properties were improved with Zr addition. The higher strength in the Zr-added alloy resulted from the presence of thermally stable Al_3Zr precipitates, which enhanced the strength via the Orowan mechanism. Moreover, these particles could retard recrystallization due to pinning the grain boundaries, which is known as the Zener pinning effect. Accordingly, the finer grain structure in the Zr-added alloy resulted in further strength improvement based on the Hall-Petch relation. It was also found that recrystallization could be prevented to some extent during solution treatment due to the presence of Zr precipitates [62, 63]. In contrast to strength, EC

dropped in the presence of Zr due to the dissolved Zr solutes in the matrix and more grain boundaries [62].

Table 2.3 Effect of Zr content of Al–Mg–Si alloys on mechanical and electrical properties [62].

Type of Al-Mg-Si alloy	Hardness (HB)	Tensile strength (MPa)	Elongation (%)	Conductivity (IACS %)
0% Zr	72	220	14.7	55.5
0.145% Zr	83	265	20	54

Lanthanum addition in AA6201 alloy exhibited a deterioration in the mechanical properties but an improvement in EC [64]. Lanthanum led to the formation of $\text{La}(\text{Al},\text{Si})_2$, depleting Si in the remaining melt. Similarly, a reduction in the Si/Fe ratio in the melt favors the formation of the Chinese script α -AlFeSi phase [65]. Chinese script α -AlFeSi has a lower stress concentration relative to sharp needle-like β -AlFeSi phases, which is favorable for strength [66]. However, Si depletion gave rise to fewer precipitates. It was reported that La addition caused the strength to drop, which was attributed to the inferiority of fewer precipitates overcoming the superiority of Fe intermetallic modification on the strengthening. Table 2.4 displays the strength and EC at various La levels. Improving EC with La addition was ascribed to a lower Si concentration in the matrix due to $\text{Al}(\text{Si},\text{La})_2$ formation [64].

Table 2.4 Mechanical properties and EC in AA6201 with La addition [64].

Alloy	Peak hardness (HB)	UTS (MPa)	Elongation (%)	Conductivity (%IACS)
1 (0% La)	95	280	20	52.6
2 (0.1% La)	98	290	24	52.3
3 (0.22% La)	83	265	22.5	54.2
4 (0.32% La)	74	240	15.5	54.6

Aside from lanthanum elements, the effect of cerium on the properties of Al-Mg-Si conductors was also investigated [67]. It was found that the Ce addition (0.3 wt.%) resulted in an EC improvement. This is because Ce in combination with Fe and Si forms AlFeSiCe compounds. Therefore, a reduction in Fe and Si levels in the matrix led to a higher EC [67]. However, Si consumption and depletion in the matrix reduced the precipitation response and strength.

The presence of Fe as an impurity is inevitable in aluminum alloys. Considering the low solubility of Fe in aluminum alloys, Fe generally exists as Fe-bearing intermetallic particles in the microstructure [66, 68]. Fig. 2.8 shows the EC and strength evolution as a function of aging time in Al-Mg-Si conductors with and without Fe [14]. The results show that EC was enhanced with the addition of Fe, but the strength dropped. Microstructural observations showed that with the addition of Fe, a continuous network of Fe-bearing intermetallics was formed in the as-cast structure. As Si atoms are usually integrated in solidified Fe-bearing intermetallics regardless of the Fe-bearing intermetallic type, the concentration of solute Si in the matrix is reduced, which favors EC improvement. However, a reduction in the Si level deteriorated the precipitation hardening, resulting in a lower strength [14, 69].

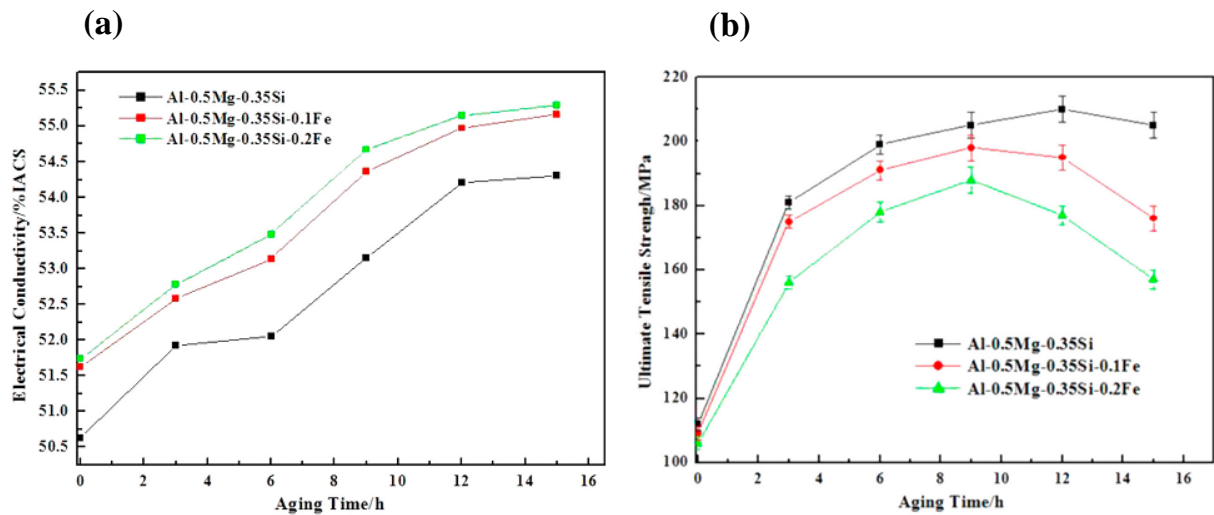


Figure 2.8 (a) EC (b) UTS in Al-0.5Mg-0.35Si alloys with/without Fe over ageing times [14].

In contrast to transition elements, Sr addition was found to increase the strength in AA6201 alloy owing to intermetallic modification and a better response to aging [28, 66]. Regarding intermetallic modification, Sr addition stabilized Chinese script α -AlFeSi phases. Before going further, it is worthwhile to address the solidification reaction of AA6063, of which the chemical composition is in the similar range as that of the AA6101 alloy. The α -Al₈Fe₂Si intermetallic phase directly solidifies from liquid metal via a eutectic reaction, followed by a peritectic reaction in which L + α -Al₈Fe₂Si transforms into L + β -Al₅FeSi [68, 70]. Considering that the β -AlFeSi phase has a higher Si concentration than the α -AlFeSi phase, Si atoms from the liquid matrix must diffuse toward the α -AlFeSi phase to transform into β -AlFeSi in the peritectic reaction. With the addition of 30 ppm Sr, it was found that a large amount of Chinese script α -AlFeSi phases stabilized and did not transform into β -AlFeSi [66]. It was suggested that strontium adsorbed to the α phase interface, retarding Si diffusion and preventing the

transformation of α -AlFeSi into β -AlFeSi in the peritectic reaction. The Chinese script α -AlFeSi phase possesses a desirable impact on the strength compared to sharp needle-like β -AlFeSi. This is related to the fact that α -AlFeSi intermetallics are compacted and have a lower stress concentration, thus improving the strength [66].

Regarding the better aging response, strontium could also improve the strength by ~15% by promoting precipitation of as-drawn wires [28]. As a result of the prevention of β -AlFeSi transformation, more silicon remained in the matrix in the Sr-added AA6201 alloy since the α -AlFeSi phase contained less Si than β -AlFeSi. Subsequently, excessive silicon increased the precipitate density. The density number of precipitates in the Sr-added AA6201 alloy was approximately double compared to Sr-free AA6201 after 3 h of aging at 175 °C. However, the EC of the Sr-containing AA6201 alloy was lower than that of the Sr-free alloy, which was mainly attributed to more dissolved excess silicon [28]. It is worth mentioning that the Sr impact on the strength was maximized when the Fe level was relatively high (~0.3 wt.%).

Flores et al. [12] investigated the effect of microalloying elements on the strength and EC of AA6201 using the optimized thermomechanical process, which is displayed in Fig. 2.9. The studied microalloying elements are Sr (0.003), In (0.01), Sn (0.013), Sb (0.05), Pb (0.08), and Bi (0.08) (all in wt.%). These amounts were chosen based on the maximum solid solubility of these elements in binary phase diagrams with aluminum. From the results in Fig. 2.9, Sn-alloy showed the highest strength (445 MPa) with low EC (48.2% IACS). However, the Bi-containing alloy exhibited a better trade-off between strength (426 MPa) and EC (52.7% IACS). Based on these results, the relation between strength and EC is similar to the trend shown in Fig. 2.2 for commercial aluminum alloys [12].

The addition of Cu and Ag to Al-Mg-Si alloys enhanced the response to age hardening [57, 71, 72]. However, to the best of the authors' knowledge, no systematic studies have been found on the effect of microalloying Cu and Ag on the optimization of strength and EC in 6xxx conductor alloys. To date, most studies have addressed the effect of Cu and Ag on the precipitation behavior and mechanical properties of Al-Mg-Si alloys.

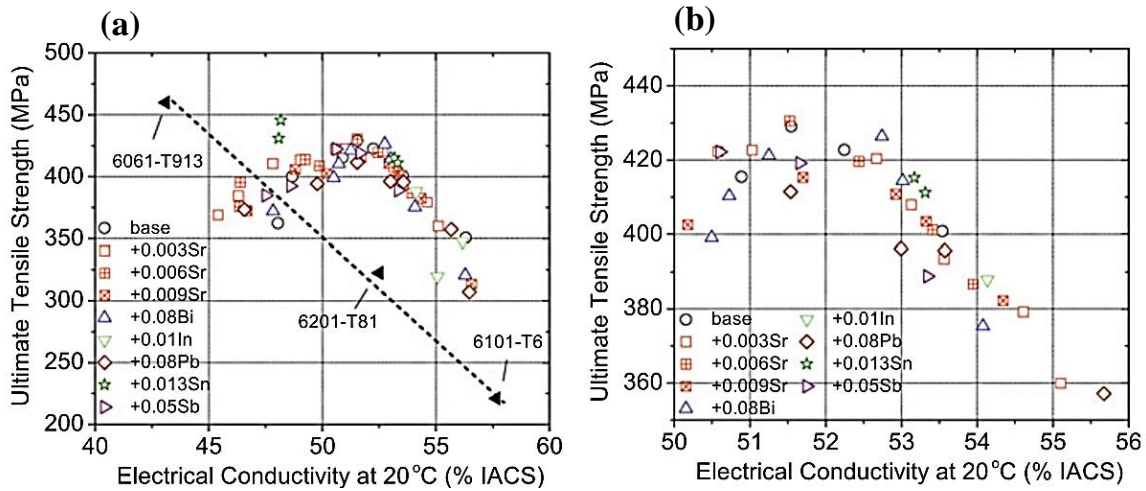


Figure 2.9 (a) A plot of strength and EC for AA6201 alloy with element additions for wires with 2.65 mm (width) square (b) enlarged view of (a) [12]

2.3.3. Grain refiners and modifiers

The addition of grain refiners and modifiers (Al-B) is considered an important step during melt treatment in aluminum conductor fabrication, as mentioned in Section 2. The presence of dissolved transition metals (TMs) mostly leads to scattering electrons and deteriorating EC [5, 6, 29]. The boron addition in the form of Al-B master alloy removes the transition metals from the liquid metal by the formation of TM boride settling down in the tundish or furnace [5, 6], resulting in a remarkable EC improvement. Boron addition also enhances the resistance against failure of lightning arcs [5, 6, 29, 73]. Fig. 2.10a displays the efficiency of AlB₂ on EC, in which

a remarkable improvement in EC could be achieved in the first few minutes of AlB_2 addition (10% settlement of AlB_2). Fig. 2.10b demonstrates that EC was enhanced with boron excess up to 75%, above which EC is deteriorated.

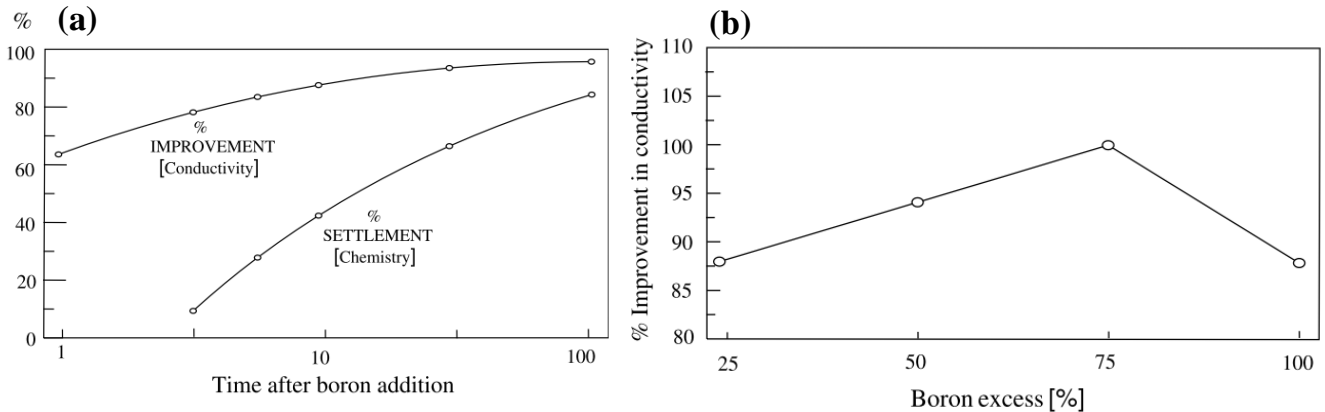


Figure 2.10 (a) % improvement in EC versus time after AlB_2 addition (b) % improvement in EC versus boron excess [5]

In Al-Mg-Si conductor alloys, the combination of grain refiner and boron additions ought to be considered concurrently to achieve better electrical and mechanical properties. In Al-0.5Mg-0.35Si conductor alloys, the addition of 0.12% boron (in the form of Al-3B master alloy) and 0.5% Al-5Ti-1B grain refiner resulted in a good combination of EC and strength in the as-cast condition [29]. The higher strength could be attributed to a fine grain structure based on the Hall-Petch relation, and the higher EC could stem from the extraction of transition elements via boron addition [29]. Accordingly, the addition of grain refiners and Al-B might lead to an enhancement of EC and strength in aluminum electrical conductors [29, 74]. Overall, the addition of a grain refiner (Al-Ti-B) improved the mechanical properties at the expense of EC. As a consequence, the amount of grain refiner (Al-Ti-B) should be as low as possible for refinement with the lowest detrimental effect on EC [29].

On the other hand, segregation of solute atoms and precipitates at grain boundaries could lead to an improvement in EC since more solutes could be extracted from the matrix [29]. Therefore, grain refinement is an important factor affecting precipitates and EC, although they have no direct influence on the precipitate crystal structure [72].

2.4. Effects of thermal and thermomechanical treatments on strength and EC

2.4.1. Thermomechanical treatments

As pointed out in Section 2.2, various thermal and thermomechanical treatments are applied to Al-Mg-Si conductor alloys during fabrication. Among those, thermomechanical treatments (i.e., aging and drawing processes) are the key tools to fulfil the requirements for strength and EC in overhead lines [12, 19, 30]. These processes could be optimized to maximize the strength via precipitation and strain hardening with a minimum loss in EC. It is of great technical interest to find a suitable approach to diminish the scattering of conducting electrons while the dislocation motions are significantly impeded. Hence, conventional and modified thermomechanical treatments will be addressed in the following sections.

2.4.1.1. Conventional thermomechanical treatments

Two important tempers are commonly used in conventional thermomechanical treatments for 6xxx series conductor alloys: T6 and T8 aging treatments. The T6 temper used for the AA6101 alloy consists of cold wire drawing, solution treatment and artificial aging, and the T81 temper employed for the AA6201 alloy is comprised of solution treatment, cold drawing and artificial aging (Fig. 2.3) [12, 32]. A higher strength could be achieved via the T8 temper relative to the T6

temper, which is mainly derived from dislocation forests formed during wire drawing. The strain hardening associated with the drawing process could be entirely recovered through the applied solution treatment in the T6 temper [30]. The dislocations in the T8 temper led to a faster diffusion rate of solutes and coarsening of the precipitates during aging. Therefore, the coarse size and heterogeneous distribution of precipitates exhibited a lower degree of precipitation strengthening in the T8 temper [75, 76], which was counterbalanced with strain hardening from drawing. From the viewpoint of EC, the T8 temper led to a higher increase in EC compared to T6 aging by depleting more solutes from the matrix into precipitates by dislocation-assisted diffusion [30]. Overall, the higher cold deformation in the wire drawing results in a higher peak strength at a shorter time since dislocations could promote precipitation kinetics [30, 77]. Accordingly, the required EC could also be achieved at a shorter aging time [7]. It can be inferred that the T8 temper ought to be used for the AA6201 alloy since it requires extracting more Mg and Si solutes from the matrix to enhance EC to the minimum required values.

The aging temperature (in T6 and T8) and the degree of cold deformation (in T8) in the drawing process are significant factors affecting the electrical and mechanical properties of conductors. With respect to the aging temperature, it was shown that the higher the aging temperature was, the higher the EC and the lower the strength at a given aging time [7, 60, 78]. At low aging temperatures, the minimum required EC might not be achieved, which could pertain to the remaining solute atoms in the matrix and the precipitates with a given interprecipitate spacing [7]. With respect to the deformation degree, it was seen that an increase in the degree of cold wire drawing could enhance strength due to strain hardening [79]. In addition, it was reported that high levels of Si and Mg could even lead to enhanced strain hardening [13]. The multiplication of dislocations during drawing only slightly deteriorates EC

[79]. Moreover, the quantitative equation shows that a large number of dislocations has a negligible detrimental impact on EC [18, 26].

Despite extensive work carried out on the effect of various degrees of cold deformation (wire drawing) on EC and strength [30], microstructure investigations along with the underlying strengthening mechanisms are still lacking in Al-Mg-Si conductors.

Natural aging (NA) is inevitable in conventional thermomechanical treatments during manufacturing Al-Mg-Si cables. After hot rolling in the Properzi process, the materials are exposed to mild quenching down to 50-65 °C, taking a few hours to reach room temperature [39]. Afterwards, the materials are shipped to the customer plant to perform the wire drawing and aging process, experiencing several weeks of NA. Therefore, NA must be taken into account in terms of strength and EC. Rometsch et al. [79] investigated the effect of NA on the ultimate tensile strength (UTS) and EC in an Al-0.5Mg-1.1Si alloy without any drawing processes. It was shown that the number of clusters and GP zones increased with prolonged NA. The formation of GP zones resulted in a higher strength and lower EC [39, 79]. NA gave an increase in the electrical resistivity due to the electron scattering of copious solute clusters and GP zones, while it slightly decreased the dissolved atoms in the matrix [79]. In addition, it was found that the NA samples showed a lower hardness in the post aging relative to the freshly quenched and aged sample (after 2 h aging) [79]. This is because the clusters and GP zones formed in NA were unstable, and they were dissolved into the matrix during artificial aging, ending with a low number density of precipitates in NA samples [80, 81].

Practically, natural aging is followed by the wire drawing process [7, 39], meaning that the drawing process might affect clusters and GP zones formed during NA. Cervantes et al. [7] studied the effect of different NA times at room temperature followed by drawing and aging on

strength and EC in AA6201 alloy containing 0.6 wt.% Mg and 0.55 wt.% Si. The NA samples showed a higher strength than the sample with no NA. Natural aging after 14 days followed by aging at 165 °C for 7 h exhibited the optimized strength and EC [7]. As mentioned above, NA from mild quenching (down to 50-65 °C) followed by the subsequent storage at room temperature due to transportation should be also taken into account. In our recent work [37], the two-step natural aging was simulated and applied to the samples and compared with those without NA in terms of hardness (strength) and EC. The natural aging was comprised of solution treatment and quenching, 10h or 20h at 70 °C followed by keeping at ambient temperature for 2 weeks, drawing (50%) and aging (180 °C), designated as 10NA and 20NA samples, respectively. Fig. 2.11 shows the plot of the strength and EC for the naturally aged samples (10NA and 20NA) and the samples without natural aging (No NA). The 10NA and 20NA samples exhibited a better compromise between strength and EC compared to No NA samples (Fig. 2.11). It should be noted that all samples exceeded the minimum required EC (52.5 %IACS) after 5 h aging. The TEM micrographs of 20NA and No NA samples after 5 h aging are displayed in Fig. 2.12 to tailor the microstructural feature with the hardness values. The dominant microstructure in No NA samples is lath-like precipitates along with few needle-shaped precipitates extended in $\langle 002 \rangle_{Al}$ direction (Fig. 2.12a), shown with arrows in Fig. 2.12a. In addition to these precipitates, the 20NA sample aged for 5 h revealed the precipitates with a smaller cross section shown with white arrows in Fig. 2.12b. As shown in Fig. 2.12d, the precipitate number density in the NA Samples is higher than those without NA owing to the presence of these fine precipitates. In the NA samples, the movement of the dense dislocations during wire drawing could shear and dissolve the GP zones into the matrix in the form of solute-enriched aggregates. Then, these aggregates evolved into these fine precipitates during postaging [37].

In Figs. 2.11 and 2.12, the 20NA-PA refer to the samples exposed to preaging (5 h at 180 °C) after the two-step NA, which will be discussed in the following section.

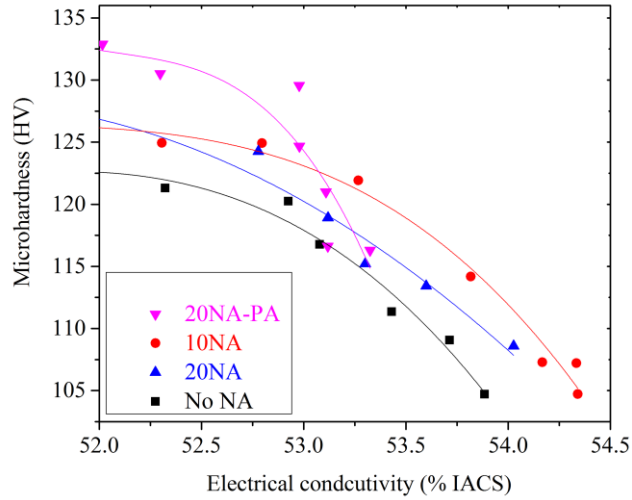


Figure 2.11 The plot of the strength and EC for samples with NA (10NA and 20NA), NA followed by preaging (20NA-PA), and without NA; all samples followed by cold wire drawing and aging at 180 °C. Reprinted with permission from [37]

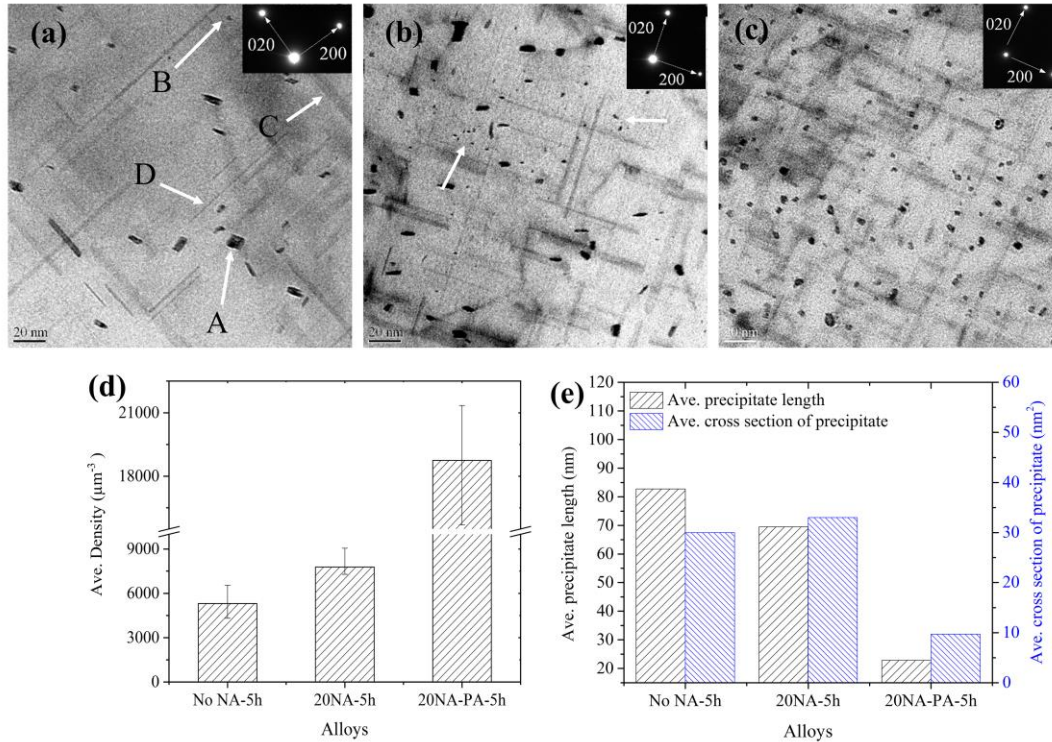


Figure 2.12 TEM images of (a) No-NA sample aged for 5 h (b) 20NA sample aged for 5 h (c) 20NA-PA sample aged for 5 h, (d) the precipitate number densities and (e) the average length and the cross section of precipitates. A and B correspond to the cross-sectional projections of lath-like and needle-shaped precipitates in $\langle 002 \rangle$ direction; C and D correspond to the longitudinal projections lath-like and needle-shaped precipitates, respectively. Reprinted with permission from [37]

2.4.1.2. Modified thermomechanical treatments

High strength in Al-Mg-Si conductors is required for carrying loads caused by wind, ice and the weight of the conductor [32]. The proper design of thermomechanical treatments is among the techniques leading to the improvement of strength in conductors. A concurrent enhancement of the strength and EC could be obtained by changing the sequence of the thermomechanical process, known as modified thermomechanical treatments (M-TMT). In some M-TMTs, the sequence of the process consisted of solution treatment, preaging, cold drawing, and resuming

artificial aging [19, 30, 31, 82, 83]. Preaging treatment can result in the formation of GP zones or precipitates.

Lin et al. [30] found that an M-TMT comprising a solution treatment, preaging for 2 h at 180 °C, cold rolling at a reduction of 70%, and reaging at 180 °C for 6 h exhibited a better combination of strength and EC (301 MPa and 58.9% IACS) for Al-0.62Mg-0.57Si alloy (in wt.%) compared to the conventional thermomechanical treatment. It was observed that GP zones were formed during 2 h preaging, and they might be sheared off by dislocations in the cold rolling process. It was stated that the sheared GP zones could be subsequently dissolved in the matrix in the form of solute-enriched aggregates rather than homogeneously distributed solutes due to the low diffusion rate of solutes in cold rolling [30, 84, 85]. Then, the aggregates evolved into precipitates during reaging. Accordingly, more solute atoms were transformed into copious precipitates, leading to higher strength and EC [30]. Moreover, Bunte et al. [31] presented another M-TMT for AA6101 alloy, composed of partial aging at 200 °C for 1 h, wire drawing (65-90% cross section reduction), and reaging. This enhanced the strength (346 MPa), EC (53.5% IACS), and torsion properties, of which the underlying microstructure was not addressed [31].

Liu et al. [19] also suggested M-TMT for an Al-1Mg-0.5Si-0.8Cu alloy (in wt.%) to outperform conventional thermomechanical treatment (C-TMT). M-TMT consisted of solution treatment, preaging at 180 °C for 5 h, cold working (80% reduction) and resuming artificial aging (at 180-240 °C). The C-TMT was comprised of cold working (80% reduction), solution treatment and artificial aging (at 180-240 °C). Fig. 2.13 displays the mechanical and electrical properties of Al-Mg-Si-Cu alloys treated by two different thermomechanical treatments. The strength and EC of the samples treated by M-TMT were higher than those of C-MTM. The higher strength of the

samples in M-TMT could pertain to the high density of dislocations and precipitates. Notably, pre-existing precipitates formed during preaging were so stable during cold working, although their morphologies were slightly changed. [19]. Notably, precipitate fragmentation was observed during plastic deformation owing to dislocation sliding [16, 86, 87]. In this M-TMT [19], the strength and EC reached 426 MPa and 53.5% IACS at 180 °C for 1 h, respectively. With further reaging (35 h), the strength and EC became 316 MPa and 57.4% IACS, respectively. An increase in EC with reaging time might mainly pertain to more precipitation of alloying elements from the matrix, through which the lattice distortion is mitigated. Conversely, prolonging the reaging caused the coarsening of precipitates, ending with a decrease in strength [19].

In M-TMT, it is often believed that the presence of precipitates could enhance strain hardening [30, 31]. In contrast, Cheng et al. [88] proved that the samples subjected to underaging and peak aging showed less strain hardening relative to the as-quenched samples in cold deformation.

In our recent work [37], preaging (5 h at 180 °C) was applied to the samples after two-step natural aging followed by the wire drawing and postaging, designated as 20NA-PA. As shown in Fig. 2.11, the 20NA-PA samples showed a better trade-off between hardness and EC compared to the NA samples and those without NA. The higher hardness above the minimum required EC (52.5 %IACS) in the 20NA-PA sample was ascribed to their considerably higher number density of the precipitates relative to the other samples (Fig. 2.12). From Fig. 2.12, it appears that the pre-existing precipitates were fragmented during wire drawing via the moving dislocations, ended up with very short precipitates. Although the preaging maximized the precipitate hardening in the 20NA-PA sample, it deteriorated the strain hardening during wire drawing compared to the to the NA samples and those without NA. However, the increased precipitation hardening is superior to the reduced strain hardening in the 20NA-PA samples [37].

On the one hand, some studies [12, 32] have dealt with applying cold drawings after aging treatment, namely, first solution treatment, artificial aging at different times, and then cold wire drawing. Flores et al. [12] reported that an optimized route (solution treatment, aging at 200 °C, and wire drawing) for AA6201 alloy shows a better combination of strength and EC relative to T6 and T8 tempers. Furthermore, Hou et al. [32] also presented an M-TMT to obtain a better strength (352.3 MPa) and EC (56% IACS), which consisted of hot rolling at 390-420 °C followed by quenching, artificial aging at 175 °C for 4 h, and wire drawing. It is worth pointing out that the contributions of dislocation hardening and grain boundary strengthening were maximized in this process by omitting the conventional solution treatment. The higher strength of the AA6201 alloy processed by M-TMT was ascribed to the contribution of precipitation hardening, strain hardening, and grain boundary strengthening [32].

Martinova [83] also worked on an M-TMT, including 90-120 °C preaging for up to 1 h, cold drawing (75-95% reduction), and reaging at 170-200 °C. It was found that M-TMT exhibited a better compromise between strength and EC than conventional TMT.

In industrial practice, applying a solution treatment could cause extra cost and a complicated process [82]. Therefore, it is recommended to frequently regulate the temperature of the cast bar at the step before hot rolling to hold the temperature of the alloys above the solvus temperature during hot rolling [38]. Lentz et al. [82] suggested an acceleration of the cooling rate of solidification (>100 K/s) for AA6101 alloy to retain Mg and Si in the matrix in twin-roll casting (TRC). The modified TRC was comprised of a high cooling rate from casting, 8 h aging at 185 °C, 80% cold rolling, and 8 h reaging at 185 °C (if necessary). This led to a strength of ~258 MPa with an EC of ~55.5% IACS in the as-rolled state and a strength of 211 MPa with an EC of ~ 57.5% IACS after reaging [82].

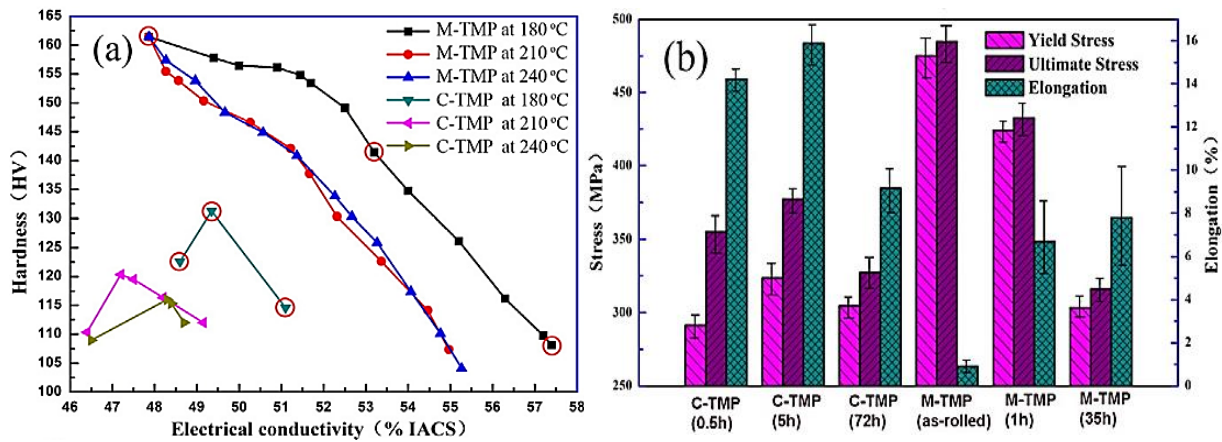


Figure 2.13 (a) hardness vs. electrical conductivity in Al–Mg–Si–Cu alloys treated by C-TMP and M-TMP; (b) mechanical properties of the C-TMP and M-TMP samples re-aged at 180 °C [19].

2.4.1.3. Other heat treatments

Aside from the aging treatment during the thermomechanical process, other heat treatments in the fabrication of conductor wires should be taken into account.

Yuna et al. [89] investigated the impact of homogenization temperature on the strength and EC in Al-Mg-Si-Ce conductor alloys. It was reported that it barely affected the strength of the alloy. However, rising the homogenization temperature from 535 °C to 560 °C led to an increase in EC from 56.5 to 57.3% IACS. With a further temperature increase up to 580 °C, EC slightly decreased to 56.8% IACS. In general, EC in the homogenized sample outperforms in the cast sample. The EC behavior as a function of homogenization temperature was attributed to the vacancy number. An increase in homogenization temperature from 535 to 560 °C augmented the

vacancy number, leading to a smaller lattice distortion and higher EC. At 580 °C, more vacancies could be formed, and the lattice parameter decreased than the ideal value. Accordingly, lattice distortion again increased, and EC deteriorated [89]. Karabay et al. [90] also found 560 °C as an appropriate homogenization temperature. In Al-Mg-Si conductor alloys containing 0.2 wt.% Fe, both EC and strength were enhanced after homogenization at 630 °C for 8 h [14]. An improvement in strength could be associated with the formation of discontinuous rod-shaped α -Al₈Fe₂Si intermetallics with lower stress concentrations during high-temperature homogenization compared to plate-like intermetallics in the as-cast microstructure. In homogenization, some α -Al₈Fe₂Si intermetallics dissolved into the matrix at elevated temperature (630 °C), and then the dissolved Fe and Si atoms might extract out of the matrix toward the remaining α -Al₈Fe₂Si phase to decrease the volume and surface area of the phase, resulting in a discontinuous rod-shaped α -Al₈Fe₂Si phase [14].

The extrusion temperature could also influence the strength and EC of conductor alloys. Liao et al. [91] studied the electrical and mechanical properties of an as-extruded Al-0.35Si-0.2Mg-0.3Ce alloy at different extrusion temperatures (460, 510 and 560 °C). The alloy extruded at 460 °C exhibited lower strength and higher EC relative to other extrusion temperatures. This extrusion temperature led to the dynamic precipitation of equilibrium noncoherent Mg₂Si particles. However, very weak dynamic precipitation could take place at 510 and 560 °C. Therefore, a lower strength at 460 °C was associated with a lower contribution of solute strengthening, and a higher EC pertained to the extraction of more solutes from the matrix [91]. In the solution heat treatment, the materials are kept at a temperature range between the solvus and the solidus line to dissolve solute atoms into the matrix [92]. In general, the extrusion temperature was recommended to be above 490 °C to achieve a favorable aging response [90].

Iraizoz et al. [9] reported 510 °C as the minimum solution treatment temperature for AA6201 (0.66% Mg, 0.53% Si and 0.20% Fe, in wt.%) to maximize the age hardening response. Indeed, the extrusion temperature is connected with the chemical composition of the samples since the alloy composition determines the solvus temperature.

Another heat treatment reported in the literature is intermediate annealing during cold wire drawing prior to aging. Wu et al. [93] investigated the effect of intermediate annealing during cold wire drawing on the mechanical properties and conductivity of an Al-0.2Mg-0.35Si-0.3Ce alloy. The drawing was initially carried out at room temperature, reducing the diameter from 10 to 4.5 mm. Then, intermediate annealing was conducted at 150, 200, 250, 300 °C for an hour. Afterwards, the rod was drawn to 3 mm at room temperature, followed by aging treatment. The highest strength (218 MPa) was achieved when the alloy was exposed to annealing at 150 °C for an hour. The strengthening effect of β'' precipitates was superior to the softening impact at 150 °C. By increasing the annealing temperature to 300 °C, the strength dropped to some extent due to the softening effect originating from overaging, recovery, and recrystallization. In contrast, EC improved with increasing annealing temperature owing to solute extraction from the matrix [93]. Zhang et al. [94] also investigated the effect of annealing temperatures ranging from 200 to 500 °C for 3.5 h on the strength and EC in Al-Mg-Si alloy cables. It was shown that a higher annealing temperature increased the EC at the expense of strength due to recovery and recrystallization.

Osuch et al. [95] studied the effect of the direct aging procedure on the age hardening response of AA6101. The procedure comprised solution treatment, followed by quenching in air down to the aging temperature and then immediate aging. Direct aging refers to precipitation during quenching in the air from the solutionization temperature to the aging temperature. Direct aging

showed a higher EC at the expense of strength compared to conventional T6. This could stem from larger precipitates and a more precipitate-free zone formed in the direct aging procedure. A lower cooling rate during air quenching from the solutionization temperature to the aging temperature led to the diffusion of more vacancies toward grain boundaries. Therefore, vacancies were depleted in the vicinity of grain boundaries, resulting in the formation of a precipitate-free zone. EC enhanced with a slight drop in strength. This heat treatment could be valuable if the EC might be taken as a priority over the strength [95].

2.4.2. Severe plastic deformation

Maximizing the area reduction in cold drawing might simultaneously enhance strength and EC. Therefore, new approaches have been developed to improve the strength and EC concurrently via severe plastic deformation (SPD) combined with artificial aging, lying strength and EC above the upper limit, as shown in Fig. 2.2 [16, 18, 35, 96]. The most well-known SPD processes are high-pressure torsion (HPT), equal-channel angular pressing (ECAP) and its modifications, accumulative roll bonding (ARB), and hydrostatic extrusion (HE) [97]. In the following section, various combinations of SPD processes and aging will be discussed in terms of electrical and mechanical properties.

Valiev et al. [16] found a desirable combination of strength and EC for AA6201 alloys using severe plastic deformation. In this study, HPT was initially performed at room temperature, followed by HPT processing at elevated temperatures (130, 180, and 230 °C). During HPT at elevated temperatures, a nanosized grain structure along with nanoscale precipitates formed.

Therefore, the higher strength was attributed to grain boundary strengthening and precipitation hardening, and superior EC was ascribed to the absence of GP zones and fewer solutes. Based on the results of Table 2.5, the best trade-off between strength (365-412 MPa) and EC (55.6-58.4% IACS) was achieved when the second HPT was performed at 130 and 180 °C. Similar results were also observed for AA6101 alloys by Sauvage et al. [18]. It is worthwhile to point out that precipitates were sheared by dislocations during SPD into spherical precipitates identified as β' -Mg₉Si₅ [16]. The strengthening effect of β' -Mg₉Si₅ precipitates could be ascribed to their small size (10-30 nm) and high number density. In addition, the lattice parameters of AA6201 at 130-230 °C were close to that of pure aluminum (4.0494 Å), showing that most solute atoms were removed from the matrix into the β' -Mg₉Si₅ phase [16, 35, 96]. Indeed, the two-step SPD led to a decrease in GP zones and solute atoms in the matrix [16, 96]. The dynamic aging in the second SPD at 130-180 °C was a vital key to enhancing precipitation hardening and grain boundary strengthening. This is because ultrafine grains and precipitates were concurrently formed with few grain boundary precipitates [16]. The segregation of solutes and precipitates at grain boundaries could somehow assist EC enhancement [18]. In contrast, Jiang et al. [25] showed that grain boundary precipitates were the predominant microstructure feature after post aging of ultrafine-grained Al-Mg-Si conductor alloys, leading to higher EC at the expense of strength.

Table 2.5 Microstructure, mechanical properties and EC of AA6201 alloy at the different conditions (d, grain size; dp, precipitate size; a, lattice parameter; CG, coarse grain; UFG, ultrafine grain) [16].

Processing	Structure	a (°Å)	UTS (MPa)	Elongation%	EC (IACS%)
SST	CG, d = 65 μm	4.0526	95	20.4	51.0
T81	CG	4.0512	330	6.1	53.6
SPD at 130°C	UFG, d = 280 nm, dp = 10 nm	4.0509	412	4.9	55.6
SPD at 180°C	UFG, d = 440 nm, dp = 30 nm	4.0505	365	8.8	58.4
SPD at 230°C	UFG, d = 960 nm, dp = 50 nm	4.0500	275	19.1	59.0

Sauvage et al. [18] showed the effect of HPT at room temperature followed by artificial aging on the hardness and EC in AA6101 alloys. Fig. 2.14 shows the variation in hardness and EC in the AA6101 alloy processed by 20 turns via HPT at room temperature followed by aging at different temperatures. Horizontal lines characterized conventional T4 (natural aging) and T6 (peak hardness) treatments of the same alloy. Based on Fig. 2.14, a good combination of hardness and EC was achieved at 130 °C owing to grain boundary strengthening and precipitation hardening. Precipitates were observed both at grain boundaries and inside grains in these samples. The AA6101 alloy treated by HPT at room temperature and aging at 100 and 130 °C showed hardness levels 20% higher than those of the T6 alloy at the end of aging (Fig. 2.14a) [18].

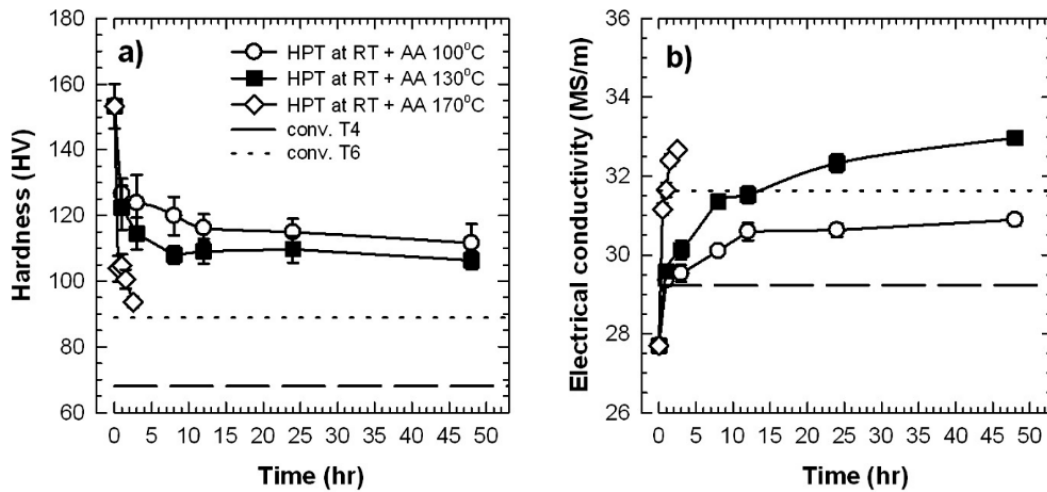


Figure 2.14 (a) Microhardness (b) EC for AA6101 processed by HPT at room temperature followed by artificial aging at various temperatures. Microhardness of the sample for T4 and T6 tempers are brought for comparison purpose [18].

Murashkin et al. [34] also reported a better combination of strength and EC for AA6101 alloys using equal channel angular pressing with parallel channel (ECAP-PC) processing above 100 °C followed by artificial aging. The main drawback of HPT and ECAP-PC (as SPD processes) is the small size of billets, limiting their application in the industry. Murashkin et al. [35] presented equal channel angular pressing-Conform (ECAP-C) producing an electrical wire from long billets. High EC (57.1% IACS) and strength (over 304 MPa) of AA6101 alloy could be achieved using (ECAP-C) at 130 °C followed by aging at 170 °C for 12 h. In this process, EC and elongation were higher than those reached at T81 process while strength is similar. As mentioned for SPD via HPT, (ECAP-C) at 130 °C also led to dynamic aging. Postartificial aging improved EC via precipitation with a slight decrease in strength. The β' phase precipitated along grain boundaries via dynamic aging in ECAP-C at 130 °C. In addition, some β' precipitates formed inside grains in subsequent artificial aging [35].

Fig. 2.15 illustrates the relation between the strength and EC for Al-Mg-Si conductors. The green box in the figure is related to conventional Al-Mg-Si conductors (EN 50183 standard), while the red box belongs to AA6201 alloy with nanosized grains and nanoscale precipitates achieved by SPD [16]. The same trend was observed for AA6101 alloy [18]. Severe plastic deformation along with aging results in the strength and EC above the upper limit for commercial aluminum conductors.

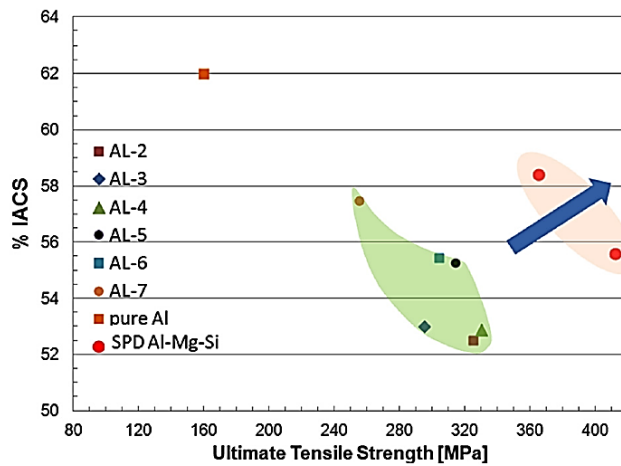


Figure 2.15 A comparison of strength and EC for (AL2–AL7) in EN 50183 standard (green box) with those obtained by severe plastic deformation (red box) for AA6201 alloy [16].

Majchrowicz et al. [33] studied hydrostatic extrusion (HE) combined with artificial aging, which could be applicable for the fabrication of electrical wires via long billets. It improved the strength owing to grain boundaries and precipitate strengthening with a relatively high EC for the AA6101 alloy. In the process after solution treatment, the materials were subjected to the HE extrusion process, of which the diameter was reduced from 20 to 10 mm, designated H10. Afterwards, these extruded materials were re-extruded down to diameters of 4 mm and 3 mm, designated H4 and H3, respectively. Finally, artificial aging was performed at 180 °C for 1-24 h. Fig. 2.16 demonstrates the evolution of strength and EC as a function of aging time for HE-

processed AA6101 and coarse-grained (CG) AA6101. Based on the results, hydrostatic extrusion led to a shorter aging time for peak hardness, meaning that precipitation kinetics were increased due to microstructural defects acting as nucleation sites for precipitates. Notably, adiabatic heating during extrusion caused the temperature to increase up to 150 °C, leading to the formation of GP zones during hydrostatic extrusion. The electrical conductivities of H3 and H4 of AA6101 were found to be much higher than those of CG AA6101. Grain boundary segregation and precipitates in extruded AA6101 gave rise to more matrix purification. HE4 of AA6101 aged at 180 °C for 7 h was identified as the best compromise between EC (58% IACS) and strength (332 MPa). Some spherical (β' -Mg_{1.8}Si or β -Mg₂Si) precipitates were observed at grain boundaries, showing overaged conditions. Hydrostatic extrusion followed by artificial aging exhibited a better combination EC and strength in comparison to the values in the EN 50183 standard [33]. As mentioned above, post artificial aging of ultrafine-grained Al-Mg-Si alloys most improved EC at the expense of strength due to more grain boundary precipitation [33].

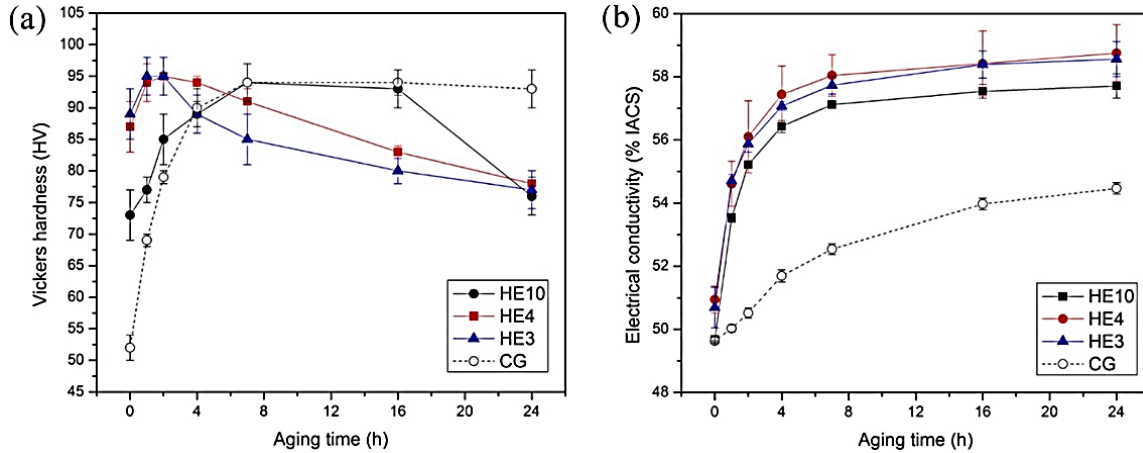


Figure 2.16 (a) Hardness (b) EC for AA6101 exposed to different hydrostatic extrusion (HE) reductions and aged at 180 °C up to 24 h [33].

Medvedev et al. [98] applied ECAP to solutionized AA6101, followed by aging at 130 °C for up to 72 h. ECAP was applied for 2, 4, and 8 passes, corresponding to strains 2.3, 4.6, and 9.2, respectively. Fig. 2.17 displays the EBSD images of the samples after 2, 4, and 8 passes without and with aging treatment. It could be deduced that an increase in the number of ECAP passes to 4 passes resulted in thickening shear bands (Fig. 2.17b). With a further increase in the number of ECAP passes to 8 passes, the shear band became thin (Fig. 2.17c). This was attributed to the dynamic recovery process at high deformation because a high dislocation density facilitates the transformation of dislocation arrays into high-angle grain boundaries. The microstructure just after the ECAP process was not uniform and comprised intersecting shear bands with small grains of ~200 nm inside and an interband matrix containing large grains of ~10-20 μm. Figs. 2.17d to 2.17f show the microstructures of samples after aging at 130 °C after 72 h for 2, 4, and 8 passes. Samples after aging tended to form uniform equiaxed grains due to dynamic recrystallization (DRX). The lower degree of equiaxed grains after 2 passes of ECAP and aging

(Fig. 2.17d) might be attributed to the lower level of strain, which was not sufficient for dynamic recrystallization [98].

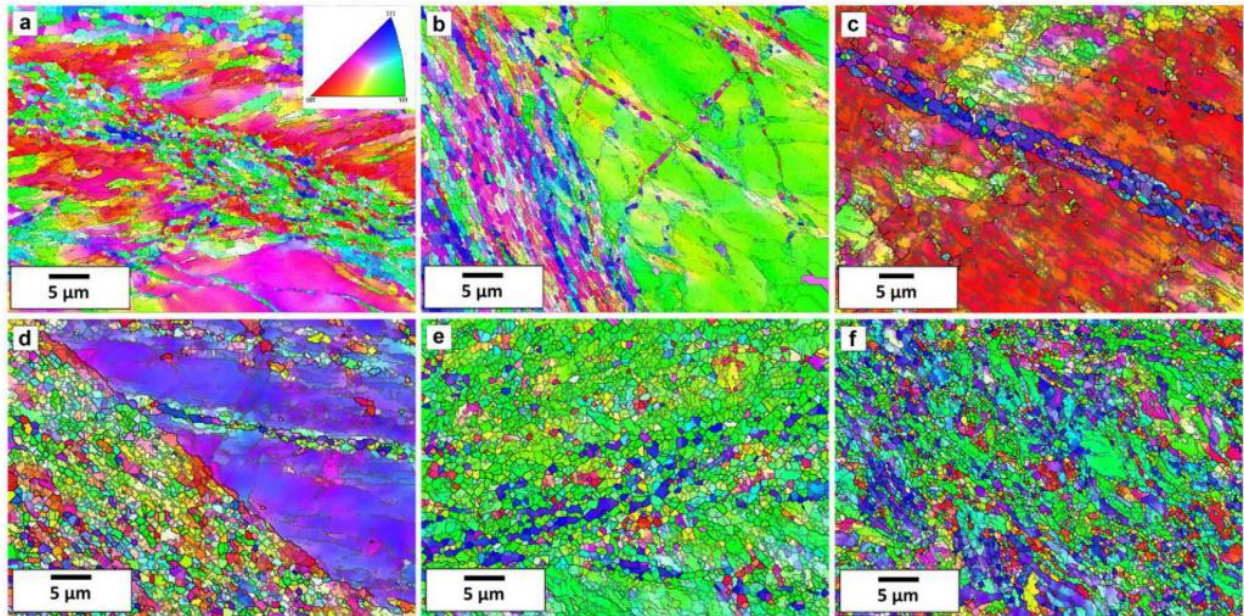


Figure 2.17 EBSD microstructure images of AA6101 Alloy after 2, 4, and 8 passes of ECAP-BP (a–c) without aging, (d–f) BP after aging at 130 °C for 72 h, in the sample cross section [98].

2.5. Recent development in modeling Al-Mg-Si conductor properties

2.5.1. Strength model in Al-Mg-Si alloys

As mentioned above, the main strengthening mechanisms in Al-Mg-Si alloys are precipitate strengthening, dislocation strengthening, grain boundary hardening, and solid solution strengthening. In general, the total strength equals the linear sum of strengthening mechanisms by assuming that they are independent, as expressed in Eq. 2.1 [15, 18, 25, 99, 100].

$$\sigma_{\text{total}} = \sigma^{\text{Al}} + \Delta\sigma^{\text{PREC}} + \Delta\sigma^{\text{DISLO}} + \Delta\sigma^{\text{GB}} + \Sigma\Delta\sigma_i^{\text{SOL}} \quad (2.1)$$

Where the σ_{total} is the total yield strength, σ^{Al} is the yield strength of the aluminum matrix, $\Delta\sigma^{\text{PREC}}$ is precipitate hardening, $\Delta\sigma^{\text{DISLO}}$ is strain hardening via dislocation forest, $\Delta\sigma^{\text{GB}}$ is grain boundary strengthening, and $\Sigma\Delta\sigma_i^{\text{SOL}}$ is the solute strengthening of elements dissolved in the aluminum matrix.

Precipitation of β''/β' are the most prominent strengthening factor in heat-treatable Al-Mg-Si alloys owing to their age hardening response. Depending on the precipitate types, the dislocation sliding is hindered by either shearing or bypassing of precipitates [99].

For shearable precipitates (β''), the increased strength could be expressed by the following equation (Eq. 2.2) [99].

$$\Delta\sigma_{\text{shear}}^{\text{PREC}} = \frac{M}{b^2 \sqrt{\beta G}} \cdot (N_v \cdot r_p)^{1/2} \cdot F^{3/2} \quad (2.2)$$

$$F = 2\beta G b^2 \cdot \left(\frac{r}{r_c}\right) \quad (2.3)$$

Where β is a constant close to 0.28, M as Taylor factor is taken as 2 [101, 102] or 3 [18, 25] to convert shear stresses into normal stresses, G is the shear modulus (26.9 GPa) of FCC Al, and b is the burger vector (0.29 nm) of the dislocations in FCC Al(110) [18], N_v is the volume density of precipitates, r_p is the mean size of precipitates, r_c is the transition radius from precipitate shearing to bypassing (5 nm), and F is the mean obstacle strength of precipitate (Eq. 2.3) [99],

For non-shearable precipitates (β'), the stress required to bypass the precipitates (Orowan mechanism) can be given in Eq. 2.4 [15, 18, 25].

$$\Delta\sigma_{\text{Or}}^{\text{PREC}} = \frac{2M\beta G b}{L^{\text{PREC}}} \quad (2.4)$$

L^{PREC} is defined as the mean particle spacing, expressed in the following equation [18].

$$L^{PREC} = \frac{1}{(Nv)^{1/3}} \quad (2.5)$$

It is worth mentioning that the strength at the minimum required EC (52.5 % IACS) for AA6201 alloy was usually achieved in the overaged condition [21]. Then, the Orowan equation was generally fitted with the precipitate strengthening model [15, 18, 25].

Strain hardening via dislocation forest is also considered as a significant strengthening factor in Al-Mg-Si conductors due to the cold deformation process. Eq. 2.6 could be used to estimate the strain hardening as a function of dislocation density [15, 18, 25, 99].

$$\Delta\sigma^{DISL} = \alpha.M.G.b. (L^{dislo})^{1/2} \quad (2.6)$$

where M, G, and b were defined above; α is a constant close to 0.3, and L^{dislo} is the density number of dislocations measured using X-ray diffraction [18].

The strength provided by grain boundaries is expressed by the well-known Hall-Petch equation (Eq. 2.7) [15, 25].

$$\Delta\sigma^{GB} = k_{HP}.d^{-1/2} \quad (2.7)$$

where k_{HP} is a scaling constant ($0.042 \text{ MPa}/\text{m}^{-1/2}$), and d is the mean grain size of the samples [25].

The increased hardness due to the solutes (particularly Mg and Si) could be estimate using Eq. 2.8 [15, 18, 25, 100].

$$\Delta\sigma^{SOL} = \sum k_i C_i^{2/3} \quad (2.8)$$

Where $\Delta\sigma^{SOL}$ is the increased hardness value for solute i, and k_i is a scaling factor for the solute i, for instance. 29 and 66.3 MPa (wt.%)^{-2/3} for k_{Mg} and k_{Si} , respectively. C_i is the concentration of the solute i (in wt.%) [15, 18, 25, 100].

2.5.2. Electrical resistivity model

As discussed in Section 2.1, the electrical resistivity is closely connected with the crystal defects. Accordingly, in Al-Mg-Si conductor alloys, the total electrical resistivity could be estimated by summing the resistivity contributions in a linear manner (Matthiessen's rule), as given in Eq. 2.9, which could be converted to the electrical conductivity (% IACS) using Eq. 2.10 [103].

$$\rho_{\text{total}} = \rho^{\text{Al}} + \Delta\rho^{\text{PREC}} + \Delta\rho^{\text{DISLO}} + \Delta\rho^{\text{GB}} + \Delta\rho^{\text{SOL}} \quad (2.9)$$

$$\text{EC (\% IACS)} = \frac{172.4}{\rho_{\text{total}} (\mu\Omega\text{cm})} \quad (2.10)$$

where the total resistivity (ρ_{total}) can be calculated by summation of the resistivity from the aluminum matrix (ρ^{Al}), precipitates ($\Delta\rho^{\text{PREC}}$), the dislocation forest formed via the cold wire drawing ($\Delta\rho^{\text{DISLO}}$), grain boundaries ($\Delta\rho^{\text{GB}}$), and the solutes ($\Delta\rho^{\text{SOL}}$).

The electrical resistivity of precipitates is estimated using Eq. 2.11 [104].

$$\Delta\rho^{\text{PREC}} = \frac{\Delta\rho^{\text{prec}}}{(L^{\text{prec}})^{1/2}} \quad (2.11)$$

where $\Delta\rho^{\text{prec}}$ is the resistivity constants ($12 \Omega(\text{nm})^{3/2}$) for the precipitates in the aluminum matrix [104].

Eq. 2.12 could be used to estimate the electrical resistivity caused by dislocations [18].

$$\Delta\rho^{\text{DISL}} = L^{\text{dislo}} \Delta\rho^{\text{dislo}} \quad (2.12)$$

$\Delta\rho^{\text{dislo}}$ is known as a resistivity constant of dislocation ($2.7 \times 10^{-25} \Omega\text{m}^3$) [18].

The grain boundary resistivity could be estimated by Eq. 2.13 [18].

$$\Delta\rho^{\text{GB}} = S^{\text{GB}} \Delta\rho^{\text{gb}} \quad (2.13)$$

Where $\Delta\rho^{\text{gb}}$ is the resistivity constants for grain boundaries ($2.6\times 10^{-16} \Omega\text{m}^2$), and S^{GB} is defined as $6/d$ (d is the average grain size) supposing that grains are spherical to calculate the grain boundary resistivity ($\Delta\rho^{\text{GB}}$) [18].

The increased electrical resistivity due to the solutes could be estimated using Eq. 2.14 [18].

$$\Delta\rho^{\text{SOL}} = \sum C_i^{\text{sol}} \Delta\rho_i^{\text{sol}} \quad (2.14)$$

Where $\Delta\rho^{\text{SOL}}$ is the resistivity contribution due to solutes; $\Delta\rho_i^{\text{sol}}$ is the resistivity constants for the solute i . For Mg and Si solutes, $\Delta\rho^{\text{Mg-sol}}$ and $\Delta\rho^{\text{Si-sol}}$ are $0.445\times 10^{-6} \Omega\text{cm} (\text{at. \%})^{-1}$ and $0.496\times 10^{-6} \Omega\text{cm} (\text{at. \%})^{-1}$, respectively [18].

2.5.3. Case study of strength and electrical resistivity models

It would be valuable to estimate the effect of various strengthening factors on the strength and electrical resistivity of aluminum conductor alloys using the models and constitutive equations described above. This will provide a great aid to design a proper thermomechanical treatment with the appropriate addition of alloying elements. In this case study, some assumptions in the microstructure and alloying elements in an Al-Mg-Si alloy (AA6201) were considered to demonstrate the impact of strengthening factors. Here, it is supposed that the microstructure of an AA6201 alloy containing 0.6% Mg and 0.6% Si (all in wt.%) is characterized by a mean particle spacing of 50 nm for β' precipitates, a dislocation number density of 10^{15}m^{-2} , and a mean grain size of 400 nm in the case of ultrafine grains obtained by severe plastic deformation. It is worth mentioning that the strengthening mechanisms are considered independent of each other. The contributions of each strengthening factors on the yield strength and electrical resistivity are shown in Fig. 2.18.

It is assumed that the mean particle spacing is 50 nm, and the Taylor factor is taken as 2. Given that a desirable EC was typically achieved in the overaged state [18, 33], the contribution of β' precipitates to the strength and electrical resistivity could be calculated using Eqs. 2.4 and 2.11, which are determined to be 175 MPa and 1.69 nm Ω , respectively, as shown in Fig. 2.18. It is evident that the mean particle spacing of precipitates is a key factor influencing the strength and electrical resistivity of the Al-Mg-Si conductor alloy.

It is also supposed that the dislocation number density is 10^{15} m^{-2} and the Taylor factor is taken as 2. The contribution of dislocations to the strength using Eq. 2.6 and electrical resistivity using Eq. 2.12 are calculated to be 148 MPa and 0.27 nm Ω , respectively. It is meaningful that strain strengthening via dislocations is extremely effective on the strength increment with a low electrical resistivity, as displayed in Fig. 2.18. It is worthwhile to note that the strain hardening in the as-quenched state outperforms that in the peak-aged condition owing to the drag effect of the solutes on dislocations [88]. Moreover, the dislocations could promote the extraction of alloying elements from the matrix to decrease electrical resistivity [30].

The average grain size of the sample is taken as 400 nm. The contribution of grain boundaries to the strength using Eq. 2.7 and electrical resistivity using Eq. 2.13 would be 67 MPa and 4 nm Ω , respectively. It shows a moderate impact of grain size on the strength even in the case of ultrafine grains but with a considerable increase in electrical resistivity, as presented in Fig. 2.18. It is worth noting that grain boundary precipitates in ultrafine grains could decrease electrical resistivity but deteriorate the age hardening response [25]. However, in the case of a normal grain size of 40 μm achievable by DC casting/extrusion or Properzi caster/hot rolling processes, the contribution of grain boundaries to the strength and electrical resistivity would be ~ 7 MPa and ~ 0.04 nm Ω , respectively, which are increasingly negligible.

For an AA6201 alloy containing 0.6% Mg and 0.6% Si, it is supposed that half of the solutes (0.3% Mg and 0.3% Si) remain in the matrix when the EC value meets the minimum required value. The contribution of Mg and Si solutes to the strength using Eq. 2.8 and electrical resistivity using Eq. 2.14 is estimated to be 42 MPa and 2.8 nm Ω , respectively.

The calculations obtained via the constitutive equations are displayed in Fig. 2.18. Accordingly, a relatively low level of solutes in the AA6201 alloy has the lowest strengthening impact among all strengthening factors with a remarkable increase in electrical resistivity. However, it has been reported that the impact of solute strengthening (especially Si) was experimentally beyond the value acquired via theoretical equations [26]. In contrast to solutes, precipitate hardening exhibited the highest strengthening effect with a relatively low electrical resistivity. The grain boundary with a nanograined structure has the most detrimental factor on electrical resistivity with a medium strengthening contribution. However, it has been reported that extensive grain boundaries lead to more purification of the matrix due to grain boundary precipitates and segregations. Finally, it is evident that strain hardening via dislocations possesses the second highest strengthening portion with negligible electrical resistivity [24].

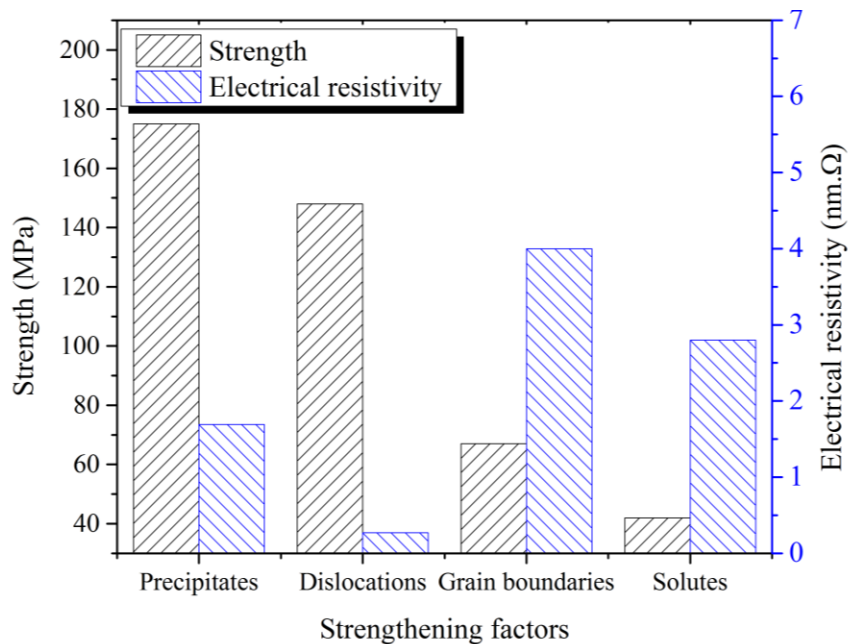


Figure 2.18 The contribution to the strength and electrical resistivity from precipitates (mean precipitate spacing = 50 nm), dislocations (density = 10^{15} m^{-2}), grain boundaries (grain size = 400 nm) and solutes (Mg = 0.3 wt.% and Si = 0.3 wt.%)

2.6. Summary

Extensive attention has been given to Al-Mg-Si 6xxx conductor alloys in recent decades owing to their excellent mechanical properties, low mass resistivity, and low cost. As discussed in this review paper, there is a general trade-off between mechanical strength and electrical conductivity, which are mutually exclusive. To improve the electrical and mechanical properties, extensive research has been done based on the variations in the main alloying elements (Mg and Si), the addition of the other alloying elements, melt treatment, applying the modified thermomechanical treatments, and maximizing the area reduction (severe plastic deformation) in the wire drawing.

Excessive Si (Mg/Si ~1) showed a better tensile strength with a desirable electrical conductivity in the coarse-grained 6xxx cables, while it exhibited superior electrical conductivity in the fine-grained 6xxx cables due to grain boundary precipitates and segregation. Some additional alloying elements (such as Sr) could boost the aging response and increase the tensile strength. Certain alloying elements (such as La and Ce) could improve electrical conductivity at the expense of strength since they were combined with Si to form new phases, depleting Si in the matrix.

The modified thermomechanical treatments led to a better combination of strength and electrical conductivity compared to conventional thermomechanical treatment. In addition, severe plastic deformation combined with aging could improve grain boundary strengthening and precipitate hardening with desirable electrical conductivity. Dynamic aging could prevent the formation of grain boundary precipitates.

A principal conclusion drawn in this review paper is that the strength should be enhanced by creating barriers (such as sessile dislocations and precipitates) for dislocation movement while having a less detrimental effect on the electrical conductivity. Experimental data and the strength and electrical resistivity models showed that precipitates and dislocations have promising effects on strength with minor negative impact on the electrical conductivity. Therefore, an M-TMT design ought to focus most on precipitate strengthening and dislocation hardening in Al-Mg-Si conductor alloys. In addition, grain boundary strengthening with nanoscale fine grains might be considered to improve the strength of Al-Mg-Si conductor alloys. Although the grain boundaries have a significant impact on the conductivity, they could indirectly lead to a less detrimental effect via grain boundary precipitates and segregation.

2.7. References

- [1] L. Pan, K. Liu, F. Breton, X. Grant Chen, Effect of Fe on Microstructure and Properties of 8xxx Aluminum Conductor Alloys, *J. Mater. Eng. Perform.* 25(12) (2016) 5201-5208.
- [2] L. Pan, F.A. Mirza, K. Liu, X.G. Chen, Effect of Fe-rich particles and solutes on the creep behaviour of 8xxx alloys, *Mater. Sci. Technol.* 33(9) (2016) 1130-1137.
- [3] L. Pan, K. Liu, F. Breton, X.G. Chen, Effects of minor Cu and Mg additions on microstructure and material properties of 8xxx aluminum conductor alloys, *J. Mater. Res.* 32(06) (2017) 1094-1104.
- [4] R.B. Kalombo, J.M.G. Martínez, J.L.A. Ferreira, C.R.M. da Silva, J.A. Araújo, Comparative Fatigue Resistance of Overhead Conductors Made of Aluminium and Aluminium Alloy: Tests and Analysis, *Procedia Engineering* 133 (2015) 223-232.
- [5] S. Karabay, Influence of AlB₂ compound on elimination of incoherent precipitation in artificial aging of wires drawn from redraw rod extruded from billets cast of alloy AA-6101 by vertical direct chill casting, *Materials & Design* 29(7) (2008) 1364-1375.
- [6] S. Karabay, Modification of AA-6201 alloy for manufacturing of high conductivity and extra high conductivity wires with property of high tensile stress after artificial aging heat treatment for all-aluminium alloy conductors, *Materials & Design* 27(10) (2006) 821-832.
- [7] E. Cervantes, M. Guerrero, J. A. Ramos, S.A. Montes, Influence of Natural Aging and Cold Deformation on the Mechanical and Electrical Properties of 6201-T81 Aluminum Alloy Wires, *Mater. Res. Soc. Symp. Proc* (2010) 03-09.
- [8] R.B. Kalombo, T.B. Miranda, P.H.C. Rocha, J.L.A. Ferreira, C.R.M. da Silva, J.A. Araújo, Fatigue performance of overhead conductors tested under the same value of H/w parameter, *Procedia Engineering* 213 (2018) 346-358.
- [9] M. Iraizoz, N. Rossello, M. Amado, Influence of Solution Heat Treatment Temperature in the Final Properties of AA6201 Drawn Wire, in: M. Hyland (Ed.), *Light Metals 2015*, Springer International Publishing (2016) 183-187.
- [10] E. Rhaïem, T. Bouraoui, F. Elhalouani, Anticorrosive Solution of 6201 Aluminum Alloy used in STEG Company's Overhead Transmission Lines, *IOP Conference Series: Materials Science and Engineering* 13 (2010).
- [11] A. Laurino, E. Andrieu, J.-P. Harouard, J. Lacaze, M.-C. Lafont, G. Odemer, C. Blanc, Corrosion Behavior of 6101 Aluminum Alloy Strands for Automotive Wires, *J. Electrochem. Soc.* 160(11) (2013) C569-C575.
- [12] F.U. Flores, D.N. Seidman, D.C. Dunand, N.Q. Vo, Development of High-Strength and High-Electrical-Conductivity Aluminum Alloys for Power Transmission Conductors, *Light Metals* (2018) 247-251.
- [13] B. Smyrak, T. Knych, A. Mamala, K. Korzeń, P. Osuch, A Study of the Influence of Strain Hardening and Precipitation Hardening Sequence on Mechanical Properties of AlMgSi Conductor Alloys, Springer International Publishing (2016) 1791-1796.

- [14] Q. Zhao, Z. Qian, X. Cui, Y. Wu, X. Liu, Influences of Fe, Si and homogenization on electrical conductivity and mechanical properties of dilute Al–Mg–Si alloy, *J. Alloys Compd.* 666 (2016) 50-57.
- [15] Y. Han, D. Shao, B.A. Chen, Z. Peng, Z.X. Zhu, Q. Zhang, X. Chen, G. Liu, X.M. Li, Effect of Mg/Si ratio on the microstructure and hardness–conductivity relationship of ultrafine-grained Al–Mg–Si alloys, *Journal of Materials Science* 52(8) (2016) 4445-4459.
- [16] R.Z. Valiev, M.Y. Murashkin, I. Sabirov, A nanostructural design to produce high-strength Al alloys with enhanced electrical conductivity, *Scripta Mater.* 76 (2014) 13-16.
- [17] G.E. Totten, D.S. MacKenzie, *Handbook of Aluminum: Vol. 1: Physical Metallurgy and Processes*, CRC Press (2003).
- [18] X. Sauvage, E.V. Bobruk, M.Y. Murashkin, Y. Nasedkina, N.A. Enikeev, R.Z. Valiev, Optimization of electrical conductivity and strength combination by structure design at the nanoscale in Al–Mg–Si alloys, *Acta Mater.* 98 (2015) 355-366.
- [19] C.H. Liu, J. Chen, Y.X. Lai, D.H. Zhu, Y. Gu, J.H. Chen, Enhancing electrical conductivity and strength in Al alloys by modification of conventional thermo-mechanical process, *Materials & Design* 87 (2015) 1-5.
- [20] E. Standard, EN 50183. Conductors for overhead lines, aluminium magnesium silicon alloy wires (2000) 1-7.
- [21] ASTM, *Annual Book of ASTM Standards, Electrical Conductors* (2002).
- [22] ASTM, *Annual Book of ASTM Standards: Nonferrous metal products. Aluminum and magnesium alloys. Section 2. Volume 02.02* (2003).
- [23] S. Karabay, E. Feyzullahoglu, Determination of early failure sources and mechanisms for Al 99.7% and Al–Mg–Si alloy bare conductors used in aerial transmission lines, *Engineering Failure Analysis* 38 (2014) 1-15.
- [24] X. Xu, Z. Yang, Y. Ye, G. Wang, X. He, Effects of various Mg/Si ratios on microstructure and performance property of Al-Mg-Si alloy cables, *Mater. Charact.* 119 (2016) 114-119.
- [25] S. Jiang, R. Wang, Grain size-dependent Mg/Si ratio effect on the microstructure and mechanical/electrical properties of Al-Mg-Si-Sc alloys, *Journal of Materials Science & Technology* 35(7) (2019) 1354-1363.
- [26] S. Nikzad Khangholi, M. Javidani, A. Maltais, X.G. Chen, Optimization of mechanical properties and electrical conductivity in Al–Mg–Si 6201 alloys with different Mg/Si ratios, *J. Mater. Res.* 35(20) (2020) 2765-2776.
- [27] S. Nikzad Khangholi, M. Javidani, A. Maltais, X.G. Chen, Investigation on electrical conductivity and hardness of 6xxx aluminum conductor alloys with different Si levels, *MATEC Web of Conferences* 326 (2020) 1-7.
- [28] M.H. Mulazimoglu, A. Zaluska, F. Paray, J.E. Gruzleski, The effect of strontium on the Mg₂Si precipitation process in 6201 aluminum alloy, *Metallurgical and Materials Transactions A* 28(6) (1997) 1289-1295.

- [29] X. Cui, Y. Wu, G. Zhang, Y. Liu, X. Liu, Study on the improvement of electrical conductivity and mechanical properties of low alloying electrical aluminum alloys, *Composites Part B: Engineering* 110 (2017) 381-387.
- [30] G. Lin, Z. Zhang, H. Wang, K. Zhou, Y. Wei, Enhanced strength and electrical conductivity of Al–Mg–Si alloy by thermo-mechanical treatment, *Materials Science and Engineering: A* 650 (2016) 210-217.
- [31] C. Bunte, M. Glassel, C. Medina, D. Zalczman, Proposed Solution for Random Characteristics of Aluminium Alloy Wire Rods Due to the Natural Aging, *Procedia Materials Science* 9 (2015) 97-104.
- [32] J.P. Hou, Q. Wang, Z.J. Zhang, Y.Z. Tian, X.M. Wu, H.J. Yang, X.W. Li, Z.F. Zhang, Nano-scale precipitates: The key to high strength and high conductivity in Al alloy wire, *Materials & Design* 132 (2017) 148-157.
- [33] K. Majchrowicz, Z. Pakieła, W. Chrominski, M. Kulczyk, Enhanced strength and electrical conductivity of ultrafine-grained Al-Mg-Si alloy processed by hydrostatic extrusion, *Mater. Charact.* 135 (2018) 104-114.
- [34] M.Y. Murashkin, I. Sabirov, V.U. Kazykhanov, E.V. Bobruk, A.A. Dubravina, R.Z. Valiev, Enhanced mechanical properties and electrical conductivity in ultrafine-grained Al alloy processed via ECAP-PC, *Journal of Materials Science* 48(13) (2013) 4501-4509.
- [35] M. Murashkin, A. Medvedev, V. Kazykhanov, A. Krokhin, G. Raab, N. Enikeev, R. Valiev, Enhanced Mechanical Properties and Electrical Conductivity in Ultrafine-Grained Al 6101 Alloy Processed via ECAP-Conform, *Metals* 5(4) (2015) 2148-2164.
- [36] X. Ji, H. Zhang, S. Luo, F. Jiang, D. Fu, Microstructures and properties of Al–Mg–Si alloy overhead conductor by horizontal continuous casting and continuous extrusion forming process, *Materials Science and Engineering: A* 649 (2016) 128-134.
- [37] S.N. Khangholi, M. Javidani, A. Maltais, X.G. Chen, Effects of natural aging and pre-aging on the strength and electrical conductivity in Al-Mg-Si AA6201 conductor alloys, *Materials Science and Engineering: A* 820 (2021) 1-12.
- [38] D. Lindholm, S. Akhtar, D. Mortensen, Numerical Simulation of Wire Rod Casting of AA1370 and AA6101 Alloys, *Light Metals* (2020) 1032-1038.
- [39] R.M. Mustafa, Production of aluminium-silicon-magnesium wrought alloy rod with application in the manufacture of extra-high conductivity AAAC for overhead electrical transmission lines, *Light Metals* (2008) 613-617.
- [40] ASM Handbook: Casting. Volume 15, ASM International (1998) 689-690.
- [41] T.G. Zhou, Z.Y. Jiang, J.L. Wen, H. Li, A.K. Tieu, Semi-solid continuous casting–extrusion of AA6201 feed rods, *Materials Science and Engineering: A* 485(1-2) (2008) 108-114.
- [42] G.A. Edwards, K. Stiller, G.L. Dunlop, M.J. Couper, The precipitation sequence in Al–Mg–Si alloys, *Acta Mater.* 46(11) (1998) 3893-3904.
- [43] J. Buha, R.N. Lumley, A.G. Crosky, K. Hono, Secondary precipitation in an Al–Mg–Si–Cu alloy, *Acta Mater.* 55(9) (2007) 3015-3024.

- [44] H.W.Z. S.J. Andersen, J. Jansen, C. Træholt, U. Tundal, O. Reiso, The crystal structure of the β'' phase in Al–Mg–Si alloys, *Acta Mater* (1998) 3283-3298.
- [45] K. Teichmann, C.D. Marioara, S.J. Andersen, K.O. Pedersen, S. Gulbrandsen-Dahl, M. Kolar, R. Holmestad, K. Marthinsen, HRTEM study of the effect of deformation on the early precipitation behaviour in an AA6060 Al–Mg–Si alloy, *Philos. Mag.* 91(28) (2011) 3744-3754.
- [46] R.S. Yassar, D.P. Field, H. Weiland, The effect of predeformation on the β'' and β' precipitates and the role of Q' phase in an Al–Mg–Si alloy; AA6022, *Scripta Mater.* 53(3) (2005) 299-303.
- [47] H. Nemour, D. Mourad Ibrahim, A. Triki, The effect of heavy cold plastic deformation on the non-isothermal kinetics and the precipitation sequence of metastable phases in an Al–Mg–Si alloy, *J. Therm. Anal. Calorim.* 123(1) (2015) 19-26.
- [48] G. Sha, H. Möller, W.E. Stumpf, J.H. Xia, G. Govender, S.P. Ringer, Solute nanostructures and their strengthening effects in Al–7Si–0.6Mg alloy F357, *Acta Mater.* 60(2) (2012) 692-701.
- [49] J.H. Chen, E. Costan, M.A. van Huis, Q. Xu, H.W. Zandbergen, Atomic Pillar-Based Nanoprecipitates Strengthen AlMgSi Alloys, *Science* 312(5772) (2006) 416-419.
- [50] H.S. Hasting, A.G. Frøseth, S.J. Andersen, R. Vissers, J.C. Walmsley, C.D. Marioara, F. Danoix, W. Lefebvre, R. Holmestad, Composition of β'' precipitates in Al–Mg–Si alloys by atom probe tomography and first principles calculations, *J. Appl. Phys.* 106(12) (2009) 123527.
- [51] S.J.A. H.W. Zandbergen, J. Jansen, Structure Determination of Mg_5Si_6 Particles in Al by Dynamic Electron Diffraction Studies, *Science* 1997, pp. 1221-1225.
- [52] ASM Handbook, Properties and Selections Nonferrous Alloys and Special-Purpose Materials (1990), 507-508.
- [53] A.K. Gupta, D.J. Lloyd, S.A. Court, Precipitation hardening in Al–Mg–Si alloys with and without excess Si, *Materials Science and Engineering: A* 316(1) (2001) 11-17.
- [54] Y. Weng, Z. Jia, L. Ding, Y. Pan, Y. Liu, Q. Liu, Effect of Ag and Cu additions on natural aging and precipitation hardening behavior in Al-Mg-Si alloys, *J. Alloys Compd.* 695 (2017) 2444-2452.
- [55] C.D. Marioara, S.J. Andersen, H.W. Zandbergen, R. Holmestad, The influence of alloy composition on precipitates of the Al-Mg-Si system, *Metallurgical and Materials Transactions A* 36(3) (2005) 691-702.
- [56] C.D. Marioara, S.J. Andersen, T.N. Stene, H. Hasting, J. Walmsley, A.T.J. Van Helvoort, R. Holmestad, The effect of Cu on precipitation in Al–Mg–Si alloys, *Philos. Mag.* 87(23) (2007) 3385-3413.
- [57] K. Li, A. Beche, M. Song, G. Sha, X. Lu, K. Zhang, Y. Du, S.P. Ringer, D. Schryvers, Atomistic structure of Cu-containing β'' precipitates in an Al–Mg–Si–Cu alloy, *Scripta Mater.* 75 (2014) 86-89.
- [58] M. Murayama, K. Hono, Pre-precipitate clusters and precipitation processes in Al–Mg–Si alloys, *Acta Mater.* 47(5) (1999) 1537-1548.

- [59] L. Ding, Z. Jia, Y. Liu, Y. Weng, Q. Liu, The influence of Cu addition and pre-straining on the natural aging and bake hardening response of Al-Mg-Si alloys, *J. Alloys Compd.* 688 (2016) 362-367.
- [60] L.-x. Cui, Z.-x. Liu, X.-g. Zhao, J.-g. Tang, K. Liu, X.-x. Liu, C. Qian, Precipitation of metastable phases and its effect on electrical resistivity of Al-0.96Mg2Si alloy during aging, *Transactions of Nonferrous Metals Society of China* 24(7) (2014) 2266-2274.
- [61] B. Smyrak, B. Jurkiewicz, M. Zasadzińska, M. Gnielczyk, P. Jałowy, The Effect of Al-Mg-Si Wire Rod Heat Treatment on Its Electrical Conductivity and Strength, *Metals* 10(8) (2020) 1-10.
- [62] W. Yuan, Z. Liang, Effect of Zr addition on properties of Al-Mg-Si aluminum alloy used for all aluminum alloy conductor, *Materials & Design* 32(8-9) (2011) 4195-4200.
- [63] T. Ikeda, T. Muto, K. Morimoto, Effects of Zirconium Addition and Solute Iron Concentration on the Softening Behavior of 6101 Aluminum Conductor Alloy, *Mater. Sci. Forum* 331-337 (2000) 595-600.
- [64] W. Yuan, Z. Liang, C. Zhang, L. Wei, Effects of La addition on the mechanical properties and thermal-resistant properties of Al-Mg-Si-Zr alloys based on AA 6201, *Materials & Design* 34 (2012) 788-792.
- [65] M. Hosseinifar, D.V. Malakhov, The Sequence of Intermetallics Formation during the Solidification of an Al-Mg-Si Alloy Containing La, *Metallurgical and Materials Transactions A* 42(3) (2010) 825-833.
- [66] M.H. Mulazimoglu, A. Zaluska, J.E. Gruzleski, F. Paray, Electron microscope study of Al-Fe-Si intermetallics in 6201 aluminum alloy, *Metallurgical and Materials Transactions A* 27(4) (1996) 929-936.
- [67] H.C. Liao, Y. Liu, C.L. Lü, Q.G. Wang, Effect of Ce addition on castability, mechanical properties and electric conductivity of Al-0.3Si-0.2Mg alloy, *Int. J. Cast Met. Res.* 28(4) (2015) 213-220.
- [68] D.G. Eskin, *Physical metallurgy of direct chill casting of aluminum alloys*, Taylor & Francis (2008).
- [69] S. Wang, K. Matsuda, T. Kawabata, Y. Zou, T. Yamazaki, S. Ikeno, Effect of TM-Addition on the Aging Behaviour of Al-Mg-Si Alloys, *Materials Transactions* 52(2) (2011) 229-234.
- [70] L. Backerud, E. Krol, J. Tamminen, *Solidification Characteristics of Aluminum Alloys: Wrought alloys*, Skanaluminium (1986).
- [71] Y. Weng, Z. Jia, L. Ding, S. Muraishi, Q. Liu, Clustering behavior during natural aging and artificial aging in Al-Mg-Si alloys with different Ag and Cu addition, *Materials Science and Engineering: A* 732 (2018) 273-283.
- [72] T. Saito, E.A. Mortsell, S. Wenner, C.D. Marioara, S.J. Andersen, J. Friis, K. Matsuda, R. Holmestad, Atomic Structures of Precipitates in Al-Mg-Si Alloys with Small Additions of Other Elements, *Adv. Eng. Mater.* 20(7) (2018).

- [73] S. Karabay, E.A. Guven, A.T. Erturk, Enhancement on Al–Mg–Si alloys against failure due to lightning arc occurred in energy transmission lines, *Engineering Failure Analysis* 31 (2013) 153-160.
- [74] X. Cui, Y. Wu, X. Liu, Q. Zhao, G. Zhang, Effects of grain refinement and boron treatment on electrical conductivity and mechanical properties of AA1070 aluminum, *Materials & Design* 86 (2015) 397-403.
- [75] M. Kolar, K.O. Pedersen, S. Gulbrandsen-Dahl, K. Marthinsen, Combined effect of deformation and artificial aging on mechanical properties of Al–Mg–Si Alloy, *Transactions of Nonferrous Metals Society of China* 22(8) (2012) 1824-1830.
- [76] M. Kolar, K.O. Pedersen, S. Gulbrandsen-Dahl, K. Teichmann, K. Marthinsen, Effect of Pre-Deformation on Mechanical Response of an Artificially Aged Al-Mg-Si Alloy, *Materials Transactions* 52(7) (2011) 1356-1362.
- [77] M. Li, H. Li, Z. Zhang, W. Shi, J. Liu, Y. Hu, Y. Wu, Effect of precipitates on properties of cold-rolled Al–Mg–Si–Sc–Zr alloy with higher temperature aging, *Mater. Sci. Technol.* 34(10) (2018) 1246-1251.
- [78] Z.H. Zhao, Q.Q. Chen, Q.F. Zhu, W.Q. Liu, G.S. Wang, Study on the Ageing Process of the 6xxx Series Aluminum Alloy Wires for Overhead Conductors, *Mater. Sci. Forum* 877 (2016) 347-355.
- [79] P.A. Rometsch, Z. Xu, H. Zhong, H. Yang, L. Ju, X.H. Wu, Strength and Electrical Conductivity Relationships in Al-Mg-Si and Al-Sc Alloys, *Mater. Sci. Forum* 794-796 (2014) 827-832.
- [80] Y. Aruga, S. Kim, M. Kozuka, E. Kobayashi, T. Sato, Effects of cluster characteristics on two-step aging behavior in Al-Mg-Si alloys with different Mg/Si ratios and natural aging periods, *Materials Science and Engineering: A* 718 (2018) 371-376.
- [81] G.H. Tao, C.H. Liu, J.H. Chen, Y.X. Lai, P.P. Ma, L.M. Liu, The influence of Mg/Si ratio on the negative natural aging effect in Al–Mg–Si–Cu alloys, *Materials Science and Engineering: A* 642 (2015) 241-248.
- [82] M.C. Lentz, M. Rengel, K. Stray, O. Engler, A modified processing route for high strength Al-Mg-Si aluminum conductors based on twin-roll cast strip, *J. Mater. Process. Technol.* 278 (2020).
- [83] Z.P. Martinova, Pre-aging effects in thermo mechanically treated 6201 aluminium alloy, *Macedonian Union of Metallurgists* (2003).
- [84] H. Li, M. Qingzhong, Z. Wang, F. Miao, B. Fang, R. Song, Z. Zheng, Simultaneously enhancing the tensile properties and intergranular corrosion resistance of Al–Mg–Si–Cu alloys by a thermo-mechanical treatment, *Materials Science and Engineering: A* 617 (2014) 165-174.
- [85] Z. Wang, H. Li, F. Miao, B. Fang, R. Song, Z. Zheng, Improving the strength and ductility of Al–Mg–Si–Cu alloys by a novel thermo-mechanical treatment, *Materials Science and Engineering: A* 607 (2014) 313-317.

- [86] M.Y.M. X. Sauvage, R. Z. Valiev, Atomic scale investigation of dynamic precipitation and grain boundary segregation in a 6061 aluminium alloy nanostructured by ECAP, *Kovove Mater.* 49 (2011) 11-15.
- [87] M. Murayama, Z. Horita, K. Hono, Microstructure of two-phase Al–1.7 at% Cu alloy deformed by equal-channel angular pressing, *Acta Mater.* 49(1) (2001) 21-29.
- [88] L.M. Cheng, W.J. Poole, J.D. Embury, D.J. Lloyd, The influence of precipitation on the work-hardening behavior of the aluminum alloys AA6111 and AA7030, *Metallurgical and Materials Transactions A* 34(11) (2003) 2473-2481.
- [89] W. Yuna, Z. Jianfeng, L. Hengcheng, W. Yongjin, W. Yuping, Effect of Homogenization Temperature on Microstructure and Conductivity of Al-Mg-Si-Ce Alloy, *J. Mater. Eng. Perform.* 25(7) (2016) 2720-2726.
- [90] S. Karabay, M. Yilmaz, M. Zeren, Investigation of extrusion ratio effect on mechanical behaviour of extruded alloy AA-6101 from the billets homogenised-rapid quenched and as-cast conditions, *J. Mater. Process. Technol.* 160(2) (2005) 138-147.
- [91] H. Liao, Y. Wu, Y. Wang, Microstructure Evolution of Al-0.35%Si-0.2%Mg-0.3%Ce Alloy During Hot Extrusion and Its Contributions to Performances, *J. Mater. Eng. Perform.* 24(6) (2015) 2503-2510.
- [92] M. Javidani, D. Larouche, Application of cast Al–Si alloys in internal combustion engine components, *Int. Mater. Rev.* 59(3) (2014) 132-158.
- [93] Y. Wu, H. Liao, J. Zhang, Effect of Intermediate Annealing Temperature and Aging on the Mechanical Properties and Conductivity of Al–0.2Mg–0.35Si–0.3Ce Wire Rod, *High Performance Structural Materials* (2018) 139-145.
- [94] J. Zhang, M. Ma, F. Shen, D. Yi, B. Wang, Influence of deformation and annealing on electrical conductivity, mechanical properties and texture of Al-Mg-Si alloy cables, *Materials Science and Engineering: A* 710 (2018) 27-37.
- [95] P. Osuch, M. Walkowicz, T. Knych, S. Dymek, Impact of the Direct Ageing Procedure on the Age Hardening Response of Al-Mg-Si 6101 Alloy, *Materials (Basel)* 11(7) (2018) 1-13.
- [96] V.D. Sitdikov, M.Y. Murashkin, R.Z. Valiev, Precipitates studies in ultrafine-grained Al alloys with enhanced strength and conductivity, *IOP Conference Series: Materials Science and Engineering* 194 (2017) 1-6.
- [97] M.Y. Murashkin, I. Sabirov, X. Sauvage, R.Z. Valiev, Nanostructured Al and Cu alloys with superior strength and electrical conductivity, *Journal of Materials Science* 51(1) (2015) 33-49.
- [98] A. Medvedev, M.Y. Murashkin, V. Kazykhanov, R.Z. Valiev, A.E. Medvedev, P.D. Hodgson, R. Lapovok, Enhancement of Mechanical and Electrical Properties in Al 6101 Alloy by Severe Shear Strain under Hydrostatic Pressure, *Adv. Eng. Mater.* 20(11) (2018).
- [99] O. Engler, C.D. Marioara, Y. Aruga, M. Kozuka, O.R. Myhr, Effect of natural ageing or pre-ageing on the evolution of precipitate structure and strength during age hardening of Al–Mg–Si alloy AA 6016, *Materials Science and Engineering: A* 759 (2019) 520-529.

- [100] T. Khelfa, M.A. Rekik, J.A. Muñoz-Bolaños, J.M. Cabrera-Marrero, M. Khitouni, Microstructure and strengthening mechanisms in an Al-Mg-Si alloy processed by equal channel angular pressing (ECAP), *The International Journal of Advanced Manufacturing Technology* 95(1-4) (2017) 1165-1177.
- [101] Y.J. Li, A.M.F. Muggerud, A. Olsen, T. Furu, Precipitation of partially coherent α -Al(Mn,Fe)Si dispersoids and their strengthening effect in AA 3003 alloy, *Acta Mater.* 60(3) (2012) 1004-1014.
- [102] Z. Li, Z. Zhang, X.G. Chen, Improvement in the mechanical properties and creep resistance of Al-Mn-Mg 3004 alloy with Sc and Zr addition, *Materials Science and Engineering: A* 729 (2018) 196-207.
- [103] W. Wen, Y. Zhao, J.G. Morris, The effect of Mg precipitation on the mechanical properties of 5xxx aluminum alloys, *Materials Science and Engineering: A* 392(1-2) (2005) 136-144.
- [104] B. Raeisinia, W.J. Poole, D.J. Lloyd, Examination of precipitation in the aluminum alloy AA6111 using electrical resistivity measurements, *Materials Science and Engineering: A* 420(1) (2006) 245-249.

Chapter 3 : Optimization of mechanical properties and electrical conductivity in Al-Mg-Si 6201 alloys with different Mg/Si ratios (Article2)

Siamak Nikzad Khangholi ¹, Mousa Javidani ¹, Alexandre Maltais ², X.-Grant Chen ¹

¹ Department of Applied Science, University of Québec at Chicoutimi, Saguenay, Québec, G7H 2B1, Canada

² Arvida Research and Development Center, Rio Tinto Aluminum, Saguenay, Quebec, G7S 4K8, Canada

This article has been published in:

Journal of Materials Research 35 (20), 2765-2776

Abstract

The effects of the Mg/Si ratio and aging treatment on the strength and electrical conductivity of Al-Mg-Si 6201 conductor alloys were investigated. Four experimental alloys with different Mg/Si ratios of 2, 1.5, 1, and 0.86 and with a constant Mg level of 0.65 wt. % were prepared. It was revealed that excessive Si (a low Mg/Si ratio) increased the peak strength, while the corresponding electrical conductivity decreased. To fulfill the minimum required electrical conductivity (52.5% IACS), the alloys with low Mg/Si ratios required a longer aging time after peak aging to improve electrical conductivity. The alloy with Mg/Si ratio of ~1 was the best candidate, exhibiting the highest strength up to 54% IACS. On the high end of electrical conductivity (54–56% IACS), the alloy with Mg/Si ratio of ~1.5 provides a better compromise between strength and electrical conductivity. Furthermore, the strengthening mechanisms and the factors influencing electrical conductivity were discussed for further optimization.

Keywords: Al-Mg-Si conductor alloys; electrical conductivity; mechanical properties; Mg/Si ratio; wire drawing

3.1. Introduction

Recently, the demand for lightweight aluminum conductors has been growing to meet the energy consumption needs in the electrical industry [1-3]. Aluminum conductors are divided into two categories: aluminum conductor steel reinforced (ACSR) and all-aluminum alloy conductor (AAAC). In the former (ACSR), commercially pure aluminum alloys such as AA1350 alloy are generally used, and the core consists of the steel to reinforce the conductors in power lines. In recent decades, AAAC has been found as an appropriate candidate in high voltage transmission lines due to it meeting the requirements of having both high mechanical properties and good corrosion resistance. Al-Mg-Si 6xxx alloys, such as AA6101 and AA6201 cables, often serve as conductors in AAAC because their strength can be enhanced via the precipitation hardening while their electrical conductivity remains relatively high [4-7].

Precipitation hardening, work hardening, solute strengthening, and grain boundary strengthening are among the strengthening mechanisms in aluminum alloys. In contrast, the electrical conductivity is governed by the movement of valence electrons. Any disturbances in the crystal lattice periodicity, which stem from defects in the crystal structure (such as vacancies, dislocations, grain boundaries and impurity atoms), cause an increase in electrical resistance [8-12]. Among those defects, dissolved atoms along with Guinier-Preston (GP) zones show the most deleterious impact on electrical conductivity [9, 10, 13]. It is evident that factors enhancing the strength of aluminum alloys also tend to reduce its electrical conductivity. As a consequence, the strength and electrical conductivity are found to be mutually exclusive [8-10, 14].

Mg and Si are the principal alloying elements in 6xxx alloys, making them age-hardenable [15]. The conventional sequences of precipitation during aging treatment are as follows: clusters of Mg and Si atoms; GP zones; β'' ; β' ; and equilibrium β -Mg₂Si [16, 17]. It was found that excessive Si relative to Mg₂Si enhanced the precipitation hardening [11, 15, 18, 19], while the additional Mg relative to Mg₂Si exhibited a negligible strengthening effect [15, 18]. The excessive Si in 6xxx series alloys leads to an increase in the number density of the β'' strengthening phase [15, 19]. Si columns act as a skeleton for the precipitates, observed in the core of precipitates from GP zones to β'' [20-22]. Moreover, the higher diffusion of Si atoms leads to the formation of Si/vacancy clusters, which have a higher binding energy than Mg/vacancy clusters, easily evolving into the subsequent strengthening precipitates with high density [15, 23]. Therefore, excessive Si promotes precipitation hardening in the 6xxx series alloys [15, 19].

The effect of excess Si on the electrical and mechanical properties in 6xxx series conductor alloys has recently been taken into consideration [9, 11, 15]. In coarse-grained Al-Mg-Si conductor alloys, it was reported that the alloys with excess Si showed a higher strength [11, 15], of which strengthening mechanisms were not discussed. In addition, in fine-grained Al-Mg-Si conductor alloys, a higher electrical conductivity was achieved owing to grain boundary precipitates in the alloys with excess Si [11]. Overall, the electrical conductivity and mechanical properties ought to be simultaneously considered in Al-Mg-Si conductor alloys. The minimum requirement of AA6201 conductor alloys for ultimate tensile strength (UTS), electrical conductivity (EC), and elongation to failure are 305 MPa, 52.5% IACS, and 3%, respectively [24-26].

Considering that the Mg/Si ratio of the main strengthening phases is approximately one (at. %) in Al-Mg-Si alloys, investigations on the effect of excess Si on the strength and EC are limited. The present work aimed to find the optimum Si level and thermo-mechanical treatments for a balance between mechanical properties and EC. In addition, the underlying mechanisms and microstructures for improving the strength and EC in Al-Mg-Si 6201 alloys were explored.

3.2. Experimental procedure

Experiments were carried out on four Al-Mg-Si 6201 alloys with an Mg/Si ratio of 2, 1.5, 1, and 0.86 (designated as Si4, Si5, Si6, and Si9, respectively, in accordance with their Si levels). In the alloys, the Mg level was kept constant (0.65 wt.%). The Si6 alloy with the Mg/Si ratio of ~1 was considered to be the reference alloy. The Si4 and Si5 alloys with Mg/Si ratios higher than one are regarded as Mg-excessive alloys, while the Si9 alloy with an Mg/Si ratio less than one is considered a Si-excessive alloy. The chemical compositions of the four alloys, as analyzed by optical emission spectroscopy, are presented in Table 3.1. To prepare the alloys, commercially pure Al, Al-50 wt.% Si master alloy, and pure Mg were melted using an electrical resistance furnace. The melt was poured into a permanent mold preheated at 250 °C to obtain cast ingots with a dimension of 30 mm x 40 mm x 80 mm. After casting, the cast ingots were scalped (1.75 mm thick from each surface) and homogenized at 560 °C for 6 h, followed by hot rolling at 350–480 °C (74% area reduction). The hot-rolled sheets were cut and machined into square bars. Afterward, a solution treatment at 540 °C for 2 h was conducted, followed by cold wire drawing (50% area reduction) to obtain the final wire diameter of 4.7 mm. Artificial aging treatment at 180 °C with different aging times was applied to the wire samples. The schematics of the wire fabrication process is shown in Fig. 3.1.

To investigate the precipitation of the different phases, differential scanning calorimetry (DSC) was conducted on the as-drawn samples with a heating rate of 10 °C/min in an argon atmosphere from 100°C to 500°C. At least, three samples were used for each condition, and the weight of samples was around 15-30 mg. The DSC results were corrected with the base line. Microhardness and tensile tests were performed to evaluate the mechanical properties. Eight measurements were conducted for the microhardness test with a force and dwell time of 25 g and 20 s, respectively. The tensile tests were performed at least three times for each condition, according to ASTM B557 and ASTM E8, with a strain rate of $8 \times 10^{-4} \text{ s}^{-1}$. In addition, EC was measured via a Sigmascop unit based on ASTM E1004 (Eddy current technique) with a frequency of 480 kHz, and the average of fifteen measurements was reported.

An optical microscope was used to investigate the grain structures along the drawing direction, and fifteen images were taken from different areas of each sample. A transmission electron microscope (TEM, JEM–2100) operated at 200 kV was used to characterize the size and the number density of precipitates. The TEM samples were taken from the section perpendicular to the drawing direction and prepared using electropolishing with an electrolyte of 30% HNO₃ and 70% methanol at a temperature between -20 °C and -30 °C. The TEM images were obtained in the <001> zone axis direction of the Al matrix. Ten TEM bright-field images were used for quantitative analysis according to the methodology provided in [27].

Table 3.1 The chemical composition of experimental alloys with various Mg/Si ratios

Alloy designation	Compositions (wt. %)					Mg/Si (in at. %)	Type
	Mg	Si	Fe	Other	Al		
Si 4	0.67	0.4	0.09	<0.05	Bal.	1.94	Mg-excessive
Si 5	0.68	0.53	0.10	<0.05	Bal.	1.47	Mg-excessive
Si 6	0.66	0.66	0.13	<0.05	Bal.	1.15	Reference
Si 9	0.68	0.89	0.10	<0.05	Bal.	0.86	Si-excessive

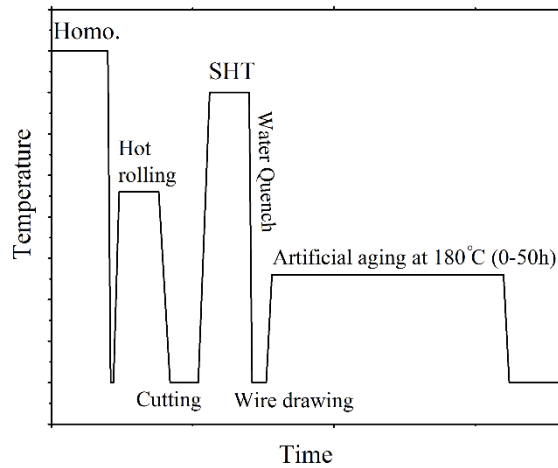


Figure. 3.1 Scheme of the wire fabrication process

3.3. Results

3.3.1. Mechanical properties and EC

Fig. 3.2a and 3.2b show the evolution of the microhardness and UTS, respectively, as a function of aging time. The Si4 and Si5 alloys showed peak hardness after 2 h, while the Si6 and Si9 alloys reached peak hardness after 1 h. The higher the level of Si, the quicker the alloy reaches the peak aging condition. The values of peak hardness for the Si4, Si5, Si6, and Si9 alloys are 114, 119, 127, and 140 HV, and the values of UTS after peak aging are 310, 338, 364, and 394 MPa, respectively. Overall, it is found that greater hardness and UTS were achieved in the alloys with higher excessive Si. Fig. 3.2c displays the elongation to failure for four alloys according to the aging time, in which the elongation increases rapidly with aging time, then gradually increases over the aging time. Fig. 3.2d demonstrates the evolution of the EC as a

function of the aging time. The results show that the EC exhibits a rapid increase before the peak aging, then increases moderately with prolonged aging time. The quick increase in EC at the early stage of aging could be attributed to the formation of precipitates at the expense of a large number of Mg and Si atoms. The alloys with higher Si contents show a lower EC at a given aging time, arising from dissolved Si atoms in the aluminum matrix.

In Al-Mg-Si 6xxx alloys, it is generally less problematic to meet the required mechanical properties owing to its strong precipitation strengthening. In the peak aging condition (Fig. 3.2b), the strengths of all four alloys are above the minimum UTS requirement (305 MPa) for 6201 conductor alloys. However, the EC values at the peak aging for the Si4, Si5, Si6, and Si9 alloys are 52.3, 52, 49, and 47.5% IACS, respectively (Fig. 3.2d), which are all below the minimum required EC (52.5% IACS). The challenge is that EC and UTS must be concurrently taken into consideration in the conductor alloys to find an optimal tradeoff between EC and UTS. The minimum required EC can only be reached after 3, 4, 5, and 34 h of aging for the Si4, Si5, Si6, and Si9 alloys, respectively, showing that the alloys with higher Si contents needed a longer aging time to enhance EC. Considering the required minimum elongation to failure (3%) [26], it is apparent that all alloys fulfill this requirement under all aged conditions after peak aging (Fig. 3.2c).

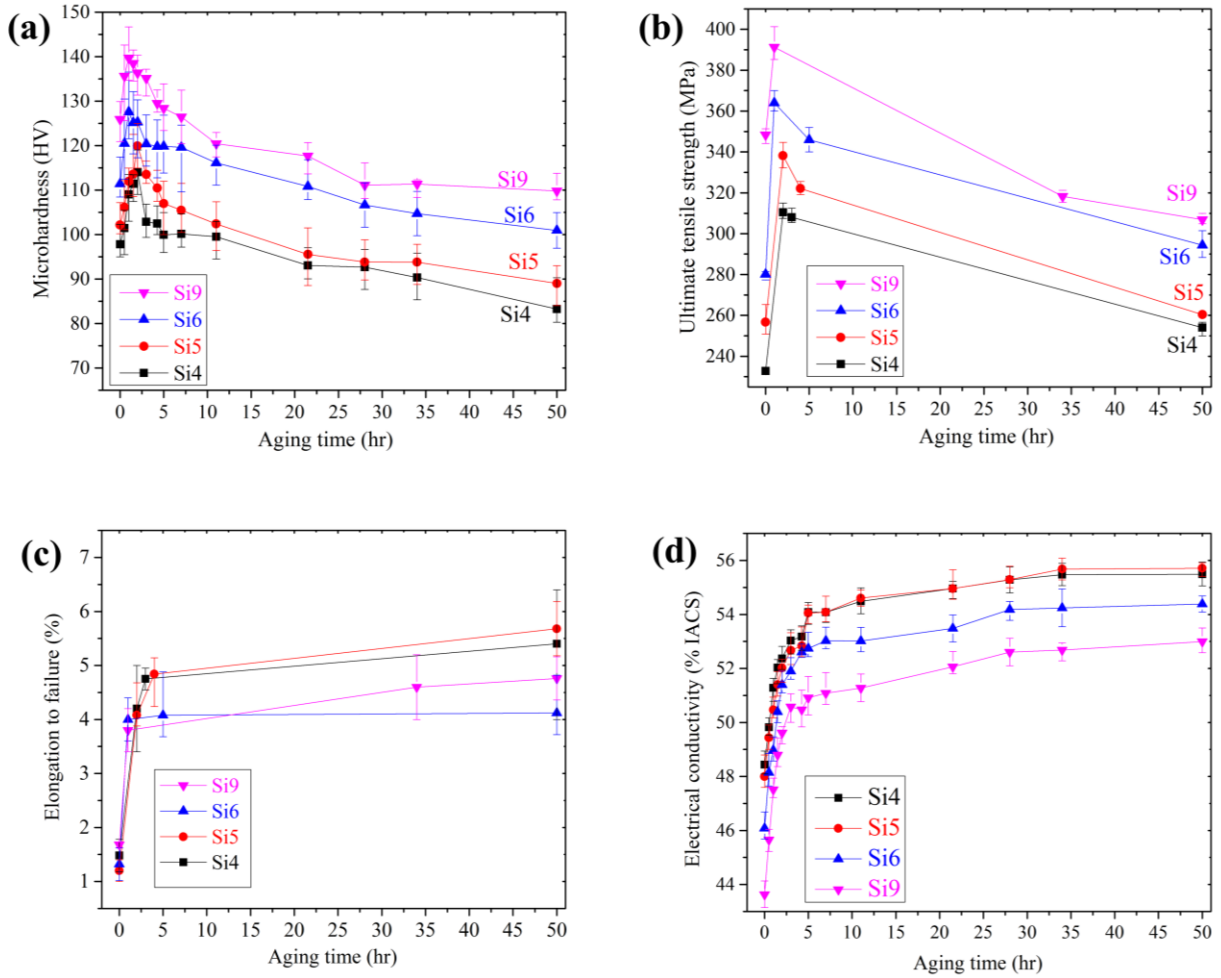


Figure. 3.2 Evolution of (a) microhardness (b) UTS (c) elongation to failure (d) EC as a function of aging time

Fig. 3.3a displays the UTS as a function of EC for the four alloys in the full range of the aging time studied. Fig. 3.3b is an enlarged view of the right corner of Fig. 3.3a, where it shows the relation between UTS and EC above the minimum UTS and EC requirements (305 MPa and 52.5% IACS respectively). It reveals that the maximum UTS levels of the alloys above 52.5% IACS for Si4, Si5, Si6, and Si9 alloys are 306, 322, 346, and 318 MPa after 3, 4, 5, 34 h of the aging, respectively. With respect to the UTS above the minimum required EC, the Si6 alloy after 5 h of aging shows the highest strength, followed by the Si5 alloy after 4 h of aging. As observed

in Fig. 3.2a and 3.2b, higher peak hardness and strength were attained in the Si-excessive Si9 alloy. However, its EC was the lowest among all alloys and increased only slowly with the aging time (Fig. 3.2d). The Si9 alloy needs a much longer aging time (at least 34 h) to reach the required EC than the other alloys, where its UTS decreased from 394 MPa at the peak aging to 318 MPa. The Mg-excessive Si4 alloy generally exhibited the lowest strength among four alloys, and it reached the required minimum EC after 3 h of aging, but its UTS was at the bottom line (306 MPa).

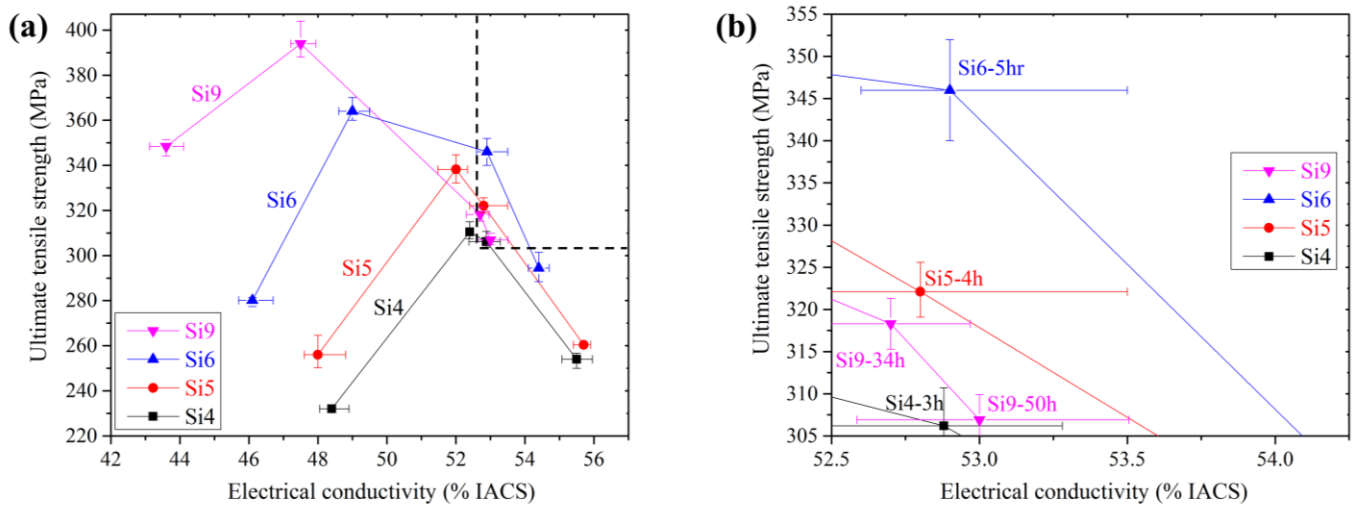


Figure. 3.3 (a) UTS versus EC of four alloys and (b) the enlarged view of the right corner of Figure. 3.3a above the minimum UTS and EC requirements (305 MPa and 52.5% IACS)

3.3.2. DSC analysis

Fig. 3.4a shows the DSC results of precipitation for the as-drawn alloys during heating with a heating rate of 10 °C/min, in which the exothermic peak I is ascribed to the precipitation of β' , and peak II is attributed to the precipitation of equilibrium β phase. The precipitation sequence was disrupted due to the presence of a high number of dislocations from cold wire drawing, acting as heterogeneous nucleation sites for β' phases [28-30]. Therefore, the precipitation of β''

was suppressed in all as-drawn alloys. Given that precipitates formed at the peak I are the main strengthening phase in the studied alloys, a close examination of the first exothermic peaks is given in Fig. 3.4b. It was determined that the onset temperature of the Si4, Si5, Si6, and Si9 alloys are 213, 213, 212 and 208 °C, and the corresponding peak temperatures are 235, 235, 233, and 230 °C, respectively. The onset and peak temperatures for precipitates shifted to lower temperatures with increasing Si levels. It reveals that the higher the Si content, the higher the precipitation kinetics. The higher silicon content led to the formation of higher density of Si-cluster in the early aging, enhancing the precipitation kinetics [15]. In addition, the precipitate amount is proportional to the size (height and width) of the peak. Precipitation peak I became higher and broader with increasing Si levels. Therefore, it is evident that excess Si promotes the higher amount of precipitates, resulting in alloys with higher Si content exhibiting higher peak hardness and UTS, as shown in Fig. 3.2a and 3.2b.

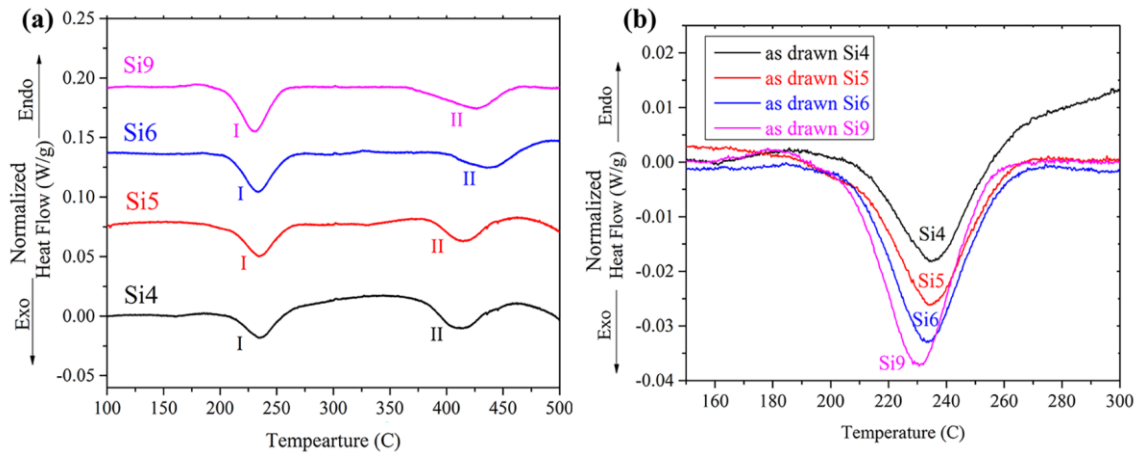


Figure. 3.4 (a) DSC curves of the different alloys in the as-drawn condition (b) the enlarged view of the precipitation peak I

3.3.3. Strain hardening of cold wire drawing

For the strength of final conductor wires, the strain hardening during cold wire drawing is also an important contribution. The strain hardening effect from wire drawing was determined by measuring the UTS and hardness difference before and after cold wire drawing without any natural aging. Yin et al. [31] observed that applying pre-straining following the solution treatment only led to the formation of a large number of dislocations without any apparent precipitates. The increase in UTS from wire drawing for Si4, Si6, and Si9 alloys is 79, 83, and 106 MPa, and the increase in microhardness is 25.5, 28.6, and 33.1 HV, respectively. It is worth mentioning that the aging at 180 °C could not affect the strain hardening contribution, which was proved in our preliminary work by the tensile testing on commercially pure drawn aluminum at different aging times up to 34 h at 180 °C. It can be deduced that the strain hardening effect increases with the Si level. Compared to the other two alloys, the Si-excessive Si9 alloy shows the largest strain hardening contribution.

3.3.4. Microstructures

For the microstructural examination, the Si4 alloy after 3 h, the Si6 alloy after 5 h, and the Si9 alloy after 34 h of aging were selected, representing a compromise between UTS and EC, designated as Si4-3h, Si6-5h, and Si9-34h alloys. Fig. 3.5 shows the grain structures for these three alloys in the drawing direction. The grains are elongated along the drawing direction. The average grain size was determined by measuring over 300 grains, being 150, 130, and 138 μm for Si4-3h, Si6-5h, and Si9-34h alloys, respectively, as shown in Fig. 3.5d. Given the fact that the experimental process is the same for all alloys and the aging at 180 °C would barely lead to

the recrystallization, it is expected that the grain sizes of three alloys are relatively similar. The large grain size in all the samples could be attributed to the casting without grain refiner.

The presence of the Fe-rich intermetallics could enhance EC by removing the Si atoms from the matrix, but the strength might be reduced via lower age hardening response. However, the volume fractions of the Fe-rich intermetallics in all three alloys are quite low (less than 0.5%). Therefore, it is reasonable to expect that the Fe-rich intermetallics have insignificant effects on both strength and EC of experimental alloys.

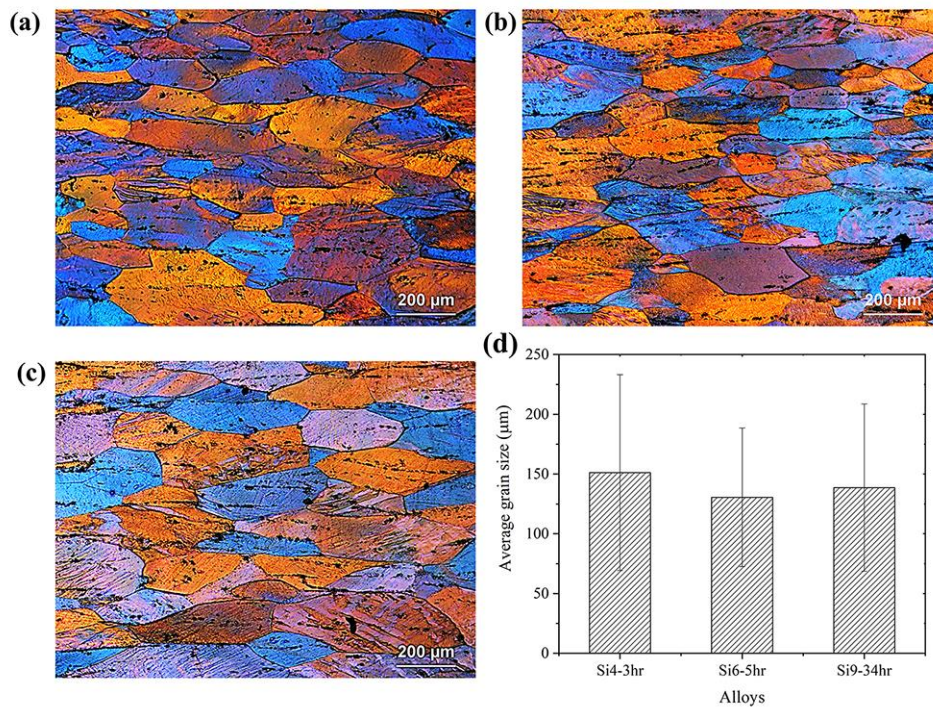


Figure. 3.5 Grain structures of (a) Si4-3h, (b) Si6-5h, and (c) Si9-34h alloys parallel in the drawing direction; (d) the average grain sizes of three alloys.

Fig. 3.6 shows the bright field TEM micrographs of Si4-3h, Si6-5h, and Si9-34h alloys, revealing the main precipitates in the aluminum matrix. Quantitative analysis was performed on the precipitates to identify the strengthening contribution of precipitates (Fig. 3.6d and e). It was

observed that the precipitate structures formed in the as-deformed samples are only hexagonal, being the structure of β' precipitates [28]. Accordingly, the conventional precipitation sequence could be bypassed by the formation of β' precipitates instead of β'' phases with the introduction of a large number of dislocations by cold deformation [28, 29]. The average lengths of the β' precipitates were 58.2, 82.8, and 171.3 nm for Si4-3h, Si6-5h, and Si9-34h alloys, while the number densities of the precipitates were 4674, 5177, and 3171 μm^{-3} , respectively. The β' precipitates were slightly coarsened in the Si6-5h alloy compared to the Si4-3h alloy, while the β' precipitates were coarsened to a great extent in the Si9-34h alloy with a long aging time in the overaging condition, as shown in Fig. 3.6. It is observed that the Si-excessive Si9-34h alloy has the largest average length and lowest number density of the precipitates, suggesting that the Si9-34h alloy possesses low contribution to strengthening by precipitation. According to DSC results, it could be deduced that the highest amount of the precipitates was achieved in Si9 alloy in the peak aged condition among all the alloys. However, it was required to significantly prolong the aging time to enhance the EC at the expense of the strength. Therefore, the Si9 alloy was subjected to a long time in the overaging stage to reach the required minimum EC, causing the coarsening of the precipitates. Owing to the highest number of precipitates, the Si6-5h alloy is expected to have the highest contribution of precipitate strengthening. Based on the DSC results, it might be inferred that the Si6 alloy has a higher precipitate amount relative to the Si4 alloy in the peak aged condition. Even after the slightly long aging time, the Si6-5h alloy still has a higher number density of the precipitates compared to the Si4-3h alloys when they both reached the minimum required EC. The grain boundary precipitates barely occur in the coarse-grained Al-Mg-Si alloys and precipitates mainly form in the grain interiors in all three alloys [11].

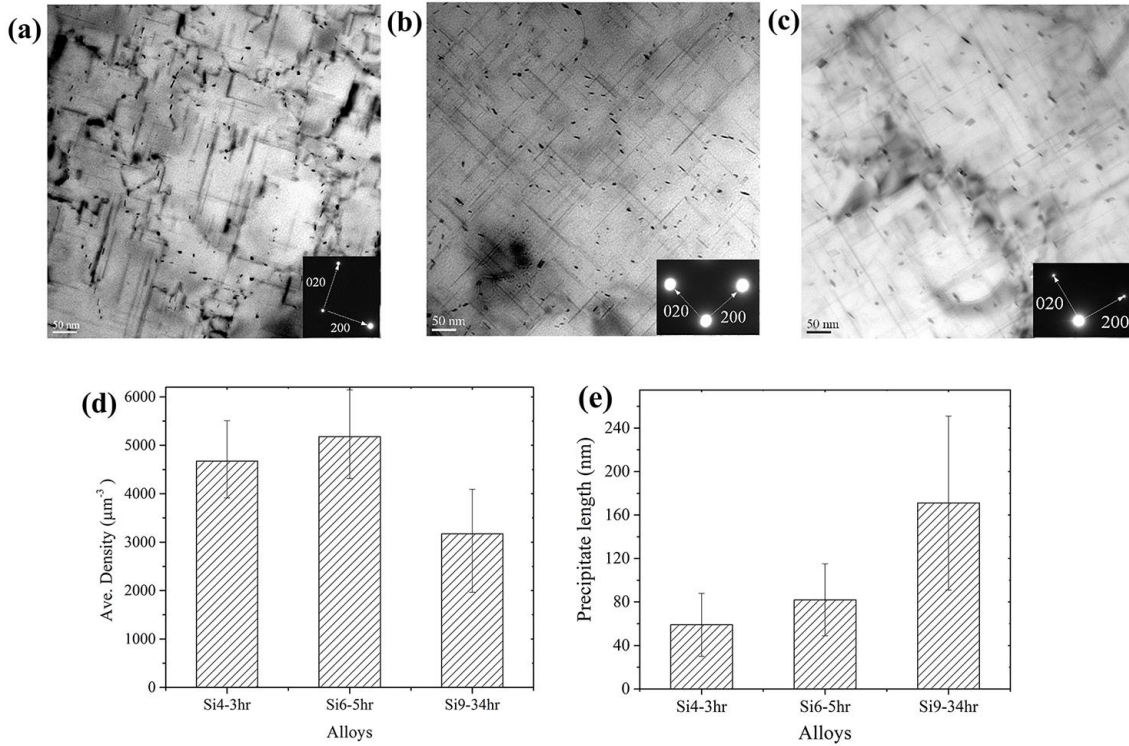


Figure. 3.6 Bright field TEM micrographs for (a) Si4-3h, (b) Si6-5h, and (c) Si9-34h alloys (d) the mean precipitate length and (e) the average number density of precipitates

3.4. Discussion

3.4.1. Correlation between strength and EC

In the peak aged condition, it was observed that the alloys with higher Si content showed greater strength, but EC is lower compared to the alloys with lower silicon content (Fig. 3.3), presumably resulting from the dissolved Si in the matrix [21]. When considering the strength and electrical conductivity simultaneously in each alloy with different aging times, it was found that the best trade-off between UTS and EC for Si4, Si5, Si6, and Si9 alloys were achieved after 3, 4, 5, and 34 h of aging, respectively. Fig. 3.7a shows the highest UTS at the minimum required EC as a function of the Mg/Si ratio for four alloys. The UTS increases first with increasing Mg/Si

ratio and reaches the maximum at Mg/Si ratio of ~1, and then dropped with a further increase of Mg/Si ratio. The order of the highest achievable strengths of the alloys with the minimum required EC is Si6-5h, Si5-4h, Si9-34h, and finally Si4-3h.

Fig. 3.7b displays the microhardness values above the minimum required EC as a function of EC, which provides an overview of the range of achievable properties in the Al-Mg-Si alloys studied. In general, the strength (hardness) decreases with increasing EC. If the strength is prioritized, the Si6 alloy with Mg/Si ratio ~1 is considered as the best candidate because it shows the highest strength up to 54% IACS among all the alloys. However, there is a restriction on the usage of the Si6 alloy at the higher EC (> 54% IACS), where the strength tends to decrease sharply. If the EC is the primary concern in the conductor alloys, the Mg-excessive Si5 alloy with Mg/Si ratio of ~1.5 provides a better compromise between strength and EC. On the high end of EC (54–56% IACS), the Si5 alloy can still maintain a reasonably high level of the strength compared to other alloys. For the Si-excessive Si9 alloy, its EC could increase no further, even after the prolonged aging time (Fig. 3.2d) and therefore, the achievable property window above 52.5% IACS is very narrow.

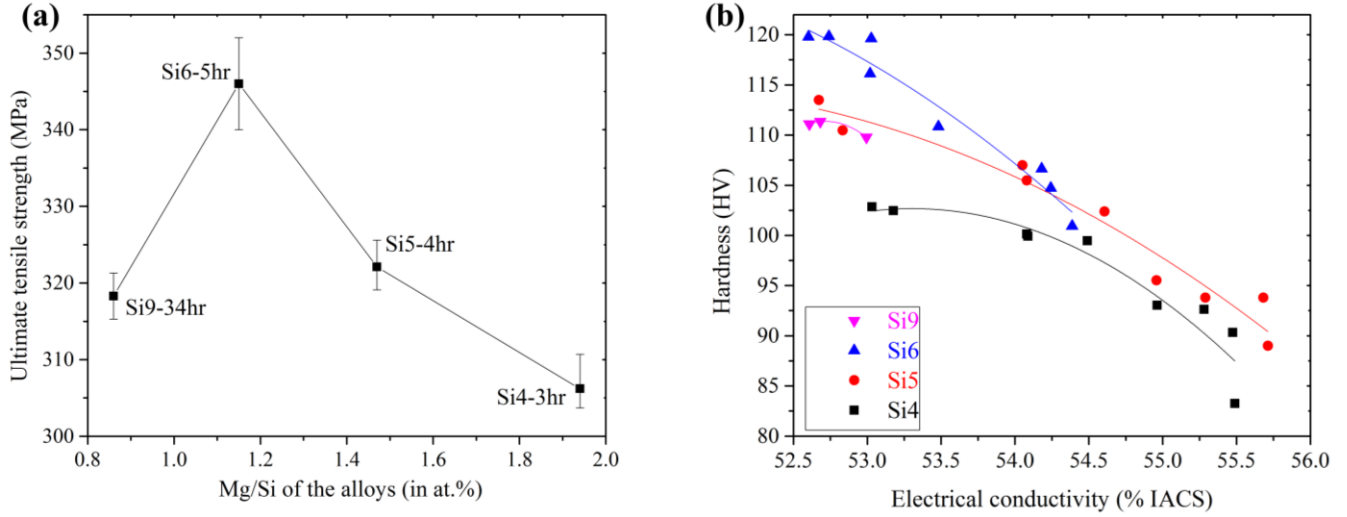


Figure. 3.7 (a) UTS as a function of Mg/Si ratio and (b) Hardness as a function of EC above the minimum required EC (52.5% IACS) for four alloys

3.4.2. Strengthening mechanisms

In this section, the constitutive equations of the classical strengthening mechanisms are applied to quantitatively describe the contributions of the microstructural features at multiple levels. Knowing the importance of the individual contribution, the analysis can also provide a theoretical basis for developing new kinds of Al-Mg-Si conductor alloys with enhanced properties. The strength (hardness) is mainly determined by the forest of dislocations, precipitates, grain boundaries, and solute atoms. Correspondingly, the hardness (HV) can be expressed in the following equation, considering that the hardness is approximately equal to one-third of the yield stress ($\Delta HV \approx \Delta \sigma / 3$) [9, 11, 32].

$$HV_{total} = HV^{Al} + \Delta HV^{dislo} + \Delta HV^{prec} + \Delta HV^{gb} + \Sigma \Delta HV_i^{sol} \quad (3.1)$$

Where HV_{total} is the total hardness, HV^{Al} is the hardness of the aluminum matrix, ΔHV^{dislo} is the contribution of forest dislocations via strain hardening in the wire drawing, ΔHV^{prec} is the

contribution of the precipitation hardening, ΔHV^{gb} is the contribution of grain boundary strengthening, and $\Sigma \Delta HV_i^{sol}$ is the hardness contribution via solute strengthening [9, 11].

The yield stress of the aluminum matrix was reported to be 34 MPa for a commercially pure 1100-O aluminum alloy [33]. Therefore, HV^{Al} could be considered as approximately 11 HV, which stems from friction stress.

The dislocations in the present alloys were mainly generated from the strain hardening by cold wire drawing with an area reduction of 50%. As mentioned earlier, the hardness increases from strain hardening were experimentally determined, and they are 25.5, 28.6, and 33.1 HV for Si4, Si6, and Si9 alloys, respectively. The Bailey–Hirsch relationship for strain hardening could be used to estimate the number density of dislocations for each alloy [13].

$$\Delta \sigma^{dislo} = \alpha M G b \rho^{1/2} \quad (3.2)$$

Where α is a dimensionless constant with a value of 0.3 for FCC Al [13], M is the Taylor factor (constant) is 2 for polycrystalline FCC Al [33, 34], G is the shear modulus with a value of 26.9 GPa in FCC Al, b is the burgers dislocation vector with a value of 0.29 nm in FCC Al₍₁₁₀₎ [13], and ρ is the number density of dislocations. By knowing the strain hardening contribution and ($\Delta HV \approx \Delta \sigma / 3$) in Eq. 3.2, the number density of dislocations for Si4, Si6, Si9 alloys could be estimated to be 2.7×10^{14} , 3.4×10^{14} , and $4.5 \times 10^{14} \text{ m}^{-2}$, respectively, which is in a good agreement with the data reported in Al-Mg-Si alloys by Sauvage et al. [13] and Zhang et al. [35].

By assuming the precipitates are evenly distributed (Fig. 3.6), the contribution of precipitation hardening could be calculated using the Orowan equation for non-shearable precipitates [13].

$$\Delta \sigma^{prec} = \frac{2M\beta Gb}{L} \quad (3.3)$$

where β is 0.28 (constant) and M , G , and b were defined above. L is the average inter-precipitate spacing, which can be estimated from the precipitate density (N).

$$L = \frac{1}{(N)^{1/3}} \quad (3.4)$$

Based on the experimental measurements on precipitate parameters (Fig. 3.6), the contribution of precipitates hardening in the hardness of Si4-3h, Si6-5h, and Si9-34h alloys were calculated to be 48.5, 50.5, and 42.5 HV, respectively.

The contribution of grain boundary strengthening can be calculated by using the well-known Hall-Petch equation [13].

$$\Delta HV^{gb} = k_{HP} d^{-1/2} \quad (3.5)$$

Where HV_{gb} is the contribution of the grain boundary hardness, k_{HP} is a scaling constant typically considered to be 35 ($HV \mu m^{1/2}$) for 6xxx series aluminum alloys [13] and d is the average grain size. Owing to the similar grain sizes in the present alloys (Fig. 3.5), the contribution of the grain boundary strengthening was calculated to be approximately 3 HV for all alloys, which is low compared to other contributors.

For the solute strengthening contribution, the following equation could be used [13].

$$\Delta \sigma_i = k_i C_i^{2/3} \quad (3.6)$$

Where $\Delta \sigma_i$ is the increased yield stress due to the solute i , k_i is a scaling factor for the solute i , and C_i is the concentration of the solute i (in wt.%). In the present Al-Mg-Si alloys, only Mg and Si solutes in the aluminum matrix were considered, and k_{Mg} and k_{Si} were 29 and 66.3 MPa (wt.%)^{-2/3} [13]. It is apparent that the strengthening effect of Si solutes is much stronger than that of Mg solutes per wt. %. Li et al. [21] reported that over half of Si amount remained in the aluminum matrix after 8 h aging at 175 °C in an Al-Mg-Si alloy with an Mg/Si ratio of one, while the majority of Mg was consumed by the precipitates. Based on this result, it could be assumed that half of Si remains in the matrix in the high Si containing Si6 and Si9 alloys for solute strengthening while half of Mg is left in the matrix of the Mg-excessive Si4-3h alloy. As

an approximate estimate using Eq. 3.6, the contribution of solute strengthening could reach 5, 11, and 13 HV in the Si4-3h, Si6-5h, and Si9-34h alloys, respectively. It is worth mentioning that the Si solute strengthening effect seems to be beyond what it is calculated with the constitutive equation since it is found that the increased hardness by rising Si from 0.4 to 0.89 wt.% is approximately 90 MPa in the as-quenched condition before wire drawing, while the constitutive equation shows only 25 MPa. Therefore, the actual Si solute strengthening effect and the Si solute level remained in the matrix ought to be accounted for when identifying the solute strengthening effect.

Fig. 3.8 shows the calculated hardness values for the Si4-3h, Si6-5h, and Si9-34h alloys with different strengthening contributions, and the measured total hardness values are also listed for comparison. Although the calculated values are slightly lower than the measured ones, the general trend is in good agreement with the experimental data. It can be clearly seen that the major strength contributions come from the precipitates and strain hardening in the present alloys. Based on the calculated data and Fig. 3.8, the higher hardness of the Si6-5h alloy relative to the Si4-3h alloy might be ascribed to higher contributions of the precipitation, strain, and solute hardening. Furthermore, the lower hardness of the Si9-34h alloy compared to the Si6-5h alloy could mainly be attributed to a lower precipitate hardening. It is also noteworthy to mention that although the Si9-34h alloy has lower precipitation strengthening compared to the Si4-3h alloy, the Si9-34h alloy exhibited a higher total hardness, owing to high contributions from strain hardening and particularly Si solute strengthening.

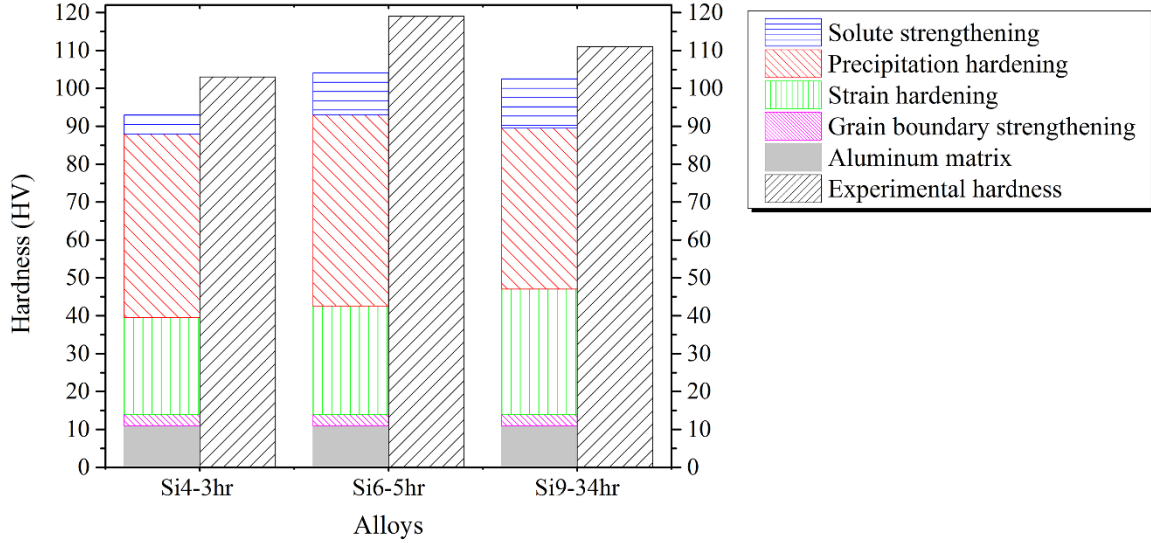


Figure. 3.8 Comparison between calculated and experimentally measured hardness for the Si4-3h, Si6-5h and Si9-34h alloys

To better understand the relation between the microstructural features and EC, Matthiessen's rule is adopted to estimate the electrical resistivity [13].

$$\rho_{\text{total}} = \rho^{\text{Alpure}} + L^{\text{dislo}} \Delta\rho^{\text{dislo}} + S^{\text{GB}} \Delta\rho^{\text{GB}} + \frac{1}{(L^{\text{prec}})^{1/2}} \Delta\rho^{\text{Prec}} + \sum C_i^{\text{sol}} \Delta\rho_i^{\text{sol}} \quad (3.7)$$

Where ρ^{Alpure} is the resistivity of the pure aluminum at room temperature ($2.655 \times 10^{-6} \Omega \text{ cm}$) [13], and $\Delta\rho^{\text{dislo}}$, $\Delta\rho^{\text{GB}}$, $\Delta\rho^{\text{Prec}}$ and $\Delta\rho_i^{\text{sol}}$ are the resistivity constants accounting for the contribution of dislocations, grain boundaries, precipitates, and solute elements in the aluminum matrix, respectively. $\Delta\rho^{\text{dislo}}$ and $\Delta\rho^{\text{GB}}$ were reported to be $2.7 \times 10^{-25} \Omega \text{ m}^3$ and $2.6 \times 10^{-16} \Omega \text{ m}^2$ [13], and $\Delta\rho^{\text{Prec}}$ to be $12 \Omega(\text{nm})^{3/2}$ [36], respectively. L^{dislo} is the dislocation density, and S^{GB} is defined as the fraction of grain boundaries, which is equal to $6/d$ (d is the mean grain size), assuming that grains are spherical. Based on the experimental data, the contributions of electrical resistivity from dislocations for Si4-3h, Si6-5h, and Si9-34h alloys are approximately 7×10^{-9} , 9×10^{-9} , $12 \times 10^{-9} \Omega \text{ cm}$, respectively, and the electrical resistivity from grain boundaries is $1 \times 10^{-9} \Omega \text{ cm}$ for

all alloys, i.e., several orders of magnitude lower than ρ^{Alpure} . Considering the electrical resistivity, ρ_{total} , of all alloys with the minimum requested EC (~53 %IACS) being $3.25 \times 10^{-6} \Omega\text{cm}$, the electrical resistivity contributions from dislocations and grain boundaries are not the controlling factors and may be neglected. L^{Prec} is defined as the precipitate spacing (in nm) in Eq. 3.7 [36]. The electrical resistivity induced by precipitates for Si4-3h, Si6-5h, and Si9-34h alloys with the precipitate spacing of 59.8, 57.8, and 68 nm is estimated to be 0.155×10^{-6} , 0.157×10^{-6} , and $0.145 \times 10^{-6} \Omega\text{cm}$, respectively, which are less than 5% of the total electrical resistivity. Due to similar precipitate spacings, the difference in the electrical resistivity from precipitates in the three alloys is almost negligible.

C_i^{sol} is the concentration of solute in the matrix, and $\Delta\rho^{\text{Mg sol}}$ and $\Delta\rho^{\text{Si sol}}$ are $0.445 \times 10^{-6} \Omega\text{cm} (\text{at. \%})^{-1}$ and $0.496 \times 10^{-6} \Omega\text{cm} (\text{at. \%})^{-1}$, respectively [13]. It is apparent that the main controlling factor of electrical resistivity originates from the solute concentrations in the Al-Mg-Si alloys. As mentioned above, a significant portion of Si remains in the matrix of the Si6-5h and Si9-34h alloys but not in that of Si4-3h alloy, and thus, Si solute atoms play an important role in limiting the EC in the present alloys. DSC analysis by Ding et al. [37] also confirmed that the excessive Si remained in the aluminum matrix. This is also the reason why the EC of the high Si containing Si6 and Si9 alloys could not largely be improved relative to the low Si containing Si4 and Si5 alloys (Fig. 3.7b). In Si4-3h, the majority of electrical resistivity stems from the Mg solute, which has less effect on solute strengthening, while the main resistivity in Si6-5h and Si9-34h alloys comes from Si solute, which has a considerable solute strengthening, as aforementioned. Furthermore, the Si solute contracts the lattice of the aluminum alloys owing to the smaller atomic size of Si compared to Al, toward the pure Al lattice parameter [15].

It is well known that precipitation from a solid solution will increase the EC of aluminum alloys because the detrimental effect of precipitates on EC is much smaller than that of solutes in the solid solution. Before reaching the peak aging, the EC sharply increases with aging time (Fig. 3.2d). However, the EC increased only slowly with increasing aging time during overaging, but the strength rapidly decreases with aging time (Fig. 3.2a). In other words, after peak aging, a small increase in the EC is accompanied by a substantial reduction in strength, which can provide little benefit in optimizing the combination of strength and electrical conductivity.

It is worthwhile to point out that strain hardening (dislocation contribution) is one of the key factors in increasing the strength in the present alloys (Fig. 3.8) while having a negligible effect on EC. Moreover, Liu et al. [14] found that dislocations aid in the extraction of alloying elements from the matrix, leading to an improvement in the EC. Consequently, promoting strain hardening can be considered as a new avenue for the design of the aluminum conductor alloys with an enhanced combination of strength and EC.

3.4.3. Comparison of achievable strength and EC in Al-Mg-Si conductor alloys

For two common Al-Mg-Si 6xxx conductor alloys that are drawn and aged, the standard hardness and EC are ~100 HV and ~53 %IACS for AA6201, and ~90 HV and ~54 %IACS for AA6101 [13]. Fig. 3.9 is shown to compare the achievable properties of two promising candidates (Si5 and Si6 alloys) in this work with the available data of Al-Mg-Si conductor alloys in the literature, although the Mg/Si ratio, process, and methodology in each study would be different. The Si6 alloy showed superior hardness in the low end of EC (52–54 %IACS) relative to the standard AA6201 alloy. Similarly, the hardness values of the Si5 alloy in the high end of EC (54–56 %IACS) are higher compared to the standard AA6101 alloy. As shown in Fig. 3.9,

the achievable combination of hardness and EC of the Si5 and Si6 alloys are also superior to the data provided in the recent publications. The present work demonstrated that the appropriate chemical composition, Mg/Si ratio, and processing could further optimize the combination of strength and EC in Al-Mg-Si conductor alloys.

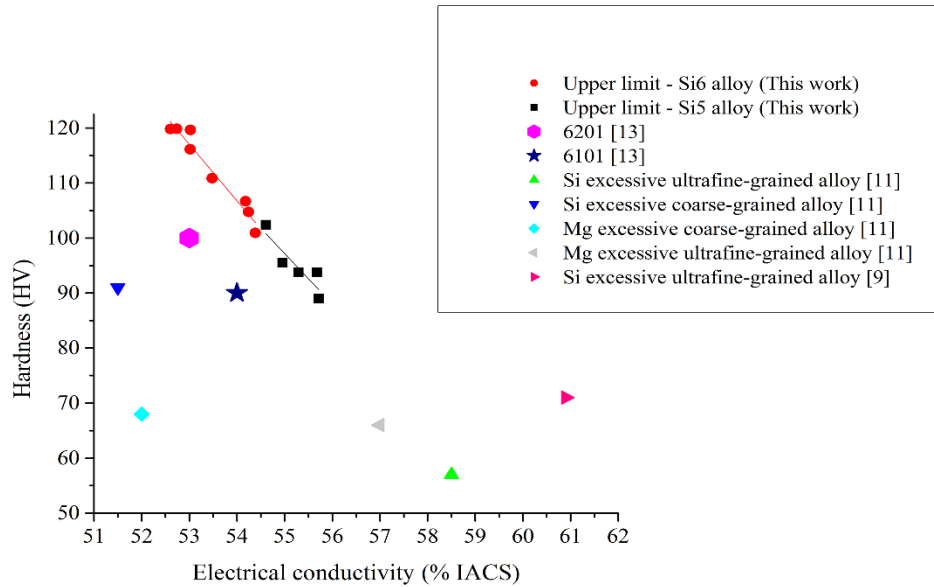


Figure. 3.9 Comparison of hardness and EC of various Al-Mg-Si conductor alloys

3.5. Conclusions

1. The excess Si (low Mg/Si ratio) of Al-Mg-Si 6201 conductor alloys produced an increase in peak strength due to high precipitation hardening, while the corresponding EC dropped in Si-excessive alloys due to having more Si dissolved in the matrix. To fulfill the minimum required EC (52.5% IACS), the alloys with low Mg/Si ratios required a longer aging time after peak aging to increase the EC.

2. Above the minimum required electrical conductivity, the Si6 alloy with the Mg/Si ratio of ~1 was considered to be the best candidate because it showed the highest strength in the EC range of 52–54 %IACS among all alloys studied. On the high end of EC (54-56 %IACS), the Si5 alloy with an Mg/Si ratio of ~1.5 provided a better compromise between strength and electrical conductivity.
3. Although the Si-excessive Si9 alloy with an Mg/Si ratio of 0.86 exhibited the highest peak strength, it needed a much longer aging time (>34 h) to reach the minimum required EC, resulting in a significant drop in the strength and a narrow window for achievable properties.
4. The constitutive equations of the classical strengthening mechanisms were applied to provide a reasonable estimate of different strengthening contributions from dislocations via strain hardening, precipitates, grain boundaries, and solid solution. The calculations were in good agreement with the experimental data. The results of the quantitative analysis indicated that precipitation strengthening and strain hardening were the two major factors contributing to strength in the present alloys. In combination with EC analysis, it was found that the strain hardening can provide a significant strength contribution with a negligible impact on EC.

Acknowledgment

The authors would like to acknowledge the financial support of the Natural Sciences and Engineering Research Council of Canada (NSERC) under the Grant No. CRDPJ 514651-17 and Rio Tinto Aluminum through the Research Chair in the Metallurgy of Aluminum Transformation at University of Quebec in Chicoutimi.

3.6. References

- [1] L. Pan, K. Liu, F. Breton, X. Grant Chen, Effect of Fe on Microstructure and Properties of 8xxx Aluminum Conductor Alloys, *J. Mater. Eng. Perform.* 25(12) (2016) 5201-5208.
- [2] L. Pan, F.A. Mirza, K. Liu, X.G. Chen, Effect of Fe-rich particles and solutes on the creep behaviour of 8xxx alloys, *Mater. Sci. Technol.* 33(9) (2016) 1130-1137.
- [3] L. Pan, K. Liu, F. Breton, X.G. Chen, Effects of minor Cu and Mg additions on microstructure and material properties of 8xxx aluminum conductor alloys, *J. Mater. Res.* 32(06) (2017) 1094-1104.
- [4] S. Karabay, Influence of AlB₂ compound on elimination of incoherent precipitation in artificial aging of wires drawn from redraw rod extruded from billets cast of alloy AA-6101 by vertical direct chill casting, *Materials & Design* 29(7) (2008) 1364-1375.
- [5] S. Karabay, Modification of AA-6201 alloy for manufacturing of high conductivity and extra high conductivity wires with property of high tensile stress after artificial aging heat treatment for all-aluminium alloy conductors, *Materials & Design* 27(10) (2006) 821-832.
- [6] E. Cervantes, M. Guerrero, J. A. Ramos, S.A. Montes, Influence of Natural Aging and Cold Deformation on the Mechanical and Electrical Properties of 6201-T81 Aluminum Alloy Wires, *Mater. Res. Soc. Symp. Proc* (2010) 03-09.
- [7] M. Iraizoz, N. Rossello, M. Amado, Influence of Solution Heat Treatment Temperature in the Final Properties of AA6201 Drawn Wire, in: M. Hyland (Ed.), *Light Metals 2015*, Springer International Publishing (2016) 183-187.
- [8] Q. Zhao, Z. Qian, X. Cui, Y. Wu, X. Liu, Influences of Fe, Si and homogenization on electrical conductivity and mechanical properties of dilute Al–Mg–Si alloy, *J. Alloys Compd.* 666 (2016) 50-57.
- [9] Y. Han, D. Shao, B.A. Chen, Z. Peng, Z.X. Zhu, Q. Zhang, X. Chen, G. Liu, X.M. Li, Effect of Mg/Si ratio on the microstructure and hardness–conductivity relationship of ultrafine-grained Al–Mg–Si alloys, *Journal of Materials Science* 52(8) (2016) 4445-4459.
- [10] R.Z. Valiev, M.Y. Murashkin, I. Sabirov, A nanostructural design to produce high-strength Al alloys with enhanced electrical conductivity, *Scripta Mater.* 76 (2014) 13-16.
- [11] S. Jiang, R. Wang, Grain size-dependent Mg/Si ratio effect on the microstructure and mechanical/electrical properties of Al-Mg-Si-Sc alloys, *Journal of Materials Science & Technology* 35(7) (2019) 1354-1363.
- [12] G.E. Totten, D.S. MacKenzie, *Handbook of Aluminum: Vol. 1: Physical Metallurgy and Processes*, CRC Press (2003).
- [13] X. Sauvage, E.V. Bobruk, M.Y. Murashkin, Y. Nasedkina, N.A. Enikeev, R.Z. Valiev, Optimization of electrical conductivity and strength combination by structure design at the nanoscale in Al–Mg–Si alloys, *Acta Mater.* 98 (2015) 355-366.
- [14] C.H. Liu, J. Chen, Y.X. Lai, D.H. Zhu, Y. Gu, J.H. Chen, Enhancing electrical conductivity and strength in Al alloys by modification of conventional thermo-mechanical process, *Materials & Design* 87 (2015) 1-5.

- [15] X. Xu, Z. Yang, Y. Ye, G. Wang, X. He, Effects of various Mg/Si ratios on microstructure and performance property of Al-Mg-Si alloy cables, *Mater. Charact.* 119 (2016) 114-119.
- [16] J. Buha, R.N. Lumley, A.G. Crosky, K. Hono, Secondary precipitation in an Al-Mg-Si-Cu alloy, *Acta Mater.* 55(9) (2007) 3015-3024.
- [17] G.A. Edwards, K. Stiller, G.L. Dunlop, M.J. Couper, The precipitation sequence in Al-Mg-Si alloys, *Acta Mater.* 46(11) (1998) 3893-3904.
- [18] L. Ding, Z. Jia, Z. Zhang, R.E. Sanders, Q. Liu, G. Yang, The natural aging and precipitation hardening behaviour of Al-Mg-Si-Cu alloys with different Mg/Si ratios and Cu additions, *Materials Science and Engineering: A* 627 (2015) 119-126.
- [19] A.K. Gupta, D.J. Lloyd, S.A. Court, Precipitation hardening in Al-Mg-Si alloys with and without excess Si, *Materials Science and Engineering: A* 316(1) (2001) 11-17.
- [20] C.D. Marioara, S.J. Andersen, T.N. Stene, H. Hasting, J. Walmsley, A.T.J. Van Helvoort, R. Holmestad, The effect of Cu on precipitation in Al-Mg-Si alloys, *Philos. Mag.* 87(23) (2007) 3385-3413.
- [21] K. Li, A. Béché, M. Song, G. Sha, X. Lu, K. Zhang, Y. Du, S.P. Ringer, D. Schryvers, Atomistic structure of Cu-containing β'' precipitates in an Al-Mg-Si-Cu alloy, *Scripta Mater.* 75 (2014) 86-89.
- [22] J.H. Chen, E. Costan, M.A. van Huis, Q. Xu, H.W. Zandbergen, Atomic Pillar-Based Nanoprecipitates Strengthen AlMgSi Alloys, *Science* 312(5772) (2006) 416-419.
- [23] C.D. Marioara, S.J. Andersen, H.W. Zandbergen, R. Holmestad, The influence of alloy composition on precipitates of the Al-Mg-Si system, *Metallurgical and Materials Transactions A* 36(3) (2005) 691-702.
- [24] F.U. Flores, D.N. Seidman, D.C. Dunand, N.Q. Vo, Development of High-Strength and High-Electrical-Conductivity Aluminum Alloys for Power Transmission Conductors, *Light Metals 2018*, pp. 247-251.
- [25] E. Standard, EN 50183. Conductors for overhead lines, aluminium magnesium silicon alloy wires (2000) 1-7.
- [26] ASTM, Annual Book of ASTM Standards, Electrical Conductors (2002).
- [27] J. Kim, C. Daniel Marioara, R. Holmestad, E. Kobayashi, T. Sato, Effects of Cu and Ag additions on age-hardening behavior during multi-step aging in Al-Mg-Si alloys, *Materials Science and Engineering: A* 560 (2013) 154-162.
- [28] K. Teichmann, C.D. Marioara, S.J. Andersen, K.O. Pedersen, S. Gulbrandsen-Dahl, M. Kolar, R. Holmestad, K. Marthinsen, HRTEM study of the effect of deformation on the early precipitation behaviour in an AA6060 Al-Mg-Si alloy, *Philos. Mag.* 91(28) (2011) 3744-3754.
- [29] R.S. Yassar, D.P. Field, H. Weiland, The effect of predeformation on the β'' and β' precipitates and the role of Q' phase in an Al-Mg-Si alloy; AA6022, *Scripta Mater.* 53(3) (2005) 299-303.
- [30] H. Nemour, D. Mourad Ibrahim, A. Triki, The effect of heavy cold plastic deformation on the non-isothermal kinetics and the precipitation sequence of metastable phases in an Al-Mg-Si alloy, *J. Therm. Anal. Calorim.* 123(1) (2015) 19-26.

- [31] D. Yin, Q. Xiao, Y. Chen, H. Liu, D. Yi, B. Wang, S. Pan, Effect of natural ageing and pre-straining on the hardening behaviour and microstructural response during artificial ageing of an Al-Mg-Si-Cu alloy, *Materials & Design* 95 (2016) 329-339.
- [32] L.F. Deschamps A, Bre´chet Y, Influence of predeformation on ageing in an Al-Zn-Mg alloy-I. Microstructure evolution and mechanical properties, *Acta Materialia*, 1998, pp. 281-292.
- [33] Z. Li, Z. Zhang, X.G. Chen, Improvement in the mechanical properties and creep resistance of Al-Mn-Mg 3004 alloy with Sc and Zr addition, *Materials Science and Engineering: A* 729 (2018) 196-207.
- [34] Y.J. Li, A.M.F. Muggerud, A. Olsen, T. Furu, Precipitation of partially coherent α -Al(Mn,Fe)Si dispersoids and their strengthening effect in AA 3003 alloy, *Acta Mater.* 60(3) (2012) 1004-1014.
- [35] J. Zhang, M. Ma, F. Shen, D. Yi, B. Wang, Influence of deformation and annealing on electrical conductivity, mechanical properties and texture of Al-Mg-Si alloy cables, *Materials Science and Engineering: A* 710 (2018) 27-37.
- [36] B. Raeisinia, W.J. Poole, D.J. Lloyd, Examination of precipitation in the aluminum alloy AA6111 using electrical resistivity measurements, *Materials Science and Engineering: A* 420(1) (2006) 245-249.
- [37] L. Ding, Z. Jia, Y. Liu, Y. Weng, Q. Liu, The influence of Cu addition and pre-straining on the natural aging and bake hardening response of Al-Mg-Si alloys, *J. Alloys Compd.* 688 (2016) 362-367.

Chapter 4 : Effects of natural aging and pre-aging on the strength and electrical conductivity in Al-Mg-Si AA6201 conductor alloys (Article3)

Siamak Nikzad Khangholi ^a, Mousa Javidani ^a, Alexandre Maltais ^b, X.-Grant Chen ^a

^a Department of Applied Science, University of Québec at Chicoutimi, Saguenay,

Québec, G7H 2B1, Canada

^b Arvida Research and Development Center, Rio Tinto Aluminum, Saguenay, Quebec,

G7S 4K8, Canada

This article has been published in:

Materials Science and Engineering: A, Volume 820, 13 July 2021, 141538

Abstract

The effects of natural aging (NA), and its combination with pre-aging (PA), on the strength and electrical conductivity (EC) of drawn Al–Mg–Si AA6201 conductor alloys were studied. Natural aging had a negative impact on precipitation before the drawing process. However, wire drawing counteracted the detrimental influence of natural aging on precipitation hardening; after drawing and post-aging, the NA samples exhibited a better combination of strength and EC compared to those of the samples that did not undergo NA. Transmission electron microscopy results show that the NA samples exhibited a higher number density of precipitates in the drawn and post-aged conditions relative to those of the samples that did not undergo NA. The combination of natural aging and pre-aging followed by wire drawing and post-aging provided the highest ultimate tensile strength (369 MPa) with an acceptable EC (53% IACS). The applied

natural aging and pre-aging modified the strengthening contributions in AA6201 conductor alloys in favor of precipitation hardening. The relationship between strength and EC was analyzed in detail using strengthening models and Matthiessen's rule based on various microstructural features.

Keywords: Al-Mg-Si conductor alloys, electrical conductivity, mechanical properties, natural aging, pre-aging

4.1. Introduction

The demand for self-supporting overhead power lines in the electrical industry has attracted broad attention for the use of Al–Mg–Si conductor alloys (such as AA6101 and AA6201 alloys) because these Al alloys provide an excellent combination of high strength with the desired electrical conductivity (EC) [1-3]. The principal strengthening mechanisms in aluminum alloys are precipitate strengthening, strain hardening, solute strengthening, and grain-boundary hardening. However, electrical resistivity originates from crystal defects, solutes, and precipitates owing to disruptions in the atomic periodicity and strain fields in a crystal structure [4-7]. Solute atoms along with GP zones are known to be strong factors that scatter conduction electrons [4, 5, 8]. Therefore, the parameters that improve the strength often cause an increase in electrical resistivity in Al–Mg–Si conductor alloys, indicating that strength and EC are mutually incompatible.

The predominant fabrication route of Al conductor cables is by means of the Properzi continuous casting–rolling (CCR) process, followed by cold wire drawing (Fig. 4.1) [2, 9]. A bar with a trapezoidal cross section (Fig. 4.1a), cast by a Properzi wheel, is directed toward an in-line

multi-stand hot-rolling process to produce a rod with a diameter of 9.5 mm (Fig. 4.1b) [10]. The rod is subsequently cold-drawn to fabricate electrical cables (Fig. 4.1c). The temperature of the cast bar prior to hot rolling is maintained above the solvus temperature of the Al–Mg–Si alloy to ensure solutionizing and optimal aging response [11]. Immediately after the rolling process, the rods are rapidly cooled to 50-65 °C by spraying an oil-in-water emulsion to prevent precipitation. The rods, which are directed to the winding process in the subsequent step, require a few hours to reach room temperature [9]. The coiled rods are eventually subjected to a wire drawing process, followed by artificial aging to optimize the strength and EC [2]. As the wire drawing process is typically implemented in a separate unit, the transportation and storage arrangements normally delay the drawing process up to several weeks. The slow cooling from 50-65 °C to the room temperature and the subsequent storage at room temperature often cause substantial natural aging before the wire drawing process. This type of natural aging in the industrial practice is slightly different as the conventional natural aging at room temperature owing to a part of aging at higher temperatures (50-65 °C).

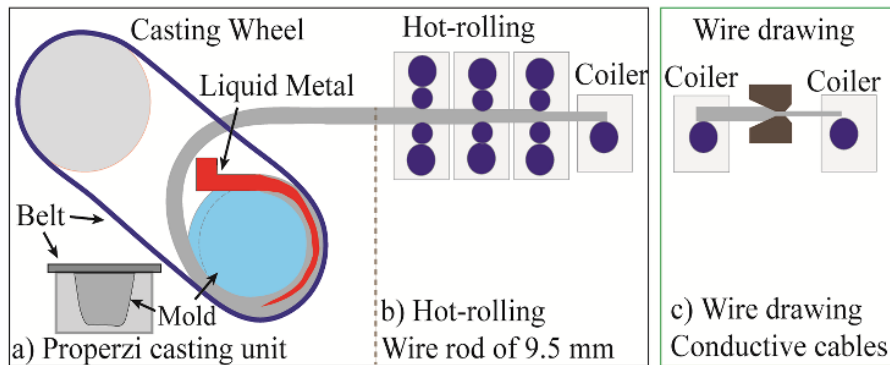


Figure. 4.1 Schematic Properzi process for aluminum conductive wires

Rometsch et al. [12] reported that natural aging without cold working results in the formation of numerous solute clusters and GP zones while slightly reducing the quantity of dissolved atoms

in the matrix. Thus, the formation of clusters and GP zones increases the strength but decreases the EC because the radius of the clusters and GP zones is smaller than the electron mean free path [7]. In practice, natural aging takes place during storage before the wire drawing process [3, 9], meaning that wire drawing might affect the clusters and GP zones that form during natural aging. Cervantes et al. [3] reported that natural aging of the AA6201 alloy at room temperature followed by wire drawing and post-aging exhibited a better combination of strength and EC compared to those of samples that did not undergo natural aging in the subsequent aging treatment, of which the underlying microstructure was not investigated.

Several studies have been devoted to the modified thermomechanical treatment (M-TMT) with artificial pre-aging before the drawing process and post-aging to attain a better trade-off between strength and EC compared to those achieved by the conventional thermomechanical treatment [13-15]. It has been reported that the presence of precipitates in samples fabricated using the M-TMT could boost strain hardening during cold deformation [13, 15], although Cheng et al. [16] observed that the samples exposed to under-aging and peak-aging exhibited less strain hardening compared to that of the as-quenched samples. Therefore, the exact strengthening mechanisms in M-TMT samples remain controversial.

Given that precipitation hardening is one of the major strengthening factors in Al–Mg–Si alloys, it is worthwhile to address the precipitation sequence during aging treatment. The precipitation sequences of the Al–Mg–Si materials in the as-quenched condition are as follows: clusters of Mg and Si atoms, GP zones, β'' , β' , and equilibrium β -Mg₂Si [17, 18]. However, cold deformation after solution treatment can disturb precipitation events owing to the presence of dislocations. In deformed samples, β' precipitation can be promoted along the dislocations, and

β'' precipitation might be bypassed [19-21]. Therefore, the precipitation sequences in the as-deformed condition can become clusters/GP zones, β' , and equilibrium β -Mg₂Si [20, 21].

In the present work, natural aging was adopted in the thermomechanical treatment to simulate the aforementioned natural aging in industrial practice. This study focuses on the evolution of the strength and EC of naturally aged and pre-aged AA6201 conductor alloys compared to those of alloys with no natural aging. The microstructural evolution under various conditions was investigated using transmission electron microscopy (TEM) and differential scanning calorimetry (DSC) analysis. The mechanisms for improving the strength and EC of AA6201 conductor alloys are discussed based on constitutive models.

4.2. Experimental procedure

An AA6201 alloy with the chemical composition of Al-0.62%Mg-0.62%Si-0.1%Fe (wt.%) was prepared in an electrical resistance furnace. The melt was cast in a steel permanent mold to obtain cast ingots with a dimension of 30 mm × 40 mm × 80 mm. After casting, the homogenization of cast ingots was conducted at 560 °C for 6 h, followed by hot rolling at 350-480°C with an area reduction of 70%. Afterward, the samples were cut and machined into the square bars. The hot-rolled materials were subjected to a solution heat treatment at 540 °C for 2h, and then water-quenched to the room temperature. The experimental procedures of natural aging and pre-aging are shown in Fig. 4.2. As the base case for the comparison, a set of samples after wire drawing without natural aging were prepared (Fig. 4.2a), designated as the No-NA samples. The natural aging was composed of 10h or 20h at 70 °C followed by keeping at room temperature for 2 weeks (Fig. 4.2b), referred to as 10NA and 20NA samples hereafter, respectively. It should be mentioned that this type of natural aging was designed to simulate the

industrial natural aging phenomenon in the lab controlled condition. Subsequently, cold wire drawing with 50% reduction was applied to the samples, producing wires with a diameter of 4.7 mm. The artificial aging at 180 °C at different aging times was applied just after wire drawing. Another set of 20NA samples was exposed to the pre-aging at 180 °C for 5h (similar to the peak-aging T6 temper), labeled as 20NA-PA samples. Then it followed by the wire drawing (50% reduction) and re-aging at different times (Fig. 4.2c).

The mechanical properties of drawn wires were characterized by microhardness and tensile strength. The HV hardness tests were carried out on the cross-sectional surfaces of the samples perpendicular to the wire drawing direction with a constant force of 25 g and dwell time of 20 s. The reported hardness value was based on an average of at least eight measurements. Tensile tests were conducted on the samples with a gage length of 250 mm at the strain rate of $8 \times 10^{-4} \text{ s}^{-1}$ according to ASTM B557 and ASTM E8. For each condition, three tensile tests were performed, and the mean strengths were reported. The electrical conductivity was determined by at least fifteen measurements using the Sigmascope method (Eddy current technique) with a frequency of 480 kHz based on ASTM E1004.

Differential scanning calorimetry (DSC) analysis was performed by the PerkinElmer machine in an argon atmosphere with a heating rate of 10 °C/min from 50°C to 550°C to reveal the precipitation behavior of the samples. At least, three samples were used for each condition, and the weight of samples was around 15-30 mg. The DSC results were corrected with the base line. The measurement of classical onset and peak temperatures was carried out based on the technique described in Ref. [22]. The precipitates and dislocations were analyzed using TEM operated at 200 kV. TEM samples were mechanically ground and then electropolished by a twin jet unit with the solution of 30% HNO₃ in methanol at the temperature between -20 and -30°C.

The foil thickness was measured by the convergent beam electron diffraction (CBED) technique. The bright-field TEM images were acquired in $\langle 001 \rangle$ zone axis for precipitates and in $\langle 011 \rangle$ zone axis for dislocation observation. The methods for precipitate statistics were elaborated in detail in Ref. [23]. The average precipitate length was measured (at least for 200 precipitates) in $\langle 200 \rangle$ and $\langle 020 \rangle$ zone axis using the image analyzer software (Image J) on TEM micrographs. The measured precipitate length was corrected based on the tilting in X and Y direction and then reported. In addition, the average cross section of precipitates was also measured (at least for 200 precipitates) in $\langle 002 \rangle$ zone axis using the same software (Image J) on TEM micrographs. The final equation to measure the precipitate density is defined as follows [23].

$$\rho = \frac{3N}{A(t+\lambda)} \quad (4.1)$$

Where N, A, t and λ stand for the number of precipitates in $\langle 001 \rangle$ zone axis, area of the matrix containing the precipitates, foil thickness on which precipitates are observed, and the corrected average precipitate length, respectively.

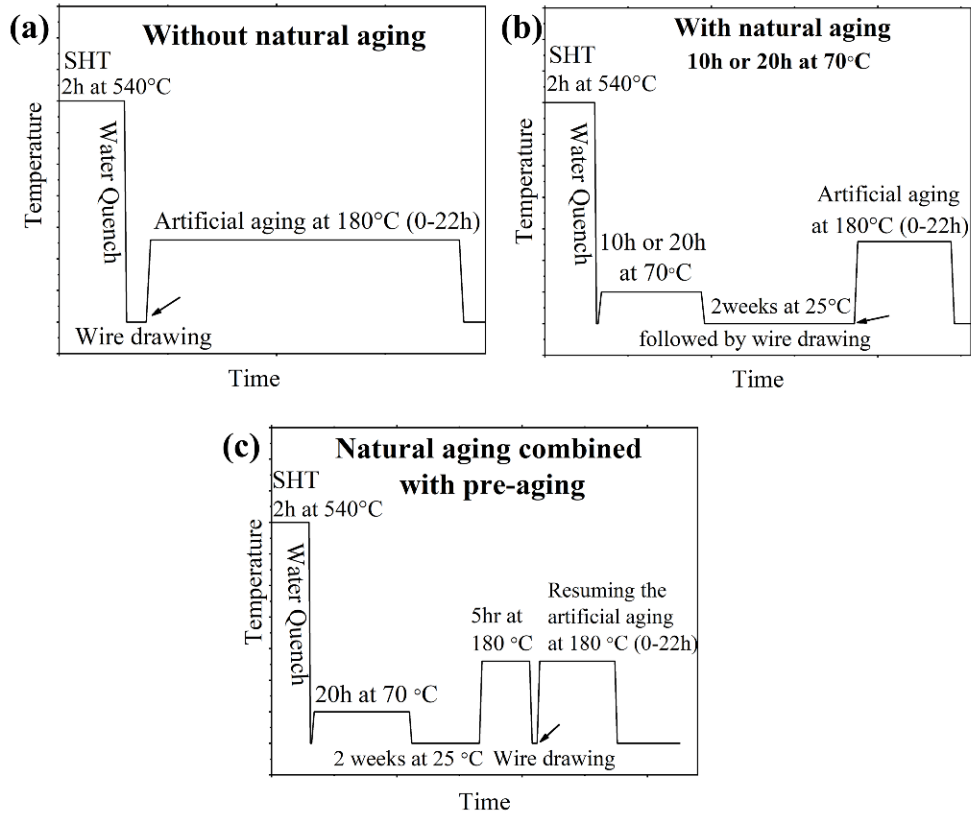


Figure. 4.2 A scheme of the experimental procedures (a) without natural aging (b) with natural aging (c) natural aging combined with pre-aging. Arrows show where wire drawing was applied

4.3. Results

4.3.1. Strength and EC

Fig. 4.3a and 4.3b show the evolution of hardness and EC during artificial aging at 180 °C, respectively. The hardness curves (Fig. 4.3a) indicate that the peak hardness of the samples with natural aging (10NA or 20NA samples) was higher than that of the No-NA samples. The hardness of the No-NA, 10NA, and 20NA samples reached 128, 133, and 138 HV, respectively, under the peak-aged condition. After peak aging, the hardness of all the samples gradually decreased with aging time. The No-NA samples reached the peak hardness in a shorter aging time compared to those of the 10NA and 20NA samples. Overall, the 20NA-PA samples

exhibited the highest hardness values at a given aging time. Given that the 20NA-PA samples reached the peak hardness before wire drawing with pre-aging at 180 °C for 5 h, its hardness after wire drawing continuously decreased with aging time, as presented in Fig. 4.3a.

Fig. 4.3b shows that the EC values for the naturally aged materials and the No-NA samples grew sharply in the early stage of aging owing to the decomposition of the supersaturated samples and then moderately increased until reaching a plateau. Although the EC values of the 20NA-PA samples improved during the pre-aging treatment to some extent, their increased EC values during the early stage of aging were less than those of the other sample conditions. Therefore, the 20NA-PA samples possessed the lowest EC at a given aging time above 5 h of aging. The EC improvement during post-aging can most probably be attributed to the extraction of solutes into precipitates because the electrical resistivities of precipitates are less than those of solutes.

The hardness and EC of the non-drawn 20NA samples are also shown in Fig. 4.3a and b for the comparison. The non-drawn 20NA samples reached the peak hardness after 5h aging, showing low precipitation kinetics due to the small number of dislocations. In addition, its EC values increased more slowly relative to the drawn samples, suggesting that dislocations could assist the extraction of more solutes into precipitates and resulting in higher EC in the drawn samples.

Fig. 4.3c shows the hardness versus EC for all aging times, and Fig. 4.3d shows an enlarged view of the hardness and EC above 52.5% IACS, which is the minimum required EC for AA6201 conductor alloys [24]. As shown in Fig. 4.3c, the non-drawn 20NA samples did not exceed the minimum required EC. Fig. 4.3d reveals that the 10NA, 20NA, and 20NA-PA samples outperformed the No-NA samples in terms of hardness and EC. The hardness of the

20NA-PA sample was superior to that of the other samples by up to 53% IACS. However, the surplus of the 20NA-PA samples reduced with a further increase in % IACS, resulting in a rather narrow window of EC and hardness above 52.5% IACS. In general, if the strength is the main concern, the 20NA-PA material (with the minimum 52.5% IACS) is an appropriate choice for conductor alloys. However, the 10NA and 20NA materials show a better combination of strength with EC when a high EC (above 53% IACS) is the priority.

Because the principal objective of this study was to improve strength while satisfying the minimum required EC, according to the results presented in Fig. 4.3, the samples aged for 5 h were chosen for further tensile tests. The ultimate tensile strength (UTS) values for the No-NA, 10NA, 20NA and 20NA-PA samples were 332, 339, 343, and 369 MPa, respectively, as shown in Fig. 4.4a along with their EC values. The NA samples exhibited a relatively higher strength than that of the No-NA samples. The 20NA-PA sample had the highest strength, while the No-NA samples showed the lowest strength among all studied samples above the minimum required EC. Fig. 4.4b shows a comparison of the UTS values of the present work with the materials (AL2 to AL7) referred to in the EN 50183 standard [26]. It is apparent that the strengths of all samples studied were above the requirements of the EN 50183 standard [24] for Al–Mg–Si cables with the conventional thermomechanical treatment. Comparing the 20NA-PA sample after 5 h of aging with AL3 at ~53% IACS, it can be deduced that the strength was improved by approximately 25% in the present work.

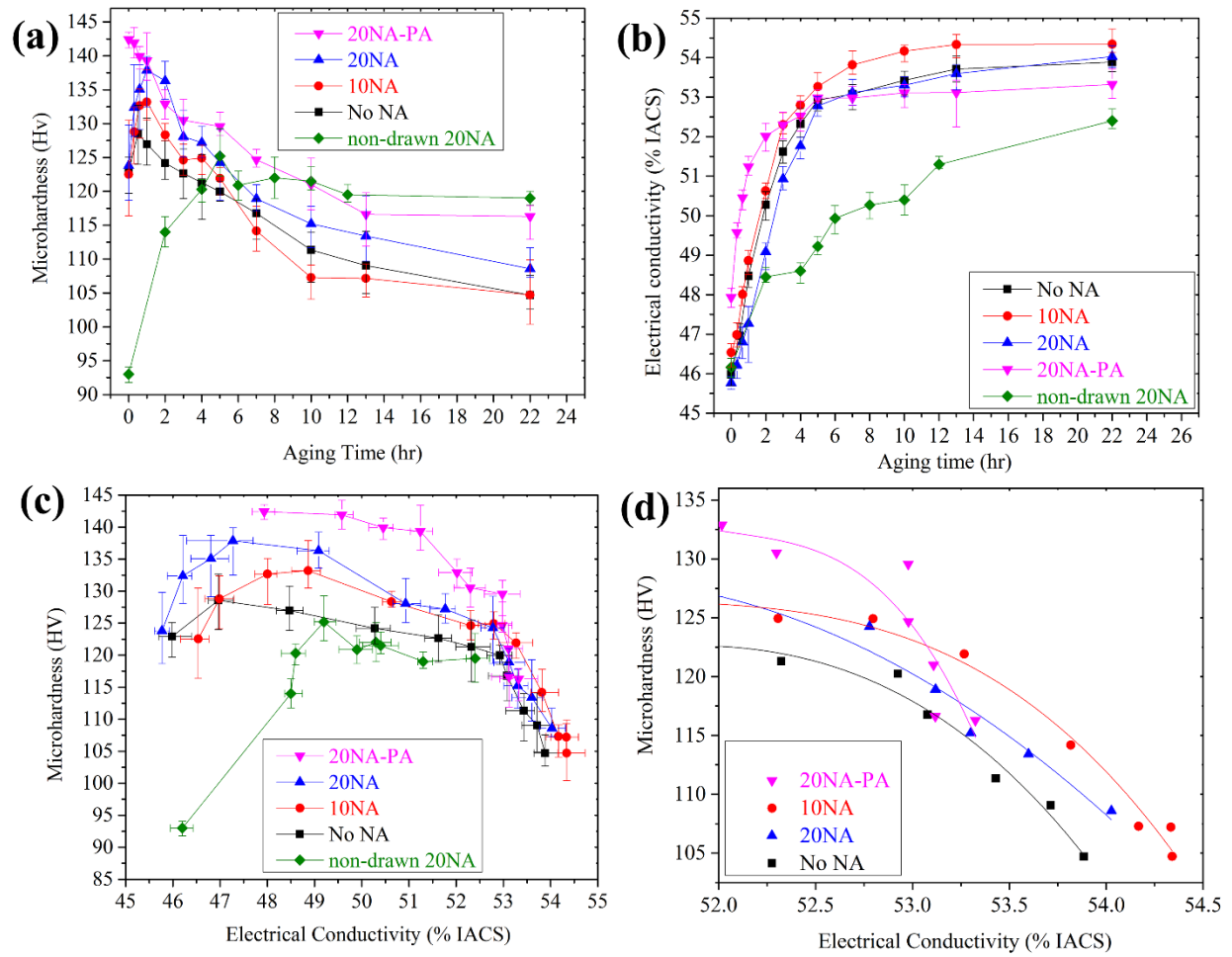


Figure. 4.3 Evolution of (a) HV hardness and (b) EC as a function of the aging time, (c) HV hardness as a function of EC for all aging times and (d) enlarged HV hardness as a function of EC above 52 % IACS. Error bars are omitted for the clarity in Figure. 4.3d.

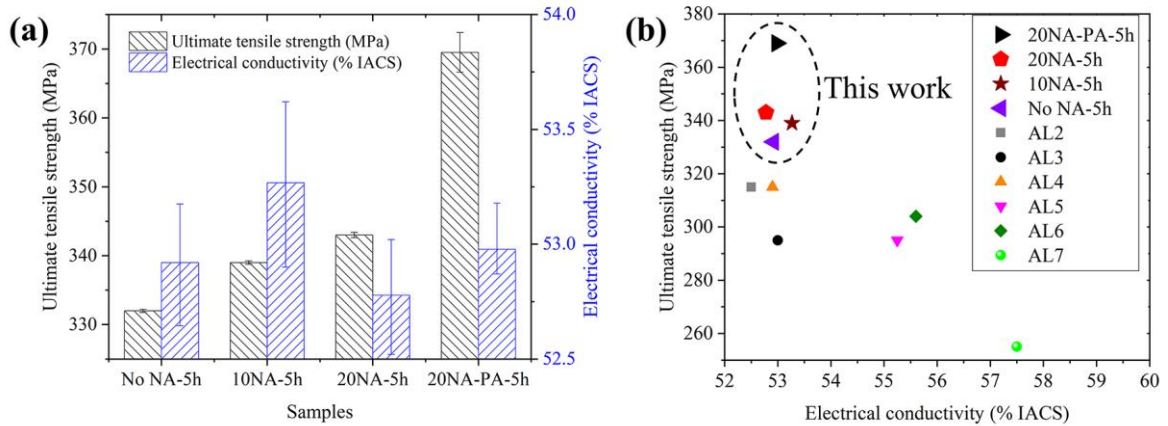


Figure. 4.4 (a) the ultimate tensile strengths above 52.5 %IACS along with their EC values and (b) comparison of the ultimate tensile strengths of the present work with the materials referred in EN 50183 standard [24] for the $\phi 4.7$ mm wires.

4.3.2. DSC analysis

Fig. 4.5 shows the results of the DSC analysis of the samples under various natural aging conditions. As shown in Fig. 4.5a, the DSC curves of the samples prior to wire drawing revealed three main exothermic peaks (I, II, and III), which correspond to the formation of β'' , β' , and β precipitates, respectively. This is consistent with the conventional precipitation sequence of these alloys [18]. Considering that the β'' precipitates are the major strengthening phase in Al–Mg–Si 6xxx alloys [18], a closer look at peak I of the three materials is shown in Fig. 4.5b. The onset temperatures of peak I for the No-NA, 10NA, and 20NA samples were 239, 244, and 243 °C, whereas the peak temperatures were 265, 267, and 266 °C, respectively. It can be deduced from the onset and peak temperatures that natural aging relatively retarded β'' precipitation before wire drawing, which most likely resulted from more vacancy consumption in the NA samples. Given that the area encompassed under peak I is proportional to the quantity of β'' precipitates, it is clear from Fig. 4.5b that natural aging caused a notable decrease in the amount of precipitation

relative to that of the freshly quenched sample (No-NA). Consequently, the AA6201 alloy was sensitive to natural aging, and natural aging was found to be detrimental prior to the drawing process.

Fig. 4.5c displays the DSC results of the samples under the as-drawn condition. It is evident that two exothermic precipitation peaks appeared after wire drawing. Heavy deformation prior to the aging treatment could disrupt early precipitation and modify the precipitation sequence. The DSC results indicate that β'' precipitation was suppressed, and β' precipitation was promoted along the dislocations in the drawn samples, as reported in Ref. [19-21]. In deformed samples, it has been reported that the I_d peak might be associated with the concurrent formation of needle-shaped and lath-like precipitates, whose crystal structures are similar to that of the β' phase. The exothermic II_d peak has been attributed to the precipitation of the β phase [19-21]. These β' -type precipitates serve as the principle strengthening phase after wire drawing. The close view of the I_d peaks in Fig. 4.5d reveals that the onset temperatures of the I_d peak for the drawn No-NA, 10NA, and 20NA samples were 213.1, 214.2, and 214.3 °C, while the peak temperatures were 238.1, 243.7, and 243.7 °C, respectively. It can be inferred that natural aging led to an increase in the onset and peak temperatures for the I_d peak. This is consistent with the relatively longer aging time required to reach peak hardness for the naturally aged samples compared to that of the No-NA sample (Fig. 4.3a). The relatively large areas of the I_d peaks in the naturally aged samples (10NA and 20NA) indicates that the strengthening precipitates were promoted with natural aging in the as-drawn state (Fig. 4.5d), which is consistent with the higher peak hardness of the naturally aged samples compared to that of the No-NA samples. When comparing the DSC results before and after wire drawing, it can be concluded that heavy deformation (cold wire drawing) could suppress the adverse effect of natural aging on the strengthening precipitates.

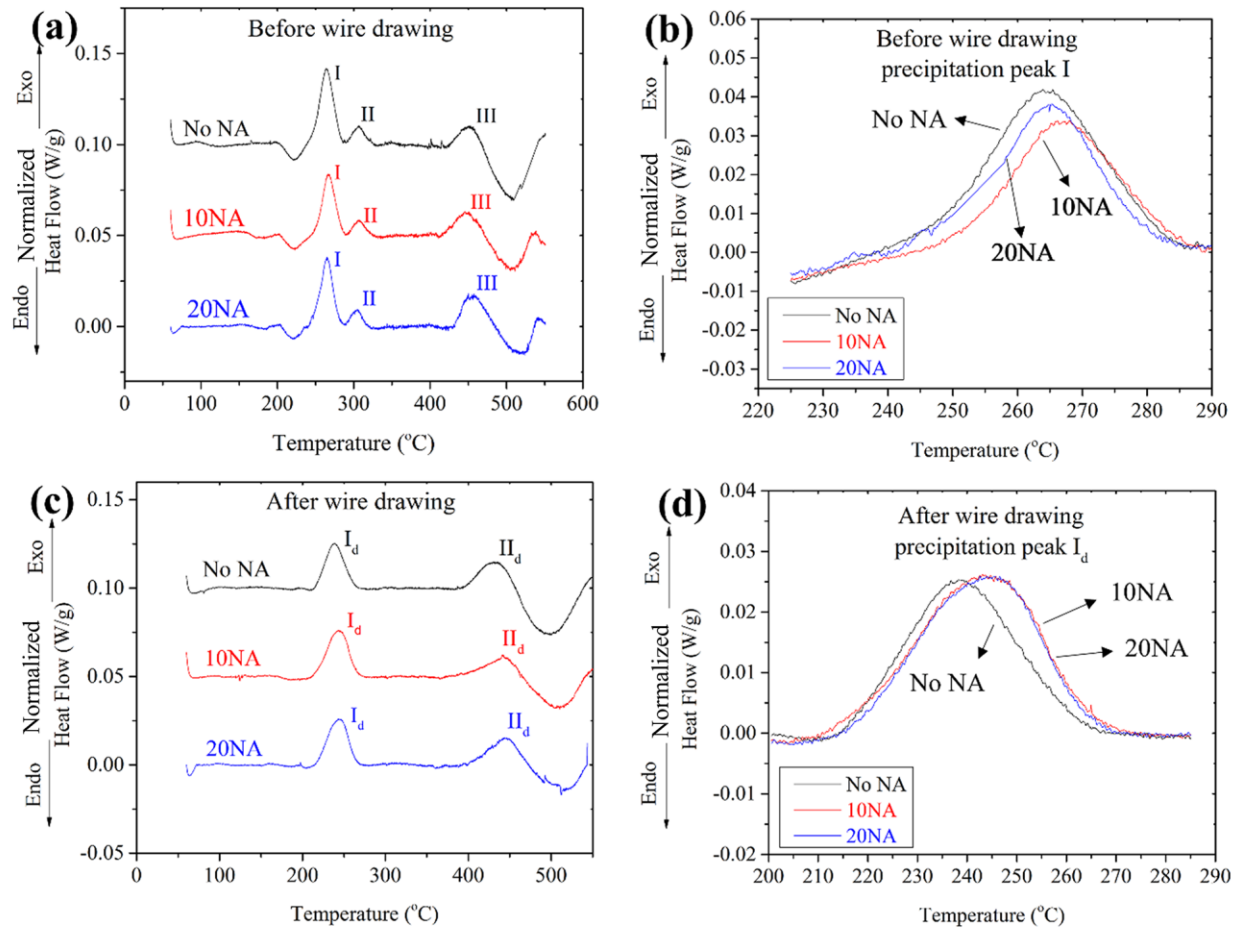


Figure. 4.5 DSC curves of the samples under different natural aging conditions, (a) before wire drawing, (b) a close view of peaks I in Figure. 4.5a, (c) after wire drawing and (d) an enlarged view of peaks I_d in Figure. 4.5c.

4.3.3. TEM microstructural analysis

To correlate the mechanical strength and precipitates, TEM micrographs of the No-NA, 20NA, and 20NA-PA samples aged at 180 °C for 5 h are shown in Fig. 4.6. As mentioned previously, the EC values of these samples were higher than 52.5% IACS. All precipitates were oriented in the $\langle 200 \rangle$ Al direction, and the dark point-like spots were cross sections of

precipitates directed along the [002] Al direction. The number densities of the precipitates are shown in Fig. 4.6d, and the mean precipitate lengths along with their cross-sectional area are shown in Fig. 4.6e. The precipitates in the No-NA and 20NA samples were identified as the β' -type phase according to the morphology of the precipitates as well as the above DSC results [19-21]. The 20NA sample aged for 5 h possessed a higher number density of precipitates relative to the No-NA sample aged for 5 h, resulting in higher hardness values at a given EC (Fig. 4.3d). The 20NA-PA sample aged for 5 h exhibited the highest precipitate number density among all samples, leading to the largest precipitate strengthening contribution (Fig. 4.3d). The precipitates in the 20NA-PA samples aged for 5 h were evenly dispersed throughout the matrix (Fig. 4.6c). The average cross section and, most notably, the length of the precipitates in the 20NA-PA sample were much smaller than those in the 20NA and No-Na samples. The results in Fig. 4.6e also show that the mean cross section of precipitates in the No-NA and 20NA samples were more or less similar, whereas the precipitate length in the 20NA sample was relatively smaller.

Fig. 4.7 shows a closer observation of the precipitates for three different samples: the No-NA sample at peak aging, the No-NA sample aged for 5 h, and the 20NA sample aged for 5 h. In the peak-aged No-NA sample, the precipitates were identified with their cross-sectional projections (laths and needles) extending in the $\langle 001 \rangle$ Al direction (white arrows in Fig. 4.7a), in which coarse lath-like precipitates along dislocations and needle-shaped precipitates were observed. The crystal structures of these precipitates were similar to that of the β' phase, as reported in Ref. [19, 20]. As mentioned previously, cold deformation (drawing) can modify the precipitation sequence by suppressing the formation of the β'' phase [19-21], as confirmed by the DSC results in Fig. 4.5. The lath-like precipitates extended along the dislocation line and were dominant in the microstructure (Fig. 4.7a). After 5 h of aging, the precipitates in the No-NA sample

coarsened (Fig. 4.6a and Fig. 4.7b) and were randomly distributed, as shown in Fig. 4.7b with white arrows. In addition to the same precipitates as those observed in the No-NA sample aged for 5 h, the 20NA sample aged for 5 h had a considerable number of precipitates with a smaller cross section, as indicated by the white arrows in Fig. 4.7c. These fine precipitates also extended in the $\langle 001 \rangle$ Al direction and were distinguishable from the coarse lath-like precipitates owing to their smaller cross section. The distribution of these fine precipitates was unrestrained by dislocations. The higher precipitate number density (Fig. 4.6d) and higher hardness values (Fig. 4.3a) in the 20NA sample compared to those of the No-NA sample after 5 h of aging could stem from the presence of these precipitates.

Fig. 4.8 shows the evolution of precipitates in the 20NA-PA samples before and after wire drawing. Before wire drawing, a large number of precipitates were observed in the 20NA-PA sample (Fig. 4.8a). After wire drawing, the precipitate length and cross-sectional area decreased considerably (Fig. 4.8b and 4.8e), while the precipitate number density decreased slightly (Fig. 4.8d). The re-dissolution of some β'' precipitates was plausible during wire drawing, as reported in Ref. [25]. Based on the size of the precipitates (~ 30 nm) in the 20NA-PA sample before wire drawing, it can be concluded that the majority of precipitates were shearable β'' precipitates [26]. The dislocations generated through drawing could consecutively shear the pre-existing β'' precipitates in the 20NA-PA samples, resulting in small fragmented precipitates; precipitate fragmentation has also been reported via dislocation sliding in plastic deformation in Ref. [5, 27, 28]. After re-aging the drawn 20NA-PA samples for 5 h to obtain the desired EC, the precipitates became coarser, and their number density decreased (Fig. 4.8c and 4.8d).

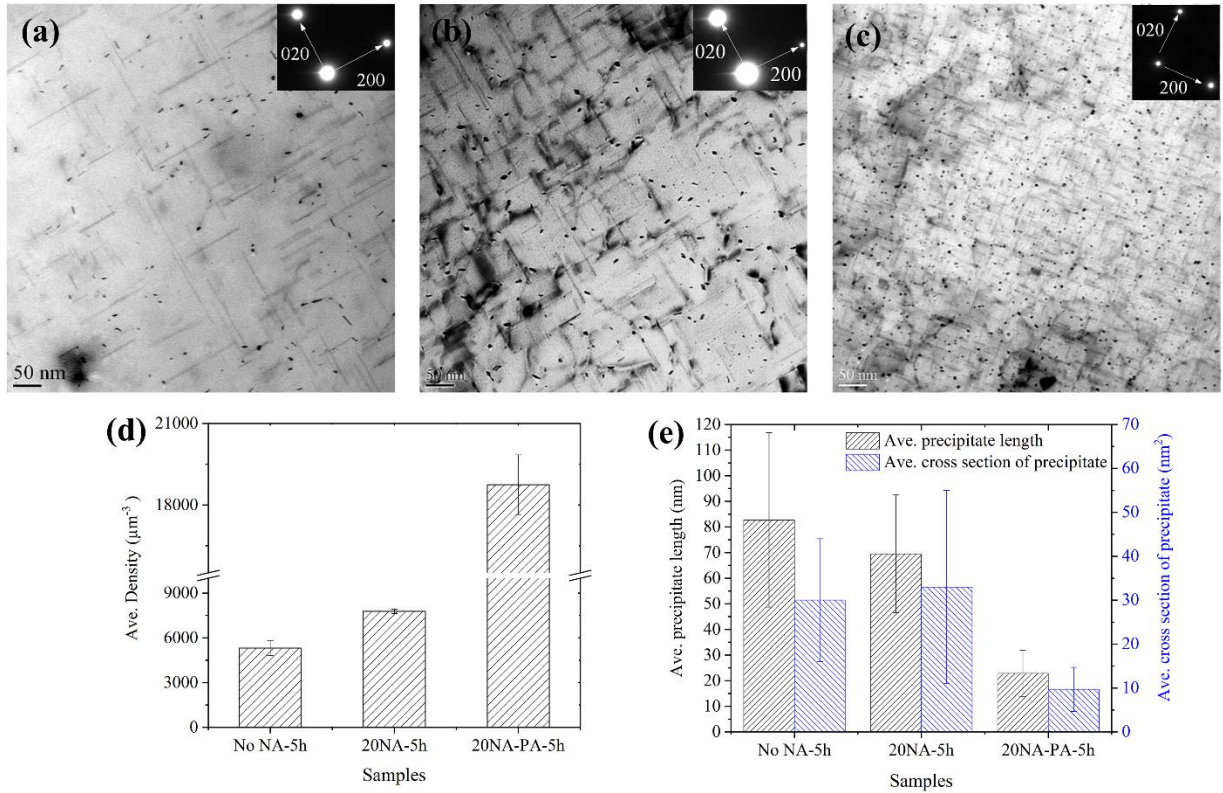


Figure. 4.6 Bright-field TEM micrographs of (a) No-NA sample after 5 h aging (b) 20NA sample after 5 h aging (c) 20NA-PA sample after 5 h aging, (d) the number density of precipitates and (e) the average length and the cross section of precipitates.

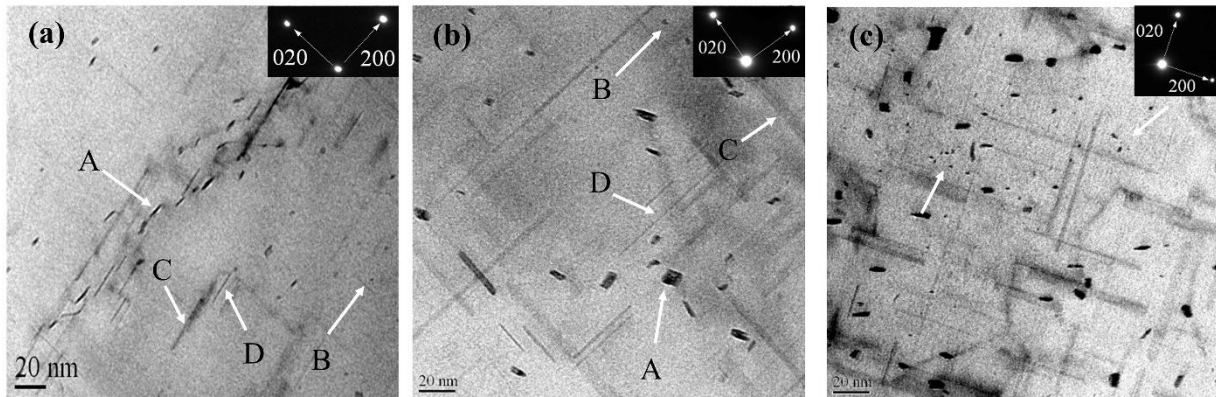


Figure. 4.7 (a) precipitates formed along the dislocations in No-NA sample at peak aging condition, (b) No-NA sample aged for 5 h, and (c) 20NA sample aged for 5 h. A and B correspond to the cross-sectional projections of lath-like and needle-shaped precipitates in $\langle 002 \rangle$ direction; C and D correspond to the longitudinal projections lath-like and needle-shaped precipitates, respectively.

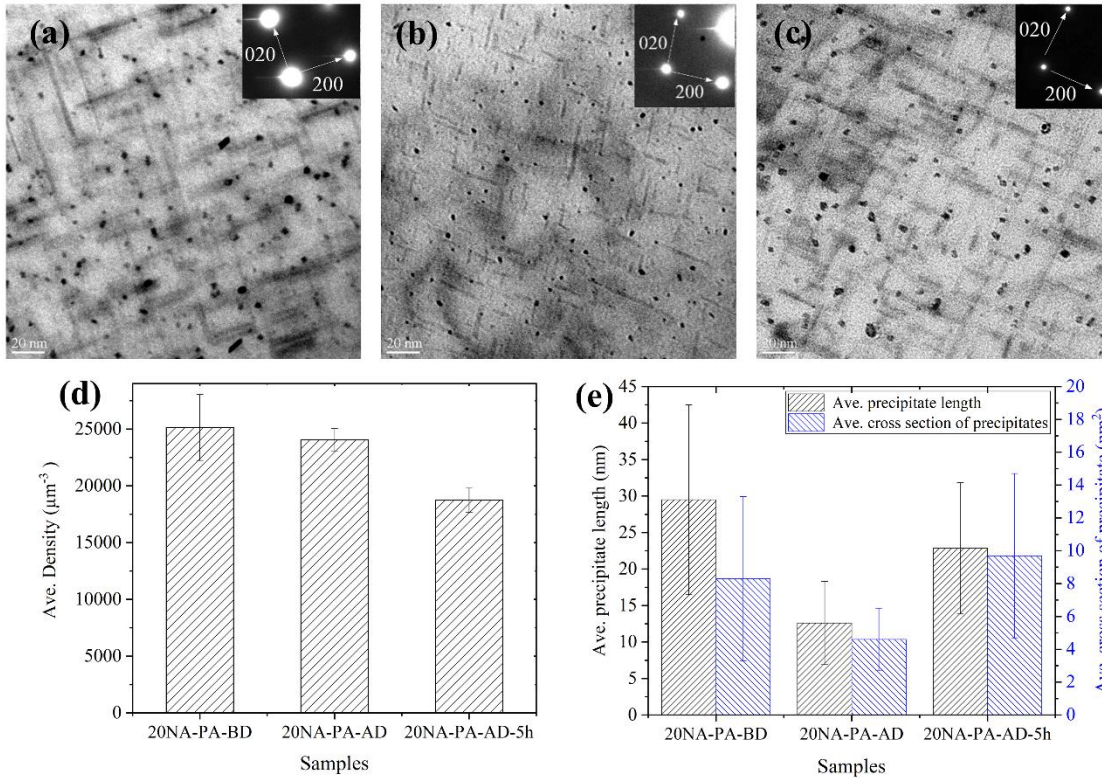


Figure. 4.8 Bright-field TEM micrographs of 20NA-PA samples (a) before wire drawing, (b) after wire drawing, (c) after wire drawing and 5 h aging, (d) the precipitate number density and (e) the average precipitate length and their cross section.

4.3.4. Strain hardening contribution

In general, strain hardening is one of the main strengthening mechanisms in Al–Mg–Si conductor alloys. The contribution of strain hardening to strengthening was determined by measuring the difference in hardness before and immediately after wire drawing without aging. The increased hardness values due to wire drawing for the No-NA, 20NA, and 20NA-PA samples were 28.6, 29.3, and 16.7 HV, respectively, as shown in Fig. 4.9. It was found that aging at 180 °C had a small effect on the recovery softening in the drawn aluminum. From Fig. 4.9, it appears that the 20NA-PA sample exhibited the least strain hardening among all samples, although a higher flow stress was required to perform the drawing [29]. In fact, the strain

hardening contribution in the No-NA and 20NA samples was similar and almost double that of the 20NA-PA sample. It is apparent that alloying elements in solid solution led to higher work hardening (in the No-NA and 20NA samples) relative to alloying elements in the form of precipitates (in the 20NA-PA sample), which is in broad agreement with Ref. [16, 25]. This can be attributed to the drag effects of solutes on the dislocations in the No-NA and 20NA samples [16].

Fig. 4.10 shows TEM micrographs of the drawn samples aged for 5 h, revealing the dislocation structures. TEM images were taken in the $\langle 011 \rangle$ zone axis close to the (111) planes because the (111) planes are major dislocation slip planes in face-centered cubic aluminum alloys. As observed in Fig. 4.10, dislocations were entangled in all the samples after the drawing process. In addition to dislocation tangle, some well-defined dislocation cells were also found in the No-NA and 20NA samples, as indicated by the white arrows in Fig. 4.10a and 4.10b, where the walls consisted of entangled dislocations. The well-defined dislocation cells were most likely formed in the samples with a higher number of dislocations (20NA and No-NA samples) [30].

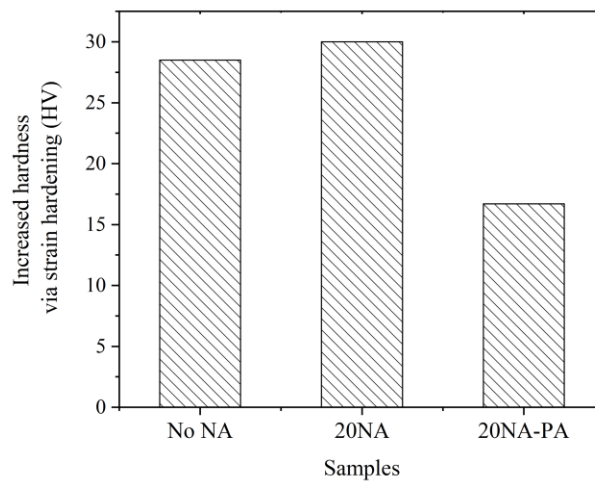


Figure. 4.9 The hardness increments via strain hardening from wire drawing in three samples.

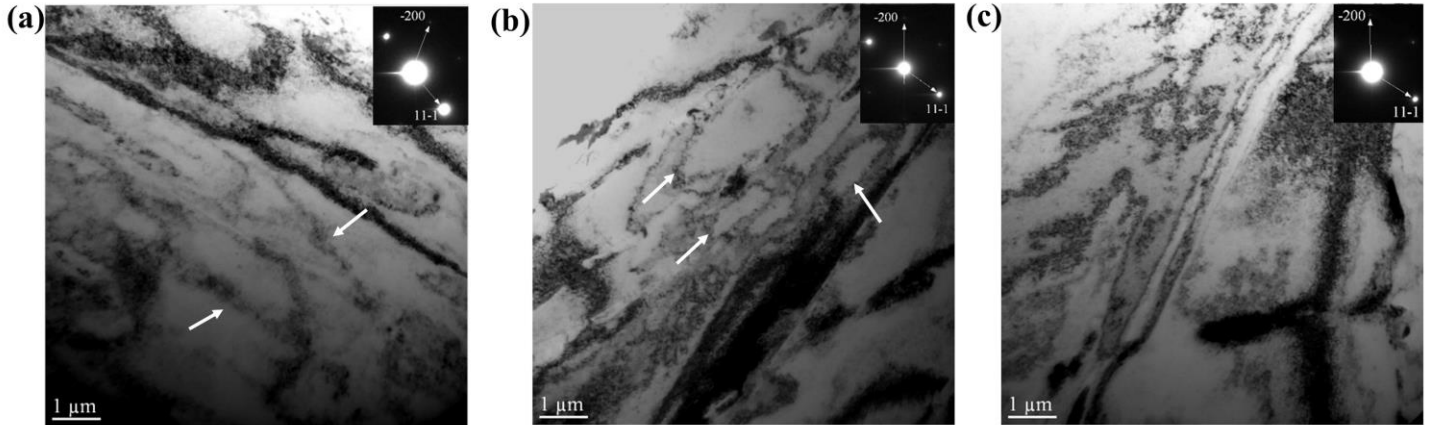


Figure. 4.10 The dislocation cell substructures for (a) No-NA ; (b) 20NA ; (c) 20NA-PA samples after 5 h aging taken from $\langle 011 \rangle$ zone axis close to (111) planes.

4.4. Discussion

4.4.1. Constitutive modeling for strength and EC

In heat-treated and deformed Al–Mg–Si alloys, several strengthening mechanisms are operative, including precipitate strengthening, solid-solution strengthening, dislocation hardening, and grain-boundary hardening. For the mechanical strength, the HV hardness of conductor materials in a given state can be simulated with the aid of different strengthening mechanisms and the corresponding constitutive equations, assuming that the contributions of the strengthening mechanisms are independent and can be added in a linear manner. It is also assumed that the yield stress is three times the hardness ($\Delta\sigma \approx 3 \times \Delta HV$) [4, 6, 31]. Then, the estimated hardness values can be compared with the experimental values. The total hardness in terms of the hardness values from the various strengthening factors can be expressed as follows:

$$HV_{\text{total}} = HV^{\text{Al}} + \Delta HV^{\text{dislo}} + \Delta HV^{\text{prec}} + \Delta HV^{\text{gb}} + \Sigma \Delta HV_i^{\text{sol}} \quad (4.2)$$

Where the total hardness (HV_{total}) is estimated by summing the hardness contribution from each component, including the aluminum matrix (HV^{Al}), the dislocation forest via strain hardening in the cold wire drawing (ΔHV^{dislo}), the flow stress contributions due to precipitates (ΔHV^{prec}), grain boundaries (ΔHV^{gb}) and the solid solution solutes ($\Sigma \Delta HV_i^{sol}$) [4, 6]. The yield stress of the aluminum matrix is in the order of 35 MPa for an annealed pure 1100-O aluminum alloy [32], and hence, HV^{Al} is considered of the order of 12 HV.

The dislocation number density in an annealed aluminum material (solution treated) is only 10^{10} - 10^{11} m^{-2} , which has a negligible contribution to the hardness [23]. Therefore, the multiplication of dislocations mainly occurred during cold wire drawing. As mentioned previously, the increased hardness values due to cold drawing were directly obtained from the hardness difference before and after wire drawing (28.6, 29.3, and 16.7 HV for the No-NA, 20NA, and 20NA-PA samples, respectively). The Bailey–Hirsch equation (Eq. 4.3) can provide an approximation of the dislocation number density for the samples [8].

$$\Delta \sigma^{dislo} = \alpha \cdot M \cdot G \cdot b \cdot \rho^{1/2} \quad (4.3)$$

Where ρ is the number density of dislocations, α is a geometric constant close to 0.3 [8], M as Taylor factor is taken as 2 to convert shear stresses into normal stresses [33], G is the shear modulus (26.9 GPa) of FCC Al, and b is the burger vector (0.29 nm) of the dislocations in FCC Al₍₁₁₀₎ [8]. Therefore, calculations showed that the dislocation number densities were 3.4×10^{14} , 3.5×10^{14} , and 1.1×10^{14} m^{-2} for No-NA, 20NA, and 20NA-PA samples, respectively, which was well agreed with the data in Ref. [8, 34].

Eq. 4.4 (Orowan equation) and Eq. 4.6 can be used to estimate precipitate strengthening for non-shearable β' [8] and shearable β'' precipitates [23], respectively.

$$\Delta \sigma_{Or}^{prec} = \frac{2M\beta Gb}{L} \quad (4.4)$$

Where β is a constant close to 0.28. M , G and b were described above. L is defined as the mean particle spacing, expressed in the following equation [8].

$$L = \frac{1}{(N)^{1/3}} \quad (4.5)$$

Where N is defined as precipitate number density.

$$\Delta\sigma_{\text{shear}}^{\text{prec}} = \frac{M}{b^2\sqrt{\beta G}} \sqrt{N \cdot r} \cdot F^{3/2} \quad (4.6)$$

$$F = 2\beta G b^2 \cdot \left(\frac{r}{r_c}\right) \quad (4.7)$$

Where r is the precipitates size (radius), r_c is the transition radius from precipitate shearing to bypassing (5nm), and F is the mean obstacle strength provided by precipitates [23].

Because the precipitates were principally non-shearable β' precipitates in the No-NA and 20NA samples, the Orowan equation (Eq. 4.4) was used to estimate the amount of precipitation hardening [8]. Accordingly, the average inter-precipitate spacings for the No-NA and 20NA samples aged for 5 h were 57.3 and 50.5 nm, and their hardness contributions were 50.8 and 57.7 HV, respectively.

For the 20NA-PA sample, the average precipitate length was in the range of the shearable β'' precipitates. However, using Eq. 4.6 for shearable precipitates, the precipitate strength was calculated to be ~15 MPa (5 HV), which far underestimated the experimental data. It appears that the nature of precipitates in the 20NA-PA sample might not be well identified based on their length because the precipitates were primarily fragmented during wire drawing and then coarsened in the over-aged state. It is worth mentioning that the hardness and precipitate number density decreased by ~10 HV and ~6000 μm^{-3} , respectively, during post-aging. It is reasonable to assume that non-shearable precipitates were the dominant feature, and the Orowan equation (Eq. 4.4) could still be used to estimate the amount of precipitate strengthening. The mean inter-

precipitate spacing and the precipitate hardness contribution were 37.6 nm and 77.4 HV, respectively, which agree well with the experimental data.

The classical Hall–Petch relationship can be employed to estimate the hardness contribution from grain-boundary strengthening [8].

$$\Delta HV^{gb} = k_{HP}d^{-1/2} \quad (4.8)$$

Where HV_{gb} is the hardness induced by grain boundaries, and k_{HP} is a scaling constant taken as $35 \text{ HV } \mu\text{m}^{1/2}$ for Al–Mg–Si aluminum alloys [8]. A comparison of the grain structure of the samples revealed that the grain sizes of all samples were similar (on the order of $130 \mu\text{m}$) because they underwent the same fabrication process. The coarse grain structure indicates that grain-boundary strengthening is only a small portion ($\sim 3 \text{ HV}$) of the total strength and can be assumed to be similar in all samples.

Solid-solution strengthening is generally ascribed to the interaction of dislocations with their surrounding solute atoms, resulting in pinning of the dislocations. Therefore, further external stress is required to unpin the dislocations from the solute regions [23]. Eq. 4.9 provides the approximate strength contribution from solid-solution strengthening [8].

$$\Delta\sigma_i = k_i C_i^{2/3} \quad (4.9)$$

where $\Delta\sigma_i$ is the strengthening contribution of solute i , k_i is a scaling factor for solute i ($k_{Mg} \approx 29$ and $k_{Si} \approx 66.3 \text{ MPa (wt.\%)}^{-2/3}$), and C_i is the concentration of solute i (in wt.%) [4, 8]. It was found that almost half of the Si remained in the matrix in 6xxx series alloys with a Mg/Si ratio of one when aged at $175 \text{ }^\circ\text{C}$ for 8 h, while most of the Mg was used in the precipitates [35]. Therefore, half of the Si solutes (0.31 wt.% Si) and 0.1 wt.% Mg could remain in the matrix of the present alloy, yielding a hardness contribution of $\sim 12 \text{ HV}$ from solid-solution strengthening.

Fig. 4.11 shows a comparison of the experimentally measured hardness with the predicted hardness for various sample conditions. Although the predicted hardness was slightly lower than the measured values, the general trend of the hardness difference under various conditions agreed well with the measured total hardness. In our previous work, we found that an increase in the Si concentration (from 0.4 to 0.89 wt.%) in Al–Mg–Si alloys led to a strength increase of ~90 MPa (~25 HV) in the as-quench state before wire drawing, while the constitutive equation predicted only ~25 MPa (~8 HV) [36]. Therefore, the amount of solid-solution strengthening might be underestimated in the strength model owing to the difficulties in experimentally determining the amounts of various solutes in the matrix. As mentioned previously, the hardness contributions of solid-solution strengthening and grain-boundary strengthening were assumed to be constant in all samples, yielding a total hardness contribution of 15 HV. Accordingly, strain and precipitation hardening are the most important contributors, exhibiting the largest contributions to the overall hardness of the samples. As presented in Fig. 4.11, both the No-NA and 20NA samples aged for 5 h exhibited almost the same amount of strain hardening. Therefore, the higher hardness of the 20NA sample relative to that of the No-NA sample after 5 h of aging is attributed to the larger contribution of precipitation strengthening in the 20NA sample.

Although the 20NA-PA sample aged for 5 h had the highest hardness above 52.5% IACS, its strain-hardening contribution was the lowest among all samples. It can be deduced from the results in Fig. 4.11 that the higher strength of the 20NA-PA sample after 5 h of aging can be ascribed to the appreciably large contribution of precipitation hardening, which was approximately 50% and 35% higher than those of the No-NA and 20NA samples, respectively.

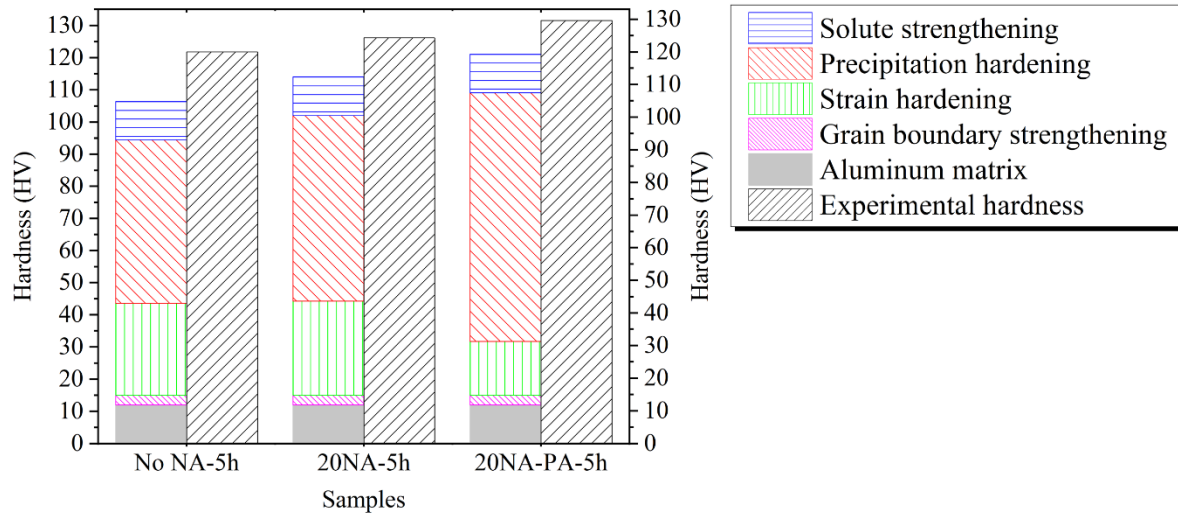


Figure. 4.11 The comparison between predicted and experimentally measured hardness for the No-NA, 20NA, and 20NA-PA samples aged at 180 °C for 5 h.

It is well known that most strengthening mechanisms cause distortions in the lattice structure of metals. It is assumed that each strengthening mechanism induces an additional increase in the electrical resistivity of metals. To understand the effect of the microstructural features on the EC of the conductor materials, Matthiessen's rule is adopted here (Eqs. 4.10 and 4.11), in which the total electrical resistivity is the sum of the contributions from various microstructural features (defects) that cause electron scattering [8, 37]. Then, the total EC (% IACS) can be obtained from the electrical resistivity (Eq. 4.12) [38].

$$\rho_{\text{total}} = \rho^{\text{Al pure}} + \rho^{\text{DISLO}} + \rho^{\text{GB}} + \rho^{\text{PREC}} + \rho^{\text{SOL}} \quad (4.10)$$

$$\rho_{\text{(total)}} = \rho^{\text{Al pure}} + L^{\text{dislo}} \Delta \rho^{\text{dislo}} + S^{\text{GB}} \Delta \rho^{\text{GB}} + \frac{\Delta \rho^{\text{Prec}}}{(L^{\text{prec}})^{1/2}} + \sum C_i^{\text{sol}} \Delta \rho_i^{\text{sol}} \quad (4.11)$$

$$\text{EC (\%IACS)} = \frac{172.4}{\rho_{\text{(total)}} (\mu\Omega\text{cm})} \quad (4.12)$$

Where $\rho_{\text{(total)}}$ is the total electrical resistivity; (ρ^{Alpure}) is the electrical resistivity of AA1350–O alloy, which is $2.79 \times 10^{-6} \text{ } \Omega \text{ cm}$ at room temperature (equivalent to 61.8 %IACS) [39]; and $\Delta\rho^{\text{dislo}}$, $\Delta\rho^{\text{GB}}$, $\Delta\rho_i^{\text{sol}}$, and $\Delta\rho^{\text{prec}}$ are the resistivity constants describing for the dislocations, grain boundaries, solute elements, and precipitates in the aluminum matrix, respectively. $\Delta\rho^{\text{dislo}}$ and $\Delta\rho^{\text{GB}}$ were defined to be $2.7 \times 10^{-25} \text{ } \Omega\text{m}^3$ and $2.6 \times 10^{-16} \text{ } \Omega\text{m}^2$, respectively [8]. L^{dislo} and S^{GB} are described as the dislocation density and the portion of grain boundaries, in which S^{GB} is defined as $6/d$ (d is the average grain size).

As mentioned above, all samples exhibited a similar grain structure and size, giving rise to the same electrical resistivity ($1 \times 10^{-9} \text{ } \Omega \text{ cm}$), which was much smaller than the resistivity of pure Al (ρ^{Alpure}). By referring to the dislocation number density in all samples, the portions of electrical resistivity from dislocations for the No-NA, 20NA, and 20NA-PA samples were estimated to be 9.2×10^{-9} , 9.5×10^{-9} , and $3 \times 10^{-9} \text{ } \Omega \text{ cm}$, respectively. Although the 20NA and No-NA samples exhibited a larger portion of the electrical resistivity due to the denser dislocation forest relative to that of the 20NA-PA sample, the dislocation contribution to resistivity for all samples was considerably smaller than ρ^{Alpure} . Considering the total electrical resistivity of all materials to be $3.25 \times 10^{-6} \text{ } \Omega \text{ cm}$ (equivalent to 53% IACS), it can be deduced that the electrical resistivity of the samples was less dependent on dislocations and grain boundaries. Raeisinia et al. [7] developed an equation showing the contribution of precipitates to resistivity based on the precipitate spacing, as shown in Eq. 4.11. For the contribution induced by precipitates, $\Delta\rho^{\text{Prec}}$ was reported to be $12 \text{ } \Omega \text{ (nm)}^{3/2}$, and L^{Prec} (in nm) represent the precipitate spacing in Eq. 4.11 [7]. Therefore, the precipitate resistivity contributions of the No-NA, 20NA, and 20NA-PA samples (aged for 5 h) were calculated to be 0.158×10^{-6} , 0.169×10^{-6} , and $0.195 \times 10^{-6} \text{ } \Omega \text{ cm}$, respectively, which were 5%-6% of the total electrical resistivity.

In Eq. 4.11, C_i^{sol} is the concentration of solute (i) in the matrix, and $\Delta\rho^{\text{Mg sol}}$ and $\Delta\rho^{\text{Si sol}}$ are defined as 0.445×10^{-6} and $0.496 \times 10^{-6} \Omega \text{ cm (at.\%)}^{-1}$, respectively [8]. The electrical resistivity from Si and Mg solute atoms was estimated to be $0.193 \times 10^{-6} \Omega \text{ cm}$, assuming the Mg and Si solute levels mentioned above. From the above analysis and calculation, it is evident that the solutes in the matrix were the primary cause of the increase in electrical resistivity, and the precipitates with a given particle spacing were the second cause of electron scattering in the studied samples.

Using Eqs. 4.10 and 4.11, the total electrical resistivities of the No-NA, 20NA, and 20NA-PA samples were calculated to be 3.151, 3.162, and 3.182 $\mu\Omega \text{ cm}$, respectively. Accordingly, the EC levels calculated using Eq. 4.12 for the No-NA, 20NA, and 20NA-PA samples were 54.7%, 54.5%, and 54.2% IACS, respectively, which are only slightly overestimated compared to the measured EC (~53% IACS) for all samples. The calculated hardness values (Eq. 4.2) and EC values (Eqs. 4.10 and 4.12) are concurrently plotted in Fig. 4.12 and compared to the experimentally measured values for all samples. The comparison with the experimental data suggests that model captures the general trend of the hardness/EC relationship fairly well. The slightly lower hardness and higher EC values estimated by the model relative to the measured values might stem from some errors in the solute-strengthening contribution because it had a reverse effect on strength relative to EC.

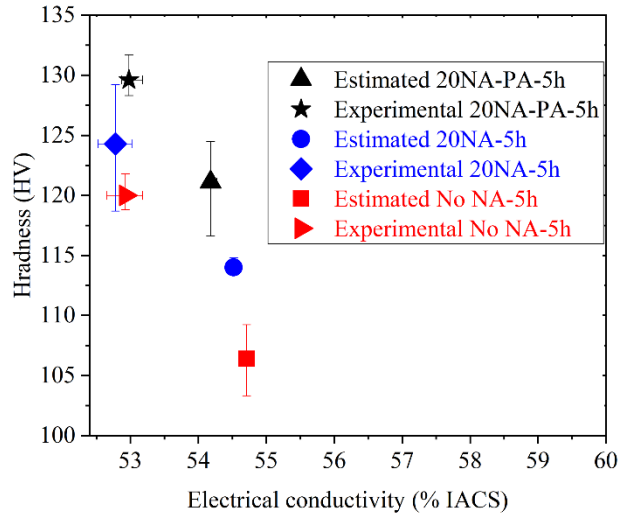


Figure. 4.12 Plot of the hardness vs the electrical conductivity (% IACS) for estimated and measured values for all drawn samples.

4.4.2. Microstructural evolution

The DSC results (Fig. 4.5a and 4.5b) demonstrate that natural aging was detrimental to the subsequent precipitation (peak I) before wire drawing. However, it was found that severe plastic deformation via cold wire drawing following natural aging could counteract the detrimental effect of natural aging, as confirmed by DSC analysis, TEM, and hardness measurements. For a better understanding, Fig. 4.13 presents a scheme of the microstructural evolution that occurred under various conditions.

The microstructure of the No-NA sample in the as-drawn condition comprised a forest of dislocations with no precipitates (Fig. 4.13a). During artificial aging, the majority of precipitation occurred along dislocations as nucleation sites [19, 20, 40]. At the peak aging condition, the preferential distribution of precipitates along dislocations was the dominant feature of the microstructure (Fig. 4.7a). After 5 h of aging, these precipitates became coarser and more homogenous (Fig. 4.7b and Fig. 4.13b). Two types of precipitates formed in the No-NA sample:

lath-like and needle-shaped precipitates, whose crystal structures had a similar hexagonal substructure as the β' precipitates [19].

In the naturally aged 20NA samples, a large number of GP zones formed, primarily over the matrix (Fig. 4.13c). In the subsequent cold wire drawing, GP zones were successively sheared owing to the dislocation movement during wire drawing. It resulted in increasing interfacial energy and reducing thermal stability of the sheared GP zones. Finally, GP zones dissolved into the matrix. It appears that they were dissolved as solute-enriched aggregates (Fig. 4.13d) rather than homogeneously dispersed solutes, as confirmed in Ref. [13, 25, 41] using high-resolution TEM. This can be attributed to the low diffusion rate of solutes in cold wire drawing. It should be noted that the dissolution of GP zones might not be due to an increase in temperature [28] because the wire was kept cool with water during drawing. It is worth mentioning that the number of dislocations that formed during drawing was relatively similar in the drawn 20NA and No-NA samples. During the subsequent aging, in addition to the precipitates that formed along the dislocations, it is possible that other phases precipitated from the enriched aggregates [25], which could be recognized by their smaller cross section but are not yet identified in the present work (Fig. 4.7c and Fig. 4.13e). The higher and wider I_d peak in the as-drawn NA sample compared to the drawn No-NA sample could be attributed to the formation of these fine precipitates along with lath-like and needle-shaped phases (Fig. 4.7c and Fig. 4.13e). Therefore, a higher number density of precipitates was obtained in the drawn 20NA sample compared to that in the drawn No-NA sample. Large lath-like precipitates along dislocations could be connected with dislocation-assisted diffusion mechanism (Fig. 4.7a). Thus, rich dislocations generated during drawing could accelerate the diffusion of solute atoms during subsequent aging. Therefore, it resulted in larger lath-like precipitates [40, 42]. On the other hand, the solute-

enriched aggregates in less dense dislocation zones could evolve into fine precipitates during aging. These precipitates would be less dependent on the dislocation-induced mechanism, and they might grow slowly during aging, leading to finer precipitates.

In the 20NA-PA condition, precipitation initially occurred in the non-deformed condition after 5 h of aging, and the microstructure consisted of predominant β'' precipitates along with a few β' phases. The precipitates were evenly distributed throughout the matrix (Fig. 4.13f). Then, wire drawing was applied to the aged samples (20NA-PA). The number of formed dislocations in the drawn 20NA-PA sample was less than that in the drawn 20NA and No-NA samples. This suggests that the strain hardening due to the solute atoms in the drawn 20NA and No-NA samples was more effective relative to the strengthening of β'' precipitates in the drawn 20NA-PA sample [25]. In the 20NA-PA sample, it was observed that precipitates were also sheared and fragmented by moving dislocations (by comparing the precipitate sizes before and after drawing, Fig. 4.8), leading to smaller precipitates (Fig. 4.13g). The number density of precipitates decreased slightly after wire drawing, which might be attributed to the re-dissolution of some β'' precipitates, as reported in Ref. [25]. After aging at 180 °C for 5 h, the precipitates were coarsened in the drawn 20NA-PA sample (Fig. 4.13h). It is plausible that some β'' precipitates were transformed into β' phases during the post-aging treatment.

It should be noted that precipitates in the drawn 20NA-PA sample after 5h of aging are uniformly distributed. This is because most precipitates were uniformly formed from the clusters and GP zones before wire drawing, and dislocations barely acted as a nucleation site. However, in drawn No-NA and 20NA samples, precipitation mainly took place after wire drawing, meaning that dislocation-induced precipitation could be dominant. Lath-like precipitates were

mainly formed along dislocations at the peak-aged condition in drawn No-NA and 20NA samples.

As discussed in Section 4.3.1, the naturally aged samples showed a better combination of strength and EC relative to those of the No-NA samples. It should be noted that the strain hardening in the No-NA and 20NA samples was more or less similar, as discussed in Section 4.3.4. Strain hardening and precipitate strengthening were the main strengthening mechanisms in the studied samples. Thus, the higher strength of the NA samples is attributed to their higher precipitate strengthening. In addition to lath-like and needle-shaped precipitates, the 20NA sample microstructure was also characterized by the presence of smaller precipitates (Fig. 4.13e and Fig. 4.7c), which were most probably enriched aggregates.

As mentioned in Section 4.3.1, the 20NA-PA sample showed the highest strength above the minimum required EC among all the samples. However, the 20NA-PA sample had the lowest strain hardening contribution compared to that of the No-NA and 20NA samples, which is schematically shown in Fig. 4.13g by the lowest number density of dislocations. In contrast, the 20NA-PA sample possessed the greatest precipitate number density among all samples, overcoming the inferiority of strain hardening in the 20NA-PA sample.

Solute and precipitates were the major sources of electrical resistivity, controlling the total resistivity. As pointed out in Section 4.4.1, the solutes caused more electrical resistivity compared to precipitates in the studied samples. Given that 20NA-PA had the highest precipitate number density, it could be deduced that the electrical resistivity of the precipitates in the 20NA-PA sample was comparatively higher than that in the No-NA and 20NA samples. Considering that the EC (53% IACS) was similar for all samples ($3.25 \times 10^{-6} \Omega \text{ cm}$), it can be concluded that

the solute resistivity in the 20NA-PA sample might be relatively lower than that in the No-NA and 20NA samples.

4.5. Conclusions

1. Natural aging combined with wire drawing (in the 10NA and 20NA samples) was found to be favorable. The natural aging samples exhibited a higher strength at a given electrical conductivity upon subsequent aging treatment compared to the samples without natural aging.
2. Natural aging combined with pre-aging (in the 20NA-PA sample) showed the highest strength above 52.5% IACS among all samples, which was higher than the strength values defined in the EN 50183 standard.
3. The higher strength of the 20NA-PA sample aged for 5 h mainly stemmed from the larger portion of precipitate strengthening. However, its dislocation hardening was smaller than that of the no natural aging and 20NA samples because solutes exhibited a stronger effect on strain hardening than shearable precipitates.
4. The pre-aging treatment prior to wire drawing maximized precipitate strengthening.
5. The relationship between strength and electrical conductivity was analyzed in detail using strengthening models and Matthiessen's rule. This approach is believed to provide a reasonable explanation for the mechanical and electrical properties of drawn Al–Mg–Si conductor alloys.

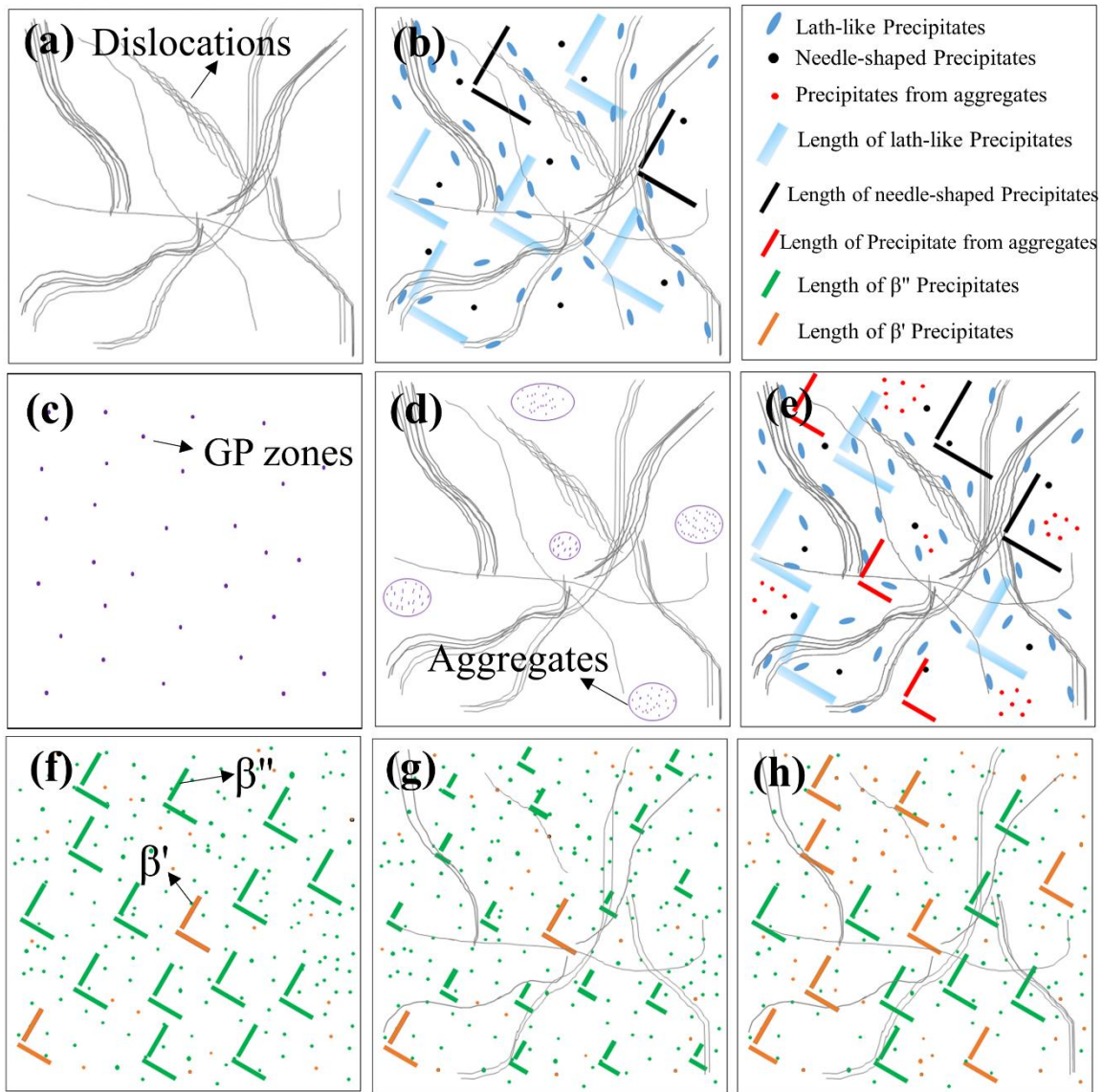


Figure 4.13 Sketches to illustrate the microstructural evolution in the samples with NA and PA compared to the conventional sample (No-NA) before and after aging treatment: (a) as-drawn No-NA sample, (b) drawn No-NA sample after 5 h aging, (c) GP zones in 20NA sample prior to wire drawing, (d) as-drawn 20NA sample, (e) drawn 20NA sample aged for 5 h, (f) 20NA-PA before wire drawing, (g) as-drawn 20NA-PA sample, and (h) drawn 20NA-PA aged for 5 h.

Acknowledgements

The authors would like to acknowledge the financial support of the Natural Sciences and Engineering Research Council of Canada (NSERC) under the Grant No. CRDPJ 514651-17 and Rio Tinto Aluminum through the Research Chair in the Metallurgy of Aluminum Transformation at the University of Quebec in Chicoutimi.

Credit authorship contribution statement

Siamak Nikzad Khangholi: Methodology, Investigation, Formal analysis, Writing – original draft. Mousa Javidani: Conceptualization, Methodology, Writing – review & editing. Alexandre Maltais: Conceptualization, Validation, Writing – review & editing. X.-Grant Chen: Conceptualization, Validation, Writing – review & editing, Project administration.

4.6. References

- [1] S. Karabay, Influence of AlB_2 compound on elimination of incoherent precipitation in artificial aging of wires drawn from redraw rod extruded from billets cast of alloy AA-6101 by vertical direct chill casting, *Materials & Design* 29(7) (2008) 1364-1375.
- [2] S. Karabay, Modification of AA-6201 alloy for manufacturing of high conductivity and extra high conductivity wires with property of high tensile stress after artificial aging heat treatment for all-aluminium alloy conductors, *Materials & Design* 27(10) (2006) 821-832.
- [3] E. Cervantes, M. Guerrero, J. A. Ramos, S.A. Montes, Influence of Natural Aging and Cold Deformation on the Mechanical and Electrical Properties of 6201-T81 Aluminum Alloy Wires, *Mater. Res. Soc. Symp. Proc* (2010) 03-09.
- [4] Y. Han, D. Shao, B.A. Chen, Z. Peng, Z.X. Zhu, Q. Zhang, X. Chen, G. Liu, X.M. Li, Effect of Mg/Si ratio on the microstructure and hardness–conductivity relationship of ultrafine-grained Al–Mg–Si alloys, *Journal of Materials Science* 52(8) (2016) 4445-4459.
- [5] R.Z. Valiev, M.Y. Murashkin, I. Sabirov, A nanostructural design to produce high-strength Al alloys with enhanced electrical conductivity, *Scripta Mater.* 76 (2014) 13-16.
- [6] S. Jiang, R. Wang, Grain size-dependent Mg/Si ratio effect on the microstructure and mechanical/electrical properties of Al-Mg-Si-Sc alloys, *Journal of Materials Science & Technology* 35(7) (2019) 1354-1363.
- [7] B. Raelisnia, W.J. Poole, D.J. Lloyd, Examination of precipitation in the aluminum alloy AA6111 using electrical resistivity measurements, *Materials Science and Engineering: A* 420(1) (2006) 245-249.
- [8] X. Sauvage, E.V. Bobruk, M.Y. Murashkin, Y. Nasedkina, N.A. Enikeev, R.Z. Valiev, Optimization of electrical conductivity and strength combination by structure design at the nanoscale in Al–Mg–Si alloys, *Acta Mater.* 98 (2015) 355-366.
- [9] R.M. Mustafa, Production of aluminium-silicon-magnesium wrought alloy rod with application in the manufacture of extra-high conductivity AAAC for overhead electrical transmission lines, *Light Metals* (2008) 613-617.
- [10] ASM Handbook: Casting. Volume 15, ASM International (1998) 689-690.
- [11] D. Lindholm, S. Akhtar, D. Mortensen, Numerical Simulation of Wire Rod Casting of AA1370 and AA6101 Alloys, *Light Metals* (2020) 1032-1038.
- [12] P.A. Rometsch, Z. Xu, H. Zhong, H. Yang, L. Ju, X.H. Wu, Strength and Electrical Conductivity Relationships in Al-Mg-Si and Al-Sc Alloys, *Mater. Sci. Forum* 794-796 (2014) 827-832.
- [13] G. Lin, Z. Zhang, H. Wang, K. Zhou, Y. Wei, Enhanced strength and electrical conductivity of Al–Mg–Si alloy by thermo-mechanical treatment, *Materials Science and Engineering: A* 650 (2016) 210-217.
- [14] C.H. Liu, J. Chen, Y.X. Lai, D.H. Zhu, Y. Gu, J.H. Chen, Enhancing electrical conductivity and strength in Al alloys by modification of conventional thermo-mechanical process, *Materials & Design* 87 (2015) 1-5.

- [15] C. Bunte, M. Glassel, C. Medina, D. Zalcman, Proposed Solution for Random Characteristics of Aluminium Alloy Wire Rods Due to the Natural Aging, *Procedia Materials Science* 9 (2015) 97-104.
- [16] L.M. Cheng, W.J. Poole, J.D. Embury, D.J. Lloyd, The influence of precipitation on the work-hardening behavior of the aluminum alloys AA6111 and AA7030, *Metallurgical and Materials Transactions A* 34(11) (2003) 2473-2481.
- [17] J. Buha, R.N. Lumley, A.G. Crosky, K. Hono, Secondary precipitation in an Al–Mg–Si–Cu alloy, *Acta Mater.* 55(9) (2007) 3015-3024.
- [18] G.A. Edwards, K. Stiller, G.L. Dunlop, M.J. Couper, The precipitation sequence in Al–Mg–Si alloys, *Acta Mater.* 46(11) (1998) 3893-3904.
- [19] K. Teichmann, C.D. Marioara, S.J. Andersen, K.O. Pedersen, S. Gulbrandsen-Dahl, M. Kolar, R. Holmestad, K. Marthinsen, HRTEM study of the effect of deformation on the early precipitation behaviour in an AA6060 Al–Mg–Si alloy, *Philos. Mag.* 91(28) (2011) 3744-3754.
- [20] R.S. Yassar, D.P. Field, H. Weiland, The effect of predeformation on the β'' and β' precipitates and the role of Q' phase in an Al–Mg–Si alloy; AA6022, *Scripta Mater.* 53(3) (2005) 299-303.
- [21] H. Nemour, D. Mourad Ibrahim, A. Triki, The effect of heavy cold plastic deformation on the non-isothermal kinetics and the precipitation sequence of metastable phases in an Al–Mg–Si alloy, *J. Therm. Anal. Calorim.* 123(1) (2015) 19-26.
- [22] G. Höhne, W. Hemminger, H.J. Flammersheim, *Differential Scanning Calorimetry: An Introduction for Practitioners*, Springer-Verlag (1996).
- [23] O. Engler, C.D. Marioara, Y. Aruga, M. Kozuka, O.R. Myhr, Effect of natural ageing or pre-ageing on the evolution of precipitate structure and strength during age hardening of Al–Mg–Si alloy AA 6016, *Materials Science and Engineering: A* 759 (2019) 520-529.
- [24] E. Standard, EN 50183. Conductors for overhead lines, aluminium magnesium silicon alloy wires (2000) 1-7.
- [25] H. Li, M. Qingzhong, Z. Wang, F. Miao, B. Fang, R. Song, Z. Zheng, Simultaneously enhancing the tensile properties and intergranular corrosion resistance of Al–Mg–Si–Cu alloys by a thermo-mechanical treatment, *Materials Science and Engineering: A* 617 (2014) 165-174.
- [26] H.W.Z. S.J. Andersen, J. Jansen, C. Træholt, U. Tundal, O. Reiso, The crystal structure of the β'' phase in Al–Mg–Si alloys, *Acta Mater* (1998) 3283-3298.
- [27] M.Y.M. X. Sauvage, R. Z. Valiev, Atomic scale investigation of dynamic precipitation and grain boundary segregation in a 6061 aluminium alloy nanostructured by ECAP, *Kovove Mater.* 49,(2011) 11-15.
- [28] M. Murayama, Z. Horita, K. Hono, Microstructure of two-phase Al–1.7 at% Cu alloy deformed by equal-channel angular pressing, *Acta Mater.* 49(1) (2001) 21-29.
- [29] T. Ye, L. Li, P. Guo, G. Xiao, Z. Chen, Effect of aging treatment on the microstructure and flow behavior of 6063 aluminum alloy compressed over a wide range of strain rate, *International Journal of Impact Engineering* 90 (2016) 72-80.

- [30] W.-S. Lee, J.-C. Shyu, S.-T. Chiou, Effect of strain rate on impact response and dislocation substructure of 6061-T6 aluminum alloy, *Scripta Mater.* 42(1) (1999) 51-56.
- [31] L.F. Deschamps A, Brechet Y, Influence of predeformation on ageing in an Al-Zn-Mg alloy-I. Microstructure evolution and mechanical properties, *Acta Mater* (1998) 281-292.
- [32] J.G. Kaufman, *Introduction to Aluminum Alloys and Tempers*, ASM International (2000).
- [33] Y.J. Li, A.M.F. Muggerud, A. Olsen, T. Furu, Precipitation of partially coherent α -Al(Mn,Fe)Si dispersoids and their strengthening effect in AA 3003 alloy, *Acta Mater.* 60(3) (2012) 1004-1014.
- [34] J. Zhang, M. Ma, F. Shen, D. Yi, B. Wang, Influence of deformation and annealing on electrical conductivity, mechanical properties and texture of Al-Mg-Si alloy cables, *Materials Science and Engineering: A* 710 (2018) 27-37.
- [35] K. Li, A. Béché, M. Song, G. Sha, X. Lu, K. Zhang, Y. Du, S.P. Ringer, D. Schryvers, Atomistic structure of Cu-containing β "precipitates in an Al-Mg-Si-Cu alloy, *Scripta Mater.* 75 (2014) 86-89.
- [36] S. Nikzad Khangholi, M. Javidani, A. Maltais, X.G. Chen, Optimization of mechanical properties and electrical conductivity in Al-Mg-Si 6201 alloys with different Mg/Si ratios, *J. Mater. Res.* 35(20) (2020) 2765-2776.
- [37] J.P. Hou, Q. Wang, Z.J. Zhang, Y.Z. Tian, X.M. Wu, H.J. Yang, X.W. Li, Z.F. Zhang, Nano-scale precipitates: The key to high strength and high conductivity in Al alloy wire, *Materials & Design* 132 (2017) 148-157.
- [38] W. Wen, Y. Zhao, J.G. Morris, The effect of Mg precipitation on the mechanical properties of 5xxx aluminum alloys, *Materials Science and Engineering: A* 392(1-2) (2005) 136-144.
- [39] ASTM, *Annual Book of ASTM Standards, Electrical Conductors* (2002).
- [40] M. Kolar, K.O. Pedersen, S. Gulbrandsen-Dahl, K. Marthinsen, Combined effect of deformation and artificial aging on mechanical properties of Al-Mg-Si Alloy, *Transactions of Nonferrous Metals Society of China* 22(8) (2012) 1824-1830.
- [41] Z. Wang, H. Li, F. Miao, B. Fang, R. Song, Z. Zheng, Improving the strength and ductility of Al-Mg-Si-Cu alloys by a novel thermo-mechanical treatment, *Materials Science and Engineering: A* 607 (2014) 313-317.
- [42] R. Lu, S. Zheng, J. Teng, J. Hu, D. Fu, J. Chen, G. Zhao, F. Jiang, H. Zhang, Microstructure, mechanical properties and deformation characteristics of Al-Mg-Si alloys processed by a continuous expansion extrusion approach, *Journal of Materials Science & Technology* 80 (2021) 150-162.

Chapter 5 : Effect of Ag and Cu additions on the strength and electrical conductivity in Al-Mg-Si alloys using conventional and modified thermomechanical treatment (Article4)

Siamak Nikzad Khangholi ^a, Mousa Javidani ^a, Alexandre Maltais ^b, X.-Grant Chen ^a

^a Department of Applied Science, University of Québec at Chicoutimi, Saguenay,
Québec, G7H 2B1, Canada

^b Arvida Research and Development Center, Rio Tinto Aluminum, Saguenay,
Quebec, G7S 4K8, Canada

This article is submitted to Journal of alloys and compounds

Abstract

The effect of adding Ag and Cu on the strength and electrical conductivity of Al-Mg-Si conductor alloys was investigated using conventional and modified thermomechanical treatments. In the conventional thermomechanical treatment, the addition of Ag and Cu moderately increased the strength above the minimum required electrical conductivity (52.5% IACS) compared to that of the base alloy. However, the modification of the thermomechanical treatment could maximize the efficiency of Ag and Cu addition at strengths above 52.5% IACS. All alloys under the modified thermomechanical treatment showed a superior strength and electrical conductivity compared to their counterparts under the conventional thermomechanical treatment, resulting in a wider window in the high end of strength and electrical conductivity. In addition, the modified thermomechanical treatment led to a shorter post-aging time to reach the minimum required EC, compared to the conventional thermomechanical treatment. The precipitate characteristics under both thermomechanical treatment conditions were analyzed and quantified using differential scanning calorimetry and transmission electron microscopy.

Strength and electrical resistivity models were then applied to understand the multiple contributions of the main strengthening mechanisms and microstructure features to the mechanical strength and electrical conductivity.

Keywords: Al-Mg-Si conductor alloys, electrical conductivity, mechanical properties, Ag/Cu additions, modified thermomechanical treatment

5.1. Introduction

Aluminum conductor alloys are increasingly used in high voltage electrical transmission lines. In general, the electrical conductivity of aluminum is approximately 62% that of copper. However, considering the equal current-carrying capacity, the weight of the aluminum conductor is only half that of the copper conductor due to its lower density [1]. Among aluminum conductors, heat-treatable Al-Mg-Si conductor alloys are widely used conductive materials in power transmission due to their excellent combination of high strength with the desired electrical properties in recent decades, strengthened by nanosized precipitates via aging treatment [2-4].

The conventional thermomechanical treatment (CTMT) in the fabrication of Al-Mg-Si conductors is comprised of quenching from the solutionization temperature and cold wire drawing followed by post-aging treatment [1]. However, some studies were allocated to the modified thermomechanical treatment (MTMT) to attain a better optimization of the strength and EC. It might consist of quenching from the solutionization temperature, pre-aging, wire drawing, and post-aging treatment [2-4]. Lin et al. [2] suggested an MTMT, in which pre-aging for 2 h at 180 °C led to a better trade-off between strength (301 MPa) and EC (58.9% IACS) for the Al-0.62Mg-0.57Si alloy. Liu et al. [3] also proposed pre-aging at 180 °C for 5 h for an Al-1Mg-0.5Si-0.8Cu alloy, resulting in a higher strength and EC compared to CTMT. In our previous

research, it was shown that a pre-aging treatment (5 h at 180 °C) in MTMT for the Al-0.62Mg-0.62Si alloy could remarkably increase the precipitate number density at the expense of the dislocation number density. Therefore, the superior precipitate strengthening overcame the inferior strain hardening, leading to a better compromise between strength (~369 MPa) and EC (~53% IACS) [5].

The impacts of principal alloying elements (Mg and Si) and additional alloying elements (Fe, La, Ce, and Sr) on the strength and electrical conductivity in 6xxx series conductors have been the subject of multiple studies [6-13]. Regarding the principal alloying elements (Mg and Si), an alloy with an Mg/Si of ~ 1 showed a better combination of strength and EC, provided the strength is taken as a main concern [6-8]. Excessive magnesium (Mg/Si > 2) exhibited an almost insignificant improvement in the strength and EC [6], while excessive silicon (Mg/Si < 1) gave a limited window of strength and EC (above the minimum required EC, 52.5% IACS for AA6201 conductor alloys [14]) with a lower strength compared to the alloy with an Mg/Si of ~ 1 [7, 8]. The addition of Fe, La, and Ce to Al-Mg-Si conductor alloys led to an improvement in the electrical conductivity at the expense of strength [9-11]. In contrast, the Sr addition could result in a better optimization of strength and EC in Al-0.6Mg-0.6Si conductor alloys due to a higher precipitation degree and intermetallic modification [12, 13].

Copper and silver additions have recently been taken into account in Al-Mg-Si alloys to promote the age hardening response [15]. It was reported that Mg-Cu and Mg-Ag clusters could form in the early stage of aging due to the stronger interaction energy between Cu/Ag atoms and Mg atoms. Therefore, these clusters with Mg-Si clusters could act as nucleation sites for the subsequent precipitates and enhance precipitation strengthening [15-17]. It was determined that Cu-/Ag-added alloys exhibited a higher strength than the base alloy due to the higher precipitate

number density [16, 17]. The Cu addition could lead to the formation of L and Q' precipitates, which coexist with β'' phases in the peak-aged condition [17, 18]. It was reported that Cu additions (0.2-1.1) wt.% to 6xxx series aluminum alloys showed a significant superiority in terms of strength [15-20]. Duan et al. [20] reported that Cu-added alloys (0.3-0.9 wt.% Cu) showed an inferior EC in the early aging time (up to 8 h), and then they showed a similar EC relative to the base alloy using two-step aging (preaging at 90 °C + postaging 180 °C). However, the maximum allowable copper content is 0.1 wt.% for AA6201 and AA6101 conductor alloys according to the ASTM B398 and B317 standards [21, 22]. Therefore, the effect of the Cu addition beyond the specified value in the standards on EC could be controversial. On the other hand, the Ag addition (~ 0.5 wt.%) also led to a higher peak hardness than that of the base alloy in the Al-Mg-Si alloys [15-17], while the effect of Ag solutes on electrical resistivity was almost negligible [23]. To the best of the authors' knowledge, the effect of individual and combined Ag and Cu additions on the comprehensive properties in terms of strength and conductivity in Al-Mg-Si conductor alloys has been scarcely reported.

The present paper aims to investigate the efficiency of individual and combined additions of Ag and Cu in terms of the strength and electrical conductivity using conventional and modified thermomechanical treatments. The microstructural features were analyzed using transmission electron microscopy (TEM) and differential scanning calorimetry (DSC). To better understand the relationship between the strengthening factors and electrical resistivity sources, strength and electrical resistivity models were adopted in this study.

5.2. Experimental procedure

The chemical compositions of the experimental alloys are listed in Table 5.1, in which the Mg, Si, and Fe levels were kept almost constant and the concentrations of Ag and Cu were varied. The alloy designation is based on the Ag and Cu levels. After preparing the molten metal in an electrical resistance furnace, the melt was poured into a permanent steel mold with dimensions of 30 mm × 40 mm × 80 mm. Afterward, the as-cast alloys were homogenized at 560 °C for 6 h and then hot-rolled at 350-480 °C with an area reduction of 70%. Square bar samples (7 mm × 7 mm) were prepared from hot-rolled sheets for cold wire drawing. Two types of thermomechanical treatments were applied to the samples: conventional thermomechanical treatments (CTMTs) and modified thermomechanical treatments (MTMTs). A schematic representation of the thermomechanical treatments is shown in Fig. 5.1. CTMT was comprised of a solution heat treatment at 540 °C for 2 h, followed by quenching, cold wire drawing (70%), and post-aging at 180 °C for 0-24 h (Fig. 5.1a). MTMT was composed of a solution heat treatment at 540 °C for 2 h, quenching, pre-aging (6 h at 180 °C), cold wire drawing (70%), and post-aging at 180 °C for 0-24 h (Fig. 5.1b). In MTMT, pre-aging at 180 °C for 6 h is similar to the peak aging of the T6 temper. The final diameter of the wire was 4.37 mm after wire drawing.

Vickers microhardness was measured with a load of 25 g and a dwell time of 20 s. Eight indentations were made to obtain the average hardness values. The tensile strength was measured using an Instron tensile machine for wire samples with a 250 mm gauge length at strain rate of $1.6 \times 10^{-3} \text{ s}^{-1}$ according to the EN 50183 standard. At least three tensile specimens were tested to confirm the experimental results for each condition. The Sigmascope method with a frequency of 480 kHz was adopted to measure the electrical conductivity of the wires according to ASTM E1004.

Differential scanning calorimetry (DSC) was conducted at least three times for each condition under an argon atmosphere using a METTLER-TOLEDO system between 25 °C and 550 °C with a heating rate of 10 °C/min. At least, three samples were used for each condition, and the weight of samples was around 15-30 mg. The DSC results were corrected with the base line. The examination of the microstructures (precipitates and dislocations) was performed using TEM operated at 200 kV. Disc-shaped specimens for TEM were mechanically ground and then electropolished using a twin jet unit with an electrolyte of 1/3 HNO₃ in methanol at temperatures between -20 °C and -30 °C. The convergent beam electron diffraction (CBED) technique was then used to measure the specimen thickness. TEM micrographs were obtained with the Al matrix in the <001> zone axis for precipitates and in the <011> zone axis for dislocation observation. The methods for the quantitative analysis of the precipitates are described in detail in Ref. [5, 24].

Table 5.1 Chemical compositions of all studied alloys (wt.%).

Alloys	Mg	Si	Ag	Cu	Fe	Ti	B	Al
Base	0.67	0.43	Trace	Tr.	0.09	0.016	0.002	Bal.
Ag3	0.66	0.39	0.30	Tr.	0.11	0.012	0.002	Bal.
Ag5	0.63	0.38	0.53	Tr.	0.11	0.012	0.003	Bal.
Cu1	0.67	0.38	Trace	0.15	0.11	0.012	0.002	Bal.
Cu3	0.63	0.37	Trace	0.28	0.10	0.012	0.003	Bal.
Cu4	0.69	0.53	Trace	0.42	0.09	0.014	0.002	Bal.
Ag3Cu1	0.66	0.38	0.32	0.15	0.16	0.015	0.003	Bal.

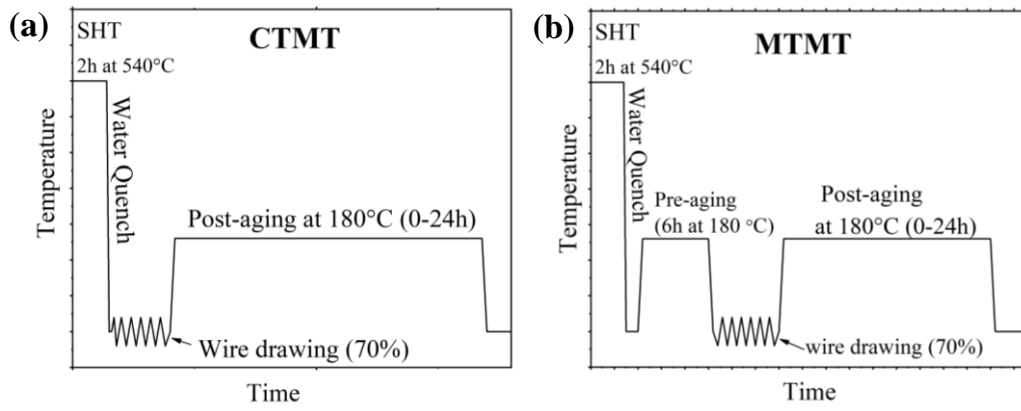


Figure 5.1 Schematic sketch of the time/temperature curves for (a) conventional thermomechanical treatment (CTMT) (b) modified thermomechanical treatment (MTMT)- Arrows show where wire drawing was carried out. The curves are just for a schematic purpose, and it does not show the time frame.

5.3. Results

5.3.1. Mechanical and electrical properties

The hardness curves during isothermal artificial aging at 180 °C immediately after wire drawing are presented in Fig. 5.2a and 5.2c for CTMT and MTMT, respectively. As shown in Fig. 5.2a, all the curves displayed similar profiles for the alloys under CTMT: the hardness sharply increased and reached its maximum after 1 h or 2 h of aging, followed by an overaging stage with a decreasing hardness. The peak hardness of the CTMT base alloy was 108 HV. The Cu4 alloy exhibited the highest peak hardness (143 HV) among all alloys in CTMT (Fig. 5.2a). Apart from the Cu4 alloy, the Ag-/Cu-containing alloys exhibited a slightly higher peak hardness (3-7 HV) compared to the base alloy in CTMT: Ag3 (108 HV), Ag5 (112 HV), Cu1 (115 HV), Cu3 (115 HV), and Ag3Cu1 (115 HV). During the overaging stage, the hardness difference between the Ag-/Cu-added alloys and the base alloy became larger. In contrast to CTMT, the hardness of the MTMT alloys continuously decreased over the aging time because these alloys

already reached the peak hardness before wire drawing (Fig. 5.2c). In general, the hardness values of the alloys processed with MTMT are higher than those of their counterparts processed with CTMT. Similar to CTMT, the Cu4 alloy showed the highest hardness values (156 HV) among all alloys using MTMT. The MTMT Ag3 (118-90 HV) and the MTMT base (117-88 HV) alloys showed a similar hardness behavior within 24 h (Fig. 5.2c). Concerning the other alloys, the aging hardening and the maximum hardness for the alloys containing Ag and Cu were greatly enhanced compared to the base alloy (5-20 HV): Ag5 (130 HV), Cu1 (122 HV), Cu3 (131 HV), and Ag3Cu1 (136 HV).

Fig. 5.2b and 5.2d show the evolution of the electrical conductivity (EC) of the experimental alloys as a function of the aging times under CTMT and MTMT, respectively. All the investigated alloys showed a rapid increase in EC in the early stage of aging (up to 4 h), followed by a slight increase in EC (4-24 h) in both CTMT and MTMT (Fig. 5.2b and 5.2d). The order of the highest achievable EC of the CTMT alloys is the base (55.4% IACS), Ag3 (54.1% IACS), Ag5 and Cu1 (54% IACS), Cu3 and Ag3Cu1 (52.6% IACS), and Cu4 (49% IACS). Interestingly, the maximum EC of the MTMT alloys is 1-2% IACS higher than their CTMT counterparts: base (56.3% IACS), Ag3 (55.8% IACS), Cu1 (55.5% IACS), Ag5 (54.9% IACS), Cu3 and Ag3Cu1 (53.7% IACS), and Cu4 (50.9% IACS). Based on Fig. 5.2b and 5.2d, the EC levels under MTMT are higher than those under CTMT at a given aging time for all alloys, showing a more solute extraction in MTMT. In general, for both thermomechanical treatments, the higher the Cu content was, the more EC was limited. The adverse effect of Cu addition on EC could be observed from the Cu1, Cu3, and Cu4 alloys in Fig. 5.2b and 5.2d. Accordingly, the EC of the Cu4 alloy did not even reach the minimum required EC (52.5% IACS) in either CTMT or MTMT (Fig. 5.2b and 5.2d). This is most likely attributed to the high level of Cu solutes

remaining in the matrix. The Cu3 and Ag3Cu1 alloys have the second lowest EC values in either CTMT or MTMT. It appears that Ag addition (in Ag3 and Ag5) showed a lower detrimental effect on EC than Cu addition.

By comparing the Cu4 alloy with other alloys (Fig. 5.2), it can be seen that there was a large hardness gap with the other alloys, either in CTMT or in MTMT. However, Cu4 alloys had the lowest EC for both thermomechanical treatments. In addition, the Ag3 and Cu1 alloys showed a similar combination of hardness and EC as the base alloy. This suggests that the effect of low Ag and Cu contents was not distinguishable on the hardness above 52.5% IACS. Therefore, the Ag5, Cu3, and Ag3Cu1 alloys were chosen for a further investigation because they showed a superior strength above 52.5% IACS compared to the base alloy.

Fig. 5.3 shows the microhardness versus EC above 52% IACS. Although 52.5% IACS is the minimum required EC, 52% IACS was chosen as the starting point for the x-axis to have more span on EC for all alloys. The results indicate that the Cu-/Ag-added alloys (Ag5, Cu3, and Ag3Cu1) slightly outperformed (~5 HV) the base alloy under CTMT. Based on Fig. 5.3, the strength/EC windows of the CTMT Cu3 and Ag3Cu1 alloys are quite limited due to the lower EC (52.6% IACS), while the Ag5 alloy exhibits a broader window in the high end of strength and EC due to the relatively higher EC (54% IACS). The base, Ag5, Cu3, and Ag3Cu1 alloys in CTMT reached a minimum EC (52.5% IACS) after 2, 4, and 24 h of aging, respectively. However, the efficiency of the Ag and Cu additions was distinctly enhanced using MTMT, meaning that the hardness/EC plots of Cu-/Ag-added alloys lay considerably above that of the base alloy (~13 HV). Using MTMT, the Ag5, Cu3, and Ag3Cu1 alloys showed a similar hardness superiority above 52.5% IACS with overall higher values compared with the base alloy. The base, Ag5, Cu3, and Ag3Cu1 alloys in MTMT exceeded 52.5% IACS after 0.5, 2, 5, and 7 h

of aging, respectively. On the other hand, the hardness/EC of all the MTMT alloys is superior to that of their CTMT counterparts, which is attributed to enhanced precipitation hardening [5]. In MTMT, the Cu3 and Ag3Cu1 alloys also had a narrower window of strength/EC relative to the Ag5 alloy, but they all showed a higher strength/EC compared to their counterparts in CTMT.

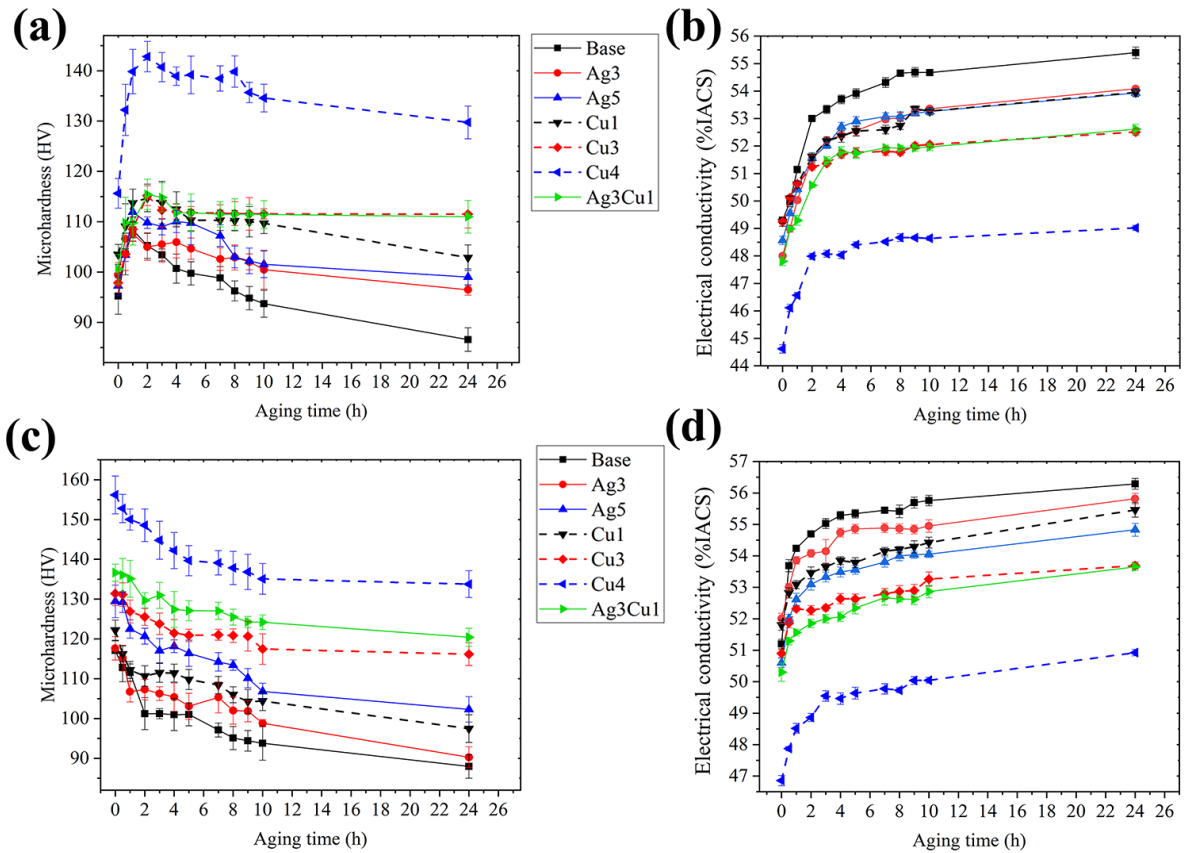


Figure 5.2 Evolution of (a) HV hardness and (b) electrical conductivity (EC) as a function of the aging time using conventional thermomechanical treatment (CTMT); (c) HV hardness and (d) electrical conductivity (EC) as a function of the aging time using modified thermomechanical treatment (MTMT)

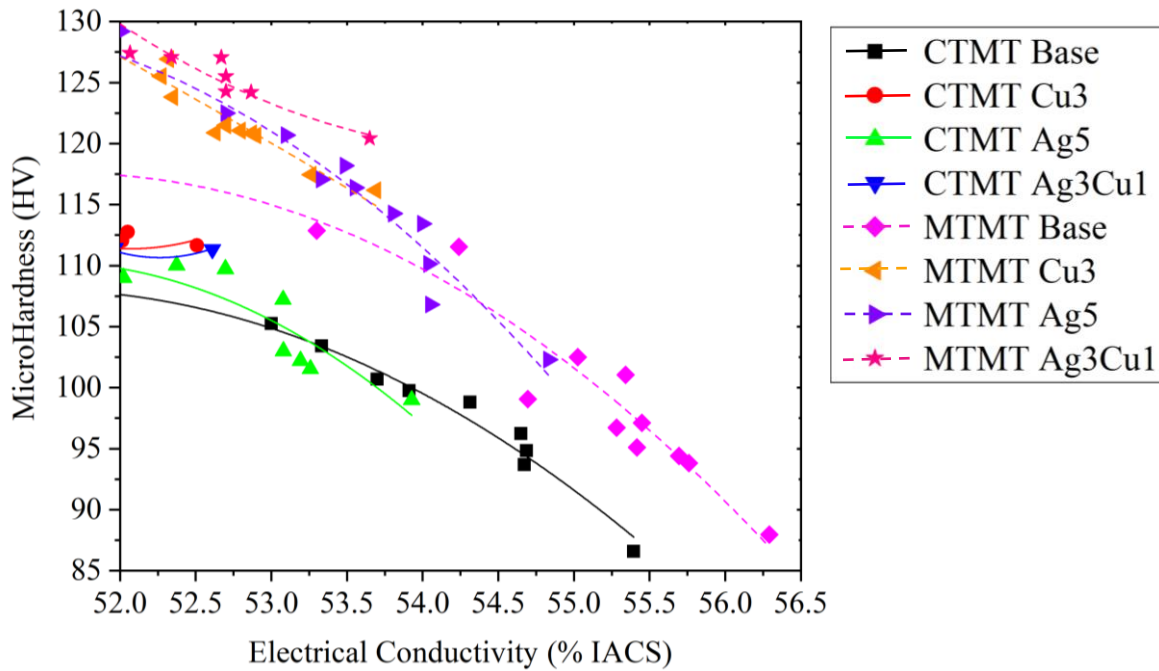


Figure 5.3 HV hardness as a function of EC above 52 %IACS for all alloys using conventional and modified thermomechanical treatment

Fig. 5.4a shows the maximum strength values of the base, Ag5, Cu3, and Ag3Cu1 alloys under CTMT and MTMT above 52.5% IACS. Using CTMT, the ultimate tensile strengths were slightly increased (~10-20 MPa) with Ag/Cu additions in the Ag5, Cu3, and Ag3Cu1 alloys above 52.5% IACS compared to the base alloy (Fig. 5.4a). However, MTMT led to considerably higher strength levels (~30-35 MPa) with Cu/Ag additions in the Ag5, Cu3, and Ag3Cu1 alloys relative to the base alloy, which is consistent with the hardness results. It is worth mentioning that the MTMT Ag5, MTMT Cu3, and MTMT Ag3Cu1 alloys exhibited a remarkably higher strength by ~50 MPa (18%) compared to the CTMT base alloy. Fig. 5.4b displays a comparison of the strength/EC of the investigated alloys with values in the EN50183 standard. It is apparent that the MTMT Ag5, MTMT Cu3, and MTMT Ag3Cu1 alloys show remarkably higher strengths than the values in the EN50183 standard above 52.5% IACS. In contrast, Cu-/Ag-added alloys

under CTMT exhibited similar strength/EC levels relative to those in the EN50183 standard. This suggests that MTMT led to maximizing the efficiency of Cu/Ag additions in terms of the strength/EC.

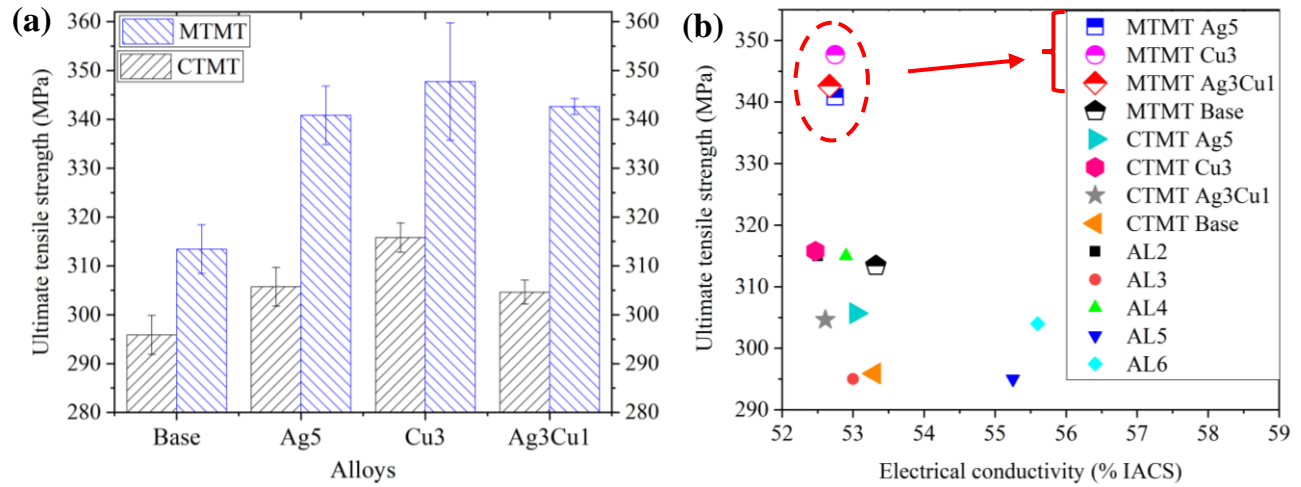


Figure 5.4 (a) the ultimate tensile strengths above 52.5 %IACS for Base-2h, Ag5-4h, Cu3-24h, and Ag3Cu1-24h alloys treated by conventional thermomechanical treatment; and for Base-0.5h, Ag5-2h, Cu3-5h, and Ag3Cu1-7h alloys treated by modified thermomechanical treatment; (b) a comparison between the strengths of the studied alloys and the values defined in EN50183 standard for the wire with a diameter of ~ 4.37mm

5.3.2. DCS results

Thermal events associated with precipitation behavior were studied via a DSC analysis. Fig. 5.5a and 5.5b show the DSC curves for the base, Cu3, Ag5 and Ag3Cu1 alloys in the as-quenched and as-drawn conditions, respectively. The DSC analysis in the as-quenched condition corresponds to the precipitation sequences in the preaging (MTMT), while the results in the as-drawn state uncovered the precipitation events in CTMT. In Fig. 5.5a, exothermic peaks I, II, and III could be correlated with the precipitate formation of β'' , β' , and β , respectively, which is consistent with the DSC results in [5, 25]. A closer look at exothermic peak I revealed that the peak temperatures of the β'' precipitation for the base, Ag5, Cu3, and Ag3Cu1 alloys are 273,

264, 270, and 254 °C, respectively. This implies that the Ag/Cu additions shifted the β'' peak to lower temperatures, indicating an accelerated precipitation rate. The Ag addition resulted in a higher precipitation rate than the Cu addition, as confirmed in [17]. The higher precipitation kinetics in the Ag5 alloys could correspond to a higher diffusion coefficient of Ag in Al relative to all other alloying elements. In addition, Ag has a strong interaction energy with Mg and vacancies, which is favorable for precipitation. Copper also has a strong interaction energy with Mg, but it has a relatively lower diffusion coefficient in aluminum [15]. It was reported that the Cu/Ag addition led to the formation of stable clusters with higher densities and larger sizes in the early stage of aging, evolving into copious subsequent precipitates [15, 16]. Based on Fig. 5.5a, no dissolution troughs were found in the Cu3 and Ag3Cu1 alloys before the β'' precipitation peak, showing more stable β'' precursors (GP zones). Comparing the as-quenched base alloy with the as-quenched Ag5 alloy (Fig. 5.5c), it can be seen that the dissolution trough (IV) in the Ag5 alloy is smaller than that in the base sample, suggesting more stable GP zones in the Ag5 alloy. In addition, the Ag5 alloy exhibited a small precipitation peak (V) at ~217 °C between the dissolution trough (IV) and β'' precipitation peak (I), which could correspond to the formation of the pre- β'' phases. Therefore, it might cause a slightly smaller β'' peak in the Ag5 alloy compared to the base alloy, which might be related to a partial consumption of the precipitation capability in precipitation peak V [17]. It is worth mentioning that precipitation peak II became larger with the addition of Ag and Cu (Fig. 5.5a), which might be ascribed to the formation of Ag-/Cu-containing precipitates. Similar results were acquired in [17, 18].

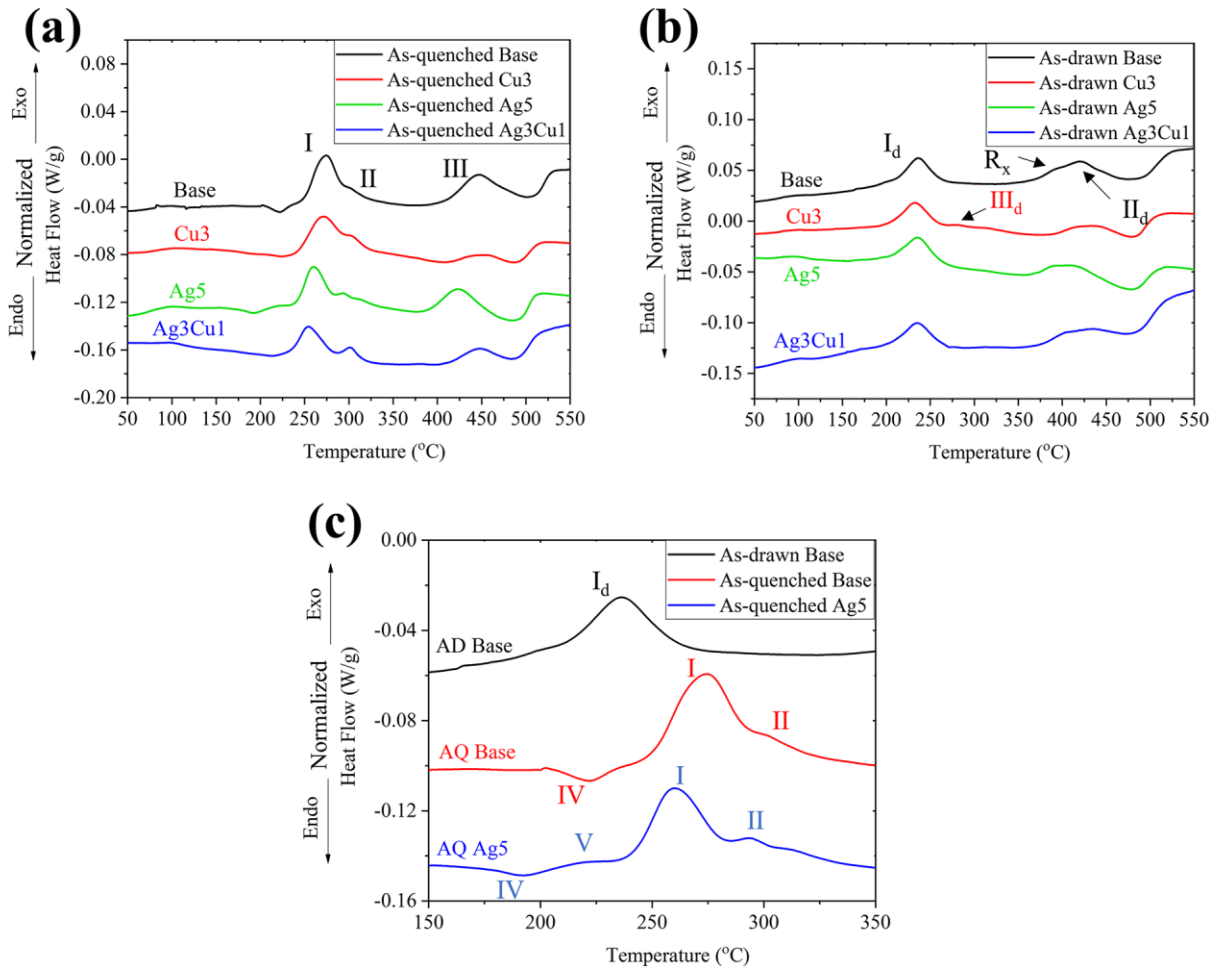


Figure 5.5 DSC curves of the base, Ag5, Cu3, and Ag3Cu1 alloys in (a) as-quenched condition and in (b) as-drawn condition; (c) an enlarged view of peaks I and II for the as-quenched base and Ag5 alloys; and a close view of peak I_d for the as-drawn base alloy; AQ stands for “as-quenched”, and AD stands for “as-drawn”.

Fig. 5.5b displays the DSC curves obtained in the as-drawn condition. As discussed in our previous works [5, 7], heavy cold deformation after solution treatment/quenching might disrupt the precipitation event. Accordingly, β' precipitation was promoted along the dislocations in the drawn samples at the expense of the β'' phases, as reported in Ref. [26-28]. Therefore, peak I_d could correspond to the simultaneous formation of needle-shaped and lath-like precipitates with a disordered β' structure. The exothermic II_d peak was associated with the formation of the β

phase [26-28]. It should be noted that materials with a high area reduction (70%) in wire drawing exhibited exothermic recrystallization peaks (R_x) at approximately 400 °C, which overlapped with the β precipitation peak, which is consistent with Ref. [27]. The peak temperatures of β' precipitation (i.e., peak I_d) for the base, Ag5, Cu3, and Ag3Cu1 alloys are 236, 236, 233, and 235 °C, respectively, showing a lower impact of the Ag/Cu addition on the precipitation rate. In addition, the Ag-/Cu-added alloys showed a slightly larger area of the β' peak (I_d) compared to the base alloy. Fig. 5.5b reveals that no dissolution troughs and no precipitation peaks were observed before peak I_d either in the Ag-/Cu-added alloys or in the base alloy. It can be deduced that the presence of the dense network of dislocations could somehow counteract the effect of Ag and Cu additions either in precipitation kinetics or in precipitation hardening, which is consistent with a lower increased peak hardness (3-7 HV) with Ag and Cu additions in CTMT. It should be noted that the Cu3 alloy revealed an extra peak (III_d) in the as-drawn condition at 260-290 °C (Fig. 5.5b). This might correspond to the formation of the Q' phase, which more easily forms in local defective zones, such as dislocations [26, 29].

A comparison of exothermic peaks I (as-quenched condition) and I_d (as-drawn condition) for the base alloy is shown in Fig. 5.5c. It can be deduced that heavy cold deformation in wire drawing could lead to a smaller first precipitation peak, meaning that wire drawing could weaken the precipitation hardening response. However, precipitation kinetics significantly increased when applying the wire drawing.

5.3.3. Precipitate observation by TEM

Fig. 5.6 shows the TEM bright-field micrographs of the four alloys (the base alloy after 2 h aging, Ag5 alloy after 4 h aging, Cu3 alloy after 24 h aging and Ag3Cu1 alloy after 24 h aging) using CTMT. It should be noted that these sample conditions are all above 52.5% IACS. All the TEM images were acquired in the $\langle 002 \rangle_{Al}$ directions, showing that all precipitates extended along the $\langle 200 \rangle_{Al}$ directions of the matrix. As discussed in our previous work [5], the dominant microstructural feature for CTMT alloys is large lath-like precipitates and needle-like precipitates with a disordered β' structure. In the Cu3 alloy, it is speculated that there is a small number of Q' phases, which corresponds to the extra peak (III_d) in Fig. 5.5b. The precipitate statistics (density, length, and cross section) under these conditions were calculated and are shown in Fig. 5.6e and 5.6f. From Fig. 5.6e, it is fairly evident that the Ag/Cu additions led to an increase in the precipitate number density by $3-4 \times 10^3 \mu\text{m}^{-3}$ in the CTMT Ag5, Cu3, and Ag3Cu1 alloys compared to the CTMT base alloy. The increased precipitate number density could correspond to the formation of Ag-/Cu-containing precipitates [29]. Therefore, the moderately higher strength in the Ag5, Cu3, and Ag3Cu1 alloys compared to the base alloy under CTMT (Figs. 5.3 and 5.4) could be ascribed to the relatively higher number density of precipitates. All alloys showed similar cross-sectional areas of the precipitates, but the average precipitate length in the Ag-/Cu-added alloys was relatively finer than that in the base alloy, which was also reported in Ref. [16]. It should be noted that the identification of the exact nature of the precipitates, which might be influenced by Ag and Cu additions, is beyond the scope of this study.

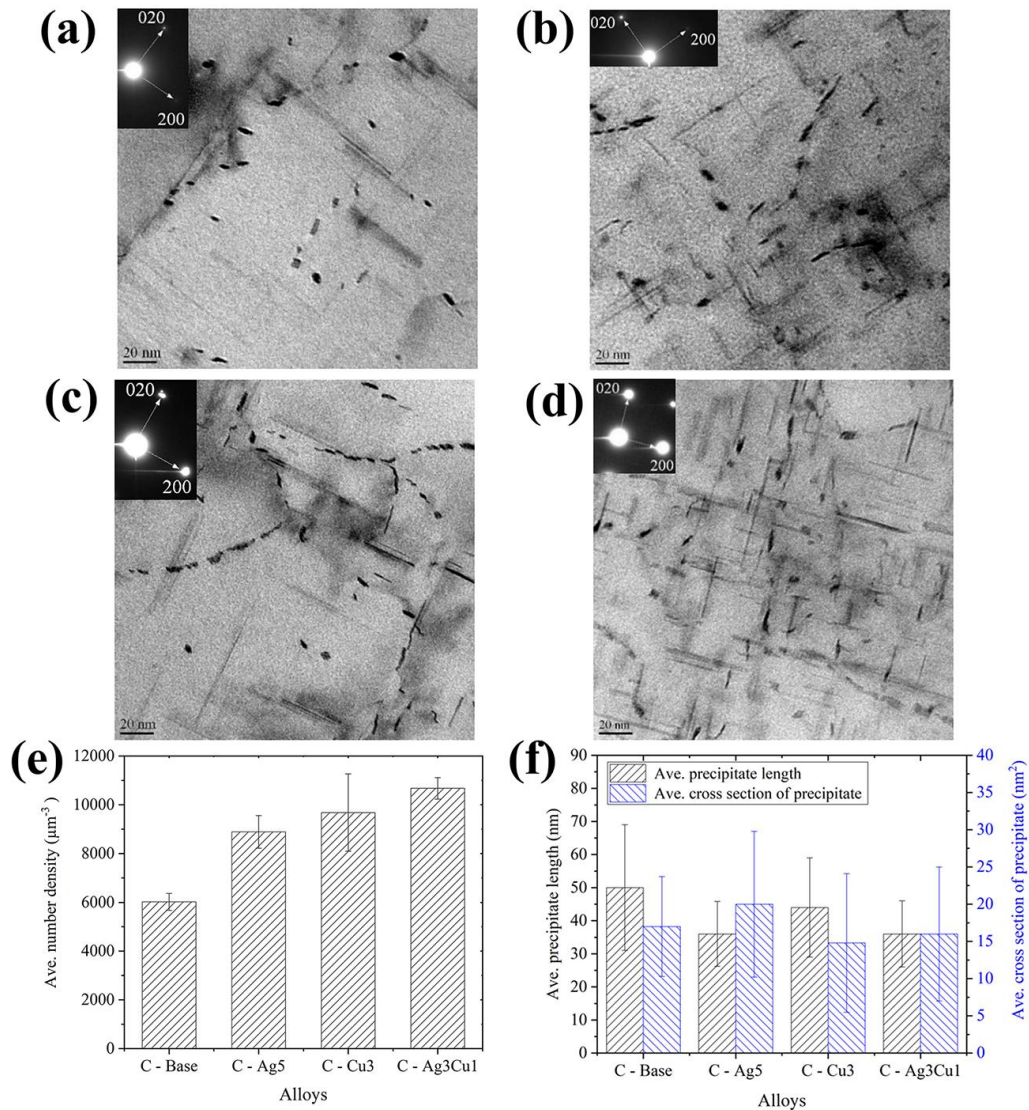


Figure 5.6 Bright-field TEM micrographs of (a) base alloy after 2h aging (b) Ag5 alloy after 4h aging (c) Cu3 alloy after 24h aging (d) Ag3Cu1 alloy after 24h aging using the conventional thermomechanical treatment; (e) the number density of precipitates (f) the average length and the cross section of precipitates. C stands for conventional thermomechanical treatment.

Fig. 5.7 shows TEM micrographs of the base, Ag5, Cu3, and Ag3Cu1 alloys immediately after preaging (6 h at 180 °C). With the addition of Ag and Cu, the average number density of the precipitates increased, and the average length of the precipitates decreased in the Ag5, Cu3, and Ag3Cu1 alloys compared to the base alloy (Fig. 5.7e and 5.7f). Similar results were reported in

Ref. [16], indicating that Ag and Cu promote precipitation. The predominant precipitates in the preaged base alloy were β'' precipitates due to their morphology and sizes [30]. It was reported that the addition of 0.5 wt.% Ag to Al-Mg-Si alloys did not change the type of precipitates, but it did lead to a higher number density of precipitates with a shorter size [17], as shown in Fig. 5.8. Kim et al. [31] reported that β'' precipitates were the predominant precipitates in Al-Mg-Si alloys containing 0.21 wt. %Cu. Therefore, it is deduced that the β'' phases are the dominant precipitates in the Cu-added alloys. Accordingly, the higher hardness values of Ag5 (117 HV), Cu3 (118 HV), and Ag3Cu1 (121 HV) alloys compared to the base alloy (107 HV) after preaging could be supported by their precipitate number density (Fig. 5.7e).

Fig. 5.8 displays the TEM images of the four alloys (base alloy after 0.5 h of aging, Ag5 alloy after 2 h of aging, Cu3 alloy after 5 h of aging, Ag3Cu1 alloy after 7 h of aging) under MTMT. It is obvious that the Ag and Cu additions in the Ag5, Cu3, and Ag3Cu1 alloys resulted in a remarkably increased precipitate number density by $7-9 \times 10^3 \mu\text{m}^{-3}$ compared to the base alloy using MTMT (Fig. 5.8e). All MTMT alloys exhibited a similar precipitate length and cross-sectional area (Fig. 5.8f). Therefore, the maximized efficiency of Ag and Cu under MTMT in terms of the strength above 52.5% IACS could be ascribed to the outstandingly increased number density of precipitates. In MTMT, the preaged precipitates could be changed during further wire drawing and postaging. The TEM results (Fig. 5.8) reveal that the precipitate sizes were more or less similar to the preaged condition for all the MTMT alloys after wire drawing. This result is likely attributed to the shearing effect on the precipitates during cold wire drawing being compensated by the coarsening of the precipitates during postaging in the overaged condition. In general, the MTMT alloys showed a denser distribution of remarkably short precipitates than the CTMT alloys, suggesting promising precipitation strengthening in the

MTMT alloys. Comparing the number density of precipitates under two thermomechanical treatments (Fig. 5.6e in CTMT and Fig. 5.8e in MTMT), it is apparent that the number density of the precipitates in the MTMT alloys is much higher than that in the CTMT alloys. It could also be inferred that wire drawing in CTMT deteriorated the precipitation hardening. This was also confirmed with the DSC results (Fig. 5.5c); the first precipitation peak (I_d) in the as-drawn base sample (CTMT) was smaller than the first precipitation peak (I) in the as-quenched base sample (MTMT).

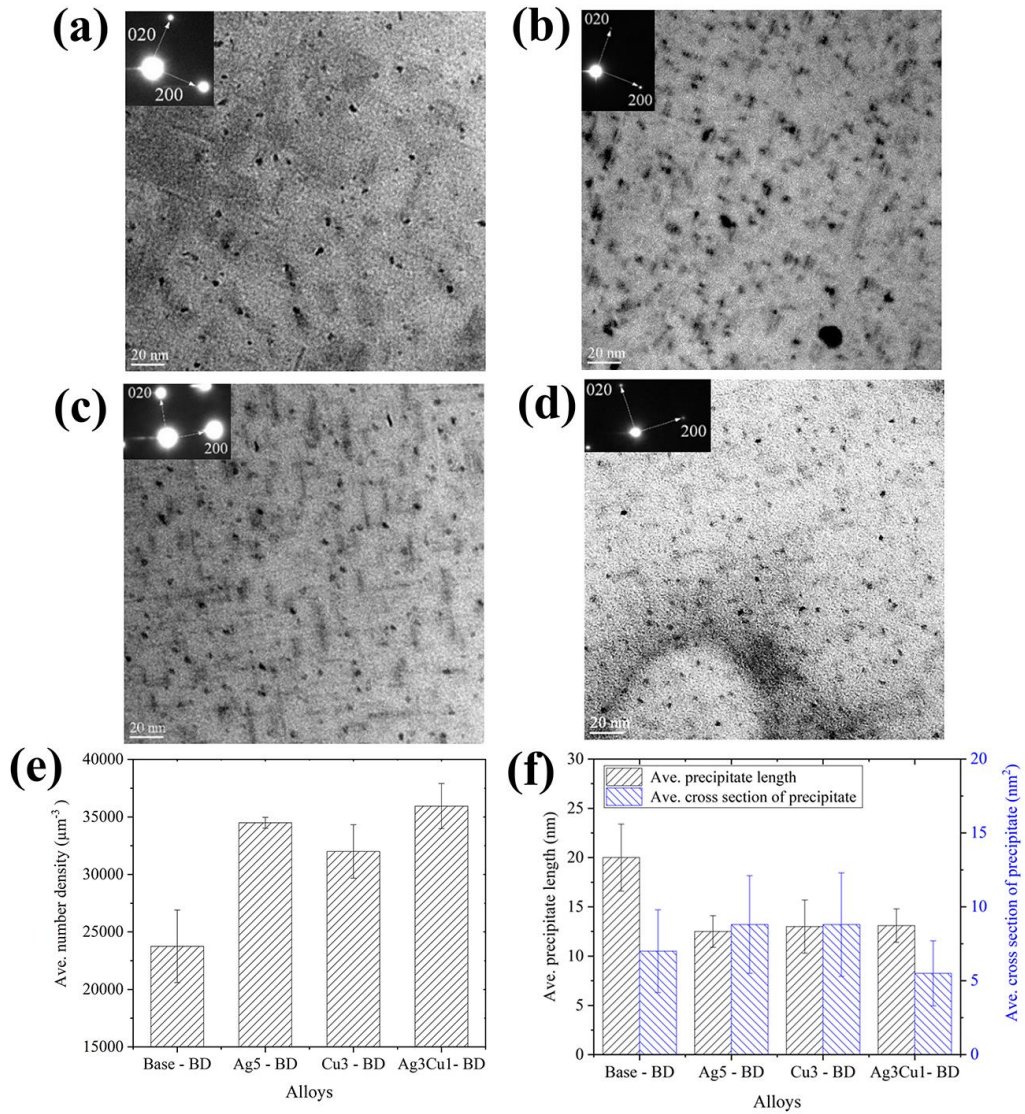


Figure 5.7 Bright-field TEM micrographs of (a) base alloy after 6h aging (b) Ag5 alloy after 6h aging (c) Cu3 alloy after 6h aging (d) Ag3Cu1 alloy after 6h aging without wire drawing (after pre-aging) (e) the number density of precipitates (d) the average length and the cross section of precipitates. BD stands for before drawing.

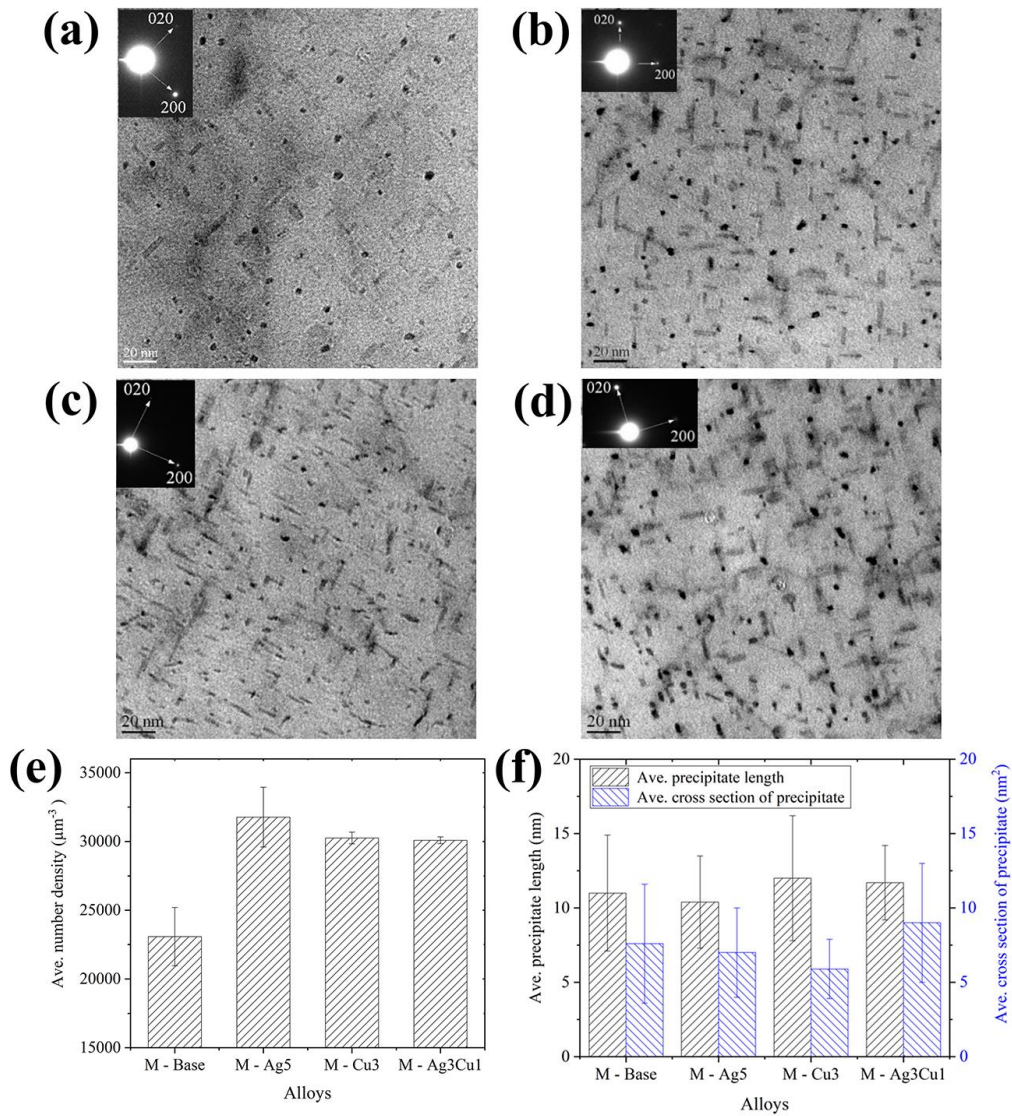


Figure 5.8 Bright-field TEM micrographs of (a) base alloy after 0.5h aging (b) Ag5 alloy after 2h aging (c) Cu3 alloy after 5h aging (d) Ag3Cu1 alloy after 7h aging using the modified thermomechanical treatment; (e) the number density of precipitates (f) the average length and the cross section of precipitates. M stands for modified thermomechanical treatment.

Fig. 5.9 shows the distribution of the partially deviated precipitates in the $\langle 001 \rangle$ zone axis for Ag3Cu1 after 7 h of aging and the Cu3 alloy after 5 h of aging under MTMT. In the enlarged areas (Fig. 5.9a and 5.9b), the deformed bands of the partially disordered precipitates could be observed in both the Cu3-5h and Ag3Cu1-7h alloys. As shown in Fig. 5.6f and 5.8f, shorter

precipitates were acquired in MTMT than in CTMT. This is consistent with our previous findings [5], showing that the pre-existing precipitates formed by pre-aging were fragmented during wire drawing. Fig. 5.9 shows that the precipitates were repeatedly sheared by the moving dislocations due to the high degree of cold deformation, causing the partially deviated precipitate band. The same observations were also observed in the base-0.5h and Ag5-2h alloys.

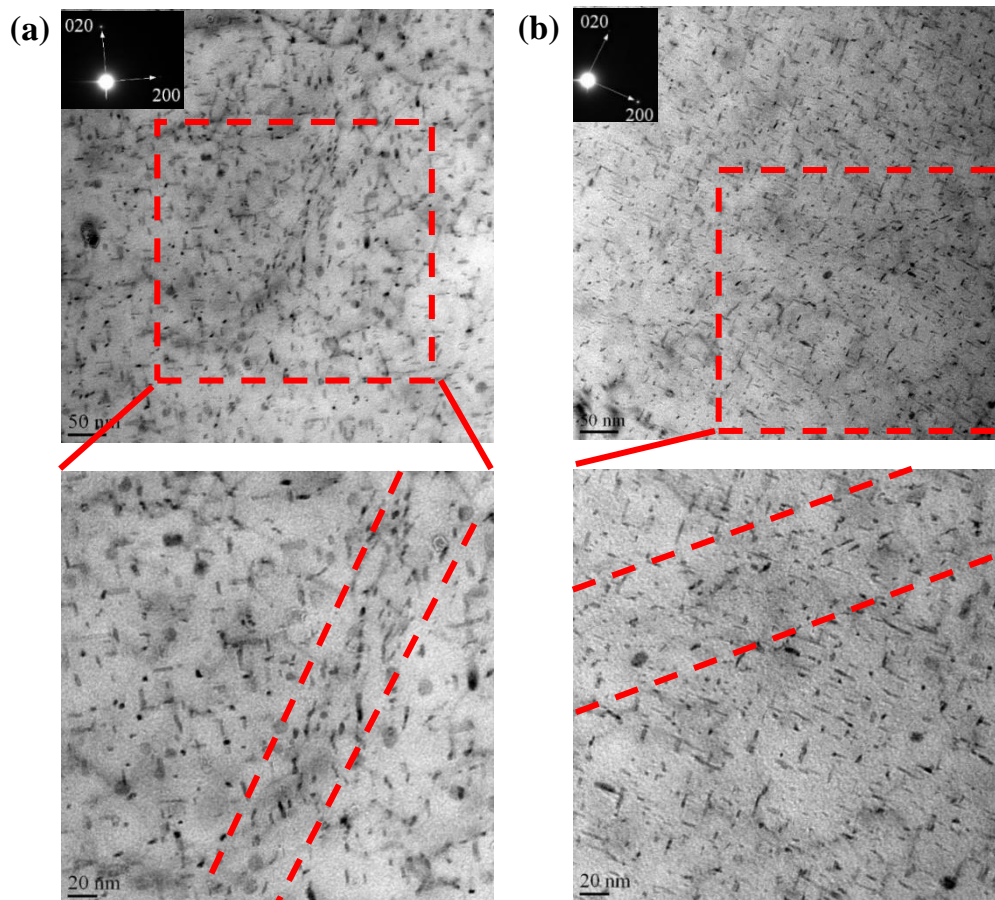


Figure 5.9 TEM micrographs to show the partially deviated precipitates in $\langle 001 \rangle$ zone axis in (a) MTMT Ag3Cu1-7h; (b) MTMT Cu3-5h alloys

5.3.4. Effect of wire drawing on strength and EC

Strain hardening is one of the most promising strengthening mechanisms in Al-Mg-Si cables, affecting the strength and electrical conductivity. Fig. 5.10 shows the increased hardness and the decreased EC due to wire drawing. The increased hardness and the reduced EC could be obtained by measuring the hardness and EC difference immediately before and immediately after wire drawing without postaging treatment. The increased hardness for the CTMT base alloy and the MTMT base, MTMT Cu₃, MTMT Ag₅ and MTMT Ag₃Cu₁ alloys were 26, 10, 13, 13, and 15 HV, respectively. It is assumed that the softening recovery would be low during aging at 180 °C, as aging at 180 °C for up to 34 h showed negligible recovery softening on commercially pure drawn aluminum [7]. It is deduced that the strain hardening contribution of the base alloy under CTMT is almost double relative to the alloys subjected to MTMT, which was also confirmed in our previous work [5] and by Ref. [32, 33]. The dislocation networks of the alloys are shown in Fig. 5.11 to correlate the work hardening contributions with the microstructure. In general, a dislocation structure with a highly complex and entangled network could be created due to the large plastic deformation. As shown in Fig. 5.11, a denser network of dislocations was created in the CTMT base alloy during wire drawing compared to all the MTMT alloys, which is consistent with their strain hardening contributions.

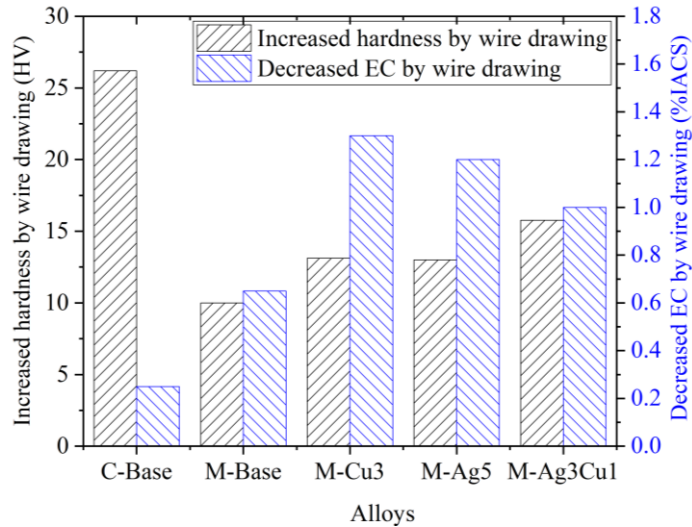


Figure 5.10 The increased hardness and decreased electrical conductivity with wire drawing in the base alloy processed by conventional thermomechanical treatment; and base, Cu3, Ag5, and Ag3Cu1 alloys processed by modified thermomechanical treatment

As displayed in Fig. 5.10, the reduced EC via wire drawing in the CTMT base, MTMT base, MTMT Cu3, MTMT Ag5 and MTMT Ag3Cu1 alloys was 0.25, 0.65, 1.3, 1.2, and 1.0% IACS, respectively. It is evident that the reduced EC in the alloys under MTMT is higher than that in the alloys under CTMT. According to the increased hardness values, the dislocation number densities created in the MTMT alloys are less than those in the CTMT alloy, contradicting the reduced EC values. The possible reason for the higher reduced EC in the MTMT alloys could be related to a slight redissolution of β'' precipitates during cold deformation. In our previous work [5], it was determined that cold wire drawing led to a slight decrease in the precipitate number density, which corresponded to the redissolution of the β'' phases during drawing. The redissolution of the precipitates during cold deformation was also reported in Ref. [33, 34]. In addition, it was reported that the denser dislocation zone showed a reduced precipitate density in regions after cold deformation of pre-aged AA6101[34], which might be an indication of the redissolution of β'' precipitates.

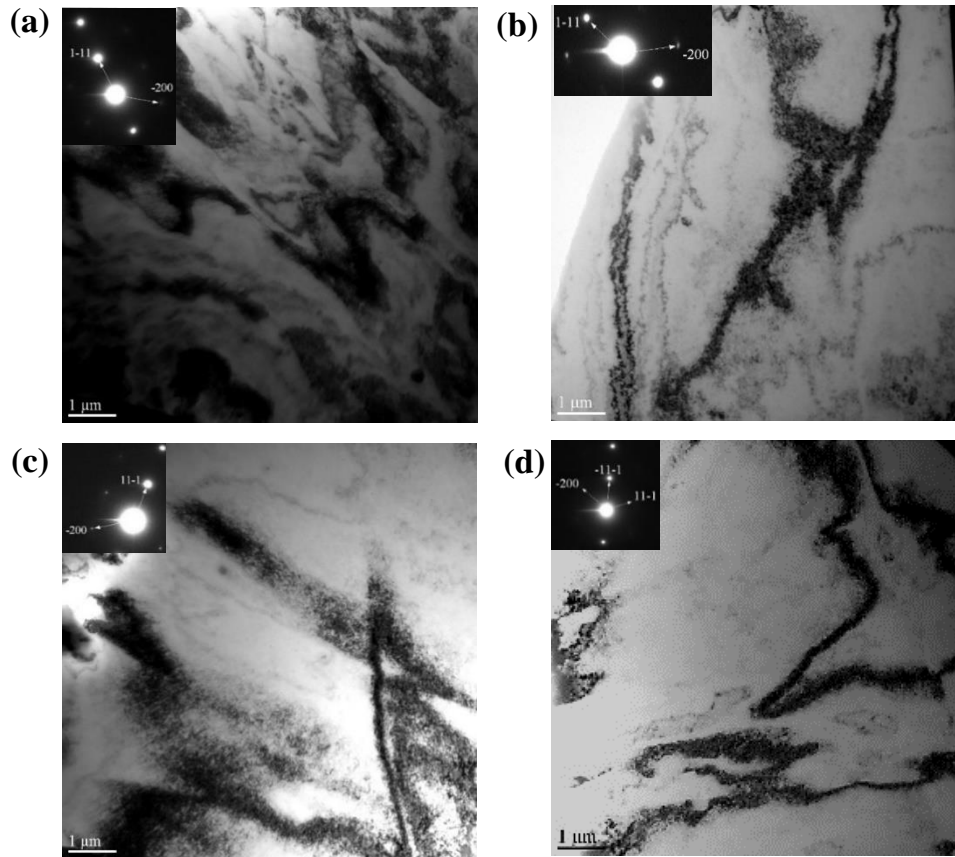


Figure 5.11 The dislocation cell substructures for (a) CTMT base after 2 h; (b) MTMT Cu3 after 5 h aging; (c) MTMT Ag5 after 2 h aging; (d) MTMT Ag3Cu1 after 7 h aging. All were taken from $\langle 011 \rangle$ zone axis close to (111) planes.

5.4. Discussion

5.4.1. Strength and EC model

To elucidate the dominant strengthening mechanism for Al-Mg-Si conductor alloys, a theoretical analysis was quantitatively conducted based on the microstructural features. The principal strengthening factors in Al-Mg-Si alloys come from the grain boundaries, dislocations, precipitates, and solid solution hardening. Given that the yield strength values (in MPa) are roughly equal to three times the hardness (in HV), the contribution of these mechanisms can be linearly added to the total hardness through the following equation [38, 39]:

$$HV_{\text{total}} = HV^{\text{Al}} + \Delta HV^{\text{dislo}} + \Delta HV^{\text{prec}} + \Delta HV^{\text{gb}} + \Sigma \Delta HV_i^{\text{sol}} \quad (5.1)$$

Where HV_{total} is the total hardness, HV^{Al} is the aluminum matrix (12 HV, considering the yield stress of an annealed pure 1100-O aluminum alloy is ~35 MPa for [35]) and ΔHV^{dislo} , ΔHV^{prec} , ΔHV^{gb} and $\Sigma \Delta HV_i^{\text{sol}}$ are the hardness contributions caused by dislocations, precipitates, grain boundaries, and solid solutions, respectively [36-38].

The main strain hardening portion was created during wire drawing. As discussed in Section 3.4, the strain hardening hardness values for the CTMT base alloy were 26 HV, and those for the MTMT base, Cu3 Ag5 and Ag3Cu1 alloys were 10, 13, 13, and 15 HV, respectively. Using the Bailey-Hirsch relationship (Eq. 5.2), the dislocation number density could be estimated for each alloy [38, 39]. Accordingly, the approximate dislocation number densities for the CTMT base alloy and for the MTMT base, Cu3, Ag5 and Ag3Cu1 alloys are $2.8 \times 10^{14} \text{ m}^{-2}$, $0.4 \times 10^{14} \text{ m}^{-2}$, $0.7 \times 10^{14} \text{ m}^{-2}$, $0.7 \times 10^{14} \text{ m}^{-2}$ and $0.9 \times 10^{14} \text{ m}^{-2}$, respectively. Later, the dislocation contributions to the electrical resistivity could be calculated for each alloy based on the dislocation number densities.

$$\Delta \sigma^{\text{dislo}} = \alpha \cdot M \cdot G \cdot b \cdot \rho^{1/2} \quad (5.2)$$

Where ρ is the dislocation number density [39], $M = 2$ is the Taylor factor [40], α is a constant (0.3 for Al), G is the shear modulus (26.9 GPa for Al), and b is the Burgers vector (2.9 \AA for Al).

The approximation of the precipitation hardening could be calculated through the Orowan bypass mechanism. For the CTMT base alloy, the predominant disordered β' precipitates were characterized as non-shearable precipitates in the overaged condition (Fig. 5.6), as discussed in Ref. [5]. For MTMT alloys, identifying the precipitate's nature might be difficult based on their morphology and size due to the shearing of precipitates during cold wire drawing and the

coarsening of precipitates during post-aging [7]. Since all MTMT alloys were in the overaged condition when they reached the minimum required EC, it is reasonable to assume that the dominant precipitates were non-shearable in MTMT. Therefore, the Orowan equation (Eq. 5.3) could be adapted to calculate the precipitation hardening.

$$\Delta\sigma_{Or}^{prec} = \frac{2M\beta Gb}{L} \quad (5.3)$$

Where M, G and b were defined in Eq. 5.2, β is a dimensionless constant (0.28), and L is the interprecipitate spacing, which is measured as $L = \frac{1}{(N)^{1/3}}$ (where N is the precipitate number density) [39]. For the contribution of precipitates to the hardness of the CTMT base alloy and the MTMT base, the Cu3, Ag5 and Ag3Cu1 alloys are estimated to be 52.3, 82.9, 90.7, 92.2, and 90.2 HV, respectively.

The hardness increment from the grain boundary strengthening could be approximated by the classical Hall-Petch equation (Eq. 5.4) [39].

$$\Delta HV^{gb} = k_{HP}d^{-1/2} \quad (5.4)$$

In this relationship, k_{HP} is the Hall-Petch coefficient ($35 \text{ HV } \mu\text{m}^{1/2}$) for 6xxx series aluminum alloys, and d is the average grain size [39]. Since the average grain sizes were measured as $\sim 380 \mu\text{m}$ for all alloys, the contribution of the grain boundary strengthening is estimated as $\sim 2 \text{ HV}$ for all alloys, which is negligible compared to the total hardness.

Solid-solution strengthening can be calculated using the following equation [41].

$$\Delta\sigma_i^{sol} = k_i C_i^{2/3} \quad (5.5)$$

In this equation, k_i is the solid solution strengthening coefficient ($k_{Mg} \approx 29$, $k_{Si} \approx 66.3$, and $k_{Cu} \approx 46.4 \text{ MPa (wt.\%)}^{-2/3}$), and C_i is the concentration of solutes in solid solution form [41]. Given that the atom sizes of Ag (144 \AA) and Al (143 \AA) are close [15, 16, 23], it seems that a solid

solution of Ag in Al alloys has a negligible strengthening effect. According to our previous work [7], it was assumed that half of the Mg might remain in the matrix of the alloy with Mg/Si ~ 2 . In addition, the Si level was considered to be negligible in Mg-excessive alloys (Mg/Si ~ 2). Li et al. [42] reported that $\sim 20\%$ of the Cu addition could be taken apart in the precipitation and that $\sim 80\%$ of the Cu atoms might be left in the matrix. Accordingly, the solute strengthening for the CTMT base alloy and the MTMT base, Cu₃, Ag₅ and Ag₃Cu₁ alloys could be approximately calculated as 5, 5, 10, 5, and 8 HV, respectively.

A summary of the predicted contribution of different hardening mechanisms and a comparison with the experimentally measured hardness values is shown in Fig. 5.12. The predicted total hardness values were generally in good agreement with the experimentally measured values under various conditions. The slightly higher predicted hardness in the MTMT alloys (Ag₅, Cu₃ and Ag₃Cu₁) might be correlated to the overestimated solute strengthening. Precipitation and strain hardening play prominent roles in strengthening with an $\sim 80\%$ contribution of the total hardness. The MTMT led to enhanced precipitation hardening at the expense of strain hardening relative to the CTMT base alloy. As shown in Fig. 5.12, with the additions of Ag and Cu (Cu₃, Ag₅, Ag₃Cu₁ alloys), the precipitation hardening was further improved under MTMT. The increased precipitation hardening in the MTMT alloys is superior to the reduced strain hardening, and therefore the precipitation strengthening accounts for $\sim 80\%$ of all strengthening mechanism contributions, except for the aluminum matrix.

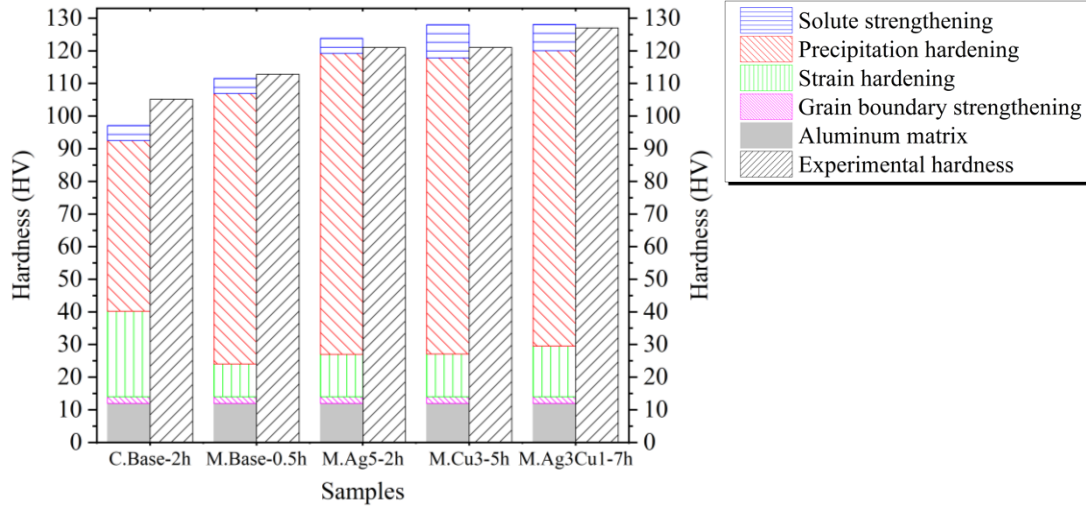


Figure 5.12 The comparison between predicted and experimentally measured hardness for C.Base-2h; M.Base-0.5h; M.Ag5-2h; M.Cu3-5h; and M.Ag3Cu1-7h alloys. C and M stand for the CTMT and MTMT, respectively.

Similar to the strengthening model, it is worth quantifying the electrical resistivity coming from the various microstructural features using Matthiessen's rule (Eq. 5.6) [43].

$$\rho_{\text{total}} = \rho^{\text{Al pure}} + \rho^{\text{DISLO}} + \rho^{\text{PREC}} + \rho^{\text{GB}} + \rho^{\text{SOL}} \quad (5.6)$$

Where ρ_{total} is the total electrical resistivity, $\rho^{\text{Al pure}}$ is the electrical resistivity of the AA1350-O alloy ($2.79 \times 10^{-6} \Omega \text{ cm}$ at room temperature) [44], and ρ^{DISLO} , ρ^{GB} , ρ^{PREC} and ρ^{SOL} are the electrical resistivity contributions from dislocations, grain boundaries, precipitates and solute atoms, respectively [38]. Eq. 5.7 could be employed to convert the electrical resistivity ($\mu\Omega \text{ cm}$) to electrical conductivity (% IACS) [43].

$$\text{EC (\% IACS)} = \frac{172.4}{\rho_{\text{total}} (\mu\Omega \text{ cm})} \quad (5.7)$$

The contribution of dislocations to the electrical resistivity could be estimated as [39].

$$\Delta\rho^{\text{DISL}} = L^{\text{dislo}} \Delta\rho^{\text{dislo}} \quad (5.8)$$

Where L^{dislo} is the dislocation density in m^{-2} , $\Delta\rho^{\text{dislo}}$ is the electrical resistivity per unit density of dislocations ($2.7 \times 10^{-25} \text{ } \Omega\text{m}^3$) [39]. Given the dislocation densities for the CTMT base alloy, and for the MTMT base, MTMT Cu3, MTMT Ag5 and MTMT Ag3Cu1 alloys, the electrical resistivities are 0.008, 0.001, 0.002, 0.002, and 0.003 $\mu\Omega \text{ cm}$ respectively, which is negligible compared to the total electrical resistivity.

The effect of precipitates on electrical resistivity of Al can be calculated through Eq. 5.9 [45].

$$\Delta\rho^{\text{PREC}} = \frac{\Delta\rho^{\text{prec}}}{(L^{\text{prec}})^{1/2}} \quad (5.9)$$

In this equation, $\Delta\rho^{\text{prec}}$ is the precipitate resistivity constant ($12 \text{ } \Omega(\text{nm})^{3/2}$), and L^{prec} is the average interprecipitate spacing (in nm) [45]. Considering the space between the precipitates, the contributions of precipitates to the electrical resistivity for the CTMT base alloy and for the MTMT base, the Cu3, Ag5 and Ag3Cu1 alloys were calculated to be 0.16, 0.20, 0.21, 0.21, and 0.21 $\mu\Omega\text{cm}$, respectively.

The impact of grain boundaries on the electrical resistivity can be evaluated as follows [39].

$$\Delta\rho^{\text{GB}} = S^{\text{GB}} \Delta\rho^{\text{gb}} \quad (5.10)$$

In this relationship, ($S^{\text{GB}} = 6/d$) is the bulk density of the grain boundaries with an average grain size (d), and $\Delta\rho^{\text{gb}}$ is the resistivity per unit concentration of grain boundaries ($2.6 \times 10^{-16} \text{ } \Omega\text{m}^2$) [39]. Considering the similar grain size for all alloys ($\sim 380 \text{ } \mu\text{m}$), the contribution of grain boundaries to resistivity is calculated as 0.0004 $\mu\Omega \text{ cm}$, which is also negligible compared to the total electrical resistivity.

The contribution of the solid solution to the electrical resistivity can be calculated by Eq. 5.11 [39].

$$\Delta\rho^{\text{SOL}} = \sum C_i^{\text{sol}} \Delta\rho_i^{\text{sol}} \quad (5.11)$$

Where C_i^{sol} is the solute concentration, and $\Delta\rho_i^{\text{sol}}$ is the resistivity per unit contribution of solute i , which is 0.445, 0.496, and 0.299 $\mu\Omega \text{ cm (at. \%)}^{-1}$ for Mg, Si [39], and Cu [46], respectively. Considering the similar atom radii of Ag and Al, a negligible electrical resistivity of the Ag solute in the Al matrix is assumed [23]. Based on the solute levels of Mg, Si and Cu, the solute electrical resistivities for the CTMT base alloy and for the MTMT base, Cu3, Ag5 and Ag3Cu1 alloys were estimated to be 0.14, 0.14, 0.21, 0.14, and 0.17 $\mu\Omega \text{ cm}$, respectively.

The total estimated electrical resistivities for the CTMT base alloy and the MTMT base, Cu3, Ag5 and Ag3Cu1 alloys are 3.101, 3.136, 3.212, 3.148, and 3.180 $\mu\Omega \text{ cm}$, respectively. Fig. 5.13 shows the contribution of the different factors to the electrical resistivity. It is apparent that the total electrical resistivity is mainly controlled by the solutes and precipitates for all alloys. The contributions of the grain boundaries and dislocations to electrical resistivity are too small to become visible. The electrical resistivities of the precipitates for the MTMT alloys are higher than those of the CTMT base alloy due to their higher precipitate number densities. Comparing Figs. 5.12 and 5.13, it is determined that the dislocations (strain hardening) showed a considerable contribution to the hardness, but with a negligible effect on the electrical resistivity.

The total estimated electrical resistivities for the CTMT base alloy and the MTMT base, Cu3, Ag5 and Ag3Cu1 alloys are 3.101, 3.136, 3.212, 3.148, and 3.180 $\mu\Omega \text{ cm}$, respectively. Fig. 5.13 shows the contribution of the different factors to the electrical resistivity. It is apparent that the total electrical resistivity is mainly controlled by the solutes and precipitates for all alloys. The contributions of the grain boundaries and dislocations to electrical resistivity are too small to become visible. The electrical resistivities of the precipitates for the MTMT alloys are higher than those of the CTMT base alloy due to their higher precipitate number densities. Comparing

Figs. 5.12 and 5.13, it is determined that the dislocations (strain hardening) showed a considerable contribution to the hardness, but with a negligible effect on the electrical resistivity.

Fig. 5.14 displays the plot of the hardness/EC for the predicted and experimental values for all alloys. The results of the hardness/EC predicted by the strength/electrical resistance models reflect the general tendency of the hardness/EC changes influenced by the main strengthening mechanisms, but the predicted values shift toward higher EC values relative to the experimental values. The reason is mainly related to the electrical resistance model, in which the predicted EC was at most 5% higher than the experimentally measured values. Based on Eq. 5.7, the estimated EC values for the CTMT base alloy and for the MTMT base, Cu3, Ag5 and Ag3Cu1 alloys are 55.59, 54.97, 53.66, 54.76, and 54.21% IACS, respectively, while the experimental EC values are 53, 53.3, 52.7, 53, and 52.7% IACS, respectively. It is worth noting that the electrical resistance of aluminum alloys is very sensitive to any crystal and microstructure change. Some crystal and microstructure parameters required in the electrical resistance model are difficult to determine and rely on the best estimation, which may vary over a relatively wide range. For instance, it is difficult to measure the solid solution level for each alloying element in a multicomponent aluminum system, even using advanced experimental techniques. However, any change in the solid solution level may result in a large change in the electrical resistance. Apparently, the current electrical resistance model based on Matthiessen's rule is still semiquantitative and needs further improvement.

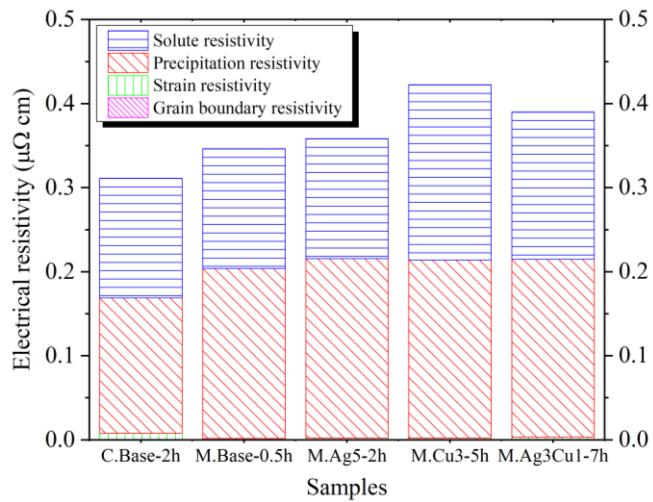


Figure 5.13 Electrical resistivity contributions of the different strengthening factors for all alloys. The resistivities of grain boundaries and dislocations to are not obvious here due to their small resistivity portions.

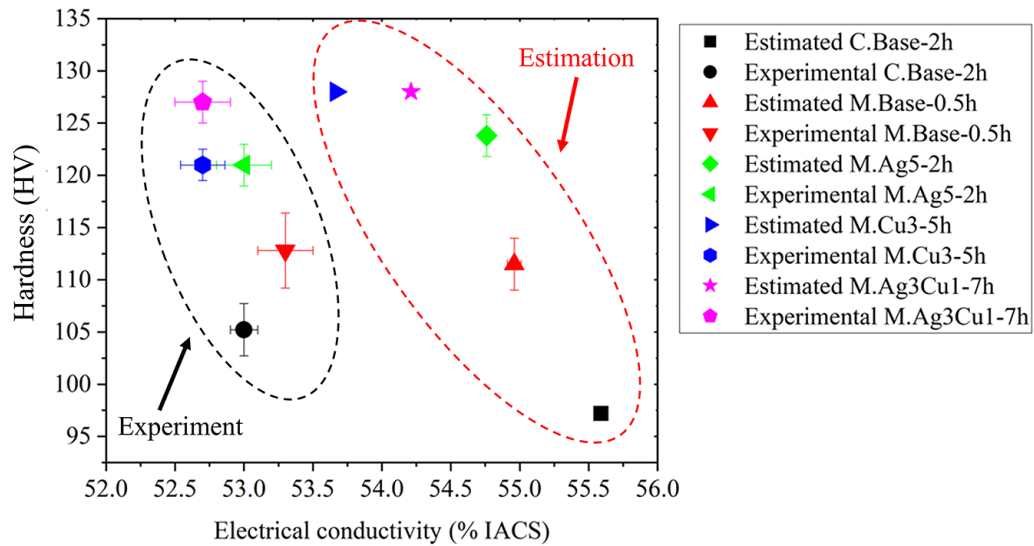


Figure 5.14 The comparison of the hardness/EC values between the estimated and experimental method

5.4.2. Correlation between strength and electrical conductivity

As shown in Fig. 5.2, the Ag and Cu additions showed a remarkable efficiency in terms of the peak hardness in MTMT (12-20 HV) and preaged conditions (10-14 HV) relative to CTMT (3-7 HV). Comparing the peak temperatures of the first precipitation peak in the as-drawn condition (i.e., peak I_d) with the as-quenched state (i.e., peak I), the copious dislocations in the CTMT alloys could somehow counteract the effect of the Ag and Cu additions on precipitation kinetics. The slightly increased peak hardness (3-7 HV) in the Cu3, Ag5 and Ag3Cu1 alloys relative to the base alloy using CTMT shows the dominant impact of the dislocations on the precipitation rather than Ag and Cu additions. Moreover, the DSC results revealed that the large quantities of dislocations prior to aging (the CTMT base alloy) could weaken the precipitation hardening response compared to the MTMT counterpart (Fig. 5.5c), which was confirmed by the TEM analysis in Fig. 5.6-5.8.

The maximum EC levels in the MTMT alloys are higher than those in the CTMT counterparts by (1-2)% IACS, suggesting that the modified thermomechanical treatment led to more purification of the matrix and a higher EC for all alloys. It should be noted that the atom radii of Al, Ag, and Cu are 1.43, 1.44, and 1.28 Å, respectively; hence, the zone misfits of Ag and Cu in the aluminum matrix are +0.7% and -10.5%, respectively [47]. Therefore, Cu could have a potentially more detrimental effect on EC than Ag, as discussed in Section 3.1. Accordingly, the alloy containing 0.42 wt.% Cu (Cu4) did not reach the minimum EC (52.5% IACS) under CTMT after 24 h of aging, while the alloy containing 0.53 wt.% Ag (Ag5) exceeded 52.5% IACS using CTMT after 4 h of aging. These results confirm that a high level of Cu in the Al-Mg-Si conductor alloy significantly limited EC in CTMT. However, MTMT could overcome the restriction of EC in Cu-added alloys, to some extent. The MTMT alloys met 52.5% IACS at a

shorter postaging time relative to the CTMT alloys (particularly Cu-added alloys), which could be an economical benefit. For instance, the Cu₃ and Ag₃Cu₁ alloys met the minimum required EC in CTMT after 24 h of aging but only after 5 and 7 h of aging in MTMT, respectively.

As displayed in Fig. 5.3, the MTMT base alloy showed a higher strength/EC than the CTMT base alloy. Furthermore, using MTMT, the Cu/Ag additions (the Ag₅, Cu₃ and Ag₃Cu₁ alloys) led to a further increased strength above 52.5% IACS relative to the base alloy. Therefore, the MTMT alloys generally exhibited a higher strength/EC than their counterparts under CTMT due to the enhanced precipitation hardening. In the traditional aging treatment (solution, quenching and aging) or preaging in this study, the contribution of the Ag/Cu atoms to the precipitation was observed with the addition of Ag and Cu [15, 16]. It was reported that the Ag and Cu atoms could remove some of the Mg atoms to form Ag/Cu-Mg clusters due to the strong interaction between Ag/Cu atoms and Mg atoms, evolving into Mg-Si-Ag/Cu co-clusters. These clusters along with the Mg-Si clusters resulted in a higher number density of stable precursors for the subsequent precipitates in Ag-/Cu-added alloys [15, 16]. It was expected that preaging in MTMT led to more Ag/Cu atoms being incorporated into copious precipitates to a significant extent, as confirmed in Ref. [15, 16]. Therefore, it is deduced that MTMT resulted in more extraction of the solutes from the aluminum matrix into the numerous precipitates, leading to a concurrently higher strength and higher EC levels.

In contrast, dense dislocations are the main favorable nucleation sites for precipitates in CTMT, particularly lath-like precipitates [5]. As mentioned earlier, Ag/Cu addition led to a slight increase in the peak hardness (Fig. 5.2) and hence a relatively higher precipitate number density under CTMT (Fig. 5.6). Therefore, it is suggested that the presence of dense dislocations might partly neutralize the efficiency of Ag/Cu atoms in clustering and precipitation.

5.5. Conclusions

1. The Ag and Cu additions had a relatively low impact on the strengths above the minimum required electrical conductivity (52.5% IACS) using a conventional thermomechanical treatment (CTMT) due to the strong effect of dislocations on the precipitation. However, the modified thermomechanical treatment (MTMT) maximized the strengthening effect of Ag and Cu additions on precipitation above 52.5% IACS. In addition, the postaging time was considerably reduced in order to reach the minimum required electrical conductivity (52.5% IACS) in MTMT compared to CTMT.
2. An increase in the Cu levels remarkably limited electrical conductivity in both CTMT and MTMT (particularly above 0.3 wt.% Cu) via the scattering electron by the remaining Cu solutes in the aluminum matrix. However, a 0.5 wt.% Ag addition in the Al-Mg-Si alloys still exhibited a reasonable electrical conductivity due to its similar atom radius to Al atoms and the small zone misfit of Ag in the aluminum matrix.
3. MTMT resulted in a wider window in the high end of strength and electrical conductivity compared to CTMT for all alloys. Pre-aging in MTMT maximized precipitation hardening at the expense of strain hardening. The superiority of precipitation hardening in the MTMT alloys led to a higher strength compared to the CTMT counterparts above the minimum electrical conductivity.
4. An improvement in precipitation strengthening could be a promising avenue in MTMT for obtaining a strength above the minimum electrical conductivity for an optimal compromise between the conflicting mechanical and the electrical properties of aluminum conductors. For instance, Ag and Cu addition under MTMT led to an increase in the precipitate

hardening contribution by 75%, while the resistivity portion of the precipitates only increased by 30%.

5. Strength and electrical resistance models were used to account for the multiple contributions of the main strengthening mechanisms and microstructure features to the mechanical strength and electrical conductivity, providing a useful tool for designing aluminum conductors and optimizing the mechanical and electrical properties.

Acknowledgment

The authors would like to acknowledge the financial support of the Natural Sciences and Engineering Research Council of Canada (NSERC) under the Grant No. CRDPJ 514651-17 and Rio Tinto Aluminum through the Research Chair in the Metallurgy of Aluminum Transformation at University of Quebec in Chicoutimi.

CRedit authorship contribution statement

Siamak Nikzad Khangholi: Methodology, Investigation, Formal analysis, Writing – original draft. **Mousa Javidani:** Conceptualization, Methodology, Writing – review & editing. **Alexandre Maltais:** Conceptualization, Validation, Writing – review & editing. **X.-Grant Chen:** Conceptualization, Validation, Writing – review & editing, Project administration.

Declaration of competing interest

The authors declare that they have no known competing financial interests or personal relationships that could have appeared to influence the work reported in this paper.

5.6. References

- [1] S. Karabay, Modification of AA-6201 alloy for manufacturing of high conductivity and extra high conductivity wires with property of high tensile stress after artificial aging heat treatment for all-aluminium alloy conductors, *Materials & Design* 27(10) (2006) 821-832.
- [2] G. Lin, Z. Zhang, H. Wang, K. Zhou, Y. Wei, Enhanced strength and electrical conductivity of Al–Mg–Si alloy by thermo-mechanical treatment, *Materials Science and Engineering: A* 650 (2016) 210-217.
- [3] C.H. Liu, J. Chen, Y.X. Lai, D.H. Zhu, Y. Gu, J.H. Chen, Enhancing electrical conductivity and strength in Al alloys by modification of conventional thermo-mechanical process, *Materials & Design* 87 (2015) 1-5.
- [4] C. Bunte, M. Glassel, C. Medina, D. Zalczman, Proposed Solution for Random Characteristics of Aluminium Alloy Wire Rods Due to the Natural Aging, *Procedia Materials Science* 9 (2015) 97-104.
- [5] S.N. Khangholi, M. Javidani, A. Maltais, X.G. Chen, Effects of natural aging and pre-aging on the strength and electrical conductivity in Al-Mg-Si AA6201 conductor alloys, *Materials Science and Engineering: A* 820 (2021) 1-12.
- [6] X. Xu, Z. Yang, Y. Ye, G. Wang, X. He, Effects of various Mg/Si ratios on microstructure and performance property of Al-Mg-Si alloy cables, *Mater. Charact.* 119 (2016) 114-119.
- [7] S. Nikzad Khangholi, M. Javidani, A. Maltais, X.G. Chen, Optimization of mechanical properties and electrical conductivity in Al–Mg–Si 6201 alloys with different Mg/Si ratios, *J. Mater. Res.* 35(20) (2020) 2765-2776.
- [8] S. Nikzad Khangholi, M. Javidani, A. Maltais, X.G. Chen, Investigation on electrical conductivity and hardness of 6xxx aluminum conductor alloys with different Si levels, *MATEC Web of Conferences* 326 (2020) 1-7.
- [9] H.C. Liao, Y. Liu, C.L. Lu, Q.G. Wang, Effect of Ce addition on castability, mechanical properties and electric conductivity of Al–0.3Si–0.2Mg alloy, *Int. J. Cast Met. Res.* 28(4) (2015) 213-220.
- [10] W. Yuan, Z. Liang, C. Zhang, L. Wei, Effects of La addition on the mechanical properties and thermal-resistant properties of Al–Mg–Si–Zr alloys based on AA 6201, *Materials & Design* 34 (2012) 788-792.
- [11] Q. Zhao, Z. Qian, X. Cui, Y. Wu, X. Liu, Influences of Fe, Si and homogenization on electrical conductivity and mechanical properties of dilute Al–Mg–Si alloy, *J. Alloys Compd.* 666 (2016) 50-57.
- [12] M.H. Mulazimoglu, A. Zaluska, J.E. Gruzleski, F. Paray, Electron microscope study of Al-Fe-Si intermetallics in 6201 aluminum alloy, *Metallurgical and Materials Transactions A* 27(4) (1996) 929-936.
- [13] M.H. Mulazimoglu, A. Zaluska, F. Paray, J.E. Gruzleski, The effect of strontium on the Mg₂Si precipitation process in 6201 aluminum alloy, *Metallurgical and Materials Transactions A* 28(6) (1997) 1289-1295.

- [14] EN 50183 standard. Conductors for overhead lines, aluminium magnesium silicon alloy wires (2000) 1-7.
- [15] Y. Weng, Z. Jia, L. Ding, S. Muraishi, Q. Liu, Clustering behavior during natural aging and artificial aging in Al-Mg-Si alloys with different Ag and Cu addition, *Materials Science and Engineering: A* 732 (2018) 273-283.
- [16] Y. Weng, Z. Jia, L. Ding, M. Liu, X. Wu, Q. Liu, Combined effect of pre-aging and Ag/Cu addition on the natural aging and bake hardening in Al-Mg-Si alloys, *Progress in Natural Science: Materials International* 28(3) (2018) 363-370.
- [17] Y. Weng, Z. Jia, L. Ding, Y. Pan, Y. Liu, Q. Liu, Effect of Ag and Cu additions on natural aging and precipitation hardening behavior in Al-Mg-Si alloys, *J. Alloys Compd.* 695 (2017) 2444-2452.
- [18] L. Ding, Z. Jia, Z. Zhang, R.E. Sanders, Q. Liu, G. Yang, The natural aging and precipitation hardening behaviour of Al-Mg-Si-Cu alloys with different Mg/Si ratios and Cu additions, *Materials Science and Engineering: A* 627 (2015) 119-126.
- [19] J. Kim, C. Daniel Marioara, R. Holmestad, E. Kobayashi, T. Sato, Effects of Cu and Ag additions on age-hardening behavior during multi-step aging in Al-Mg-Si alloys, *Materials Science and Engineering: A* 560 (2013) 154-162.
- [20] S. Duan, K. Matsuda, Y. Zou, T. Wang, Influence of two-stage ageing process and Cu additions on conductive Al alloys based on AA 6063, *Materials Research Express* 6(10) (2019).
- [21] ASTM, Annual Book of ASTM Standards: Electrical Conductors. Section 2. Volume 02.03 (2002).
- [22] ASTM, Annual Book of ASTM Standards: Nonferrous metal products. Aluminum and magnesium alloys. Section 2. Volume 02.02 (2003).
- [23] A. Mamala, T. Knych, P. Kwaśniewski, A. Kawecki, G. Kiesiewicz, E. Sieja-Smaga, W. Ścieżor, M. Gnielczyk, R. Kowal, New Al-Ag Alloys for Electrical Conductors with Increased Current Carrying Capacity, *Archives of Metallurgy and Materials* 61(4) (2016) 1875-1880.
- [24] O. Engler, C.D. Marioara, Y. Aruga, M. Kozuka, O.R. Myhr, Effect of natural ageing or pre-ageing on the evolution of precipitate structure and strength during age hardening of Al-Mg-Si alloy AA 6016, *Materials Science and Engineering: A* 759 (2019) 520-529.
- [25] G.A. Edwards, K. Stiller, G.L. Dunlop, M.J. Couper, The precipitation sequence in Al-Mg-Si alloys, *Acta Mater.* 46(11) (1998) 3893-3904.
- [26] R.S. Yassar, D.P. Field, H. Weiland, The effect of predeformation on the β'' and β' precipitates and the role of Q' phase in an Al-Mg-Si alloy; AA6022, *Scripta Mater.* 53(3) (2005) 299-303.
- [27] H. Nemour, D. Mourad Ibrahim, A. Triki, The effect of heavy cold plastic deformation on the non-isothermal kinetics and the precipitation sequence of metastable phases in an Al-Mg-Si alloy, *J. Therm. Anal. Calorim.* 123(1) (2015) 19-26.
- [28] K. Teichmann, C.D. Marioara, S.J. Andersen, K.O. Pedersen, S. Gulbrandsen-Dahl, M. Kolar, R. Holmestad, K. Marthinsen, HRTEM study of the effect of deformation on the early precipitation behaviour in an AA6060 Al-Mg-Si alloy, *Philos. Mag.* 91(28) (2011) 3744-3754.

- [29] L. Ding, Z. Jia, Y. Liu, Y. Weng, Q. Liu, The influence of Cu addition and pre-straining on the natural aging and bake hardening response of Al-Mg-Si alloys, *J. Alloys Compd.* 688 (2016) 362-367.
- [30] H.W.Z. S.J. Andersen, J. Jansen, C. TrÆholt, U. Tundal, O. Reiso, The crystal structure of the β'' phase in Al-Mg-Si alloys, *Acta Mater* (1998) 3283-3298.
- [31] J. Kim, C. Daniel Marioara, R. Holmestad, E. Kobayashi, T. Sato, Effects of Cu and Ag additions on age-hardening behavior during multi-step aging in Al-Mg-Si alloys, *Materials Science and Engineering: A* 560 (2013) 154-162.
- [32] L.M. Cheng, W.J. Poole, J.D. Embury, D.J. Lloyd, The influence of precipitation on the work-hardening behavior of the aluminum alloys AA6111 and AA7030, *Metallurgical and Materials Transactions A* 34(11) (2003) 2473-2481.
- [33] H. Li, M. Qingzhong, Z. Wang, F. Miao, B. Fang, R. Song, Z. Zheng, Simultaneously enhancing the tensile properties and intergranular corrosion resistance of Al-Mg-Si-Cu alloys by a thermo-mechanical treatment, *Materials Science and Engineering: A* 617 (2014) 165-174.
- [34] J.K. Sunde, C.D. Marioara, S. Wenner, R. Holmestad, On the microstructural origins of improvements in conductivity by heavy deformation and ageing of Al-Mg-Si alloy 6101, *Mater. Charact.* 176 (2021) 1-11.
- [35] J.G. Kaufman, *Introduction to Aluminum Alloys and Tempers*, ASM International 2000.
- [36] Y. Han, D. Shao, B.A. Chen, Z. Peng, Z.X. Zhu, Q. Zhang, X. Chen, G. Liu, X.M. Li, Effect of Mg/Si ratio on the microstructure and hardness-conductivity relationship of ultrafine-grained Al-Mg-Si alloys, *Journal of Materials Science* 52(8) (2016) 4445-4459.
- [37] S. Jiang, R. Wang, Grain size-dependent Mg/Si ratio effect on the microstructure and mechanical/electrical properties of Al-Mg-Si-Sc alloys, *Journal of Materials Science & Technology* 35(7) (2019) 1354-1363.
- [38] A. Mohammadi, N.A. Enikeev, M.Y. Murashkin, M. Arita, K. Edalati, Developing age-hardenable Al-Zr alloy by ultra-severe plastic deformation: Significance of supersaturation, segregation and precipitation on hardening and electrical conductivity, *Acta Mater.* 203 (2021) 1-16.
- [39] X. Sauvage, E.V. Bobruk, M.Y. Murashkin, Y. Nasedkina, N.A. Enikeev, R.Z. Valiev, Optimization of electrical conductivity and strength combination by structure design at the nanoscale in Al-Mg-Si alloys, *Acta Mater.* 98 (2015) 355-366.
- [40] Y.J. Li, A.M.F. Muggerud, A. Olsen, T. Furu, Precipitation of partially coherent α -Al(Mn,Fe)Si dispersoids and their strengthening effect in AA 3003 alloy, *Acta Mater.* 60(3) (2012) 1004-1014.
- [41] O.R. Myhr, O. Grong, S.J. Andersen, Modelling of the age hardening behaviour of Al-Mg-Si alloys, *Acta Mater.* 49(1) (2001) 65-75.
- [42] K. Li, A. B  ch  , M. Song, G. Sha, X. Lu, K. Zhang, Y. Du, S.P. Ringer, D. Schryvers, Atomistic structure of Cu-containing β'' precipitates in an Al-Mg-Si-Cu alloy, *Scripta Mater.* 75 (2014) 86-89.

- [43] W. Wen, Y. Zhao, J.G. Morris, The effect of Mg precipitation on the mechanical properties of 5xxx aluminum alloys, *Materials Science and Engineering: A* 392(1-2) (2005) 136-144.
- [44] ASTM, *Annual Book of ASTM Standards, Electrical Conductors* (2002).
- [45] B. Raeisinia, W.J. Poole, D.J. Lloyd, Examination of precipitation in the aluminum alloy AA6111 using electrical resistivity measurements, *Materials Science and Engineering: A* 420(1) (2006) 245-249.
- [46] L. Pan, K. Liu, F. Breton, X.G. Chen, Effects of minor Cu and Mg additions on microstructure and material properties of 8xxx aluminum conductor alloys, *J. Mater. Res.* 32(06) (2017) 1094-1104.
- [47] D.A. Porter, K.E. Easterling, *Phase Transformations in Metals and Alloys, Third Edition (Revised Reprint)*, Taylor & Francis (1992).

Chapter 6 Conclusions

General conclusions

In this project, it was shown that the choice of the optimum levels of alloying elements (Mg, Si, Ag, and Cu) could lead to a better combination of the strength and electrical conductivity. However, to get the maximized effect of these alloying elements on the precipitate strengthening, it was required to apply the modified thermomechanical treatment (pre-aging) to the samples. The modified thermomechanical treatment remarkably increased the precipitate strengthening. In the Al-Mg-Si alloys with Mg/Si of ~ 2 (in at. %), the modified thermomechanical treatment not only increased the strength but also improved the electrical conductivity, which stems from the extraction of the solutes out of the matrix into the copious precipitates.

In addition, the models of electrical resistivity (Matthiessen's rule) and strength tailored the microstructural features with the strength and electrical conductivity. Based on these models, it was found that the precipitates could outstandingly increased the strength with a moderate electrical resistivity via the modified thermomechanical treatment (pre-aging). However, the strain hardening became almost half with applying pre-aging compared to the conventional thermomechanical treatment. The strength and electrical resistivity models showed that the dislocation hardening has a significant portion of the strengthening while a negligible resistivity was found for the dislocations in the conventional thermomechanical treatment. However, it was proved that the introduction of the dense dislocations during the wire drawing deteriorated the precipitate hardening to some extent in the conventional thermomechanical treatment. The strength and electrical resistivity models revealed that the solute atoms led to a low portion of the strengthening with a relatively high electrical resistivity. The summary of the conclusions from all parts is listed below.

1. The higher peak hardness with a lower electrical conductivity was acquired in the alloys with lower Mg/Si ratios ($\text{Mg/Si} \leq 1$) compared to those with higher Mg/Si ratios ($1 \leq$

Mg/Si \leq 2) in the conventional thermomechanical treatment. The Si excessive alloys (Mg/Si \leq 1) were exposed to a longer overaging time to meet the minimum required EC (52.5% IACS).

2. If the strength is the priority, the alloy with the Mg/Si ratio of \sim 1 showed the highest strength in the EC range of 52.5–54 %IACS among all alloys studied under the conventional thermomechanical treatment. However, the alloy with an Mg/Si ratio of \sim 1.5 could be considered as an appropriate alternative on the high end of EC (54-56 %IACS), provided the electrical conductivity is the main concern.
3. The Si-excessive alloy (Mg/Si \approx 0.86) showed the highest peak strength. However, this alloy was required to be exposed to more overaging ($>$ 34 h) to exceed EC (52.5 %IACS). It gave rise to the considerably reduced strength and a limited window of strength and electrical conductivity.
4. The impact of natural aging and modified thermomechanical treatment (pre-aging) on the strength and electrical conductivity were studied for Al-Mg-Si alloy in the second part of this project. The alloy with Mg/Si \sim one was chosen for this research because it showed the highest strength above the minimum required electrical conductivity in the first part.
5. DSC results showed that the natural aging without the following wire drawing was detrimental in terms of precipitation response. However, the wire drawing counteracted the negative effect of the natural aging on the strengthening and turned it into a benefit; meaning that the naturally aged samples showed a higher strength above 52.5 %IACS relative to the samples without natural aging after wire drawing and post-aging.
6. The higher strength of the naturally aged samples compared to the samples without natural aging above 52.5 %IACS was ascribed to their higher precipitate number density, while they exhibited a similar strain hardening contribution.
7. The pre-aging following the natural aging (the modified thermomechanical treatment) showed the highest strength (\sim 369 MPa) above 52.5% IACS among all samples. The pre-

aging treatment prior to wire drawing maximized precipitate strengthening while the strain hardening portion reduced. Accordingly, the superiority in the precipitate strengthening overcame the inferiority in the strain hardening for the 20NA-PA sample, leading to the highest strength among all samples above 52.5 %IACS.

8. The Ag and Cu additions to Al-Mg-Si conductor alloys ($Mg/Si \approx 2$) were investigated using the modified the conventional thermomechanical treatment. The modified thermomechanical treatment (pre-aging) was chosen because it exhibited a higher strength compared to the conventional thermomechanical treatment in the second part of this project.
9. The maximized effects of Ag and Cu additions on the strengthening above 52.5 %IACS were acquired under the modified thermo-mechanical treatment rather than the conventional thermomechanical treatment. Besides, a shorter post-aging time was required for the modified thermomechanical treatment during post-aging to reach 52.5 %IACS compared to the conventional thermomechanical treatment, which might be economically benefit.
10. The modified thermomechanical treatment led to a superior electrical conductivity (1-2 %IACS) and a higher strength (5-20 HV) relative to the conventional thermomechanical treatment.
11. Modifying the thermomechanical treatment led to the remarkably increase in precipitate strengthening in the base alloy at the expense of strain hardening. The Ag and Cu additions further increased the precipitate strengthening under the modified thermomechanical treatment. Therefore, the precipitates play promising roles in the modified thermomechanical treatment to meet the conflicting properties of the conductors because they exhibited a high strengthening portion with a medium electrical resistivity.

12. The copper additions more reduced the electrical conductivity relative to the Ag additions due to its larger misfit in the aluminum matrix in either the conventional or the modified thermomechanical treatment.

Recommendations

In this project, an improvement of the strength and electrical conductivity were acquired via optimizing Mg/Si ratios, modifying thermomechanical treatment, and adding the Ag and Cu additions. There yet remains several additional issues that are worth investigating. Herein, some suggestions for future work are proposed.

1. Finding an appropriate intermediate aging might be a key factor leading to the high strength with a desirable electrical conductivity.
2. The Sc and Zr additions to the Al-Mg-Si conductor alloys might be interesting since these alloying elements could make a better strength at room and elevated temperatures along with the thermal stability.
3. Given that the Al-Mg-Si conductor alloys might be exposed to the creep deformation, it is worthwhile to investigate how to improve their creep resistance under the service condition.
4. A comprehensive study is needed to reveal the effect of microalloying elements, such as Sr and Bi, on the electrical and mechanical properties of Al-Mg-Si 6xxx conductor alloys.
5. As the grain structures were somehow large in this project, it is worth maximizing the precipitate strengthening above the minimum required electrical conductivity in the fine-grained Al-Mg-Si conductor alloys produced by the severe plastic deformation.
6. In this project, the strength was increased above the minimum required electrical conductivity. On the other hand, it could be interesting to enhance electrical conductivity above the minimum required strength.
7. The Ag additions to the Al-Mg-Si conductor alloys with Mg/Si of one under the modified thermomechanical treatment is recommended to investigate in terms of the evolution of the strength and electrical conductivity.

Appendix I: Supporting information for article 2

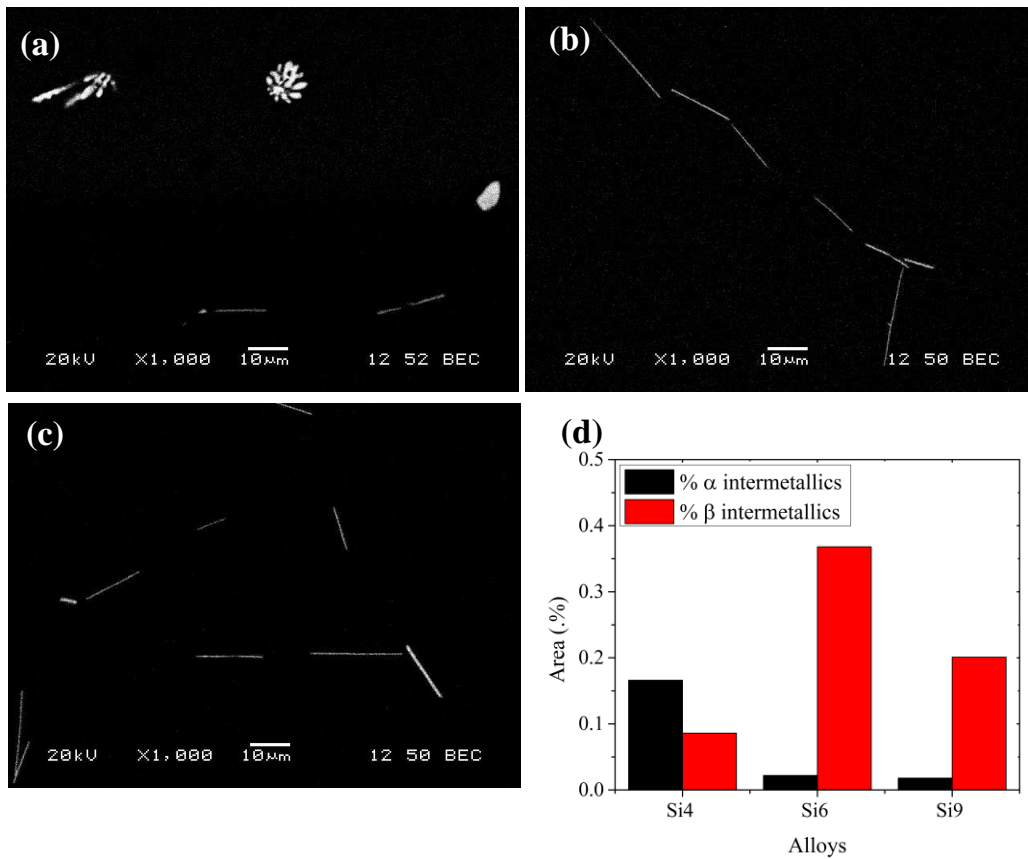


Figure (AI) 1 Distribution of Fe-rich intermetallics after homogenization in (a) Si4 (b) Si6 (c) Si9 alloys; (d) the area percentage of Fe-rich intermetallics in three alloys

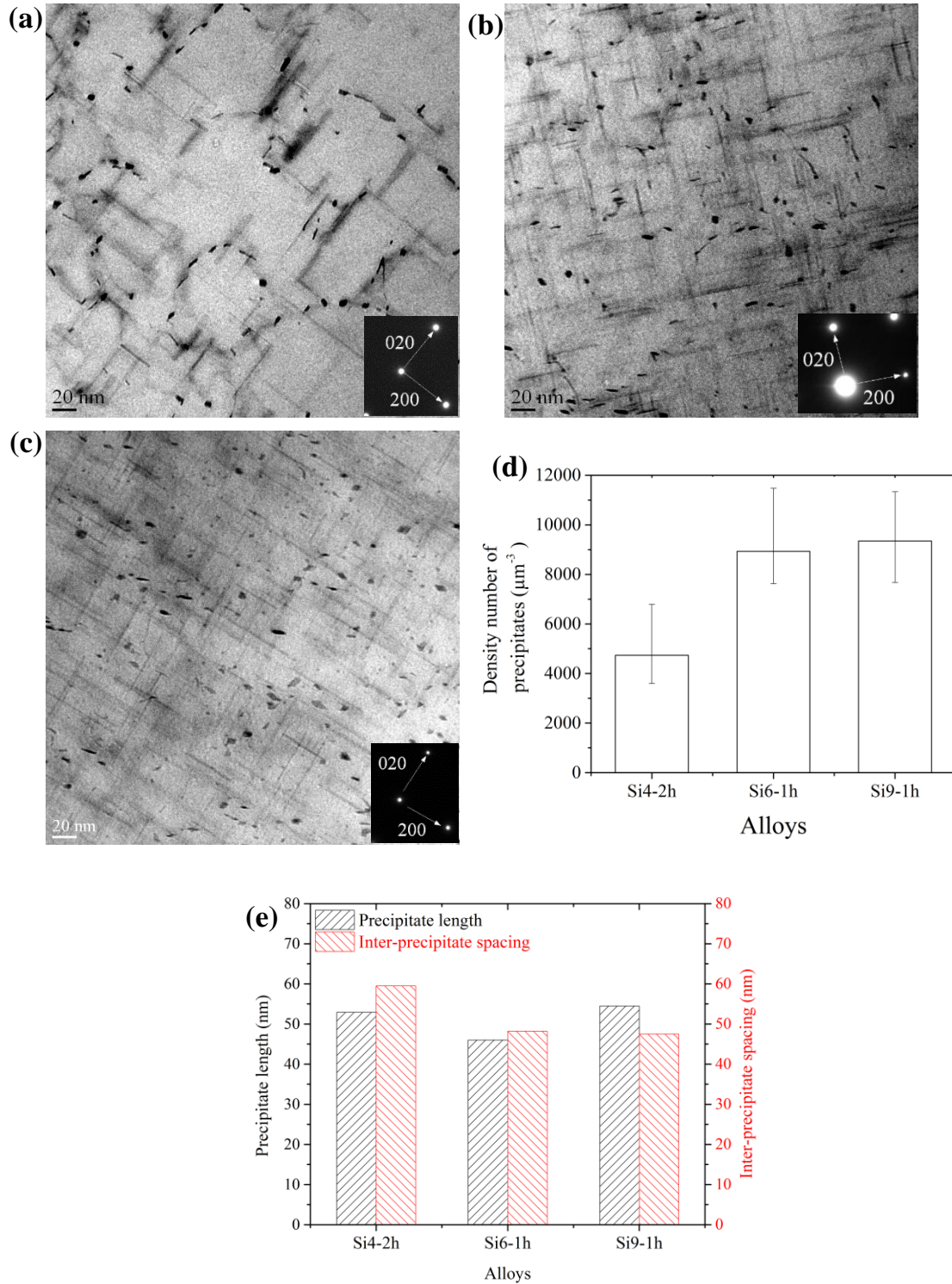


Figure (AI) 2 Precipitate distribution at peak aging state for (a) Si4 alloy after 2h (b) Si6 alloy after 1h (c) Si9 alloy after 1h (aging at 180 °C); (d) the average number density of precipitates for three alloys; (e) the mean precipitate length and inter-precipitate spacing for three alloys

Appendix II: The general description of procedure

Fig. 1 and Fig. 2 display the general description of processing fabrication from the casting to the wire drawing. As shown in Fig. 1a, first the alloys were cast in a steel permanent mold (preheated at 250 °C) to obtain cast ingots form of Y-block (Fig. 1a). Then they were cut into the rectangular cube (Fig. 1b), followed by scalping (Fig. 1c). Afterwards, the homogenization process was carried out at 560°C for 6h. The homogenized samples were preheated at 500 °C, and then the hot rolling process was performed in several passes, by which the thickness decrease from 26.5mm to 7.6mm. It should be noted that the temperature of the samples was kept in 380-480 °C during the hot rolling process. The detailed description of the hot rolling process is summarized in table. 1 Then this plate with 7.6mm thickness was cut into square bars (6.5-7mm * 6.5-7mm). Afterwards, the solution treatment at 540 °C for 2h was applied to the samples. Finally, the cold wire drawing and aging heat treatment (at 180 °C) were carried out. In the cold wire drawing, the square bars (6.5-7mm * 6.5-7mm) were drawn into the wires with the diameter of 4.3-4.7mm.

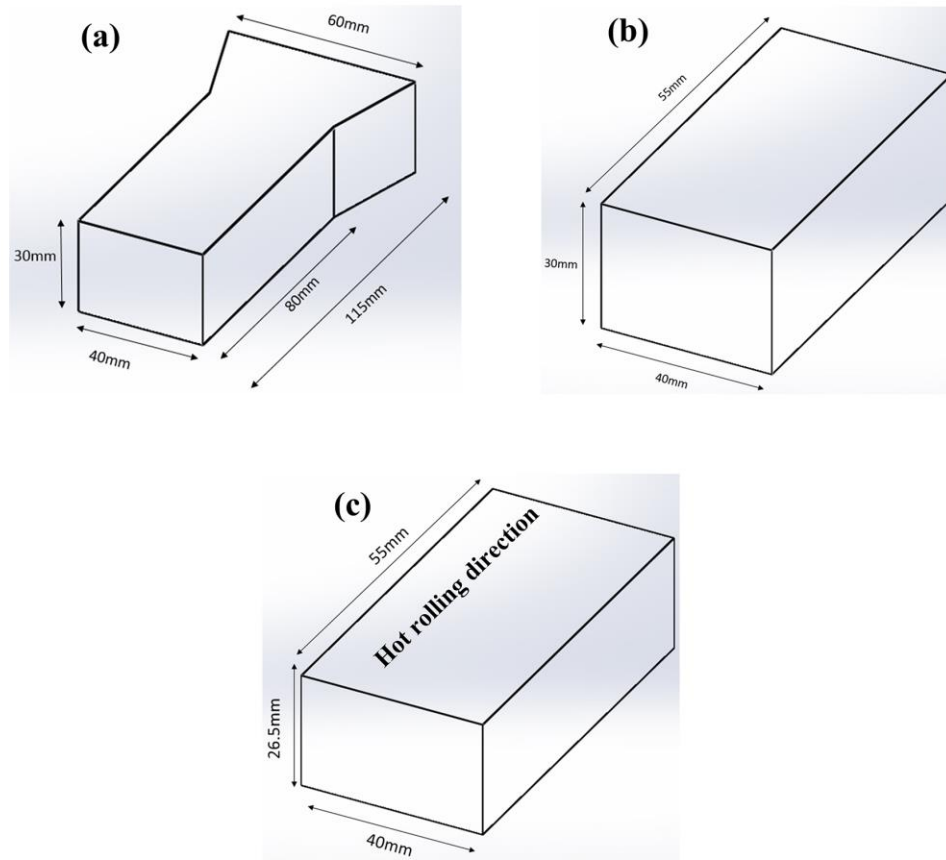


Figure (AII) 3 (a) Casting the alloys in the shape of Y-block; (b) Cutting the as-cast samples in rectangular block (30mm*40mm*55 mm); (c) Scalping (1.75mm from each side)

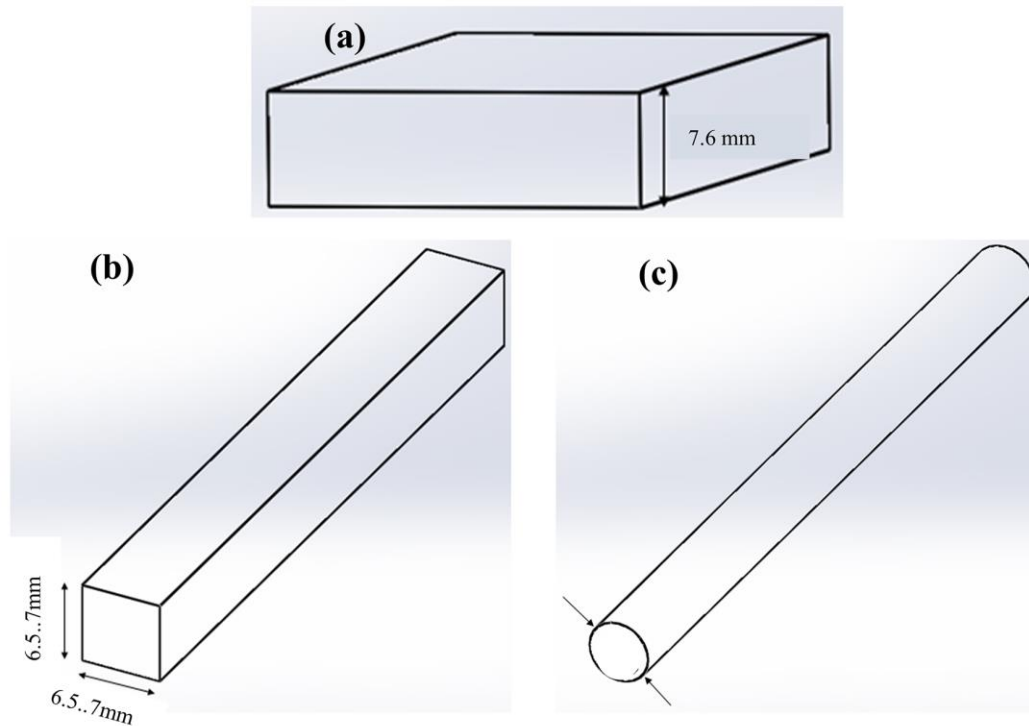


Figure (AII) 4 (a) Performing the hot rolling process on the plate with the thickness of 26.5mm into 7.6mm at 380-480°C; (b) Cutting and machining the hot-rolled samples into the square rods with the cross section of (6.5...7mm)*(6.5...7mm); wire drawing down to the diameter of 4.3...4.7mm

Table (AII) 1 General description of the hot rolling process

No.	Description
1	Keeping the samples at 500 °C for 2h (initial plate thickness = 26.5mm)
2	Reducing the thickness by two passes (1 st pass = 2.4mm- 2 nd pass = 1.6mm), then keeping at 500°C/20min
3	Reducing the thickness by two passes (1 st pass = 1.6mm- 2 nd pass = 3.2mm), then keeping at 500°C/20min
4	Reducing the thickness by one pass (3.2mm), then keeping at 500°C for 20min
5	Reducing the thickness by one pass (3.2mm), then keeping at 500°C for 20min
6	Reducing the thickness by one pass (1.6mm), then keeping at 500°C for 20min
7	Reducing the thickness by one pass (2mm), then quenching into water

List of the publications

Journal papers:

1. Optimization of mechanical properties and electrical conductivity in Al–Mg–Si 6201 alloys with different Mg/Si ratios, “SN Khangholi, M Javidani, A Maltais, XG Chen” - **Journal of Materials Research** 35 (20), 2765-2776
2. Effects of natural aging and combined pre-aging on the strength and electrical conductivity in Al-Mg-Si AA6201 conductor alloys, “SN Khangholi, M Javidani, A Maltais, XG Chen” - **Mater. Sci. Eng. A (820), 2021, 141538.**
3. Investigation on electrical conductivity and hardness of 6xxx aluminum conductor alloys with different Si levels, “SN Khangholi, M Javidani, A Maltais, XG Chen” **MATEC Web of Conferences 326.**
4. Critical review on recent progress in Al-Mg-Si conductor alloys, “SN Khangholi, M Javidani, A Maltais, XG Chen” – submitted to **Journal of Materials Research, under journal review.**
5. Effect of Cu and Ag on the strength and electrical conductivity in Al-Mg-Si cable using conventional and modified thermo-mechanical treatment, “SN Khangholi, M Javidani, A Maltais, XG Chen”, submitted to **Journal of alloys and compounds.**

Posters

1. Optimization of electrical conductivity and mechanical properties in 6xxx conductor alloys with various Mg/Si ratios, “Siamak Nikzad Khangholi, X. Grant Chen, Mousa Javidani”, REGAL Students’ Day, Chicoutimi, Canada, October. 2019.

2. Effect of natural aging on the strength and electrical conductivity in Al-Mg-Si AA6201 conductor alloys, “SN Khangholi, M Javidani, A Maltais, XG Chen”, REGAL Students’ Day, Chicoutimi, Canada, November. 2020.
3. Effect of Ag and Cu additions on the strength and electrical conductivity in Al-Mg-Si alloys using conventional and modified thermomechanical treatment, “SN Khangholi, M Javidani, A Maltais, XG Chen”, REGAL Students’ Day, Chicoutimi, Canada, November. 2021.

Presentation

1. Improvement of Mechanical Strength and Electrical Conductivity in Al-Mg-Si Conductor Alloys, “SN Khangholi, M Javidani, A Maltais, XG Chen”, REGAL Students’ Day, Chicoutimi, Canada, November. 2021.

